Star Formation in the Perseus Molecular Cloud: A Detailed Look at Star-Forming Clumps with Herschel

by

Sarah I. Sadavoy
B.Sc., York University, 2007
M.Sc., University of Victoria, 2009

A Dissertation Submitted in Partial Fulfillment of the
Requirements for the Degree of

DOCTOR OF PHILOSOPHY

in the Department of Physics and Astronomy

Star Formation in the Perseus Molecular Cloud: A Detailed Look at Star-Forming Clumps with Herschel

by

Sarah I. Sadavoy
B.Sc., York University, 2007
M.Sc., University of Victoria, 2009

Supervisory Committee

Dr. J. Di Francesco, Co-Supervisor
(Physics and Astronomy)

Dr. S. Ellison, Co-Supervisor
(Physics and Astronomy)

Dr. K. Venn, Departmental Member
(Physics and Astronomy)

Dr. N. Frank, Outside Member
(Chemistry)

Supervisory Committee

Dr. J. Di Francesco, Co-Supervisor
(Physics and Astronomy)

Dr. S. Ellison, Co-Supervisor
(Physics and Astronomy)

Dr. K. Venn, Departmental Member
(Physics and Astronomy)

Dr. N. Frank, Outside Member
(Chemistry)

ABSTRACT

This dissertation presents new *Herschel* observations at 70 μm, 160 μm, 250 μm, 350 μm, and 500 μm of the Perseus molecular cloud from the *Herschel* Gould Belt Survey. The Perseus molecular cloud is a nearby star-forming region consisting of seven main star-forming clumps. The *Herschel* observations are used to characterize and contrast the properties of these clumps, and to study their embedded core populations. First, we probed the exceptionally young clump, B1-E. Using complementary molecular line data, we demonstrate that B1-E is likely fragmenting into a first generation of dense cores in relative isolation. Such a core formation region has never been observed before. Second, we use complementary long wavelength observations at 850 μm to study the dust properties in the larger, more active B1 clump. We find that *Herschel* data alone cannot constrain well the dust properties of cold dust emission and that long wavelength observations are needed. Additionally, we find evidence of dust grain growth towards the dense cores in B1, where the dust emissivity index, β, varies from the often assumed value of $\beta = 2$. In the absence of long wavelength observations, however, assuming $\beta = 2$ is preferable over measuring β with the *Herschel*-only bands. Finally, we use the source extraction code, *getsources*, to identify the core populations within each clump from the *Herschel* data. In addition, we use complementary archival infrared observations to study their populations of young

stellar objects (YSOs). We find that the more massive clumps have an excess of older stage YSOs, suggesting that these regions contracted first. Starless cores are typically associated with peaks in the column density, where those found towards regions of higher column density also have higher average densities and colder temperatures. Starless cores associated with a strong, local interstellar radiation field, however, have higher temperatures. We find that the clumps with the most prominent high column density tails also had the highest fractions of early-stage YSOs. This relation suggests that the quantity of high column density material corresponds to recent star formation activity.

Contents

List of Tables

List of Figures

ACKNOWLEDGEMENTS

I
am
very
grateful
to many
people. To
my supervisor,
James, thank you
for being an amazing
mentor and guide. This
thesis is possible because
of you. To my supervisory committee, thank you for your support and advice. To Shadi,
Cassie, Andy, Rachel, Helen, and Scott, thank you for being such amazing
collaborators and friends. To my fellow astronomy grads, thank you
for astroBEER and for ensuring that I had fun too. To Jenny,
Philippe, and the entire Herschel and JCMT GBS
consortia, thank you for the opportunity to
take a lead role with exceptional
data. To the astronomers, telescope
operators, and staff scientists too many
to name, thank you everyone for all of the
help along the way. Lastly, to my wonderful
family, thank you for your unfailing love
and encouragement. Thank you Mom,
Dad, Robin, Mike, and Jake.
Everything that I am is
because of all
of you.

DEDICATION

To everyone who inspired my interest in Astronomy.

It started with trips to open, dark spaces to watch meteor showers as a child. It blossomed with a special unit on Astronomy in Grade 5 by a student teacher. It grew with a visit to York Observatory to see a comet through a telescope as a teen. It matured with the chance to work at the York Observatory while in high school.

All of these events and all of you made this thesis possible. Thank you one and all.

Chapter 1

Introduction

Stars form in dense regions of molecular gas and dust. These regions, called **molecular clouds**, are typically $\sim$ 10 parsec (1 pc = 3.086 x 10^{18} cm) in size and have densities of $\sim$ 300 particles cm^{-3}, nearly 100 times more dense than the interstellar medium (ISM; Stahler & Palla 2005). Molecular clouds are also very cold. Due to their high densities, the interiors of molecular clouds are well shielded from the interstellar radiation field, which would otherwise ionize and heat the interior gas (Evans et al. 2001). Furthermore, molecular gas is an efficient coolant. In molecular clouds, molecules can be excited through collisions. This energy is then re-radiated at longer wavelengths and easily escapes the cloud. Thus, molecular clouds tend to have temperatures of < 50 K. Such cold, dense environments are necessary for gravity to dominate over thermal pressures and allow gas to condense into stars (Stahler & Palla 2005). Figure 1.1 shows the CO column density (i.e., the amount of material in the line of sight) for the Taurus Molecular Cloud. In particular, Figure 1.1 shows that molecular clouds are highly structured with a complex network of dense filaments. Along the filaments are dense clumps, which are $\sim$ 1 pc substructures of densities $\gtrsim$ 1 x 10^3 cm^{-3}.

Higher column densities of gas and dust along the line-of-sight can increase the cloud opacity. Opacity denotes the amount of emission removed from a beam of light propagating through a medium such that $\tau_\lambda = 1$ defines a unitless distance where the beam intensity at some wavelength is reduced by 1/e. In astronomy, opacity is often expressed in terms of the "optical depth." At high optical depths ($\tau_\lambda \gg 1$) the light received comes mostly from a short distance into the medium (i.e., only the outer surface can be detected), and the medium is designated "optically thick" or opaque. Conversely, at low optical depth emission ($\tau_\lambda \ll 1$) the light received comes

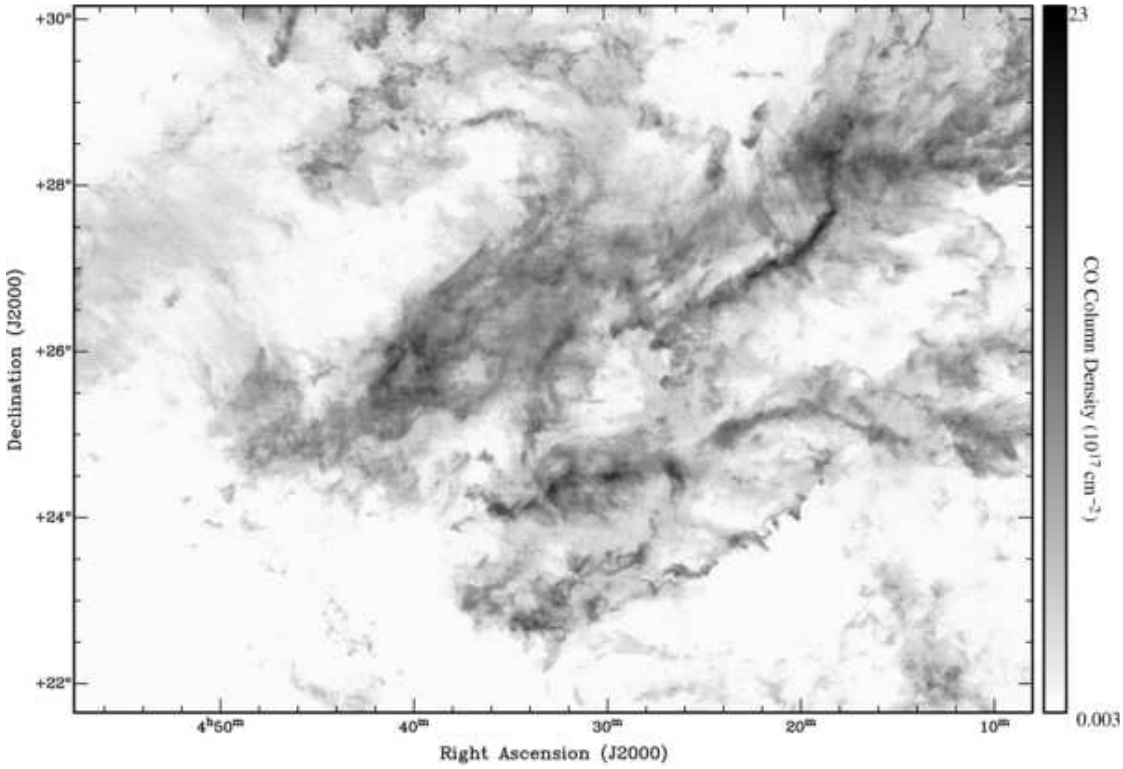

Figure 1.1: CO column densities towards the Taurus Molecular Cloud. Column densities were determined from the ^{13}CO $J = 1 \rightarrow 0$ line emission. Figure from Pineda et al. (2010b).

from long distances into the medium or perhaps the entire medium, and the medium is designated "optically thin" or transparent. Optical depth depends on the characteristics of the material along the line-of-sight. In molecular clouds, the optical depth of molecular emission lines depends on abundances (higher column densities) such that highly abundant molecules have optically thick lines. The optical depth of dust continuum emission depends on the abundance of dust and the wavelength of light (Stahler & Palla 2005). For example, Figure 1.2 shows visual and near-infrared continuum observations of a small cloud, Barnard 68 (B68). At the shortest wavelengths (0.44 - 0.90 μm), B68 is opaque to background starlight, but at longer wavelengths (2.16 μm), B68 becomes transparent and background stars are visible. Thus, B68 is optically thick to optical radiation but optically thin at longer wavelengths.

Molecular clouds are primarily composed of molecular hydrogen (H_2) gas. Unfortunately, H_2 is a symmetric molecule with no electric dipole moment. H_2 molecules can radiate via quadrupole transitions, but temperatures > 500 K are required to populate these higher energy levels. Since molecular clouds have typical tempera-

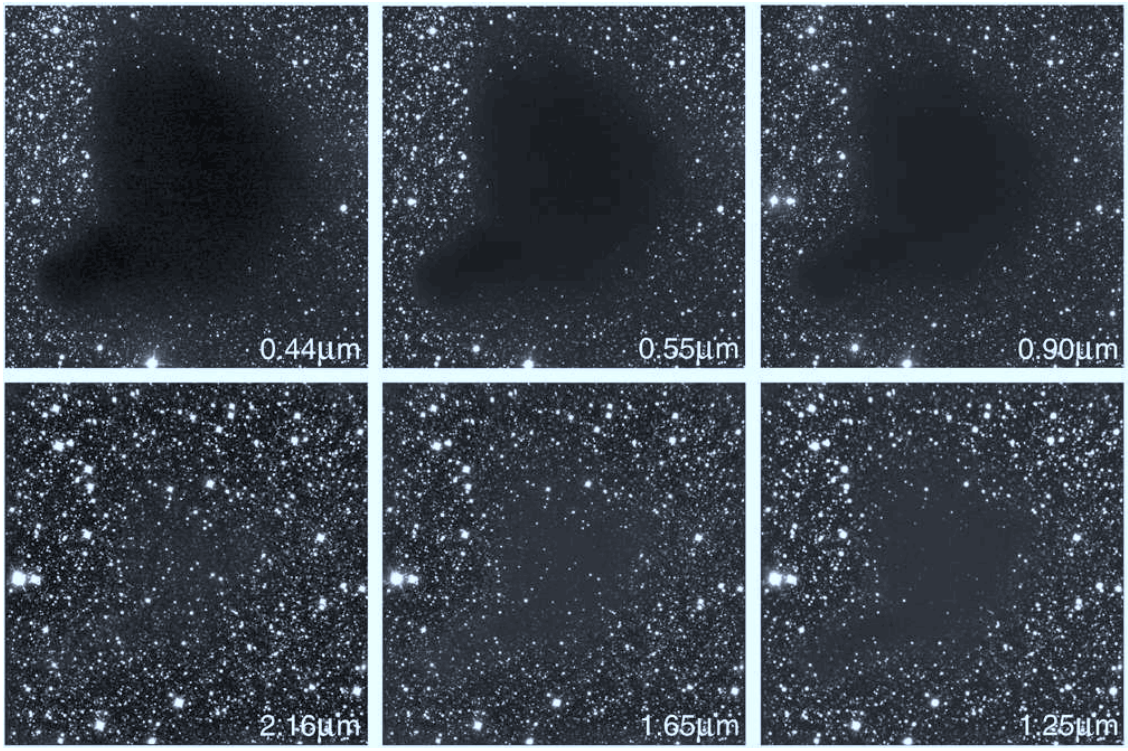

Figure 1.2: The molecular clump Barnard 68 (B68) in the constellation Ophiuchus. B68 has a mean density of $\sim 10^4$ cm^{-3} (Burkert & Alves 2009), which makes the region opaque to background stars at visible wavelengths (i.e., 0.44 μm). At near-infrared wavelengths (bottom panels), the cloud is optically thin and background starlight can propagate through the dense cloud. This image was taken from an ESO press release, http://www.eso.org/public/outreach/press-rel/pr-1999/phot-29-99.html.

tures < 50 K, these higher energy levels are unpopulated and H_2 gas is generally undetected in emission. Molecular gas studies in molecular clouds instead favour the next most abundant molecule, CO. Unlike H_2, CO can be easily excited via collisions at very cold temperatures. For example, the rotational $J = 1$ state is ~ 5.5 K above the rotational ground state ($J = 0$), resulting in a $J = 1 \rightarrow 0$ radiative transition at 2.6 mm (Combes 2004, Stahler & Palla 2005). The CO molecule, however, is optically thick at high densities ($\gtrsim 10^3$ cm^{-3}), meaning we can only probe the gas properties near the surface of the cloud with the CO $(1-0)$ transition. Alternatively, isotopologues of CO, such as ^{13}CO or C^{18}O, are less abundant. Thus, their line emission is more optically thin and better able to trace the gas deeper in the cloud that can be at higher density. Figure 1.3 compares the $J = (1-0)$ spectrum for CO, ^{13}CO, and C^{18}O towards a region in the Taurus-Auriga Molecular Cloud. The CO profile

is significantly broadened beyond what would be expected from thermal or turbulent motions, indicating that the emission is saturated and optically thick. In contrast, the $C^{18}O$ profile appears narrow, indicating that $C^{18}O$ line is optically thin and can trace material at deeper depths and higher column densities (Stahler & Palla 2005).

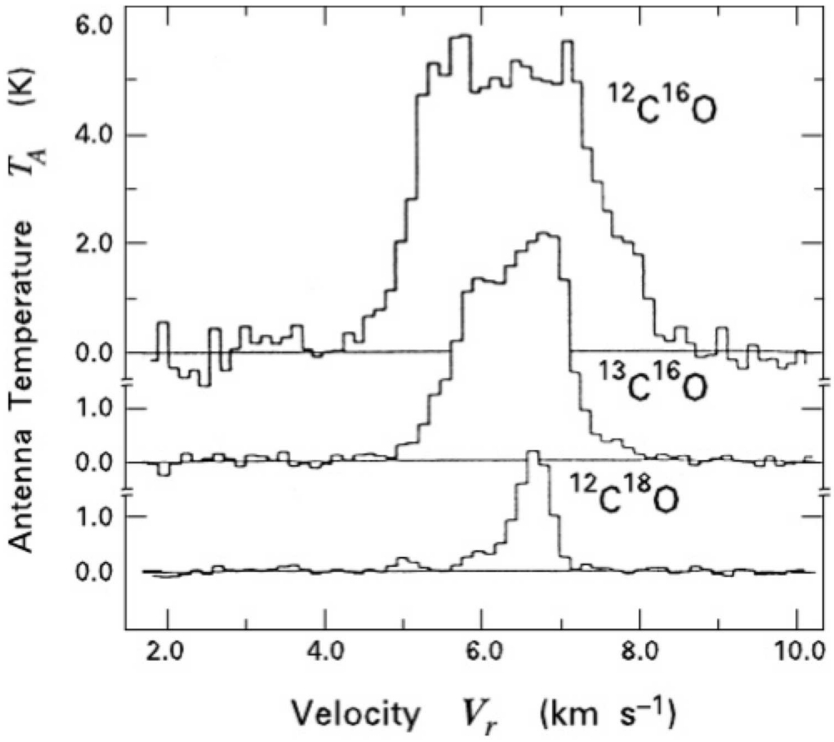

Figure 1.3: Line emission from 3 CO isotopologues towards the Taurus-Auriga cloud system. The three lines have different profiles due to different optical depths. *Top:* The main CO isotopologue is significantly broadened due to its high optical depth. *Middle:* The ^{13}CO isotopologue is less optically thick than the CO line, and is slightly broadened. *Bottom:* The $C^{18}O$ isotopologue is optically thin, resulting in narrow and Gaussian-like line emission. Figure from Stahler & Palla (2005).

In addition to molecular gas, molecular clouds also have high column densities of dust. Here, dust refers to complex carbon grains, roughly 1 μm in size or less. Dust grains block light from background sources and the measure of lost light is called extinction, such that regions of high extinction are generally dense and dusty. Visual extinction, A_V, can be measured by the difference in visual magnitudes (brightness) of light between extincted and unextincted objects. Since dust grains are typically ~ 1 μm, short wavelengths (i.e., optical and ultraviolet wavelengths) are more significantly scattered or absorbed (Stahler & Palla 2005). For example, Figure 1.2 shows that B68 is highly extincted (optically thick) at $\lambda < 1$ μm, but the cloud becomes more

optically thin (transparent) at $\lambda > 1$ μm. At still longer wavelengths (i.e., $\gtrsim 100$ μm), the cold dust grains within the cloud itself emit most of their own thermal emission. Figure 1.4 shows the optically thin dust emission from the B68 cloud at far-infrared and submillimeter wavelengths. Note how well the dust emission traces the dust extinction from the optical observations (Figure 1.2). For reference, the dust emission at 50 K has a continuum peak at ~ 60 μm, whereas dust emission at 10 K has a continuum peak at ~ 300 μm.

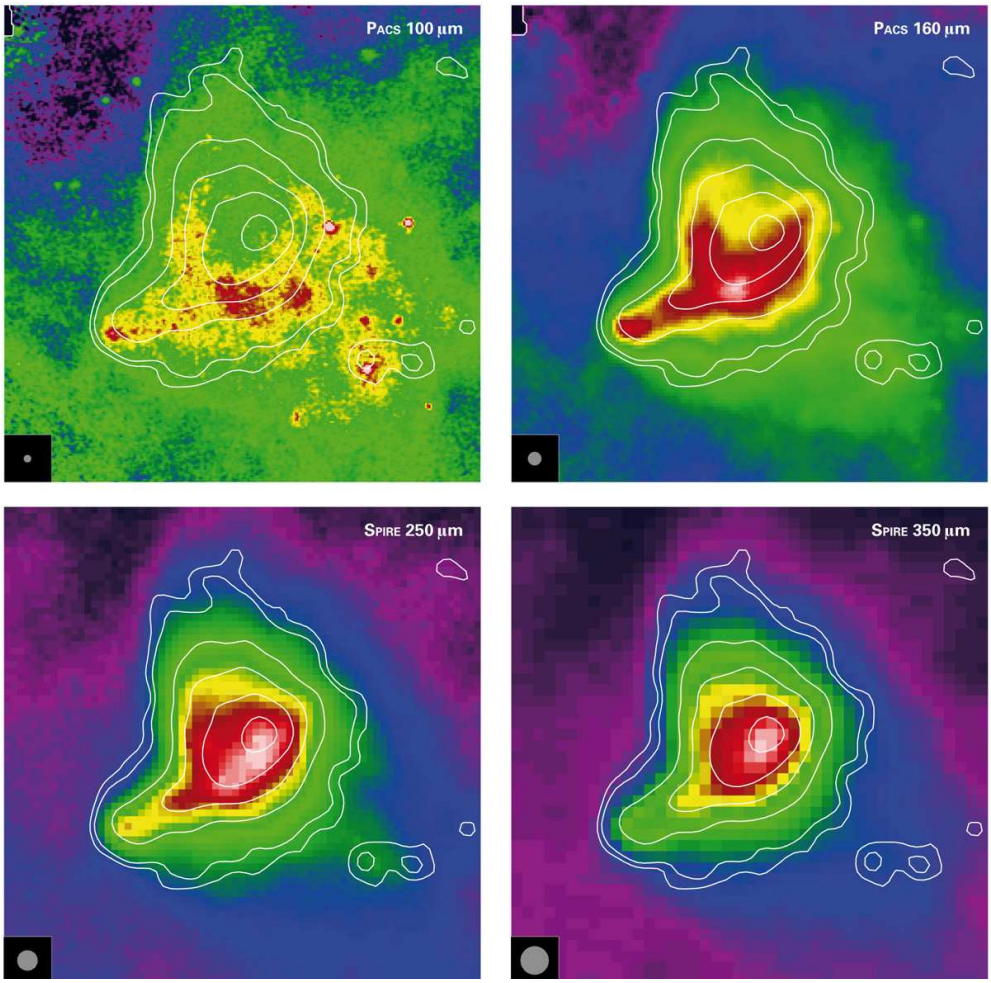

Figure 1.4: Dust emission towards B68. Emission at ~ 100 μm traces warmer dust, whereas emission at ~ 250 μm traces the colder envelope. The white lines correspond to emission at 870 μm and the colour scale corresponds to an arbitrary flux scale at each wavelength. At these long wavelengths, the cloud is optically thin. This image was taken from Nielbock et al. (2012).

Figure 1.5 shows the Rosette Molecular Cloud at 3 different wavelengths; 70 μm (blue), 160 μm (green), and 250 μm (red). The red material probes the coldest

dust components of the cloud whereas the blue material reveals the warmer regions, perhaps locations where dust is heated by nearby luminous young stars. As with the CO maps (see Figure 1.1), the dust continuum maps trace regions of high density and reveal a wealth of substructure. Unlike the CO data, however, dust emission is optically thin. Thus, continuum dust maps sample the dust emission through the entire line-of-sight and can be used to estimate masses and the column densities of cloud structures like filaments and clumps (assuming a gas-to-dust mass ratio).

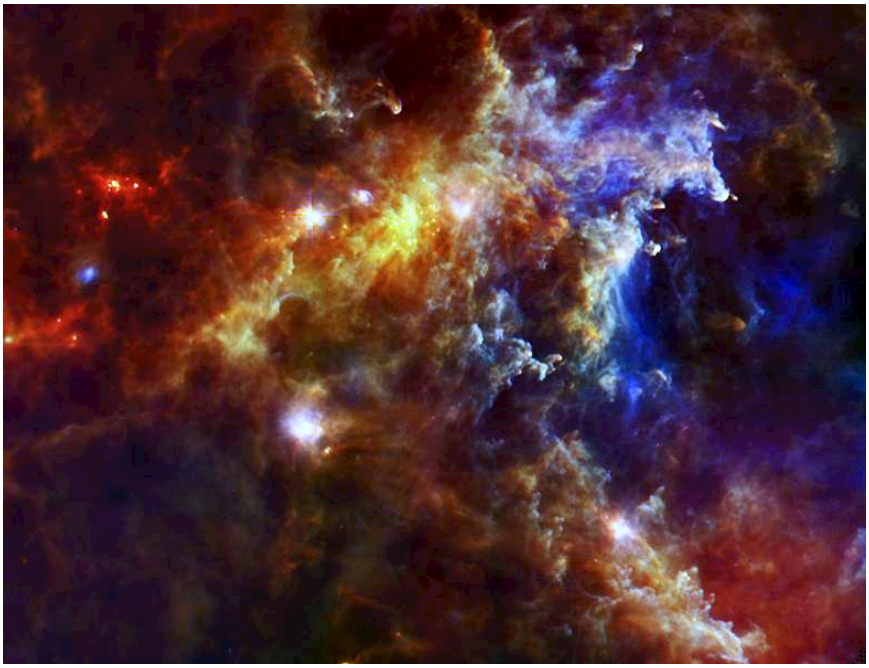

Figure 1.5: A three-colour image of the Rosette Molecular Cloud with 70 μm (blue), 160 μm (green), and 250 μm (red) continuum emission. These data obtained with the *Herschel* PACS and SPIRE instruments as part of the *Herschel* OB Young Stars (HOBYS) Key Programme. Red emission shows cold dust ($\sim$ 10 K) and blue emission shows warmer dust ($\sim$ 40 K). Image credit: ESA/PACS & SPIRE Consortium/HOBYS Key Programme Consortia.

Dust continuum maps have also revealed very cold ($\sim$ 10 K), very dense ($\gtrsim$ 10^4 cm^{-3}), small ($\sim$ 0.1 pc) objects, often called **dense cores** (or simply "cores"), embedded in molecular cloud clumps and along filaments (Di Francesco et al. 2007). At such low temperatures, submillimetre continuum maps (e.g., Figure 1.4 and Figure 1.5) are the best probes of the dust content in these dense cores. Furthermore, at such low temperatures ($<$ 20 K), CO and its isotopologues tend to sublimate onto dust grains, thereby depleting these molecules from the gas and making their line transitions poor tracers of cold, dense cores (e.g., Bergin et al. 1995; Kramer et al.

1999). For example, observations of dense cores often show absorption at 4.67 μm attributed to CO ices (e.g., Chiar et al. 1994). As CO freezes onto dust grains, molecules that are destroyed in chemical reactions with CO, like nitrogen-bearing molecules (e.g., NH_3 or N_2H^+), become more abundant. Thus, gas in dense cores are best studied through high density tracers like NH_3 or N_2H^+ (van Dishoeck 2009).

The dense cores are very important stages of star formation. These structures are the precursors for new stars, forming either single stars or a small stellar systems (Di Francesco et al. 2007). Thus, the physical conditions of the dense cores should impact the properties of their stellar products. Dense cores typically have masses similar to the Sun ($M_\odot \sim 2 \times 10^{33}$ g), as measured by the optically thin (transparent) dust emission at submillimetre wavelengths (Di Francesco et al. 2007). Core mass can be estimated from the simple relation:

$$M = \frac{S_\nu d^2}{\kappa_\nu B_\nu(T)}, \tag{1.1}$$

where S_ν is the flux density (energy per area per second) at a given frequency, d is the distance to the cloud, κ_ν is the dust opacity, and $B_\nu(T)$ is the black body function at a given dust temperature. The black body function is,

$$B_\nu = \frac{2h\nu^3}{c^2}\left(\frac{1}{\exp(h\nu/kT)-1}\right). \tag{1.2}$$

A core will collapse when gravitational contraction overwhelms internal supports. Internal supports include thermal pressure, turbulent (non-thermal) pressure, or magnetic pressure (Klein et al. 2007). Thermally supported cores at 10 K will become unstable at masses at $\gtrsim 1$ $M_\odot$. A collapsing core will form a protostar or young stellar object (YSO). Figure 1.6 illustrates the different stages of YSOs, in evolutionary order. We describe the different stages below:

The earliest YSO stage is called a Class 0 protostar. Class 0 YSOs were first identified by André et al. (1993), as an overabundance of YSOs with dust continuum profiles peaking at long wavelengths. A Class 0 protostar is deeply embedded in a thick, dusty envelope, which contains more mass than the protostar. Due to the thick envelope, the *protostar* is not observed directly. Instead, the YSO is identified by reprocessed dust emission at far-infrared wavelengths. Thus, Class 0 YSOs tend to resemble simple, dusty blackbody functions. The Class 0 phase is also the main accretion phase and can be marked by very prominent bipolar outflows (e.g., Bontemps

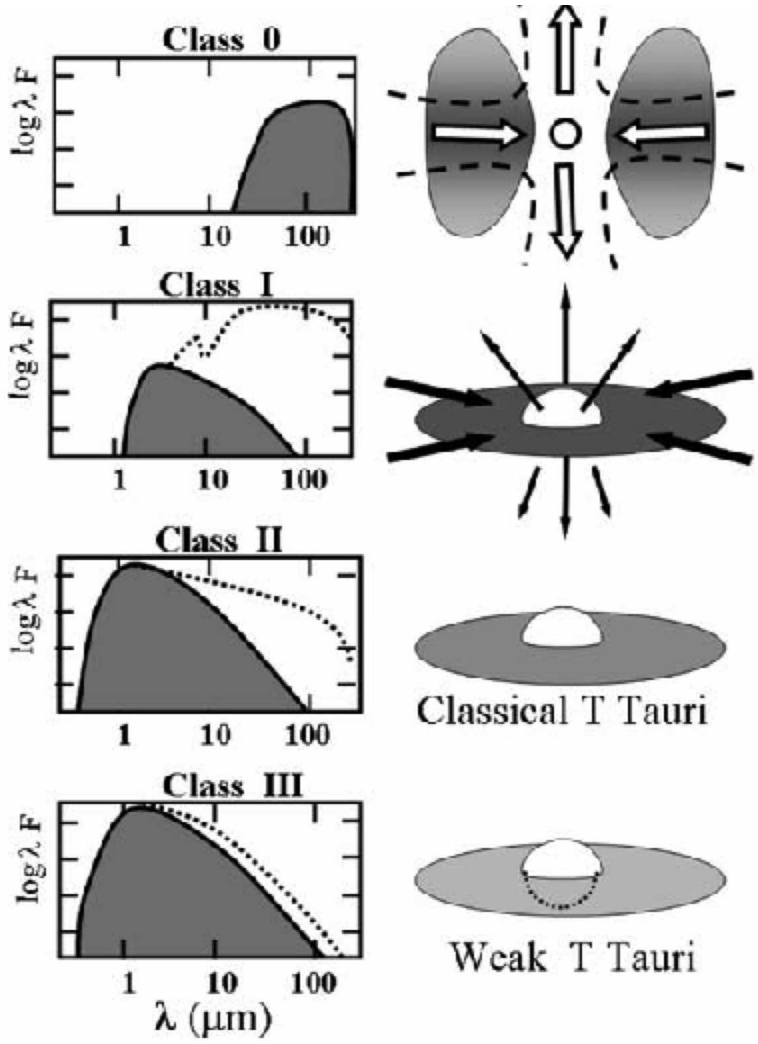

Figure 1.6: Illustration of the protostellar stages (Class 0, Class I, Class II, and Class III), see text for more details. The Flat spectral class is not shown. Figure from Maeder (2009).

et al. 1996; Gueth & Guilloteau 1999).

As the protostar contracts and accretes material, its mass increases. When the protostar mass is comparable to the envelope mass, the protostar is called a Class I object. At this stage, the spectral energy distribution (SED[1]) shows excess infrared emission from an accretion disk. During the Class I stage, the parent envelope infalls onto the disk, and the protostar accretes this material through the disk (White et al. 2007).

With time, the envelope is dissipated. The envelope-clearing stage is considered

[1]The distribution of flux with wavelength.

a transition where the infrared SED flattens at infrared wavelengths. YSOs in this stage are called Flat sources. Flat YSOs were first identified by Greene et al. (1994), and are considered to be embedded within an envelope. (Note, that Figure 1.6 does not include the Flat stage, which occurs between Class I and Class II YSOs.)

Once the envelope has cleared, the protostar is often referred as a pre-main sequence star. There are two distinct pre-main sequence stages, the Class II and Class III stages, respectively. The Class II/III stages also called classical T-Tauri stars and weak-line T-Tauri stars, respectively (André & Montmerle 1994). For a Class II source, the YSO is surrounded by a thick, dusty disk. Thus, Class II sources often show significant excesses at far-infrared wavelengths (e.g., Weintraub et al. 1989). Eventually, radiation from the central YSO and planet formation processes within the disk will both dissipate the disk, resulting in the final stage, the Class III stage. For a Class III YSO, infrared excesses are minimal. Here, the YSO contracts and heats into a fully formed star (see André et al. 2000; Stahler & Palla 2005; White et al. 2007).

We note that these YSO classes are determined empirically from observations and may not necessarily reflect the true evolutionary state of the YSO. For example, inclination effects can result in improper classifications based on the observed SED (e.g., Crapsi et al. 2008). Thus, YSO classifications are conducted on a best-effort basis.

From numerous surveys of core and YSO populations in nearby Galactic molecular clouds, star formation appears to be confined to regions of high column density. For example, Johnstone et al. (2004) and Kirk et al. (2006) found relationships between core incidence and extinction for the Ophiuchus and Perseus clouds, respectively. These authors suggested that core formation requires a minimum threshold ($A_V \gtrsim 5$) of material. Similarly, André et al. (2010) and Lada et al. (2009) each compared two clouds, one actively forming stars and the other relatively quiescent, and each found that the more active cloud was composed of higher column densities of material (by a factor of ~ 10) than those of the quiescent cloud. For example, André et al. (2010) suggested a threshold gas column density of ~ 6 x 10^{21} cm^{-2} was needed for filamentary structure to form dense, star-forming cores via gravitational instabilities. All of these studies emphasize that cores require a minimum column density (extinction) of material of $A_V \sim 7$ to condense from the bulk cloud. Nevertheless, it is important to sample different environments.

Our current knowledge of dense cores and YSOs is mainly limited to nearby Galac-

tic clouds (i.e., within 500 pc). Present instruments generally yield insufficient spatial resolution at larger distances to probe objects on the scales of cores. Local Galactic clouds, however, are mainly undergoing "low-mass" star formation, that is, these clouds are not producing high-mass OB associations. Galactic "high-mass" star formation is found in more distant ($\gtrsim 1$ kpc) molecular clouds. As such, we cannot probe high-mass star-forming regions to the same spatial scales as low-mass ones (see e.g., Motte et al. 2007). Similarly, we cannot easily compare extragalactic star-forming regions to those in our Galaxy. Current studies of extragalactic star formation have focused on relating the star formation rate (determined from infrared luminosity) of a galaxy to its gas content. This relation, known as the Schmidt-Kennicutt relation, shows a strong correlation where the star formation rate increases with gas surface densities (Kennicutt 1998). Figure 1.7 shows the Schmidt-Kennicutt relation over a large range of gas surface densities. The trend, however, appears to deviate at lower gas surface densities (Wyder et al. 2009). Recent observations of nearby Galactic molecular clouds have noted a similar turnover (e.g., see Heiderman et al. 2010). In addition, Arzoumanian et al. (2011) noted that there is a characteristic scale length for dense filaments which results in a comparable gas surface density (~ 150 $M_\odot$ pc^{-2}). Thus, the correlation between star formation and gas surface density seen in extragalactic SFRs may be tied to the unobserved cloud substructure.

Star formation is very relevant to other topics in astronomy. First, models of galaxies and star clusters often invoke a "star formation law" to produce an initial stellar population. Generally, stellar populations are thought to be formed universally with a constant distribution of masses, though the constancy of this distribution remains unclear. Since stellar mass determines a star's evolutionary path, chemical enrichment, and ultimate end, the choice of stellar populations greatly influences the evolution of the system. For example, stellar processes such as winds and supernovae return energy and processed material into the interstellar medium (ISM). Second, some galaxies are classified by their level of star formation activity (i.e., starburst galaxies), and local Galactic molecular clouds can help explain trends observed in extragalactic SFRs (see Figure 1.7). Third, star formation is directly related to planet formation. Theories of planet formation suggest planets can only form while a young star has a disk (Lissauer 1993). This condition constrains the timescale for planets to form and accumulate mass. Thus, it is important to understand protostellar evolution to accurately constrain planet formation.

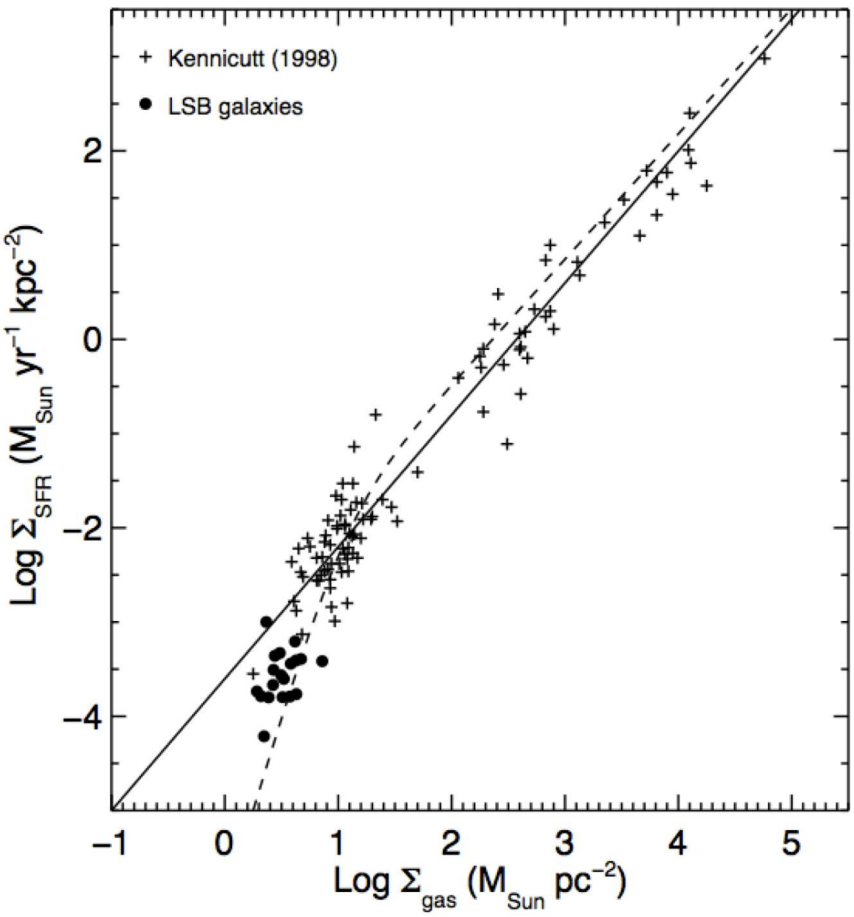

Figure 1.7: Schmidt-Kennicutt Relation comparing low-surface brightness galaxies (circles) with spiral galaxies and starbursts (pluses) from Kennicutt (1998). The solid line shows the linear fit to galaxies with high surface gas density. The dashed curve shows the predicted relation from the Krumholz et al. (2005) model. This Figure was taken from Wyder et al. (2009).

The Perseus Molecular Cloud

For this thesis, we will characterize the star formation activity in the Perseus molecular cloud to understand star formation in more detail. The Perseus molecular cloud is located at a distance of $\sim$ 235 pc (Hirota et al. 2008), part of a region known as the Gould Belt (Herschel 1847; Gould 1879). The Gould Belt is a large, gaseous band that contains more than half the young stellar systems within 600 pc (Torra et al. 2000). Figure 1.8 shows the location of several nearby molecular clouds. Most of these molecular clouds, including Perseus, are within the Gould Belt or the expanding shell. The origin of the Gould Belt is unclear, however. In one theory, the Gould Belt is formed by supernovae shock waves originating from a previous generation of

high-mass stars (e.g., Olano 1982; Perrot & Grenier 2003), whereas another theory suggests the Gould Belt is formed by giant cloud impacts with the Galactic plane (e.g., Comerón & Torra 1994; Bekki 2009).

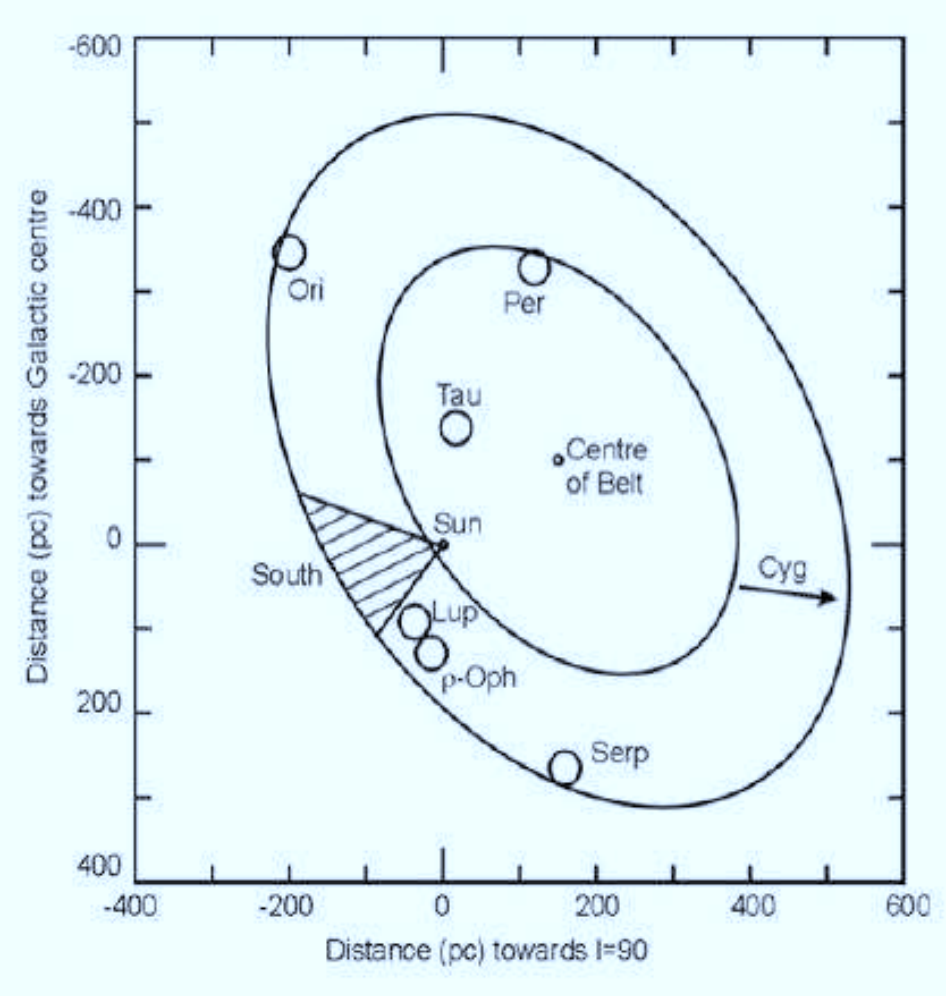

Figure 1.8: The Gould Belt in galactic coordinates. Several nearby star-forming regions are also shown. The Gould Belt is tilted by $\sim 20°$ from the Galactic Plane (Torra et al. 2000). Image credit: JAC/GBS-JLS, http://www.jach.hawaii.edu/JCMT/surveys/gb/

The Perseus molecular cloud is likely influenced by the Per OB2 association, one of the nearest OB associations[2]. A runaway B0 star from the Per OB2 association, HD 278942, is closest to Perseus and may be directly influencing its evolution and properties (Bally et al. 2008; Ridge et al. 2006b). The Perseus cloud itself consists of several large complexes, hereafter **clumps**, arranged along a chain. Figure 1.9

[2]OB associations are high-mass stellar clusters containing large groups of O-type ($\gtrsim 18$ $M_\odot$) and B-type ($\sim 4 - 18$ $M_\odot$) stars (Binney & Merrifield 1998).

shows an optical image of the cloud. The clumps appear as dark patches that block background starlight. Perseus spans $\sim 5^\circ$ by 1.5° ($\sim$ 21 pc by 6 pc, at a distance of 235 pc) and has a total cloud mass of $\sim 10^4$ $M_\odot$ (Ungerechts & Thaddeus 1987; Sadavoy et al. 2010). Perseus also has a large velocity gradient between the Western edge and Eastern edge of the cloud (Ridge et al. 2006b).

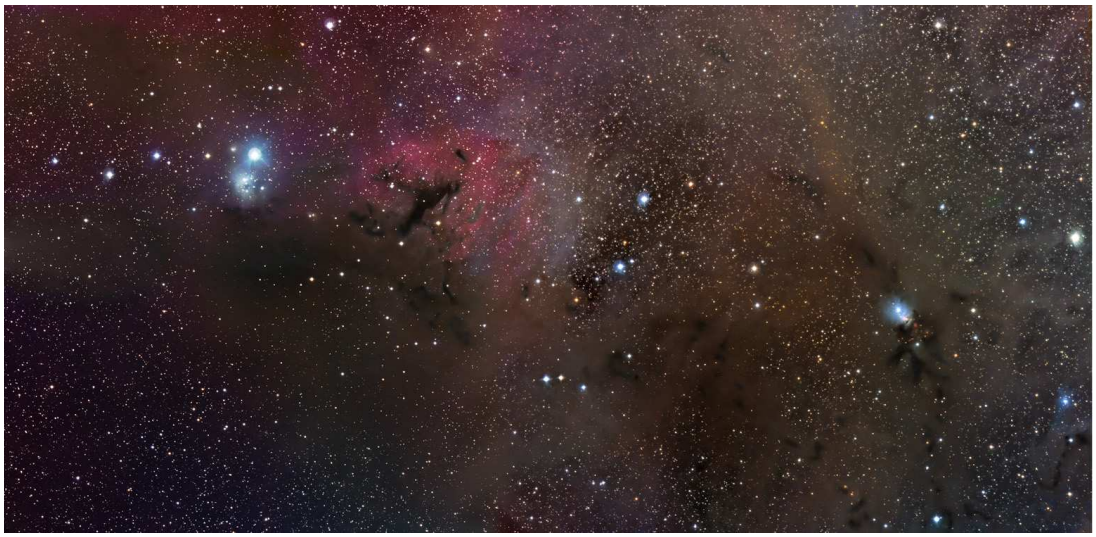

Figure 1.9: An optical image of the Perseus molecular cloud. The high density (high optical depth) material is seen as dark patches obscuring the background starlight. This image was taken by Adam Block (see www.caelumobservatory.com).

Perseus is very active, with rich populations of dense cores, embedded YSOs, and pre-main sequence stars. Other nearby star-forming regions, such as Polaris and Taurus are more quiescent (e.g., André et al. 2010; Kirk et al. 2013). Additionally, since Perseus is relatively nearby, we have excellent angular resolution to resolve the dense core and YSO populations. Furthermore, Perseus has both low- and intermediate-mass star formation within clustered and isolated regions (Bally et al. 2008). Perseus is too small to form very high-mass stars (i.e., O-type stars), but it does contain several late-type B stars[3]. Finally, observations have revealed a dust and gas shell from a nearby B-star towards the Eastern region of the cloud. Impacts from expanding shells are thought to collapse clouds and trigger star formation (Ridge et al. 2006b). Thus, Perseus is a rich star-forming region with some very interesting features.

[3]For reference, main sequence O-stars typically have masses of $M \gtrsim 18$ $M_\odot$, whereas B-stars have masses of $4 \lesssim M \lesssim 18$ $M_\odot$ (Binney & Merrifield 1998). For Perseus, the binary system HD 281159 contains the most massive star within the IC348 cluster, with a mass of ~ 6 $M_\odot$ (Preibisch et al. 2003; Herbst 2008).

In addition, the clumps in Perseus have a variety of masses, sizes, and populations. For example, Perseus has two large clumps, IC348 and NGC1333, with large clusters of YSOs and dense cores (e.g., Gutermuth et al. 2009). In Figure 1.9, the regions of bright blue emission correspond to reflection nebulae (star light scattering off dust) from the nearby embedded clusters in IC348 (left) and NGC1333 (right). Perseus also has several smaller clumps with smaller dense core and YSO populations (e.g., Jørgensen et al. 2007; Enoch et al. 2009; Evans et al. 2009), and the Perseus B1-E clump, which has no apparent star formation activity (Kirk et al. 2006). Thus, Perseus represents a variety of environments.

Finally, Perseus has been well-studied by a number of recent surveys. For example, the entire cloud was mapped in the infrared ($3.6 - 24$ μm) by the *Spitzer* Space Telescope (see Jørgensen et al. 2006; Rebull et al. 2007). In addition, submillimeter and millimeter continuum data of key clump regions are readily available (see Di Francesco et al. 2008; Enoch et al. 2006). Several current surveys will expand the (sub)millimeter continuum data for Perseus (e.g., Ward-Thompson et al. 2007a). Perseus has also been sampled with a variety of molecular tracers. Nearly the entire cloud was mapped in CO (1-0) and ^{13}CO (1-0) for the COMPLETE survey (see Ridge et al. 2006a), and sections of the cloud have been mapped in CO (3-2) line emission (e.g., see Curtis & Richer 2011). Perseus has also been sparsely sampled in higher density tracers, such as NH_3 and N_2H^+ (Rosolowsky et al. 2008; Kirk et al. 2007). For the high density tracers, observations were primarily restricted to the dense cores. Finally, Perseus also has readily available extinction maps using all-sky near-infrared observations (e.g., Ridge et al. 2006a).

Thus, Perseus is an ideal molecular cloud to study star formation. This thesis will utilize new observations of the Perseus molecular cloud for a detailed study of its star formation activity. The goals of this thesis are (1) to use the new observations to identify core and YSO populations and generate the most complete catalogue for each and (2) to characterize the core and YSO populations across the different clumps. Generally, comparisons of star forming regions compare one cloud to another (i.e., Jørgensen et al. 2007; Enoch et al. 2008; Sadavoy et al. 2010). With this thesis, we will compare and contrast the core and YSO populations within the clumps in Perseus to determine if star formation is affected by local differences within a single cloud.

Chapter 2

Instrumentation and Data

2.1 Instrumentation

Since molecular clouds are generally cold ($\lesssim$ 50 K), the thermal emission from dust towards these regions peak at submillimeter wavelengths. Unfortunately, the Earth's atmosphere can be very opaque at submillimeter wavelengths due to water absorption. Figure 2.1 shows the atmospheric transmission with wavelength. At optical or radio wavelengths, the atmosphere is transparent, whereas at submillimeter wavelengths the atmosphere is almost entirely opaque. At high elevations (above most water vapour), we are able to achieve transmission windows at certain submillimeter bands (i.e., at 850 μm; Naylor et al. 2000). Additionally, balloon-borne telescopes (i.e., BLAST) or telescopes aboard airplanes (i.e., SOFIA) are able to rise above most atmospheric water vapour for better transmission (Pascale et al. 2008; Tremblin et al. 2012). Nevertheless, for negligible transmission losses, one must observe from space.

The *Herschel* Space Observatory is a space-based submillimeter telescope (see Figure 2.2). Launched in May of 2009, *Herschel* orbits the Sun at the second Sun-Earth Lagrangian point[1]. This positioning provides a stable thermal environment and good sky visibility (Pilbratt et al. 2010). *Herschel* represents one of the "cornerstone missions" for the European Space Association (ESA) and is also part of the ESA Horizons Programme.

Herschel has a 3.5 m Cassegrain mirror and two imaging cameras onboard: the Photodetector Array Camera and Spectrometer (PACS; Poglitsch et al. 2010) and the Spectral and Photometric Imaging Receiver (SPIRE; Griffin et al. 2010). *Herschel*

[1]The second Langrangian point, L2, is located 1.5 million km beyond the orbit of the Earth in the same direction as the Earth-Sun line.

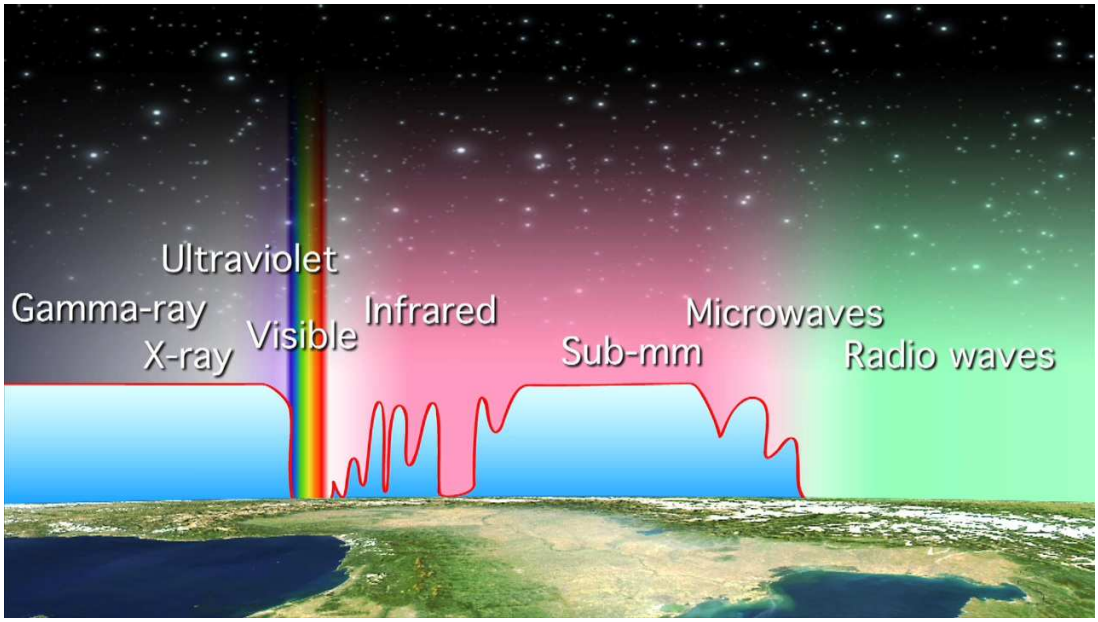

Figure 2.1: Opacity due to Earth's atmosphere. At optical and radio wavelengths, the atmosphere is mainly transparent (optically thin), and radiation at these wavelengths from astronomical sources is able to transmit to the ground. For far-infrared and submillimeter wavelengths, however, the atmosphere is opaque, and thus, photons at those wavelengths are difficult to measure from the ground. This image was taken from the Universe Today (http://www.universetoday.com/46614/explore-the-universe-with-scienceesa/).

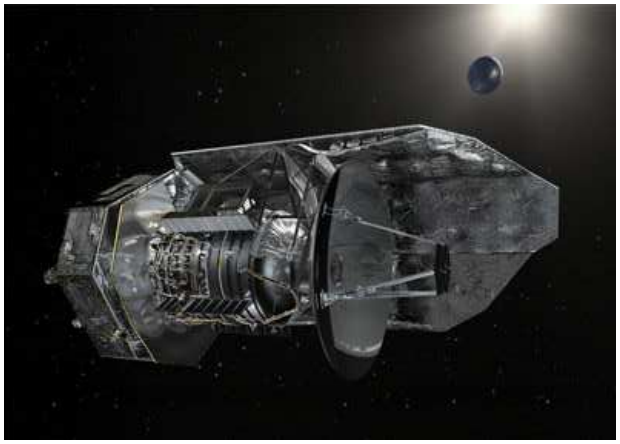

Figure 2.2: The *Herschel* space observatory at the second Langrangian point. The primary mirror is 3.5 m in diameter. The sun shield blocks sunlight from the telescope and keeps the electronics cool. Image credit: ESA (Image by AOES Medialab).

is designed to be a far-infrared (PACS) and submillimetre (SPIRE) telescope, and since such emission is usually very faint, the instruments are cooled to very cold temperatures (~ 0.3 K) with liquid helium. At such cold temperatures, *Herschel* has extremely low background noise (Griffin et al. 2006).

Both PACS and SPIRE are designed with bolometers, which are very sensitive temperature gauges that measure small variations in resistance due to changes in temperature induced by incident radiation (Rohlfs & Wilson 2004). The PACS imager can observe at either 70 μm or 100 μm and at 160 μm, simultaneously. In comparison, the SPIRE imager can observe at 250 μm, 350 μm, and 500 μm simultaneously. Due to water vapour in Earth's atmosphere, these wavelengths have low transmission to the ground. At best, there are small windows of opportunity at high altitudes (e.g., on Mauna Kea) but even these windows still suffer from atmosphere effects. Figure 2.3 shows the atmosphere transmission at the SPIRE wavelengths over Mauna Kea under "dry" (low water vapour) conditions. Thus, wavelengths of 70 - 500 μm (those of the PACS and SPIRE bands) can only be well explored in space. For the SPIRE bands, *Herschel* provides the first opportunity to achieve such observations (Gear & Griffin 2000).

Furthermore, these instruments can be used separately or simultaneously in "Parallel Mode". *Herschel* observations have angular resolutions ranging from $\sim 8''$ (at 70 μm) to $\sim 36''$ (at 500 μm). These resolutions are comparable to the $\sim 14''$ angular resolution of SCUBA at 850 μm and far superior to the $\gtrsim 120''$ angular resolution of most extinction maps. With a relatively large mirror, the SPIRE and PACS instruments have excellent sensitivity and angular resolution.

2.2 Observations and Reduction

Herschel observed Perseus as part of the *Herschel* Gould Belt Survey (André & Saraceno 2005). The western half of Perseus was observed in February 2010 and the eastern half of Perseus was observed a year later in February 2011. The *Herschel* observations were taken in Parallel Mode, resulting in simultaneous coverage at 5 wavelength bands, with the 70 μm and 160 μm PACS channels and the 250 μm, 350 μm, and 500 μm SPIRE channels. The western half of Perseus covers roughly 6 square degrees and the eastern half of Perseus covers 4.5 square degrees.

The PACS and SPIRE raw data were reduced using the Herschel Interactive Pro-

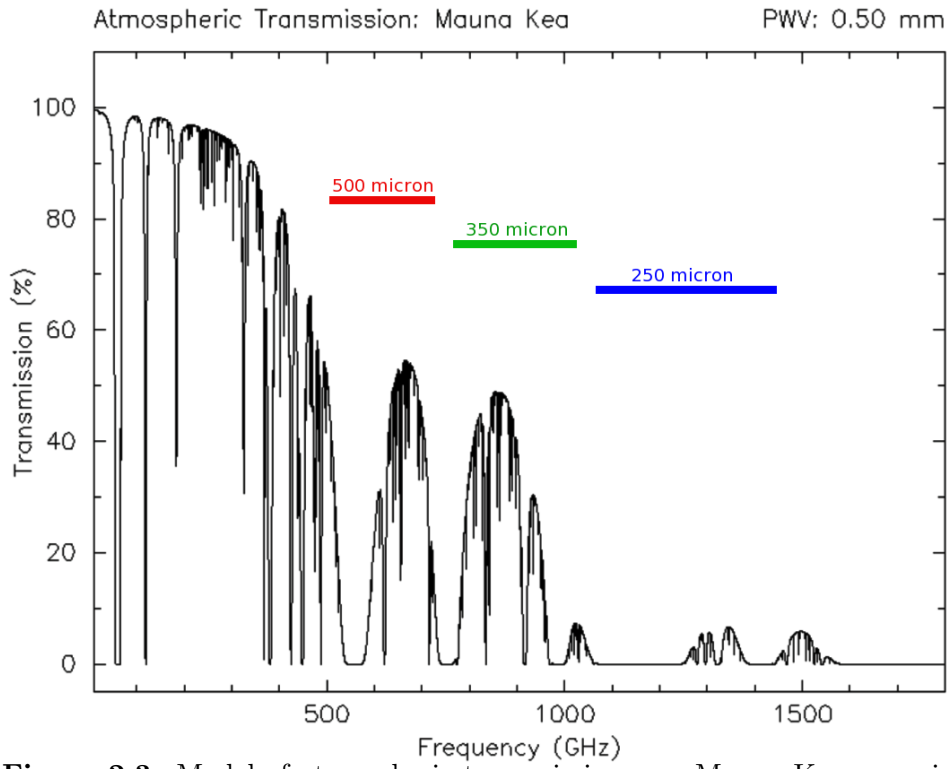

Figure 2.3: Model of atmospheric transmission over Mauna Kea assuming a precipitable water vapour level of 0.5 mm (dry conditions). The SPIRE bands are centered at 250 μm (1200 GHz), 350 μm (850 GHz), and 500 μm (600 GHz) are shown for comparison. This image was generated using the CSO Atmospheric Transmission Interactive Plotter, see http://www.submm.caltech.edu/cso/weather/atplot.shtml.

cessing Environment (HIPE[2]). Reduction scripts were modified from the standard scripts by M. Sauvage (PACS) and P. Panuzzo (SPIRE). For PACS, we were concerned with removing glitches (detection spikes due to cosmic rays) and stripes (low frequency brightness variations due to temperature fluctuations in the cryogenics) in the final map. For SPIRE, bad instrument baselines from the cryogenics and calibrations are very important to correct (Roussel 2012).

For both PACS and SPIRE, we started with the initial raw data (called Level 0). The first step of data processing converts the units from digital readout to voltages. Additionally, the processing applies the telescope astrometry (i.e., time stamps), general housekeeping information (i.e., filter identification, scan rate), and basic masking for bad channels (e.g., dead pixels) to the data, after which the data are considered to be at Level 0.5. The next step of data processing computes the pointing informa-

[2]HIPE is a joint development by the Herschel Science Ground Segment Consortium, consisting of ESA, the NASA Herschel Science Center, and the HIFI, PACS and SPIRE consortia.

tion for each bolometer and converts the data units into fluxes using the calibration information. For both PACS and SPIRE, we used the most up-to-date calibration information at the time of the reduction. Observation glitches (i.e., from cosmic rays) are also detected at this stage as sudden jumps in the bolometer timeseries with shallow declines. At the end of this stage, we have observed flux timeseries for each bolometer. The data products at this stage are called Level 1. The final reduction step is to convert the bolometer timeseries into a sky map, or the Level 2 products.

For both PACS and SPIRE, we used the *scanamorphos* routine (Roussel 2012), which is an external mapmaker designed for bolometer arrays, to obtain the Level 2 products. We found *scanamorphos* superior to the HIPE mapmakers (naivemap or madMap) in reducing large-scale stripes and negative artifacts around bright sources. In brief, *scanamorphos* computes the map coordinates from the Level 1 products and flags the telescope "turnaround" data (i.e., data taken at the start or end of a scan while the telescope was accelerating). *Scanamorphos* also makes use of the redundancy in the observations (each section of the sky is observed by multiple bolometers at multiple times) to correct for low-frequency noise (brightness drifts) in the observations. Unlike other mapmakers (i.e., madMap), *scanamorphos* does not assume a noise model. Furthermore, *scanamorphos* removes glitches identified in the Level 1 products and includes prescriptions to mask and remove glitches missed by the pipeline. The final maps are projected onto a grid with a specified pixel size. Unless specified otherwise, we adopted pixel sizes of $3.2''$, $4.5''$, $6.0''$, $10.0''$, and $14.0''$ for the 70 μm, 160 μm, 250 μm, 350 μm, and 500 μm maps, respectively, to ensure Nyquist sampling.

For PACS, cosmic rays were removed through the standard second level deglitching algorithm rather than the Multiresolution Median Transform (MMT) deglitcher, which was the initial deglitching algorithm. The MMT deglitcher was intended for deep fields only, and as such, generally removed source flux with the cosmic rays. Glitches were identified using a 6σ cut of the weighted flux of each readout towards a given map pixel. For SPIRE, a given map pixel is sampled less, and as such, glitches are more difficult to distinguish from bright sources. We used wavelet decomposition[3] (HIPE task waveletDeglitcher) to detect and remove glitches in the SPIRE timeseries. This method assumes glitch shapes are similar to Dirac δ-functions. Additionally, we found that *scanamorphos* was able to remove most striping artifacts from bad baselines or drift corrections.

[3]A wavelet decomposition breaks up the signal into a set of independent wavelets.

Chapter 3

Cloud Structure: B1-East

In this chapter, we present continuum observations of the Perseus B1-E region from the *Herschel* Gould Belt Survey. These *Herschel* data reveal a loose grouping of substructures at $160 - 500$ μm not seen in previous submillimetre observations. We measure temperature and column density from these data and select the nine densest and coolest substructures for follow-up spectral line observations with the Green Bank Telescope. We find that the B1-E clump has a mass of ~ 100 $M_{\odot}$ and appears to be gravitationally bound. Furthermore, of the nine substructures examined here, one substructure (B1-E2) appears to be itself bound. The substructures are typically less than a Jeans length from their nearest neighbour and thus, may interact on a timescale of ~ 1 Myr. We propose that B1-E may be forming a first generation of dense cores, which could provide important constraints on the initial conditions of prestellar core formation. Our results suggest that B1-E may be influenced by a strong, localized magnetic field, but further observations are still required.

3.1 Introduction

Molecular clouds are highly structured regions of dust and gas. They contain dense, small-scale, star-forming "cores" ($\lesssim 0.1$ pc) that are usually clustered into larger-scale clumps and organized along filaments (Williams et al., 2000; Ward-Thompson et al., 2007a; Di Francesco et al., 2007; André et al., 2010). The cause of this hierarchical structure, where the large-scale clouds (~ 10 pc) with moderate densities ($\sim 10^2$ cm^{-3}) produce filaments, clumps, and dense cores at higher densities ($\gtrsim 10^4$ cm^{-3}), is not well understood (Bergin & Tafalla, 2007).

Molecular clouds form dense cores when diffuse gas is compressed. Current theories for core formation primarily focus on two ideas: that cores form via (1) turbulent compression of diffuse gas (e.g., Larson, 1981; Mac Low & Klessen, 2004; Dib et al., 2009), or (2) the motion of neutral material between magnetic field lines or ambipolar diffusion (e.g., Mestel & Spitzer, 1956; Mouschovias, 1976; Kunz & Mouschovias, 2009). Both mechanisms and gravity likely play important roles in star formation, but it is unclear whether one mechanism would dominate in all situations (i.e., clustered or isolated star formation and low-mass or high-mass star formation). Furthermore, theoretical studies also suggest that additional processes, such as radiation feedback (i.e., Krumholz et al., 2010) or large-scale shocks associated with converging flows (i.e., Heitsch et al., 2011), can influence molecular cloud structure and thus, core formation. Additionally, recent *Herschel* studies have shown that filaments are very prominent in star forming regions and likely have an important role in the formation of dense substructures in molecular clouds (e.g., André et al., 2010; Arzoumanian et al., 2011).

Surveys of core populations in molecular clouds indicate that cores are confined to regions of high column density. Johnstone et al. (2004) and Kirk et al. (2006) found a relationship between core occurrence and extinction for the Ophiuchus and Perseus clouds, respectively, suggesting that there is a core formation threshold at $A_V \gtrsim 5$. Similarly, Lada et al. (2009) and André et al. (2010) each compared two clouds with different degrees of star formation activity and each found that the more active cloud was composed of higher column density material (by a factor of ~ 10) than the quiescent cloud. These studies emphasize that cores require a minimum column density (extinction) of material to condense from the bulk cloud (see also Heiderman et al., 2010).

The precursors to cores are difficult to identify. Dense cores are often influenced by processes such as nearby outflows and radiation feedback from a previous epoch of nearby star formation, and observations of them cannot be used to constrain the dynamic properties of the initial core-forming material (Curtis & Richer, 2011). Without knowing the *initial* conditions and processes that cause cores to form from diffuse gas, we cannot accurately model their formation or evolution. Thus, identifying and analyzing a core forming region without earlier episodes of star formation would be exceedingly useful to constrain how molecular clouds form star-forming substructures.

In this chapter, we use observations from the *Herschel* Gould Belt Survey to explore a ~ 0.1 deg^2 clump roughly 0.7° east of the B1 clump (Bachiller & Cernicharo,

1986) within the Perseus molecular cloud. This region, hereafter called B1-E, has material at high extinction (i.e., $A_V > 5$) similar to the core formation threshold. Despite this high extinction, previous submillimetre and infrared continuum observations suggest that B1-E contains neither dense cores nor young stellar objects (e.g., Enoch et al., 2006; Kirk et al., 2006; Jørgensen et al., 2007; Evans et al., 2009). In contrast, our *Herschel* observations show substructure that was not detected by these other far-infrared and submillimetre continuum studies. Furthermore, we use recent Green Bank Telescope (GBT) observations to quantify in part the kinematic motions of the densest substructures seen in the *Herschel* data.

We propose that B1-E is forming a first generation of dense cores in a pristine environment. In Section 3.2, we describe our *Herschel* and GBT observations. In Section 3.3 we describe the properties we derive from our data. In Section 3.4 we discuss the implication of our results and compare our observations to theoretical models. Finally, in Section 3.5 we summarize the chapter.

3.2 Data

3.2.1 *Herschel* Observations

The western half of Perseus, including B1-E, was observed at $70 - 500$ μm as part of the *Herschel* Gould Belt Survey (André & Saraceno, 2005; André et al., 2010). The 70 μm observations of B1-E, however, are less sensitive due to the fast scan rate (60 arcsec s^{-1}) and low emission from cold material (see Section 3.3.1). Thus, we will not include the 70 μm observations in our discussion. For a full explanation of the observations, see Pezzuto et al. (2012).

The PACS and SPIRE raw data were reduced using HIPE version 5.0 and reduction scripts written by M. Sauvage (PACS) and P. Panuzzo (SPIRE) that were modified from the standard pipeline. For SPIRE reduction, we used version 4 of the calibration tree. The final maps were created using the *scanamorphos* routine developed by Roussel (2012), adopting pixel scales of 6.4″, 6.0″, 10.0″, and 14.0″ for the 160 μm, 250 μm, 350 μm, and 500 μm bands, respectively. By default, *scanamorphos* sets a much smaller pixel scale, whereas our adopted pixel scale corresponds to the default size from the HIPE mapmaking tools. For a full explanation of the data reduction, see Chapter 2. We also adopt beam sizes of 13.4″, 18.1″, 25.2″, and

36.6″ for the 160 μm, 250 μm, 350 μm, and 500 μm bands respectively[1] (see Griffin et al., 2010; Poglitsch et al., 2010). Assuming a distance to Perseus of 235 pc (Hirota et al., 2008), *Herschel* can detect structure on scales of ~ 0.04 pc at 500 μm. Figure 3.1 shows a three-colour image of Western Perseus with labels for B1-E and other prominent subregions.

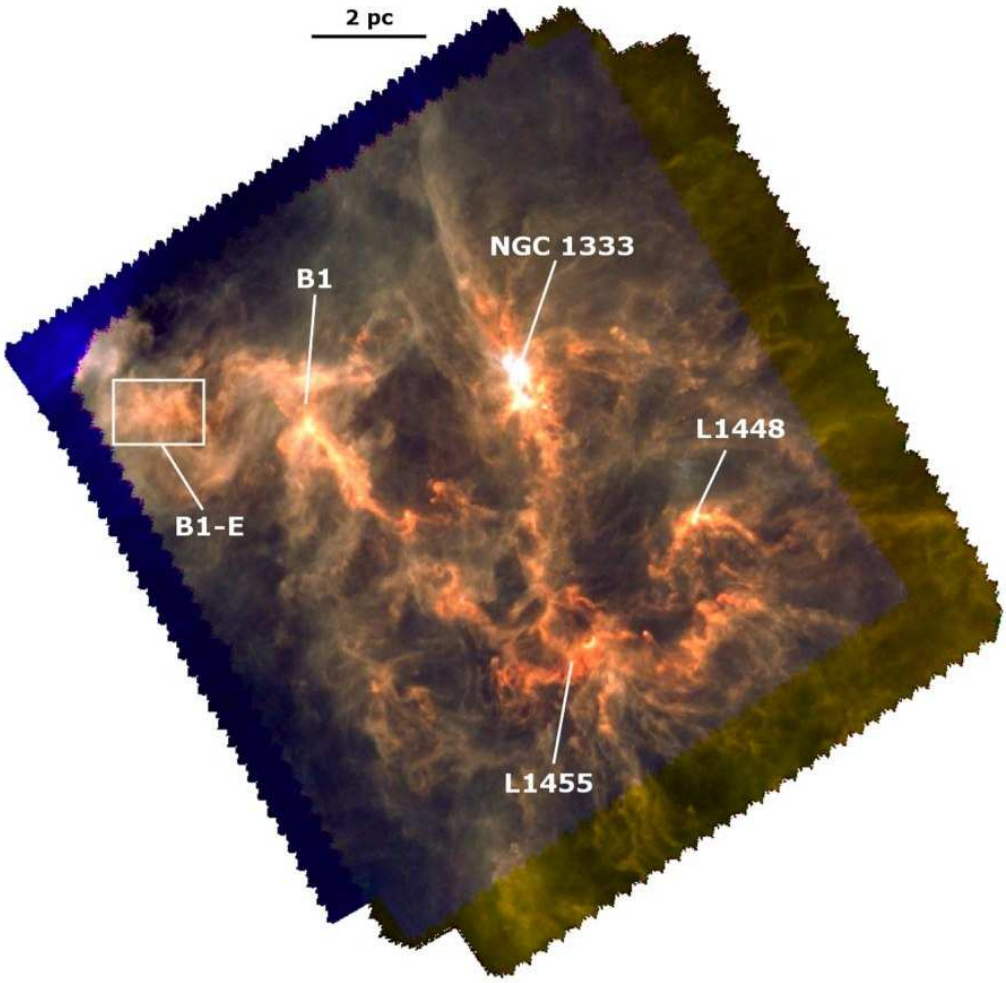

Figure 3.1: Three-colour image of the western half of the Perseus molecular cloud. Colour mosaic was generated using *Herschel* 160 μm, 250 μm, and 350 μm observations. The white box denotes our boundary for B1-E for subsequent figures. The other prominent clumps in Western Perseus are also labeled.

Unlike previous ground-based submillimetre instruments, *Herschel* can detect

[1]Due to the fast scan rate, the 160 μm beam is slightly elongated along the scan direction. Thus, we adopt the geometric mean (i.e., $R_{eff} = \sqrt{ab}$) as the beam size, where the elongated beam dimensions are from Poglitsch et al. (2010).

large-scale diffuse emission (e.g., Schneider et al., 2010; Miville-Deschênes et al., 2010; Arzoumanian et al., 2011). Additionally, *Herschel* has excellent sensitivity to low-level flux. For example, Figure 3.2 compares SCUBA 850 μm observations of B1-E (smoothed to 23″ resolution; Di Francesco et al., 2008) with the new SPIRE 250 μm observations (at 18″ resolution). The SPIRE 250 μm data show prominent substructures not identified in the SCUBA 850 μm data, though several faint features at 850 μm appear to agree with the brighter structures in the 250 μm map. With the higher sensitivity of *Herschel*, we are able to identify clearly structures in B1-E that were too faint, i.e., $< 3\ \sigma$, to be robust detections with SCUBA.

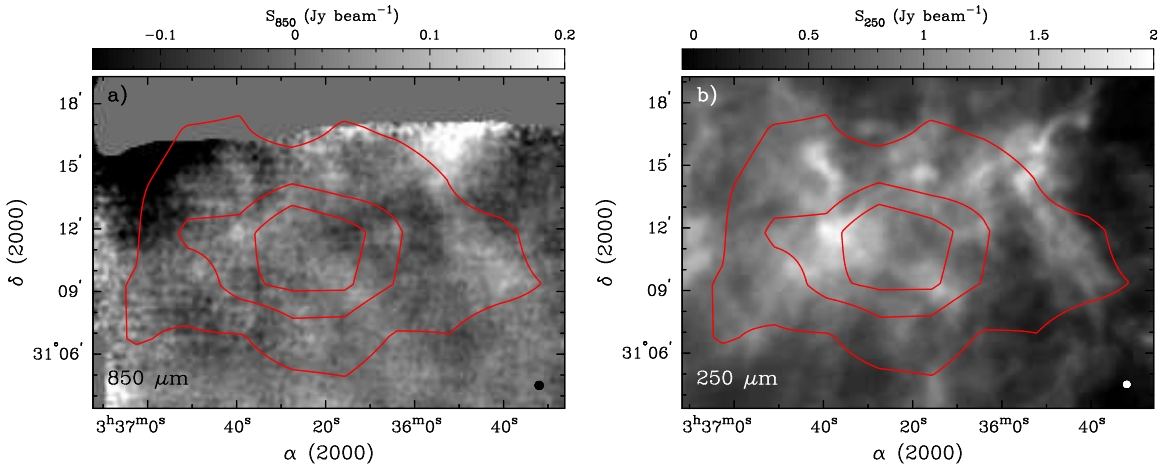

Figure 3.2: Observations of Perseus B1-E from (a) SCUBA 850 μm and (b) SPIRE 250 μm maps. The SCUBA data came from the Extended SCUBA Legacy Catalogue (see Di Francesco et al., 2008). Contours represent extinction levels of $A_V = 5$, 7, 8 magnitudes from the COMPLETE extinction map (Ridge et al., 2006a) and the filled circles show the beam sizes of 23″ for smoothed SCUBA data at 850 μm and 18″ for SPIRE data at 250 μm.

3.2.2 GBT Observations

We selected nine compact substructures with the largest column density values in our *Herschel*-derived H_2 column density map of B1-E (see Section 3.3.2) for complementary follow-up observations with the new K-band Focal Plane Array (KFPA) receiver on the GBT[2]. Our targets, hereafter named B1-E1 to B1-E9 according to decreasing peak column density, were observed on 03 March 2011 with single-pointings. We used the KFPA receiver with one beam and four spectral windows to observe each

[2]The GBT is a 100 m telescope operated by the National Radio Astronomy Observatory.

target simultaneously in NH_3 (1,1), NH_3 (2,2), CCS ($2_1 - 1_0$), and HC_5N (9-8) line emission at 23.6945 GHz, 23.7226 GHz, 22.3440 GHz, and 23.9639 GHz, respectively. Similar to Rosolowsky et al. (2008), we made frequency-switching observations with 9-level sampling and 12.5 MHz bandwidth over 4096 spectral channels in each window to achieve a velocity channel width of $v_{ch} \approx 0.0386$ km s^{-1} at 23.69 GHz. B1-E1 to B1-E8 were observed for $\sim$ 1120 seconds, each. B1-E9 was observed for $\sim$ 840 seconds.

We reduced the GBT data using standard procedures in GBTIDL[3] for frequency-switched data. In brief, individual scans from each spectral window were filtered for spikes or baseline wiggles, folded, and then averaged. Baselines were obtained for the averaged spectra by fitting 5th-order polynomials to line-free channel ranges at the low- and high-frequency edges of each band, and were then subtracted. To improve the detection levels, the data were smoothed with a boxcar kernel equal to two channels in width. The reduced data were exported from GBTIDL into standard FITS files using routines of AIPS^{++} developed by G. Langston. Further analysis was conducted in MIRIAD[4] and IDL (Interactive Data Language). The 1 σ noise levels were typically $\sim 0.01 - 0.02$ K per channel. At 23.69 GHz, the GBT beam is $\sim 33''$ and the beam efficiency is $\eta_b = 0.825$.

Table 3.1 gives the positions, peak H_2 column density, and the detected line emission of these targets. The main NH_3 (1,1) component was detected at $> 3\ \sigma$ towards all nine targets and CCS ($2_1 - 1_0$) line emission towards several. The NH_3 (2,2) and HC_5N (9-8) lines were only detected toward B1-E2.

3.3 Results

3.3.1 SED Fitting to *Herschel* Data

We corrected the arbitrary zero-point flux offset in each *Herschel* band using the method proposed in Bernard et al. (2010) that is based on a comparison with the Planck HFI (DR2 version, see Planck HFI Core Team et al., 2011) and IRAS data. In addition, each map was convolved to the resolution of the 500 μm map ($36.6''$) and regridded to $14''$ pixels. The map intensities of the $160 - 500$ μm bands were then fit

[3]GBTIDL is a special IDL package specific to the GBT.

[4]Multichannel Image Reconstruction, Interactive Analysis, and Display (MIRIAD) software is developed by the Berkeley Illinois Maryland Array (BIMA) group. See Sault et al. (1995) for more details.

Table 3.1: GBT Target Information

Source	α (J2000) (h:m:s)	δ (J2000) ($^\circ$ $'$ $''$)	N(H_2)[a] (cm^{-2})	Detections[b]
B1-E1	3:35:55.0	31:14:16	1.9×10^{22}	NH_3 (1,1); CCS
B1-E2	3:36:04.4	31:11:47	1.7×10^{22}	NH_3 (1,1); NH_3 (2,2); CCS; HC_5N
B1-E3	3:35:52.1	31:15:39	1.5×10^{22}	NH_3 (1,1); CCS
B1-E4	3:35:51.0	31:12:34	1.5×10^{22}	NH_3 (1,1)
B1-E5	3:36:37.3	31:11:41	1.5×10^{22}	NH_3 (1,1)
B1-E6	3:36:41.0	31:15:05	1.4×10^{22}	NH_3 (1,1)
B1-E7	3:36:39.0	31:14:27	1.4×10^{22}	NH_3 (1,1); CCS
B1-E8	3:36:05.0	31:14:28	1.3×10^{22}	NH_3 (1,1); CCS
B1-E9	3:36:18.5	31:14:31	1.3×10^{22}	NH_3 (1,1)

[a]Peak *Herschel*-derived H_2 column density towards the sources. See Section 3.3 for more details.
[b]Line emission detected towards each source.

by the modified black body function,

$$I_\nu = \kappa_\nu B_\nu(T)\Sigma \tag{3.1}$$

where κ_ν is the dust opacity, B_ν is the black body function (Equation 1.2), T is the dust temperature, and Σ is the gas mass column density. Note that $\Sigma = \mu m_H \mathrm{N}(H_2)$, where μ is the mean molecular weight, m_H is the hydrogen mass, and N(H_2) is the H_2 gas column density. Hereafter, column density refers to the H_2 gas column density, unless specified otherwise. For consistency with other papers in the Gould Belt Survey (e.g., André et al., 2010),

$$\kappa_\nu = 0.1(\nu/1000\ \mathrm{GHz})^\beta\ \mathrm{cm}^2\ \mathrm{g}^{-1}, \tag{3.2}$$

where β is the dust emissivity index. The SED fits were made using the IDL program *mpfitfun* by C. B. Markwardt. In brief, *mpfitfun* performs a least-squares comparison between the data and a model function by adjusting the desired parameters until a best fit is achieved.

Fitting β requires a plethora of data, particularly along the Rayleigh-Jeans tail (e.g., $\lambda > 300$ μm at 10 K), to remove degeneracies in the model fits (Doty & Leung, 1994; Shetty et al., 2009b). Since we have only two photometric bands (350 μm and 500 μm) along the Rayleigh-Jeans tail, we assume $\beta = 2$, consistent with the

adopted β in other *Herschel* first-look studies (e.g., André et al., 2010; Arzoumanian et al., 2011). There is some evidence for $\beta \approx 2$ in recent Planck studies (see Planck Collaboration et al., 2011a,b, and references therein). Adopting $\beta = 2$ here provides good fits to our data (see below).

Figure 3.3 shows the dust temperatures and column densities across B1-E resulting from the modified black body fits to each pixel for the $160 - 500$ μm bands, assuming flux uncertainties of 15% based on calibration uncertainties (see Griffin et al., 2010; Poglitsch et al., 2010), $\mu = 2.33$, and $\beta = 2$. Temperature and column density in B1-E are highly structured (see Figures 3.3a and 3.3b), where regions of higher column density are also associated with slightly cooler temperatures and regions of lower column density have slightly warmer temperatures. Most of the cooler, high column density material ($\gtrsim 6 \times 10^{21}$ cm^{-2}) is clumped into a central ring-like structure (i.e., slight depression is seen towards the very centre).

Figures 3.3c and 3.3d show the number histograms of temperature and H_2 column density, respectively. These distributions are non-Gaussian. The sample mean and standard error about the mean for the temperature and column density are 14.1 K $\pm$ 0.8 K and $(6.3 \pm 2.7) \times 10^{21}$ cm^{-2}, respectively, where the standard error of the mean is computed from,

$$SE = \sqrt{\frac{1}{N-1} \sum (x_i - \bar{x})^2}, \tag{3.3}$$

where $\bar{x}$ is the population mean for the sample of size N.

These mean values agree well with previously estimated quantities for this region. For example, Schnee et al. (2005) measured a mean dust temperature of ~ 14 K for the B1-E region using the ratio of IRAS 60 μm and 100 μm flux densities to estimate dust temperature. Additionally, extinction data from the COMPLETE survey (see contours in Figures 3.2 and 3.3) suggest a mean column density of $(5.3 \pm 1.5) \times 10^{21}$ cm^{-2}, assuming $N(H_2)/A_V = 10^{21}$ cm^{-2} mag^{-1}. Using a higher resolution extinction map from S. Bontemps (see Sadavoy et al. 2010), we find a mean column density of $(6.3 \pm 3.6) \times 10^{21}$ cm^{-2}. These two column densities agree very well with our measured value of $(6.3 \pm 2.7) \times 10^{21}$ cm^{-2} and they are also similar to the threshold column density for dense core formation from the extinction analysis in Perseus by Kirk et al. (2006), 5×10^{21} cm^{-2}. For comparison, Figure 3.3d includes the Kirk et al. column density threshold as a dashed line. Although B1-E does not appear filamentary, there is ample material from which dense cores may form. With *Herschel* data, André et al. (2011) found a threshold column density of 7×10^{21} cm^{-2} for dense structures to form

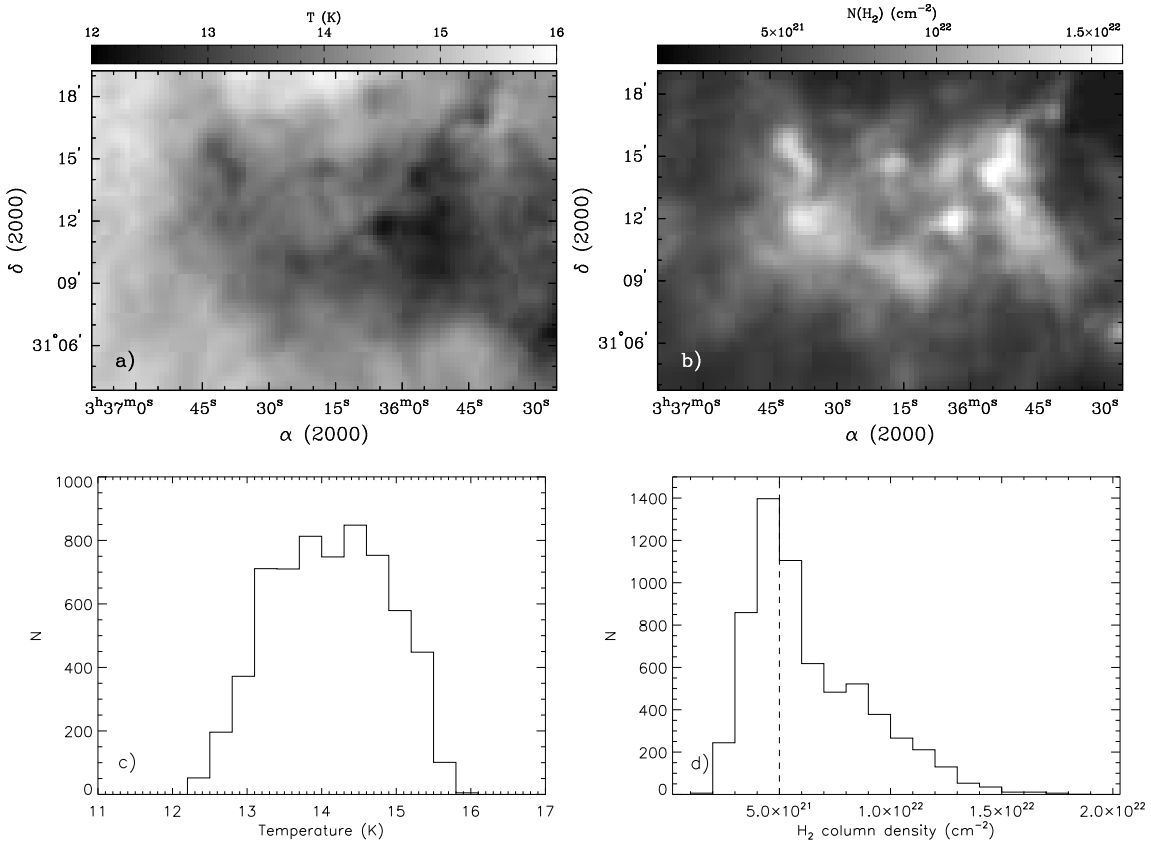

Figure 3.3: SED-fitting results for B1-E. *Top panels* shows the temperature (a) and H_2 column density (b) maps across B1-E as measured from SED-fitting to 160 - 500 μm data, according to Equations 3.1 and 3.2 and assuming $\beta = 2$. *Bottom panels* show the histograms of the above maps. The temperature histogram (c) uses a bin size of 0.3 K and the H_2 column density histogram (d) uses a bin size of 1×10^{21} cm^{-2}. For comparison, the dashed line in panel (d) indicates the observed column density threshold (from extinction) for core formation from Kirk et al. (2006).

in Aquila via thermal instabilities along a filament at 10 K.

3.3.2 Column Density Profiles

One of the more prominent core models is the Bonnor-Ebert sphere (Bonnor, 1956; Ebert, 1955), which represents the density profile of a sphere in hydrostatic equilibrium under the influence of an external pressure. The Bonnor-Ebert sphere has a flat inner density distribution and a power-law density downtrend at larger radii. Many prestellar cores, i.e., dense cores that are gravitationally bound but do not show evidence of a central luminous protostar, have shown Bonnor-Ebert-like profiles (e.g., Ward-Thompson et al., 1999; Alves et al., 2001).

With the excellent spatial resolution of *Herschel*, we can measure the column density profiles for individual B1-E substructures. First, we identified the *locations* of peak column density using the 2D Clumpfind algorithm (Williams et al., 1994). Briefly, Clumpfind identifies intensity peaks and then uses closed contours at lower intensity levels to assign boundaries. We will discuss the nine highest column density substructures identified by Clumpfind (B1-E1 to B1-E9) for this chapter. Second, we measured the azimuthally-averaged column density profile of our nine sources using the *ellint* task in MIRIAD. For simplicity, we used circular annuli of $10''$ width for $r > 7''$. For the central radii ($r < 7''$), we assume the peak column density. We caution that several of our sources appear elliptical and our circular approximation is meant to provide a broad, first-look analysis.

Figure 3.4 shows the column density profiles, where the column density values are plotted from the centre of each annulus. For comparison, Figure 3.4 also shows the beam profile (solid grey curve), a "generic" column density profile convolved with the beam (dashed grey curve) and an analytical Bonnor-Ebert profile convolved with the beam (dotted curve). For both analytic profiles, we follow the approximation from Dapp & Basu (2009) and assume a temperature of $T = 10$ K, a central density of $n = 10^6$ cm^{-3} and a constant of proportionality of $k = 0.54$, where $k \approx 0.4$ for a singular isothermal sphere and $k \approx 1$ for a collapsing cloud. Our observed column density profiles are much wider than the models, likely due to contaminating material in the foreground or far-background along the line of sight, hereafter called LOS material. Towards the centre of each source, the analytic models and observed profiles are more similar, since the source column density dominates over the LOS level, whereas in the power-law roll-off, the LOS material is likely more significant and the profiles deviate from the analytic models. Unfortunately, the column density of such extended material is difficult to distinguish from the source column density. To estimate its contribution towards each source, we used the subsequent column density at the location where the power-law slope in the column density profile flattened or began to increase. Thus, the LOS material level ranges from $\sim 8 \times 10^{21}$ cm^{-2} for B1-E9 to $\sim 11 \times 10^{21}$ cm^{-2} for B1-E1 or roughly 60% of the peak column density. These LOS column densities are very conservative and could overestimate their actual contributions by as much as a factor of 2. Indeed, these values are larger than the mean B1-E column density of 6.3×10^{21} cm^{-2}.

Figure 3.5 shows a comparison of our nine column density profiles after correcting each profile for LOS material and normalizing to the respective peak column density,

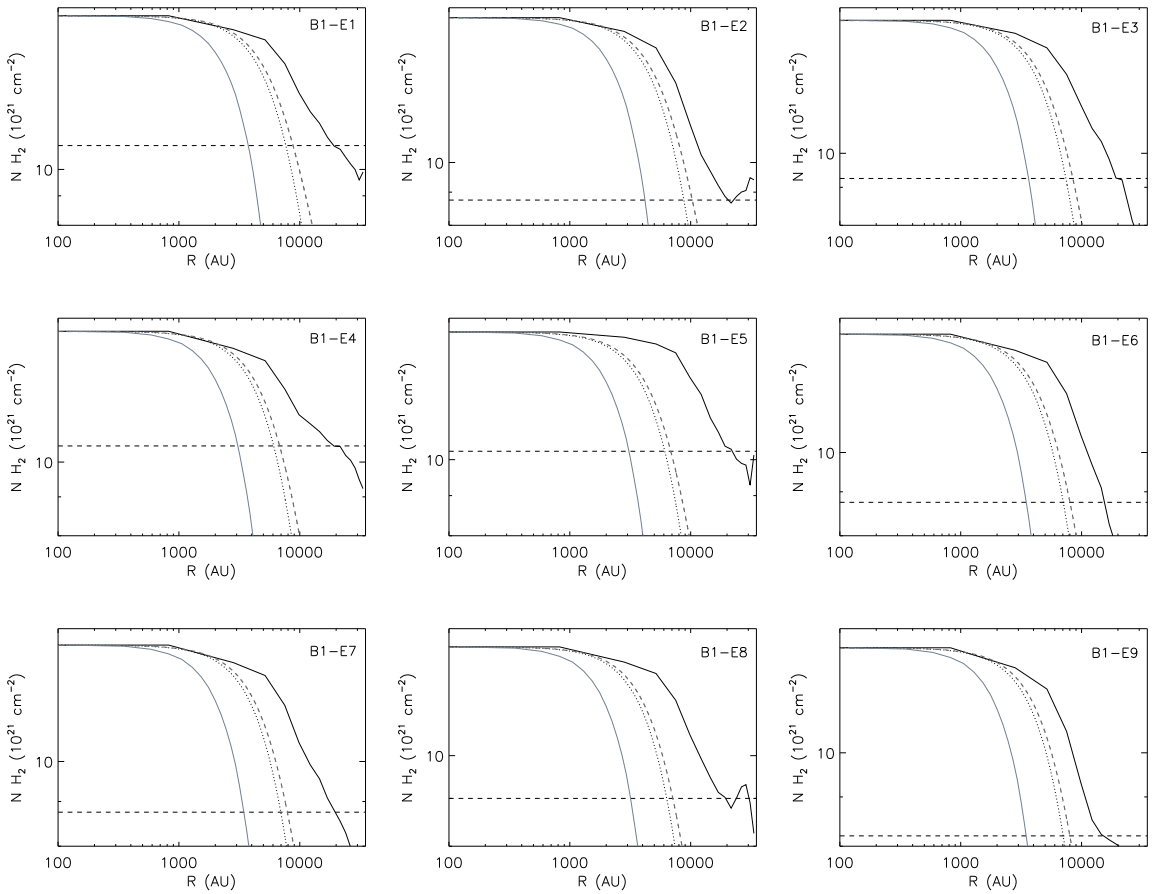

Figure 3.4: The azimuthally-averaged column density profiles for the nine sources in B1-E, assuming a distance of 235 pc. The profiles were measured using circular annuli with a thickness of $10''$ for $r > 7''$. Note that the central area is defined by a circle of radius $7''$ but plotted at $3.5''$. The dashed horizontal line indicates our estimate for the non-source line-of-sight (LOS) material. For comparison, the dotted curve and dashed curve illustrate a Bonnor-Ebert column density profile and a "generic" $[1+(r/a)^2]^{-0.5}$ column density profile following Dapp & Basu (2009). For both analytic curves, we assume a temperature of 10 K and a central density of $n = 10^6$ cm^{-3} and convolved the profiles with a $36.6''$ beam. The grey solid curve shows the beam profile. The analytical profiles and the beam profile are scaled to the peak column density. Note that both axes are logarithmic.

and includes the Bonnor-Ebert profile, generic profile, and beam profile from Figure 3.4. All nine profiles follow a shape similar to those of the analytic models, with a flat centre and steep falloff towards larger radii. Additionally, all profiles but B1-E5 generally appear more centrally concentrated than the models, implying that B1-E5 is the least compact. The column density profiles do show some differences with the models, however, such as steeper fall-offs.

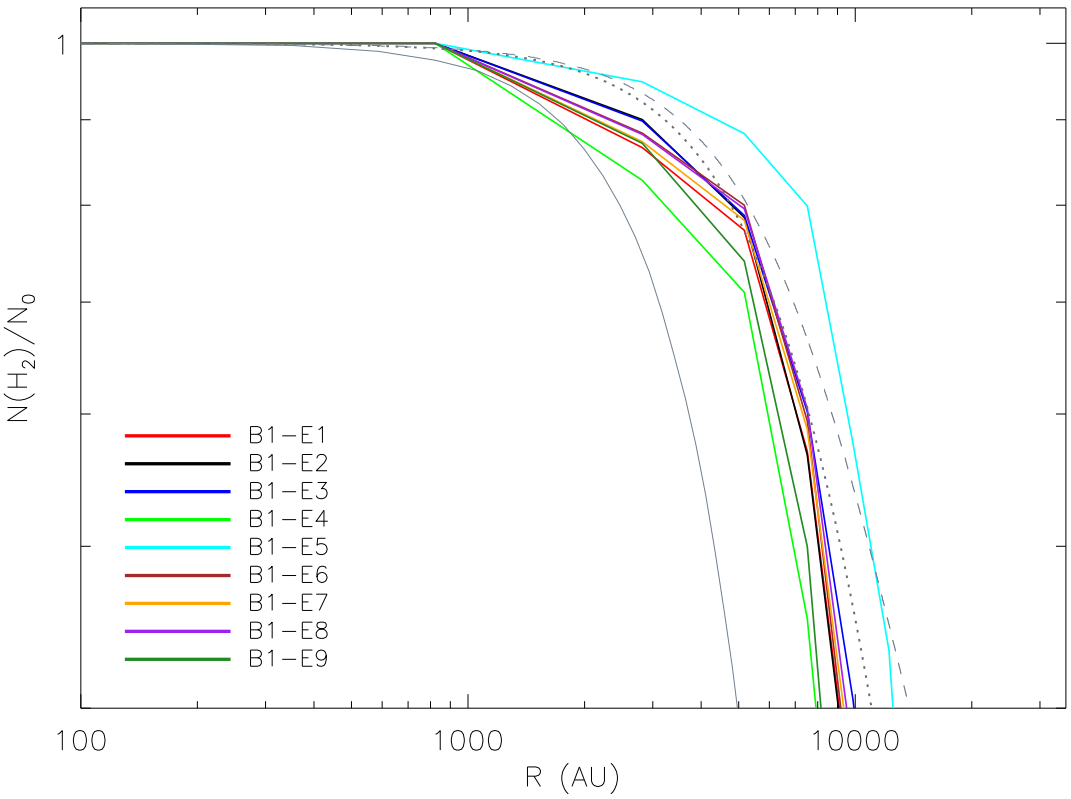

Figure 3.5: Normalized, corrected column density profiles for sources in B1-E. The column density profiles were determined from azimuthally-averaged annuli (see Figure 3.4) with the line-of-sight (LOS) material subtracted out to produce column density profiles for the compact substructures only. The grey solid, dotted, and dashed curves are the same as for Figure 3.4.

3.3.3 Substructures

We estimated source sizes and masses based on Gaussian fits to the LOS-subtracted column density profiles. Source size was defined by the full width at half maximum (FWHM) of the Gaussian (i.e., R = FWHM/2). Since B1-E6 and B1-E7 have a small projected separation of $\sim 50''$, we truncated both to $31''$ radii[5] to ensure that we mostly measured column densities unique to each. Thus, our analyses of B1-E6 and B1-E7 are biased toward the denser, central regions unlike those of the other sources. Subtracting out the LOS material limits the influence from nearby extended material and generally fits only the denser, embedded object. If we include the LOS material, the estimated source sizes generally increase by $\lesssim$ 20%. Isolated

[5]Deconvolved radii are $\approx 25''$.

substructures, like B1-E2 or B1-E8, have sizes that vary by $\sim 5\%$ and substructures embedded in extended profiles like, B1-E1 or B1-E4, have sizes that vary by 24% and 37%, respectively.

Table 3.2 lists the adopted properties for our sources, including their deconvolved radii, estimated (upper and lower) masses, and average densities, assuming they are perfect spheres and dividing the (upper and lower) source masses with their spherical volumes, $\frac{4}{3}\pi R_d^3$, where R_d is the deconvolved radius. We consider two mass and density limits: the lower limits subtract out the LOS material and the upper limits include the LOS material. Note that, by our definition of source size, we are measuring the inner regions of each profile where core precursors are most likely to arise. Since we are using the Gaussian FWHM to estimate the source size, the true source sizes, including any diffuse envelopes, may be larger by a factor of 2. Source mass was estimated by summing over the column density and assuming a mean molecular weight of $\mu = 2.33$. These results provide a reasonable first look at the *relative* sizes and masses of these sources.

Table 3.2: Column Density Determined Properties

Source	R_d[a] (AU)	M[b] ($M_\odot$)	n[c] (10^4 cm^{-3})
B1-E1	7.1×10^3	$0.6 - 1.6$	$5.9 - 17$
B1-E2	6.9×10^3	$0.6 - 1.4$	$6.7 - 15$
B1-E3	7.7×10^3	$0.5 - 1.5$	$4.0 - 12$
B1-E4	6.0×10^3	$0.3 - 1.0$	$4.3 - 18$
B1-E5	9.3×10^3	$0.5 - 2.0$	$2.4 - 9.1$
B1-E6[d]	5.9×10^3	$0.3 - 1.0$	$5.7 - 17$
B1-E7[d]	5.9×10^3	$0.3 - 0.9$	$5.6 - 17$
B1-E8	7.2×10^3	$0.3 - 1.2$	$3.1 - 12$
B1-E9	5.4×10^3	$0.3 - 0.8$	$5.8 - 18$

[a] Object radii were estimated from Gaussian fits to the column density profile ($R = \mathrm{FWHM}/2$). Radii were deconvolved with a 36.6″ beam.

[b] Masses are taken from integrating out the column density profiles. The lower limit measurements subtract the LOS material from the column density profiles. The upper limit measurements do not subtract the LOS material from the column density profiles.

[c] Average density determined from the mass and volume.

[d] B1-E6 and B1-E7 are truncated to measure column density *unique* to each source.

3.3.4 Line Emission

Kirk et al. (2007) and Rosolowsky et al. (2008) each attempted to identify dense gas towards B1-E via high spatial resolution line observations in N_2H^+ and NH_3, respectively. They observed several "blind" pointings towards B1-E and found no strong detections. Unlike previous continuum studies, our *Herschel* data have identified several cold, dense substructures in B1-E (see Figure 3.3) and these were not directly probed by either Kirk et al. or Rosolowsky et al. Using our *Herschel* results, we selected the nine substructures with the highest column densities for follow-up observations with the GBT in NH_3 (1,1), NH_3 (2,2), CCS ($2_1 - 1_0$), and HC_5N (9-8) line emission. Figure 3.6 shows the locations of our nine targets (see also Table 3.1).

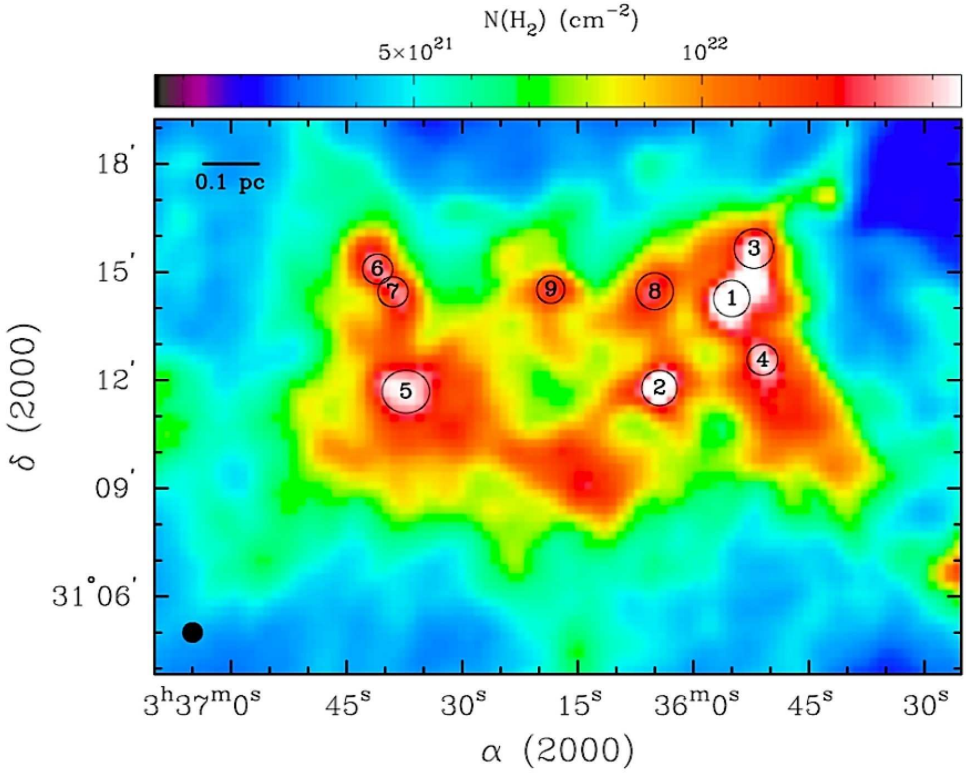

Figure 3.6: Locations of substructures in B1-E overlaid on our *Herschel*-derived column density map. Numbers indicate the positions of peak column densities and the relative magnitude of the column density peak (see also Table 3.1). The thin black circles show the deprojected source sizes (see Section 3.3.3). The dark filled circle shows the GBT beam ($\sim 33''$) at 23.69 GHz.

3.3.4.1 NH_3 Detections

We detected NH_3 (1,1) emission towards all nine targets. We fit the NH_3 (1,1) hyperfine lines with multiple Gaussian components using the following equation;

$$\tau(v) = \tau_{1,1} \sum_{i=1}^{18} \alpha_i \exp\left[-4 \ln 2 \left(\frac{v - v_i - v_{lsr}}{\Delta v}\right)^2\right] \tag{3.4}$$

where $\tau_{1,1}$ is the optical depth for the (1,1) transition, α_i is the transition weight, v_i is the velocity of the hyperfine line (for a given rest frequency), v_{lsr} is the velocity of the source with respect to the local standard of rest, and Δv is the FWHM of the line. We used the hyperfine frequencies and weights from Kukolich (1967) and Rydbeck et al. (1977) and derived the values for $\tau_{1,1}$, v_{lsr}, and Δv from the fits. Figure 3.7 shows example fits to the NH_3 spectra. Table 3.3 lists centroid velocity (v_{lsr}) and observed velocity line width (Δv) from the NH_3 (1,1) fits, the kinetic gas temperature from comparisons of the NH_3 (1,1) and (2,2) line emission, and the resulting thermal and non-thermal velocity dispersions for all nine sources.

For B1-E2, we could derive the kinetic gas temperature using NH_3 (1,1) and NH_3 (2,2) line emission, whereas we could only determine upper limits for our other sources. We use our NH_3-derived kinetic temperature of $T_K = 10.27$ K $\pm$ 0.38 K for B1-E2 and adopt the mean NH_3-derived kinetic temperature of 11 K from the survey of Rosolowsky et al. (2008) for our other sources. As an estimate of the uncertainty, we use the dispersion in the kinetic temperatures from the Rosolowsky et al. data, 2 K, (see Enoch et al., 2008). Note that these gas temperatures correspond to the denser, colder inner layers where ammonia is excited, whereas the dust temperatures (see Section 3.3.1) represent an average of all the material along the line of sight, i.e., including the lower density envelopes. For more information on extracting kinetic temperatures from NH_3 line emission, see Friesen et al. (2009).

Table 3.3 also lists the thermal velocity dispersion, σ_T, and the non-thermal velocity dispersion, σ_{NT}. We determined σ_T from the kinetic temperature and σ_{NT} from

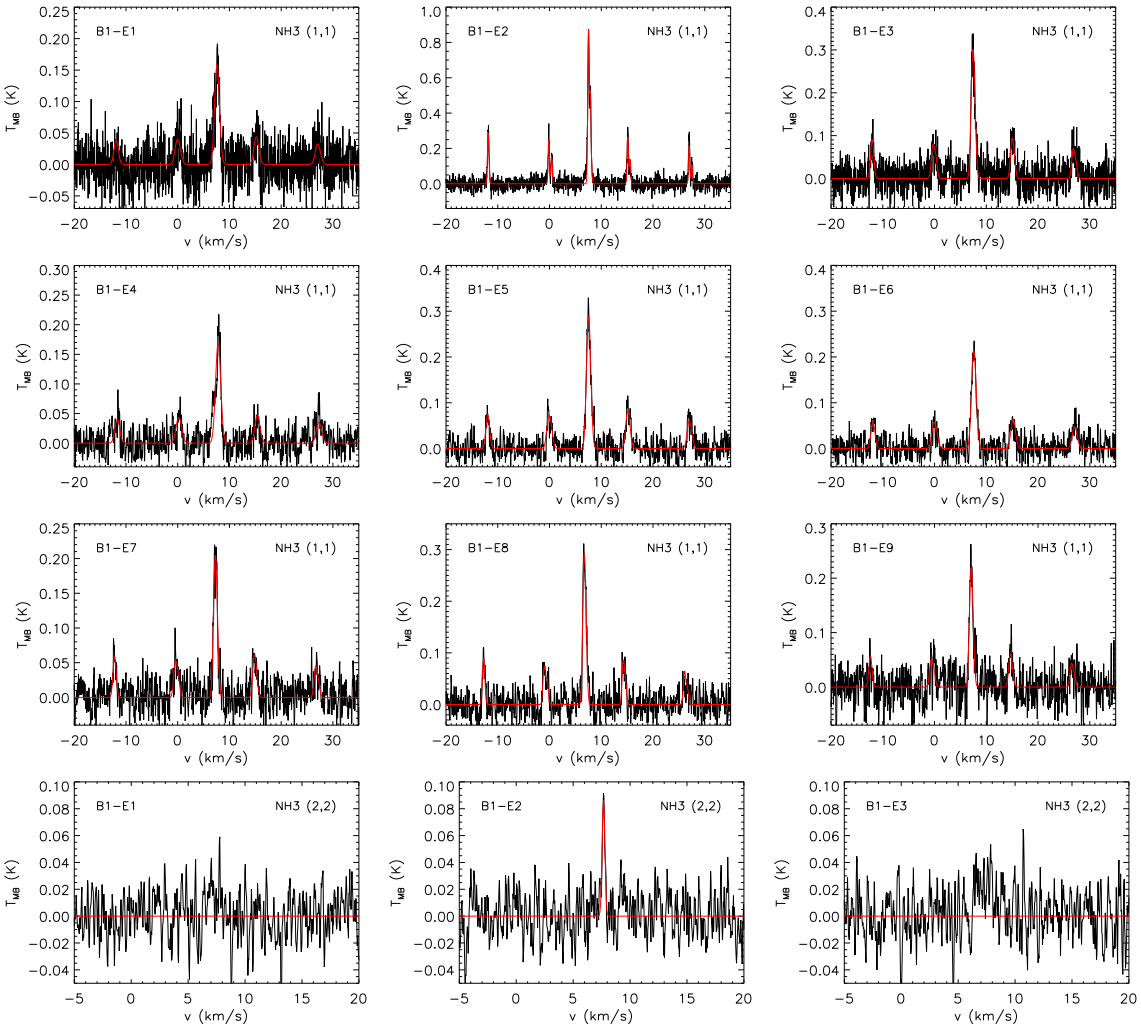

Figure 3.7: Fits to NH_3 (1,1) and (2,2) spectra. Note the hyperfine components visible for the NH_3 (1,1) spectrum of B1-E2. The NH_3 (2,2) spectra were smoothed by a boxcar with a 2-channel width to improve the visual appearance. For comparison, we show two undetected NH_3 (2,2) observations.

the line widths via,

$$\sigma_T = \sqrt{\frac{k_b T_K}{\mu_{NH_3} m_H}} \tag{3.5}$$

$$\sigma_{NT} = \sqrt{\sigma_{obs}^2 - {\sigma_T}^2}, \tag{3.6}$$

where k_b is the Boltzmann constant, T_K is the kinetic temperature, $\mu_{NH_3} = 17.03$ is the mean molecular weight of NH_3, m_H is the atomic hydrogen mass, and σ_{obs} is the total velocity dispersion of the lines, $\sigma_{obs} = \Delta v_c / \sqrt{8 \ln 2}$, where Δv_c is the velocity

Table 3.3: Properties from NH_3 (1,1) and NH_3 (2,2) Line Spectra

Source	v_{lsr} (km s^{-1})	Δv^a (km s^{-1})	$T_K{}^b$ (K)	$\sigma_T{}^c$ (km s^{-1})	σ_{NT} (km s^{-1})
B1-E1	7.61 ± 0.02	0.99 ± 0.06	< 27	0.073 ± 0.007	0.42 ± 0.03
B1-E2	7.67 ± 0.002	0.29 ± 0.005	10.3 ± 0.4	0.071 ± 0.001	0.10 ± 0.003
B1-E3	7.47 ± 0.01	0.68 ± 0.03	< 16	0.073 ± 0.007	0.28 ± 0.02
B1-E4	7.82 ± 0.01	1.08 ± 0.04	< 27	0.073 ± 0.007	0.45 ± 0.02
B1-E5	7.57 ± 0.01	0.83 ± 0.02	< 19	0.073 ± 0.007	0.34 ± 0.01
B1-E6	7.61 ± 0.01	0.91 ± 0.03	< 23	0.073 ± 0.007	0.38 ± 0.02
B1-E7	7.31 ± 0.01	0.71 ± 0.03	< 24	0.073 ± 0.007	0.29 ± 0.02
B1-E8	6.78 ± 0.01	0.54 ± 0.02	< 20	0.073 ± 0.007	0.21 ± 0.01
B1-E9	7.11 ± 0.01	0.69 ± 0.04	< 32	0.073 ± 0.007	0.28 ± 0.02

[a]The velocity FWHM from the best-fit models uncorrected for channel resolution.

[b]Kinetic temperature towards each source. For B1-E2, we measured the kinetic temperature from NH_3 (1,1) and NH_3 (2,2) line emission. For our other sources, we used a 3 σ upper limit for NH_3 (2,2) to estimate the upper limit of T_K.

[c]The thermal line width of B1-E2 was determined using the derived kinetic temperature, T_K = 10.27 K ± 0.38 K. For the remaining sources, we adopted 11 K, the mean NH_3-derived kinetic temperature from Rosolowsky et al. (2008) with an uncertainty of 2 K from the dispersion of the kinetic temperature in that survey (see Enoch et al., 2008).

line width corrected for the channel resolution, $\Delta v_c{}^2 = \Delta v^2 - v_{ch}^2$. Using the NH_3 study by Rosolowsky et al. (2008), we adopted $T_K = 11$ K for all our targets except B1-E2, where we used our derived gas temperature, $T_K = 10.27$ K $\pm$ 0.38 K.

3.3.4.2 CCS and HC_5N Detections

CCS ($2_1 - 1_0$) was detected towards five targets (see Table 3.1) and HC_5N (9-8) was detected towards only B1-E2. Figure 3.8 shows examples of these spectra. We fit the CCS ($2_1 - 1_0$) and HC_5N (9-8) spectra with single Gaussians. The velocities determined for most CCS ($2_1 - 1_0$) detections and the single HC_5N (9-8) detection were similar to those found from NH_3, suggesting these dense gas tracers are probing the same region as the NH_3 emission. The CCS ($2_1 - 1_0$) spectra for B1-E1 and B1-E8, however, revealed fairly different values. For B1-E1, the CCS ($2_1 - 1_0$) line emission appears redshifted by ~ 0.3 km s^{-1} (14 σ) with respect to the NH_3 (1,1) line emission, whereas for B1-E8, the CCS ($2_1 - 1_0$) line emission is redshifted by ~ 0.1 km s^{-1} (1.5 σ). The redshifted CCS ($2_1 - 1_0$) emission in B1-E1 may be tracing a different region of dense gas from the NH_3 emission, such as a region undergoing infall

(e.g., see Swift et al., 2005).

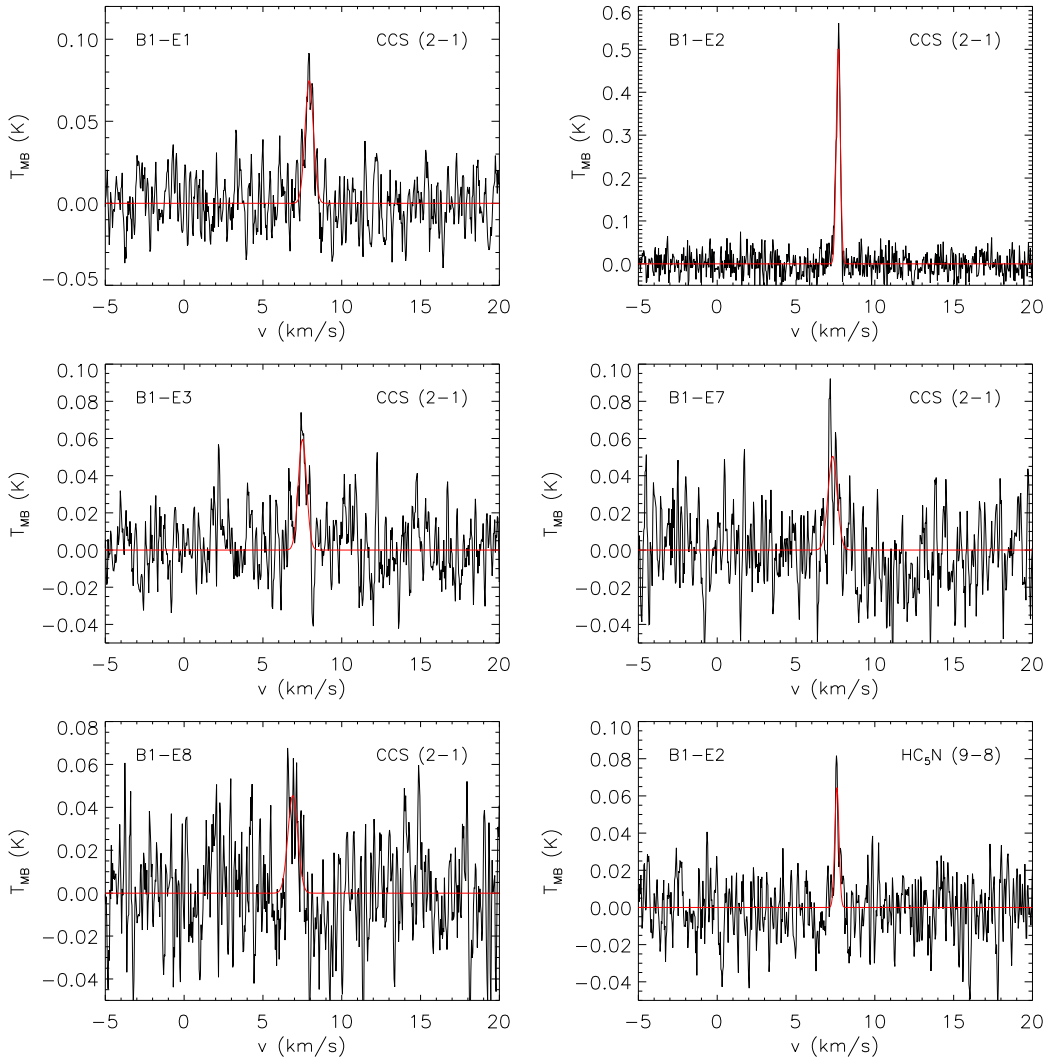

Figure 3.8: Fits to the detected CCS ($2_1 - 1_0$) and HC_5N (9-8) spectra. The weaker CCS ($2_1 - 1_0$) spectra and the B1-E2 HC_5N (9-8) spectra were all smoothed by a boxcar with a 2-channel width to improve the visual appearance of the lines. The B1-E2 CCS ($2_1 - 1_0$) spectrum was not smoothed.

3.4 Discussion

Our *Herschel* data have revealed extensive substructures within B1-E for the first time. Such faint substructures may represent an early evolutionary stage in star formation, where a first generation of cores is forming from lower density material. Thus, it is important to characterize the substructures seen in these *Herschel* maps.

3.4.1 Comparison with Jeans Instability

The minimum length scale for gravitational fragmentation in a purely thermal clump or cloud is described by the Jeans length, $\lambda_J = (c_s^2 \pi / G\rho)^{1/2}$, where c_s is the thermal sound speed, G is the gravitational constant, and ρ is the density of material (Stahler & Palla, 2005). In terms of temperature and number density, we find,

$$\lambda_J = 0.21 \left(\frac{T}{10 \text{ K}}\right)^{0.5} \left(\frac{n}{10^4 \text{ cm}^{-3}}\right)^{-0.5} \text{pc}. \tag{3.7}$$

Ideally, the Jeans length should be calculated for the gas temperature and gas density. In small, dense scales (i.e., $\gtrsim 10^5$ cm^{-3}; Di Francesco et al., 2007), the gas and dust temperatures are coupled, whereas in larger, more diffuse scales, the gas and dust are decoupled and the gas may be warmer than the dust (Young et al., 2004; Di Francesco et al., 2007; Ceccarelli et al., 2007). The central region of B1-E containing the substructures, i.e., the area contained within N(H_2) $> 6 \times 10^{21}$ cm^{-2}, has a mass of ~ 110 M$_\odot$ and an effective radius ($R_{eff} = \sqrt{A/\pi}$) of ~ 0.46 pc. Approximating B1-E as a sphere, we find an average density of $\sim 5 \times 10^3$ cm^{-3}, suggesting that the the gas and dust in B1-E are likely decoupled such that the mean dust temperature of ~ 14 K (see Section 3.3.1) is a lower limit to the gas temperature. Assuming a lower limit gas temperature of 14 K and $n = 5 \times 10^3$ cm^{-3}, the lower limit $\lambda_J \approx 0.35$ pc. Note that the kinetic temperatures measured in Section 3.3.4.1 correspond to the smaller, denser scales where the gas and dust temperatures should be coupled and not the scales measured here.

The minimum projected separations between our nine substructures are generally between 0.1 pc and 0.19 pc, with a median value of ~ 0.13 pc for all nine sources. Recall, however, that B1-E6 and B1-E7 have an angular separation of ~ 0.05 pc, a factor of 2 closer than any other pair of substructures. Despite their close proximity, B1-E6 and B1-E7 show different centroid velocities (see Table 3.3), and therefore, cannot be considered a single object. Also, we can only measure the projected 2-D separations between our nine substructures and not their physical 3-D separations. Assuming a typical inclination angle of 60°, our median separation is ~ 0.15 pc for all nine substructures or ~ 0.17 pc excluding B1-E6 and B1-E7.

The median minimum separation is a factor of two smaller than our best estimate of the Jeans length, though our Jeans length estimate is, itself, uncertain within a factor of a few. The fact that we find a minimum separation that is less than the Jeans

length is still interesting and could indicate gravitational fragmentation followed by bulk contraction of the B1-E group, but the overall uncertainties in determining the minimum separations and Jeans length make this difficult to validate. Additionally, B1-E does not appear to be filamentary (see Figure 3.6) and therefore, the clump could be extended along the line of sight resulting in more significant radial distances between substructures.

For the substructures, we use the Jeans mass to explore their thermal stabilities. Similar to the Jeans length, the Jeans mass is a critical mass scale for gravitational fragmentation such that cores with $M > M_J$ are thermally unstable (Stahler & Palla, 2005). This critical mass can be described as,

$$M_J = 2.9 \left(\frac{T}{10 \text{ K}}\right)^{1.5} \left(\frac{n}{10^4 \text{ cm}^{-3}}\right)^{-0.5} \text{M}_\odot. \tag{3.8}$$

The B1-E substructures have average densities of $n \sim 1 \times 10^5$ cm^{-3} (see Section 3.3.3). Furthermore, we found a gas temperature for B1-E2 of $\sim$ 10 K. Note, that this gas temperature corresponds to the denser B1-E2 substructure and should not be assumed for the lower density B1-E clump. Assuming $T = 10$ K and $n = 1 \times 10^5$ cm^{-3}, the critical Jeans mass is $M_J \approx 0.9$ M$_\odot$. Several of the substructures have mass limits on order of the Jeans mass (see Table 3.2), suggesting that these sources are approaching a critical, unstable mass. Thus, the B1-E substructures are interesting prospects for future studies of substructures evolution.

3.4.2 Time Scale for Interactions

From the *Herschel* observations, the B1-E substructures appear linked (see Figure 3.6), which might indicate that they are interacting. The timescale for any two substructures to interact can be estimated from the typical separation between the substructures and their velocity dispersion. For simplicity, we adopt the average projected separation between all nine substructures of $\sim$ 0.40 pc. For an inclination angle of 60°, the typical separation between the substructures is $d_{ave} \sim 0.46$ pc. To estimate the velocity dispersion of the sources, we use the dispersion of the centroid velocities of NH_3 (1,1) from all nine objects. The weighted 1D centroid velocity dispersion is $\sigma_{1D} \approx 0.24$ km s^{-1} and assuming symmetry, the 3D velocity dispersion[6] is $\sigma_{3D} \approx 0.42$ km s^{-1}. Thus, the B1-E substructures have an interaction timescale of

[6]Assuming $\sigma_{3D}^2 = \sigma_r^2 + \sigma_\phi^2 + \sigma_\theta^2 = 3\sigma_r^2$.

~ 1 Myr, a factor of two larger than recent estimated prestellar core lifetimes and less than the expected protostellar core lifetime (e.g., Kirk et al., 2005; Ward-Thompson et al., 2007a; Enoch et al., 2008). Furthermore, this timescale corresponds to the interaction time between any two substructures and not the interaction time between nearest neighbour substructures. Given that the nearest neighbour separation is a factor of ~ 3 smaller than the typical separation adopted here, these substructures have the potential to interact prior to forming stars. Thus, competitive accretion may be significant during further evolution of B1-E (e.g., Bonnell et al., 2001; Krumholz et al., 2005; Bonnell & Bate, 2006).

3.4.3 Comparison with Virial Equlibrium

Not all dense substructures will form cores and stars. For example, a core with kinetic energy from internal motions that exceeds its gravitational binding energy may be transient and unable to form persistent dense structures or stars. According to McKee (1999), a core is gravitationally bound if the virial parameter, α_v, is

$$\alpha_v = \frac{M_{virial}}{M} = \frac{5\sigma_v^2 R}{GM} \lesssim 2 \tag{3.9}$$

where σ_v is the velocity dispersion, R is the radius, and M is the mass.

B1-E has an effective radius of 0.46 pc (see Section 3.4.1). We estimate the velocity dispersion using the centroid velocity dispersion from Section 3.4.2, $\sigma_{3D} = 0.42$ km s^{-1}. This velocity dispersion was derived from the motions of the individual substructures and thus, reflects the turbulence in the cloud that first created the substructures rather than the thermal velocity dispersion of the gas. The expected thermal velocity of the gas is less than 0.42 km s^{-1}, and thus non-thermal support is important. Assuming $R = 0.46$ pc and $\sigma_v = 0.42$ km s^{-1}, B1-E has a virial mass of ~ 96 M$_\odot$, or $\alpha_v \approx 0.9$ for a clump mass of 110 M$_\odot$ (see Section 3.4.1). These results imply that B1-E is itself gravitationally bound and thus, likely to form dense cores and stars in the future.

For the individual substructures, velocity dispersions were determined from NH_3 (1,1) line widths, after estimating the non-thermal component (σ_{NT}; see Table 3.3) and the thermal component (c_s) for a mean molecular weight of $\mu_{H_2} = 2.33$. Table 3.4 shows our values for the total velocity dispersion, σ_v, the ratio of the velocity dispersion to the thermal sound speed, the virial mass, M_{virial}, and the virial param-

eter, α_v, for each substructure. Most of the virial parameters are $\gg 2$, suggesting that these substructures themselves are not gravitationally bound and thus, may not necessarily represent persistent objects. B1-E2 has the smallest virial parameter, $1 \lesssim \alpha_v \lesssim 3$, however, and may be itself gravitationally bound. B1-E8 and B1-E3 have lower limit estimates of $\alpha_v \sim 3$ and given that we know α_v only within a factor of a few, these sources may also be gravitationally bound. These virial limits, however, depend greatly on the source mass, which can vary by a factor of ~ 4 depending on our treatment of the LOS material (see Section 3.3.3). To be bound, these candidates must have negligible LOS material towards them, which is very unlikely. Thus, B1-E2 is the only strong candidate for being gravitationally bound.

Table 3.4: Virial Analysis Properties

Source	σ_v (km s^{-1})	σ_v/c_s[a]	M_{virial} ($M_\odot$)	α_v[b]
B1-E1	0.46 ± 0.03	2.3 ± 0.3	8.5 ± 4.8	5 - 14
B1-E2	0.22 ± 0.005	1.1 ± 0.03	1.8 ± 0.9	1 - 3
B1-E3	0.34 ± 0.02	1.7 ± 0.2	5.1 ± 2.9	3 - 10
B1-E4	0.49 ± 0.02	2.5 ± 0.3	8.2 ± 4.5	8 - 27
B1-E5	0.40 ± 0.03	2.0 ± 0.2	8.3 ± 4.5	4 - 17
B1-E6	0.42 ± 0.02	2.2 ± 0.2	6.0 ± 3.3	6 - 20
B1-E7	0.35 ± 0.02	1.8 ± 0.2	4.1 ± 2.3	5 - 14
B1-E8	0.29 ± 0.02	1.5 ± 0.2	3.4 ± 2.0	3 - 11
B1-E9	0.34 ± 0.03	1.7 ± 0.2	3.6 ± 2.1	4 - 12

[a] Velocity dispersion divided by sound speed, assuming $T = 11$ K for all substructures except B1-E2 where $T = 10.27$ K.

[b] Virial parameter considering the upper and lower mass limits for each substructure (see Table 3.2).

Most B1-E substructures have very large virial parameters and are thus, expected to be unbound. In comparison, the Jeans mass (see Section 3.4.1) is a mass scale for only gravitational fragmentation in a thermal clump and does not include the contributions from non-thermal support. Several of the substructures with $\alpha_v \gg 2$ have masses on order of the Jeans mass, ~ 0.9 $M_\odot$, suggesting that the Jeans mass analysis is too simplistic and does not well represent the evolutionary state of these structures. For example, the substructures may have significant turbulent motions. With only one potentially bound substructure (B1-E2), it is difficult to determine if B1-E will eventually form several cores or no cores at all (i.e., these substructures are all transient).

The substructures themselves show large line widths (see Table 3.4), atypical of dense prestellar cores, which are subsonic. In particular, B1-E2 has the narrowest line profiles (by at least a factor of 2) and the strongest line detections, suggesting that this object is the most evolved of the substructures. These observations hint at a possible dynamic evolution, where dense cores first contain significant non-thermal, turbulent motions which dissipate into coherent, quiescent dense cores. If so, the substructures in B1-E may become more bound over time as their turbulent support is dissipated, a process which may explain the narrower lines toward B1-E2.

Note that we assume $T_K = 11$ K for our substructures (except B1-E2). In Section 3.3.4.1, we found upper limits for kinetic temperature > 11 K (see Table 3.3). Furthermore, we are using a simplified virial equation in Equation (3.9). Ideally, the virial equation includes magnetic pressure and surface pressure terms which can either assist gravity in the collapse or help in the support of a clump (e.g., see Nakamura & Li, 2008). Our observations, however, do not measure these quantities and thus, we use a simplified virial equation. Nevertheless, B1-E2 is special with respect to the other substructures. Indeed, we may have the first observations of a core precursor.

3.4.4 Comparison with Other Star Forming Regions

B1-E has column densities well above $\sim 5 \times 10^{21}$ cm^{-2}, the core formation threshold reported by Kirk et al. (2006). Since the other clumps with similarly high column densities are actively forming stars, it is reasonable to expect B1-E to do the same in the near future. Furthermore, Lada et al. (2010) found a good correlation between the number of YSOs in a cloud (or clump) with the cloud mass above $A_K > 0.8$ (or $A_V > 7.3$) for several star forming regions. Based on their extinction threshold, we find a clump mass of ~ 90 M$_\odot$ for N(H$_2$) $> 7.3 \times 10^{21}$ cm^{-2} and thus, we could expect ~ 10 YSOs to form in B1-E. With *Herschel*, we have detected several substructures with moderate densities of $\sim 10^5$ cm^{-3} (see Table 3.2), similar to what is often defined for dense cores, i.e., $\gtrsim 10^4$ cm^{-3} (Bergin & Tafalla, 2007).

These substructures, however, were not well detected by SCUBA at 850 μm (see Figure 3.2) or Bolocam at 1 mm, two instruments normally associated with detections of dense cores (e.g., Kirk et al. 2006; Enoch et al. 2006). The substructures in B1-E also have supersonic velocity dispersions. In general, low-mass starless cores have subsonic velocity dispersions (e.g., Myers, 1983; Kirk et al., 2007; André et al., 2007; Pineda et al., 2010a) whereas protostellar cores can have supersonic velocity disper-

sions (e.g., Gregersen et al., 1997; Di Francesco et al., 2001). Since we see no evidence of protostellar activity whatsoever (i.e., from *Spitzer* data), these substructures are likely unevolved. Thus, the B1-E substructures are not traditional dense cores.

Since B1-E has the potential to form dense cores, we propose that it is fragmenting into a first generation of dense cores and that its substructures are core precursors. Furthermore, B1-E is isolated from YSOs and young stars, so the region is unaffected by environmental processes such as outflows or winds. A nearby expanding dust shell, seen in IRAS 60 μm and 100 μm data (Ridge et al., 2006b), may be sweeping material towards B1-E, though the ring itself does not appear to be directly interacting with this clump. This shell may have a larger impact on the evolution of structure in B1-E in the future.

A relatively pristine core forming region is exceedingly rare. The only additional case may be the inactive high extinction clump (211) identified in L1495 by Schmalzl et al. (2010), though further detailed studies of that clump are still necessary to determine what, if any, substructures are forming cores and stars. A collection of starless cores in Aquila form a similar grouping as in B1-E, however this region has two known protostars nearby ($\lesssim$ 1 pc) and so is not as pristine as B1-E (Könyves et al., 2010, see their Figure 5). Therefore, more observations of B1-E should provide some insight into core formation (transient or persistent) in molecular clouds.

3.4.5 Comparison with Core Formation Models

Core formation simulations attempt to recreate molecular cloud fragmentation, implementing factors such as gravitational collapse, magnetic pressure, and turbulent energy. Many recent studies have argued that models of core formation must consider both ambipolar diffusion and turbulence (e.g., Li & Nakamura, 2004; Dib et al., 2007; Nakamura & Li, 2008; Basu et al., 2009a,b; Gong & Ostriker, 2011). Magnetic fields introduce an additional pressure support that opposes gravitational collapse, whereas turbulence either opposes collapse by introducing kinetic energy support or induces collapse via energy dissipation from compressive shocks.

Several recent studies have examined the effects of different magnetic field and turbulent flow properties (e.g., Li & Nakamura, 2004; Basu et al., 2009a; Price & Bate, 2009). In particular, these simulations examine fragmentation in subcritical (where magnetic fields dominate over gravity) and supercritical (where gravity dominates over magnetic fields) regimes with dissipating turbulent flows. In the *subcritical*

simulations, the fragmenting clouds generally form cores in relative isolation and with less filamentary morphologies, such as ring-like distributions of loose core groups (see also Li & Nakamura, 2002). These cores tend to form more slowly, i.e., fragmentation is suppressed by the strong magnetic field, and since large-scale turbulent flows are generally damped, the velocity field is generally subsonic. (Note that Basu et al., 2009a, find that strong magnetic fields can induce oscillations and create a supersonic velocity field, i.e., $\lesssim 3c_s$.) In contrast, *supercritical* simulations generally form cores associated with filaments, and these cores tend to form relatively quickly and can move supersonically through their environment.

An isolated core forming region is necessary to test model predictions and constrain initial conditions of dense gas before the onset and influence of nearby stars and internal protostars. Thus, B1-E is an ideal target for such measurements (see Section 3.4.4). From our observations, B1-E contains a small, loose grouping of substructures. Although the substructure morphology observed in B1-E is not entirely ring-shaped, the distribution hints at an inclined ring-like structure. Furthermore, if star formation is triggered, it is surprising that B1-E, which is bookended by two highly active and more evolved clumps, IC 348 to the far east and NGC 1333 to the far west, contains no evidence for evolved star formation itself. Furthermore, IC 348 shows many evolved pre-main sequence stars and NGC 1333, though appearing younger, has many YSOs (Bally et al., 2008; Herbst, 2008; Walawender et al., 2008), suggesting that B1-E is not part of an age gradient.

These observations suggest that *B1-E is influenced by a strong, localized magnetic field.* Further tests of this scenario would be possible by observing the entire velocity field for B1-E. Instead, we could only estimate the bulk velocity field from the relative motions of the individual substructures (from line centroids; see Section 3.4.2), $\sigma_{3D} = 0.42$ km s^{-1}. Additionally, we do not have direct measurements of the gas temperature for the B1-E clump. If we use the mean B1-E dust temperature of 14 K as the lower limit gas temperature, $c_s \gtrsim 0.22$ km s^{-1} and the velocity field within B1-E may be supersonic by $\lesssim 2c_s$. These motions can arise in either subcritical or supercritical clouds, though the latter is generally associated with supersonic velocities.

Direct measurements of the magnetic field would also be useful to constrain its role in B1-E. Unfortunately, very little magnetic field information is available here. Goodman et al. (1990) measured optical polarization towards all of Perseus, and for B1-E, they found strong, ordered polarization vectors reaching $\sim 9\%$ polarized light, a factor of two higher than any other dense region in Perseus. While these polarization

observations may suggest a strong magnetic field is associated with the B1-E region, these observations are dependent on the field viewing angle. Also, these data were obtained at very low resolution resulting in only three vectors coinciding with B1-E.

A strong magnetic field does not necessarily relegate turbulent compression or gravity to minor roles in the evolution of B1-E. Indeed, Nakamura & Li (2008) suggest that core forming regions exhibit different phases where magnetic fields, gravity, and turbulence are sometimes dominant and sometimes secondary. For example, they suggest that core forming regions begin with strong magnetic fields and strong turbulence, such that gravity is a secondary effect. After the turbulent energy dissipates, gravitational collapse can proceed via magnetic field lines. Indeed, B1-E has several substructures with significant turbulent motions whereas B1-E2, which appears more evolved, has dissipated its turbulence. Furthermore, with no outflows or nearby young stars, there are no feedback mechanisms to replenish the turbulence in B1-E. Therefore, B1-E provides the unique opportunity to determine how energy is distributed in a core forming region.

3.5 Conclusions

With recent *Herschel* dust continuum observations from the *Herschel* Gould Belt Survey, we identified substructure in the Perseus B1-E region for the first time. With our *Herschel* data, we determined the temperature and column density across the region. We selected the nine highest column density substructures for complementary observations with the GBT. We summarize our main conclusions as follows:

1. B1-E contains a loose collection of roughly a dozen prominent substructures. This morphology is atypical of most star forming regions, which produce dense clusters and organize material along filaments. Such a loose collection of cores can be produced in magnetically subcritical simulations (e.g., see Li & Nakamura, 2002; Basu et al., 2009a) influenced by a strong magnetic field. Furthermore, a strong magnetic field will delay the onset of star formation, which may explain the age discrepancy between B1-E and the other nearby clumps in Perseus, IC 348 and NGC 1333.

2. The B1-E clump as a whole is gravitationally bound with an estimated virial parameter of $\alpha_v \approx 0.9$. Therefore, B1-E is likely to form dense cores and stars. Assuming $T = 14$ K and $n = 5 \times 10^3$ cm^{-3}, we find a Jeans length within the

entire B1-E clump of ~ 0.35 pc, accurate within a factor of a few. We measure a median nearest neighbour separation of ~ 0.15 pc for our nine substructures (~ 0.17 pc excluding B1-E6 and B1-E7), for an inclination of 60°. Thus, the substructures have a median minimum separation that is less than the Jeans length by a factor of two. This smaller length scale could indicate that B1-E contracted after the observed substructures formed.

3. Several of the B1-E substructures have masses on order of the Jeans mass (~ 0.9 $M_\odot$), assuming $T = 10$ K and $n = 1 \times 10^5$ cm^{-3}. Nevertheless, most substructures have large virial parameters ($\alpha_v \gg 2$) indicating that they are gravitationally unbound. The large virial parameter suggests that non-thermal motions are significant and that the Jeans mass does not well represent the critical mass scale for these substructures. B1-E2 is the only substructure with a small virial parameter ($1 \lesssim \alpha_v \lesssim 3$) and, due to its narrow line emission, may be gravitationally bound. Furthermore, NH_3 (2,2) and HC_5N (9-8) were only detected towards B1-E2. Thus, B1-E2 is an excellent candidate for a core precursor.

4. The B1-E substructures have a substantial centroid velocity dispersion (~ 0.42 km s^{-1}) resulting in an interaction timescale of ~ 1 Myr, assuming an average separation of ~ 0.46 pc. This timescale is well within the lifetime of protostellar cores. Thus, competitive accretion may play a significant role in the evolution of structure in B1-E.

The B1-E region appears to be an excellent candidate for future core formation. Further studies, however, are necessary to explore the dust and dynamics of the bulk gas in B1-E. For example, additional submillimetre continuum data along the Rayleigh-Jeans tail (e.g., with SCUBA-2) will improve SED-fitting and more accurately probe the dust emissivity index, β, size, and mass. To date, our *Herschel* observations of B1-E are the only well detected continuum data for the region. Additionally, our GBT observations are the only high resolution kinematic data for B1-E, and we observed only the nine highest column density substructures seen with *Herschel*. These data illustrate the potential of B1-E to be a core forming region. Future observations of *both* the magnetic field strength and the turbulent velocities are necessary to probe further how B1-E will evolve.

Chapter 4

Dust Properties: B1

In this chapter, we present *Herschel* observations from the *Herschel* Gould Belt Survey and SCUBA-2 science verification observations from the JCMT Gould Belt Survey of the B1 clump in the Perseus molecular cloud. We determined the dust emissivity index using four different techniques to combine the *Herschel* PACS+SPIRE data at $160 - 500$ μm with the SCUBA-2 data at 450 μm and 850 μm. Of our four techniques, we found the most robust method was to filter-out the large-scale emission in the *Herschel* bands to match the spatial scales recovered by the SCUBA-2 reduction pipeline. Using this method, we find $\beta \approx 2$ towards the filament region and moderately dense material and lower β values ($\beta \gtrsim 1.6$) towards the dense protostellar cores, possibly due to dust grain growth. We find that β and temperature are more robust with the inclusion of the SCUBA-2 data, improving estimates from *Herschel* data alone by factors of ~ 2 for β and by $\sim 40\%$ for temperature. Furthermore, we find core mass differences of $\lesssim 30\%$ compared to *Herschel*-only estimates with an adopted $\beta = 2$, highlighting the necessity of long wavelength submillimeter data for deriving accurate masses of prestellar and protostellar cores.

4.1 Introduction

Molecular clouds are composed of dust and molecular gas ranging from $\sim 10^2$ cm^{-3} for the large-scale, low-density cloud to $> 10^4$ cm^{-3} for the dense cores (Bergin & Tafalla 2007). These molecular clouds are often traced by their cold dust emission, which peak at far-infrared or submillimeter wavelengths, and many studies have used optically thin dust emission to measure masses and column densities of cores and filaments (e.g.,

Kirk et al. 2006; Enoch et al. 2009; André et al. 2010; Arzoumanian et al. 2011). A key parameter to convert dust emission into mass (or column density) is the dust opacity, which corresponds to the ability of dust grains to absorb radiation. Unfortunately, the dust opacity is one of the most difficult observational measurements, and uncertainties in the dust opacity can result in significant mass uncertainties (Henning et al. 1995; Shirley et al. 2011; Martin et al. 2012). Since dust populations in molecular clouds are expected to change due to dust coagulation and the formation of icy mantles in the densest environments (Draine & Lee 1984; Ossenkopf & Henning 1994), it is important to determine the dust opacity for both the large-scale cloud and the small-scale cores.

Generally, submillimeter dust opacities assume a power-law form such that $\kappa_\nu \sim \nu^\beta$, where β is the dust emissivity index. Since the SEDs of cold, dusty star forming regions are best represented by greybody emission, β is critical to the SED fit. Several studies have attempted to determine β towards specific prestellar or protostellar cores using long-wavelength submillimeter emission (e.g., Friesen et al. 2005, Schnee et al. 2010, Shirley et al. 2011). These studies, however, were limited in wavelength coverage and poor map sensitivities. Conversely, recent observations with *Herschel* extend our ability to measure cold dust emission to larger-scales over multiple wavelengths. In particular, PACS and SPIRE have provided unprecedented sensitivity for far-infrared and submillimeter wavelengths at 70 - 500 μm, which cover the SED peak from cold dust at $T \sim 10 - 40$ K. Both β and temperature, however, affect the curvature of the black body function, and thus, are degenerate towards the SED peak. To break this degeneracy, β can be constrained from the Rayleigh-Jeans tail of the SED (Doty & Leung 1994; Shetty et al. 2009b), i.e., $\lambda \gg 300$ μm for cold star-forming regions at $T \lesssim 30$ K. Therefore, additional long-wavelength data at good resolution and sensitivity are necessary to constrain the dust emissivity.

These requirements make the Submillimetre Common-User Bolometer Array-2 (SCUBA-2; Holland et al. 2013) at the James Clerk Maxwell Telescope (JCMT) an excellent complement to PACS and SPIRE data. SCUBA-2 can simultaneously observe at 450 μm and 850 μm, both at higher resolutions than the three SPIRE bands (the JCMT primary mirror is five times larger than *Herschel*'s). Therefore, SCUBA-2 observations provide necessary data along the Rayleigh-Jeans tail and excellent spatial resolution at longer wavelengths.

To explore possible variations of β towards cold cores, we have combined PACS+ SPIRE data with SCUBA-2 data from the JCMT Gould Belt Survey (GBS) for the

first time. For this study, we have selected the B1 clump of the Perseus molecular cloud. B1 was previously observed with *Herschel* as part of the *Herschel* GBS (see Chapter 3; Pezzuto et al. 2012), and was the first field of the JCMT GBS (Ward-Thompson et al. 2007b) that nominally reached the SCUBA-2 survey depth. B1 is a nearby star-forming region at 235 pc (Hirota et al. 2008) with a total clump mass of $\sim$ 1200 $M_{\odot}$ and $\sim$ 10 dense submillimeter cores grouped into a central cluster (Kirk et al. 2006). B1 is also relatively young (compared with the nearby NGC 1333 and IC 348 clumps), containing a high percentage ($>$ 40 %) of Class I YSOs (see Chapter 1), of which several drive outflows (Jørgensen et al. 2008; Bally et al. 2008). Furthermore, a recent study by Pezzuto et al. (2012) suggests that two dense cores in B1 are excellent candidates for first hydrostatic cores based on *Herschel* detections at $\gtrsim$ 100 μm with no corresponding Spitzer detections at 24 μm. Additionally, *Herschel* observations of B1 revealed several pillar-like structures (see Figure 3.1), suggesting that a strong ionization front may be influencing the clump. This front likely originates from 40 Per, a high mass main sequence star in the Perseus OB2 region (see Bally et al. 2008).

This chapter is organized as follows: In Section 4.2, we describe our *Herschel* and SCUBA-2 datasets, as well as CO $(3-2)$ observations of B1. In Section 4.3, we show our results, first from our SCUBA-2 continuum and CO $(3-2)$ observations, and then from fitting SEDs to the *Herschel*-only bands. In Section 4.4, we determine β using the PACS+SPIRE and SCUBA-2 bands following four different techniques to combine these data. In Section 4.5, we use our most robust technique to probe the variations in dust opacity and core mass, and we discuss the implications of our analyses for future studies that will combine SCUBA-2 and PACS+SPIRE data. In Section 4.6, we summarize our results.

4.2 Data

4.2.1 Herschel Observations

We re-reduced Western Perseus with version 7.0 of HIPE in the same manner as described in Chapter 2 and updated calibration corrections; we used the PACS Calibration Set v26 and the SPIRE Calibration Tree 6.1 for our PACS and SPIRE reductions, respectively. The final maps were produced using version 11 of *scanamorphos* (see Chapter 2).

4.2.2 SCUBA-2 Observations

B1 was observed at 450 μm and 850 μm with SCUBA-2 as part of Science Verification (hereafter, S2SV) observations for the JCMT GBS in October 2011. SCUBA-2 is a bolometer detector with $\sim$ 10000 pixels spread over eight science arrays for a field of view of $\sim$ 45 arcmin^2 (Holland et al. 2013). For comparison, the predecessor bolometer detector, SCUBA, contained only 128 pixels over two science arrays for a field of view of $\sim$ 5 arcmin^2 (Holland et al. 1999). For S2SV, all eight science grade arrays (four arrays for each band) were available.

The B1 clump was observed six times on October 18 in very dry (Grade 1; $\tau_{225} <$ 0.05) weather and three more times on October 19 in poorer conditions (Grade 3; $\tau_{225} < 0.1$). Each observation used a PONG1800 observing pattern (Dempsey et al. 2012; Holland et al. 2013), which involved mapping a $38' \times 38'$ square box centered at $3^h33^m12^s.7$, $+31°06'48''$ (J2000) with a mapping speed of 480 arcsec s^{-1} and scan spacing of $30''$. The box was mapped 5 times, rotating the sides by 18° with respect to the sky between each coverage to produce a well-sampled circular map of $\sim 30'$ diameter. This pattern was repeated to increase the sensitivity of the map. Two of the six observations on October 18 were made at high elevations ($> 65°$), which caused erratic telescope tracking motions during the PONG-mode mapping and introduced corrugated artifacts into the respective images.

The S2SV observations were reduced using the *Starlink* SMURF version 1.4.0 package (Jenness et al. 2011; Chapin et al. 2013) and the *makemap* routine, which generates a map of the sky by iteratively fitting a number of different signals in the data. These signals included the common mode signal (caused by atmospheric emission and oscillations in the refrigerator system), the gain of each bolometer, the atmospheric extinction, and the astronomical signal. The mapmaker iterated until a convergence parameter was reached[1]. Each observation was reduced independently in this manner and then an initial coadded map was produced from the independent observations. We combined the four good observations in Grade 1 weather, rejecting the three Grade 3 observations and two corrugated Grade 1 observations.

An initial coadded map was used to generate a mask that encompassed all parts of the map that contain significant levels of flux. This mask was used to re-reduce

[1]The convergence parameter was defined as $\bar{C_i} = \frac{1}{N_i} \sum |F_{i,p} - F_{i-1,p}| / \sqrt{\sigma_{i,p}}$, where i is the i^{th} iteration, p corresponds to each pixel within the current mask, N_i is the total number of pixels within the mask, $F_{i,p}$ is the flux in each pixel for the ith iteration of the map, and $\sigma_{i,p}$ is the variance in each pixel for the ith iteration. The convergence parameter was measured as an average over all pixels. The ith iteration converged when $\bar{C_i} \leq 0.001$.

all of the data in the manner described above, except the astronomical signal is only retained between each iteration if it lies within the masked area. The purpose of using the mask in this manner was to prevent spurious artifacts in the low sensitivity regions of the map. For simplicity, the mask was generated corresponding to those regions with signal-to-noise ratios $\gtrsim 5$ at 850 μm. Regions outside the mask, however, were not used in any analysis, as the data there did not iterate to convergence. We tested the robustness of the maps by inserting artificial sources into the raw data and recovering reliable fluxes in the final map. Figure 4.1 shows the final reduced maps, highlighting the masked regions. The same mask was used for the 450 μm reductions.

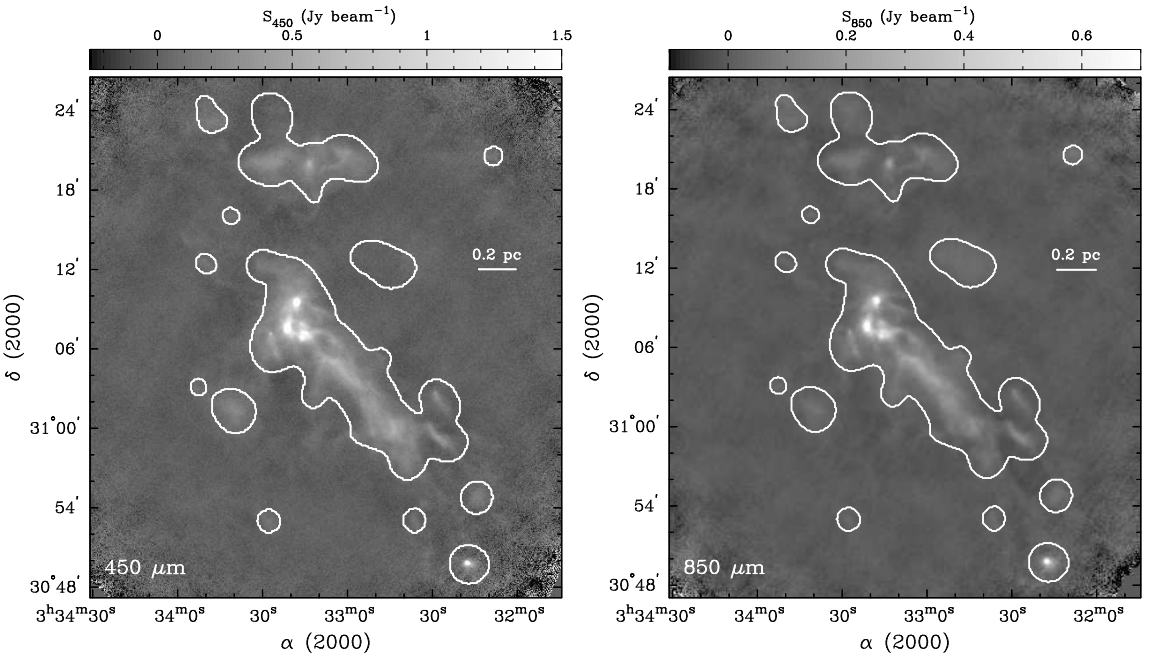

Figure 4.1: SCUBA-2 observations of the B1 clump at 450 μm (left) and 850 μm (right). Contours show the masked regions used in the reductions. Areas outside of the mask have uncertain fluxes.

We used flux conversion factor (FCF) values of 491 Jy beam^{-1} pW^{-1} and 556 Jy beam^{-1} pW^{-1} for the 450 μm and 850 μm maps, respectively, based on observations of standard calibration sources that include planets, asteroids, and stars (Dempsey et al. 2012, Dempsey et al. 2013). These FCF values corresponded to the version of *Starlink* used in our reduction. We adopted a calibration uncertainty of 10% across the SCUBA-2 850 μm map (Dempsey et al. 2012). For the 450 μm band, however, atmospheric variability becomes more significant, even in Grade 1 weather. Therefore, we adopted a 50% calibration uncertainty at 450 μm, which was

the typical flux error at 450 μm adopted for the SCUBA Legacy Survey (Di Francesco et al. 2008). We acknowledge that such a large calibration error is conservative and with further investigation, will be improved. The final 1 σ rms sensitivity of the observed SCUBA-2 map was $\sim$ 7 mJy beam^{-1} at 850 μm over a 6$''$ pixel grid. The effective 1 σ point source sensitivity integrated over the beam area was $\sim$ 3 mJy, the target set by the SCUBA-2 Gould Belt Legacy Survey (Ward-Thompson et al. 2007b). For the 450 μm map, the final 1 σ rms sensitivity was $\sim$ 28 mJy beam^{-1} over 4$''$ pixel grid for an equivalent point source sensitivity of $\sim$ 11 mJy over the beam area.

The SCUBA-2 beam contains two components, the primary beam and an error beam (e.g., Di Francesco et al. 2008). The 450 μm and 850 μm primary beams are $\sim 8''$ and $\sim 13''$ and the error beams are $\sim 25''$ and $\sim 48''$, respectively. At 450 μm, the error beam accounted for $\sim$ 40% of the volume, whereas at 850 μm, the error beam accounted for $\sim$ 25% of the volume and the volume is proportional to the beam amplitude and beam area (Dempsey et al. 2013; see also Section 4.3.1). For this chapter, we adopted effective Gaussian beams with FWHM values of 9.3$''$ and 14.2$''$ for 450 μm and 850 μm, respectively. These effective beams correspond to a single Gaussian with the same volume as the combined observed primary and error beams.

4.2.3 HARP Observations

We mapped the B1 clump in CO $(3-2)$ line emission with the Heterodyne Array Receiver Program (HARP; see Buckle et al. 2009 and references therein) on June 29, 2012 in good Grade 2 weather ($\tau_{225} < 0.08$) over 3 hours. In brief, the HARP instrument consists of sixteen heterodyne detectors arranged in a 4×4 pixel grid and covering a frequency range of 325 - 375 GHz. Observations from HARP are processed by the Auto-Correlation Spectral Imaging System (ACSIS; Jenness et al. 2008). For these observations, only fourteen receptors were functional. We made two position-switch raster maps (in orthogonal directions) over a $30' \times 30'$ region coincident with the S2SV-mapped region. The backend was configured to 1 GHz bandwidth over 2048 channels for a velocity channel width of ~ 0.42 km s^{-1}.

The data were reduced using the ORAC-DR (Cavanagh et al. 2008) pipeline for ACSIS, and the reduction recipe outlined below can be found in the latest *Starlink* release. Heterodyne detectors are notorious for noisy baselines due to external interferences. Rather than reject the entire spectra from these detectors, we performed

an iterative reduction to remove suspect spectra from the time series while keeping the good spectra, thereby improving the signal-to-noise and the coverage of the final spectral map. The reduction pipeline can be broadly divided into two parts:

First, we performed an initial processing of each observation, which includes chronological sorting of the raw time-series cube and a quality-assurance stage. Of particular relevance to the B1 data was the removal of spectra affected by high and low frequency interferences. To identify these interferences, we trimmed the excessively noisy ends of the spectra and excluded the spectral region where the astronomical signal was present. High-frequency noise (3 to 4 spectral elements) was detected using a one-dimensional Laplacian filter along the spectral axis for each receptor, and the affected blocks of spectra were identified by a threshold rms profile along the time axis. Low-frequency oscillations (or distortions in the baseline) were found by smoothing features smaller than 100 pixels, and we summed the rms deviations from the best-linear baseline fit to measure the non-linearity for each spectrum. Again, we used a threshold to identify spectra that contained low frequency artifacts. Spectra or whole receptors that failed quality assurance were rejected.

Second, we applied an iterative procedure, which refined the baseline subtraction at each cycle. We combined and regridded all the raw time series cubes into a group spatial cube. Then, we applied a baseline subtraction and smoothing so that the astronomical emission was located within the group cube using clump finding. The emission defines a further mask, which is converted back to a time series and is applied to the raw time-series cube for the next iteration. In practice one iteration was sufficient.

We converted the final reduced data from T_A^* to T_{MB} using a main beam efficiency of $\eta_{MB} = 0.61$. The final reduced data were smoothed to 0.85 km s^{-1}, resulting in a line sensitivity of $\sim$ 0.3 K per channel. Since the SCUBA-2 and HARP data were observed at the same facility, both data were taken at very similar resolutions ($\sim 14''$). Having both the continuum and line data at the same resolution is very advantageous. Sun et al. (2006) made a more complete CO $(3-2)$ survey of the entire Perseus cloud with the KOSMA 3m telescope. These data, however, have much lower spatial resolution ($\sim 82''$), and therefore, comparisons to the HARP or SCUBA-2 data at $\sim 14''$ are difficult.

4.3 Results

Figure 4.2 shows the observations at 160 μm, 450 μm, 500 μm, and 850 μm for the central B1 region. Ground-based submillimeter continuum detectors like SCUBA-2 contend with rapidly varying atmospheric signals that greatly affect the detection of radiation. To remove the atmospheric emission, we effectively filter-out all large-scale structure from the maps, including the large scale astronomical signals. For our SCUBA-2 data, this effective spatial filtering corresponds to all angular scales of $\gtrsim 2.5'$ based on tests of the mapmaker to recover Gaussians of various sizes (see Appendix B for more details). Therefore, we believe that structures of $\lesssim 2.5'$ are recovered fully by SCUBA-2. Conversely, space-based instruments like those on-board *Herschel* are free from these limitations and can recover the diffuse large-scale emission. For our *Herschel* observations, we can recover spatial scales within half a scan length ($\sim 1.5^{\circ}$).

Another key difference between the SCUBA-2 and *Herschel* observations is resolution. The *Herschel* resolutions are $\sim 8.4'', 13.5'', 18.2'', 24.9''$, and $36.3''$ at 70 μm, 160 μm, 250 μm, 350 μm, and 500 μm, respectively for parallel mode observations at 60 arcsec s^{-1} scan rates. Comparatively, the SCUBA-2 resolutions are $\sim 9''$ and $14''$ for the 450 μm and 850 μm bands, respectively. For clustered environments, the gain in resolution brought by SCUBA-2 at these long wavelengths is important for measuring the properties of compact sources. For instance, some of the compact objects within the central B1 region are blended at the longer *Herschel* wavelengths but separated out with the SCUBA-2 observations (e.g., see the B1-bN and B1-bS cores in Figure 4.2).

4.3.1 SCUBA-2 and HARP Analyses

Molecular line contamination is significant if the line flux measured over the continuum band boosts the continuum signal over the expected value from dust emission alone (White et al. 2003). In cold star-forming regions, line contamination is most prominent from rotational transitions of CO, the second most abundant molecule in molecular clouds. While the *Herschel* data are largely free of line contamination[2], the SCUBA-2 850 μm band is susceptible to contamination from the CO $(3-2)$ line transition at 345.796 GHz, which lies in the middle of the band and is commonly

[2]The 350 μm band can be contaminated by the high excitation transition CO $(7-6)$ at 806.652 GHz, though we believe such contamination should be negligible towards B1. See Section C.

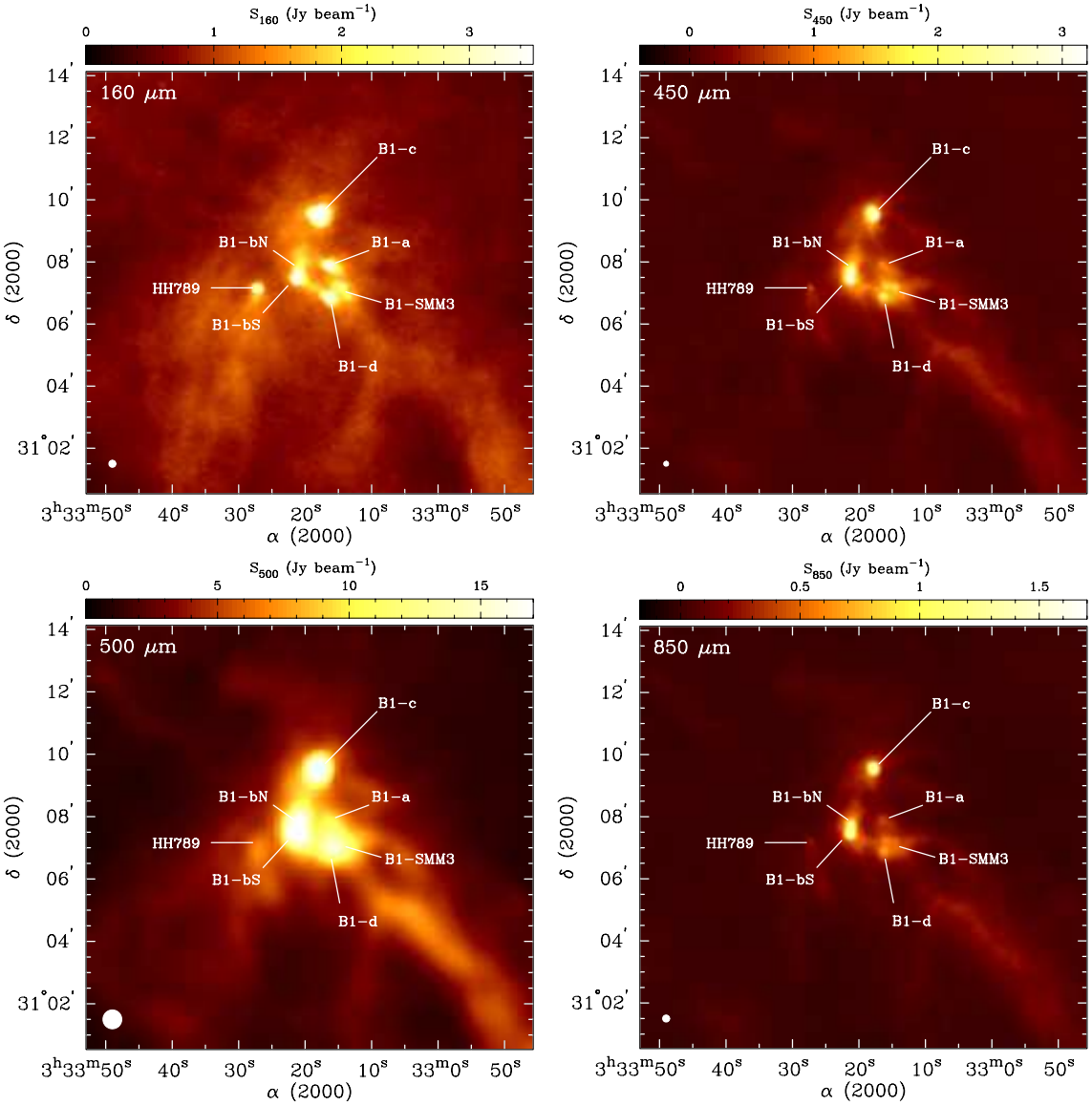

Figure 4.2: Observed continuum maps from PACS at 160 μm (upper left), SCUBA-2 at 450 μm (upper right), SPIRE at 500 μm (lower left), and SCUBA-2 at 850 μm (lower right). Note that several compact objects with PACS and SCUBA-2 are blended at 500 μm. The observed resolutions are $\sim 13''$ at 160 μm, $\sim 9''$ at 450 μm, $\sim 36''$ at 500 μm, and $\sim 14''$ at 850 μm. These maps reveal several known sources in the central B1 region (see Jørgensen et al. 2007; Hatchell et al. 2007).

detected in star-forming regions. Additionally, CO $(6-5)$ line emission at 691.473 GHz can contaminate the 450 μm band; see Appendix C. For a recent summary of the effects of line contamination on observed submillimeter fluxes, see Drabek et al. (2012).

Since the 850 μm continuum bandpass is very wide ($\sim$ 35 GHz), molecular lines

need to be both bright and broad to make significant contributions to the observed continuum emission (Johnstone et al. 2003). We determined the contribution of CO (3−2) line emission to the continuum using the same technique as Drabek et al. (2012). For more details, see Appendix C. Unlike SCUBA-2, the HARP CO $(3-2)$ line data recover large-scale structures since they were obtained using a reference position free of line emission at a much larger angular distance from the target positions. Therefore, we ran the integrated intensity CO $(3-2)$ map through the SCUBA-2 reduction pipeline to produce a filtered CO flux map that includes only emission on the same spatial scales as the 850 μm data (see Appendix B). The filtered CO $(3-2)$ line emission contributed $\lesssim 70$ mJy beam^{-1} ($\lesssim 100$ K km s^{-1}) to the 850 μm continuum emission with the most significant contributions towards the outflows associated with the protostellar cores B1-c and B1-d.

Figure 4.3 compares the 850 μm map before and after the CO $(3-2)$ line contamination was removed. In the left panel, the two lobes of CO $(3-2)$ emission along the northern outflow clearly dominate the continuum flux, contributing up to $\sim 90\%$ of the total 850 μm flux at the positions of the outflow. Aside from these outflows, the corrected 850 μm map (right panel) shows little difference with the original map (left). The CO $(3-2)$ line emission contributes $\lesssim 15\%$ of the total 850 μm flux for the central region of B1 and $\lesssim 1\%$ for the rest of the B1 clump.

Hereafter, the observed 850 μm data have been corrected for CO $(3-2)$ line contamination. For comparisons with *Herschel* data, we convolved both the CO-corrected 850 μm map and the observed 450 μm map to the 500 μm resolution of $36.3''$. For the 450 μm map, both the main beam and error beam were considered in the convolution[3], whereas for the 850 μm map, we found that the relative power in the error beam was not as significant.

4.3.2 Herschel-Only Results

We used the PACS 160 μm and the SPIRE 250 μm, 350 μm, and 500 μm data to estimate the dust properties in B1. Since the PACS 70 μm band can trace non-equilibrium emission from very small dust grains (Martin et al. 2012) and warm dust emission from protostellar sources (as opposed to the cool envelope traced by the

[3]For the 450 μm map, the error beam has a FWHM of $\sim 25''$, which is smaller than the 500 μm beam. We convolved a two-component Gaussian beam with a main component of $7.9''$ and an error component of $25''$ to $34.25''$ for an effective resolution of $36.3''$. Without considering the error beam, the 450 μm fluxes would be overestimated by $\lesssim 10\%$.

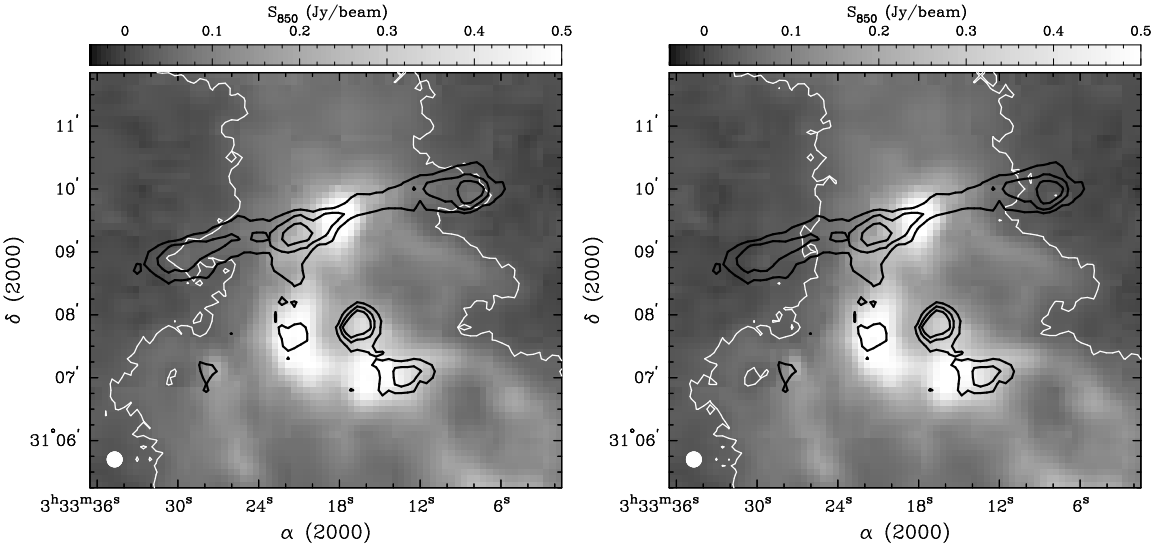

Figure 4.3: Comparisons between 850 μm continuum emission and CO (3−2) line emission. *Left:* Background image shows the uncorrected 850 μm continuum map. Black contours corresponds to CO $(3-2)$ line emission at levels of 10 mJy beam^{-1}, 20 mJy beam^{-1}, and 30 mJy beam^{-1}. The CO data were filtered using the SCUBA-2 pipeline (see Appendix B). The white contours show 850 μm continuum emission at 30 mJy beam^{-1}. *Right:* Background image shows the 850 μm continuum map with the filtered CO line emission subtracted out. The white contours show corrected 850 μm emission at 30 mJy beam^{-1}. The SCUBA-2 and HARP data have a common resolution of $\sim 14.2''$, shown as a white circle.

longer wavelengths), we do not include those data in our analysis. As in Chapter 3, we corrected the arbitrary zero-point flux offset in each band using Planck HFI and IRAS data, and we convolved each map to the same resolution ($36.3''$, or the 500 μm beam FWHM) and projected all maps onto a common grid of $14''$ pixels.

For the PACS and SPIRE bands, minor colour correction factors ($\lesssim 3\%$) are necessary (for more details, see Pezzuto et al. 2012 and Appendix D). Table 4.1 lists our adopted colour correction factors and uncertainties, assuming $\beta \approx 1.5 - 2.5$ and T ≈ 10 K $- 15$ K. Additionally, we estimated the pixel-to-pixel rms sensitivity by selecting several areas relatively free of diffuse emission in the Perseus West map (see Figure 3.1). Table 4.1 lists the approximate 1 σ rms uncertainties at the native resolution of each band and for the convolved maps ($36.3''$ resolution). Since the selected regions were not entirely free of emission, these sensitivity measurements can be considered upper limits to the true map noise. These map sensitivities also depend greatly on the processing, such as the mapmaker. The observed 1 σ rms noise estimates are within a factor of ~ 2 of the expected 1 σ rms noise errors according to the *Herschel*

observation planning tool (HSpot)[4].

Table 4.1: Adopted Colour Corrections and Flux Uncertainties

Band	160 μm	250 μm	350 μm	500 μm
Colour Correction[a]	1.01	1.02	1.01	1.03
Colour Uncertainty[b]	5%	0.8%	1%	2%
rms_ν (mJy beam^{-1})[c]	20	18	15	20
$\mathrm{rms}_{36.3}$ (mJy beam^{-1})[d]	80	60	30	20

[a] Average colour corrections for each band, where $I_{corrected} = CC \times I_{obs}$. These values assume $T \approx 10 - 15$ K and $\beta \approx 1.5 - 2.5$. See Appendix D.

[b] Uncertainties refer to the fractional uncertainty in the average colour correction based on the range of accepted colour corrections. These uncertainties do not include the calibration uncertainties.

[c] Approximate 1σ rms noise in the *Herschel* maps for relatively blank regions at the native resolution of each band.

[d] Approximate 1σ rms noise in the convolved *Herschel* maps for relatively blank regions at $36.3''$ resolution.

Table 1 excludes additional errors from flux calibration. Flux calibration depends on a number of factors, including the calibration files used in the reduction and the mapmaker. Based on point sources, the flux calibration uncertainties are roughly 5% for PACS[5] and 7% for SPIRE[6]. Since we are interested in extended emission and our observations were taken with the fast (60 arcsec s^{-1}) scan rate resulting in elongated beams, we adopted 10% flux calibration errors for both PACS and SPIRE. To simulate these uncertainties, we generated 1000 random correction factors following a Gaussian with a mean of 1.0 and a HWHM of 0.1. Since the flux calibrations are correlated for each instrument (M. Griffin, private communication), we assumed the same flux calibration corrections for the three SPIRE bands and a separate randomly generated set of corrections for the PACS 160 μm band. We applied the randomly-selected PACS and SPIRE calibration correction factors appropriately across the maps.

For each pair of correction factors, we fit the resulting SEDs pixel-by-pixel (see Chapter 3) to identify the broad distribution of best-fit SED parameters within the

[4]HSpot is a joint development by the Herschel Science Ground Segment Consortium, consisting of ESA, the NASA Herschel Science Center, and the HIFI, PACS and SPIRE consortia.

[5]From the "Assessment analysis of the extended emission calibration for the PACS red channel", http://herschel.esac.esa.int/twiki/bin/view/Public/PacsCalibrationWeb.

[6]From the SPIRE Observers Manual, http://herschel.esac.esa.int/Docs/SPIRE/pdf/spire_om.pdf

calibration uncertainties. We fit each SED with the modified black body function,

$$I_\nu = \kappa_{\nu_0}(\nu/\nu_0)^\beta B_\nu(T)\Sigma. \tag{4.1}$$

As in Chapter 3, we assume $\kappa_{\nu_0} = 0.1\text{cm}^2\ \text{g}^{-1}$ at $\nu_0 = 1000$ GHz. We also adopt a mean molecular weight per unit hydrogen mass of $\mu = 2.8$, for a cloud of 71% molecular hydrogen gas, 27% helium, and 2% metals (e.g., Kauffmann et al. 2008). Note that $\Sigma = \mu m_H \text{N}(\text{H}_2)$ is the gas mass column density of material with mean molecular mass μm_H and gas column density $\text{N}(\text{H}_2)$.

Most *Herschel* GBS analyses (e.g., André et al. 2010; Arzoumanian et al. 2011) fit SEDs across the $160-500$ μm *Herschel* bands assuming $\beta = 2$ (Hildebrand 1983). To test this assumption, we used Equation 4.1 to fit the *Herschel* $160-500$ μm data assuming (1) $\beta = 1.5$, (2) $\beta = 2.0$, (3) $\beta = 2.5$, and (4) β is a free variable. We applied the colour correction factors (see Table 4.1) and the random distribution of calibration correction factors to the observed emission. For the flux uncertainties, we added in quadrature the colour calibration uncertainties and the map sensitivities (see Table 4.1). Figure 4.4 shows the distributions of SED-derived parameters for a single example pixel towards the B1-a core. For our sample pixel, when β is fixed, the temperature distributions are narrow despite the wide range in calibration correction factors. The mean temperature, however, varies from $T \approx 14$ K for $\beta = 1.5$ to $T \approx 10.5$ K for $\beta = 2.5$. Allowing β to vary produces broad Gaussian-like temperature and β distributions with mean values of 13.6 K $\pm$ 1.2 K and 1.63 ± 0.26, respectively. These broad distributions suggest that the *Herschel* calibration uncertainties result in significant uncertainties for the SED parameters.

Furthermore, Figure 4.5 highlights the β-temperature degeneracy of SED-fitting with the *Herschel* bands only. First, we generated fluxes assuming (1) $T = 10$ K, $\text{N}(\text{H}_2) = 10^{23}$ cm^{-2}, and $\beta = 2.25$ and (2) $T = 14$ K, $\text{N}(\text{H}_2) = 6 \times 10^{21}$ cm^{-2}, and $\beta = 1.75$. Second, we fitted the generated *Herschel* band fluxes with our dusty black body models assuming $\beta = 1.5, 2.0$, and 2.5 and no calibration uncertainties. The solid curves show the best-fit SED models to the dust emission for the first case and the dashed curves show the best-fit SED models for the second case. For both cases, the generated data were moderately well fit by all three values of β. Note that the *Herschel* bands cover the region illustrated by the grey box where the model curves are largely degenerate. The error bars indicate an uncertainty of 10% to illustrate the range of uncertainty from the calibration. (Recall, instrument calibration is correlated

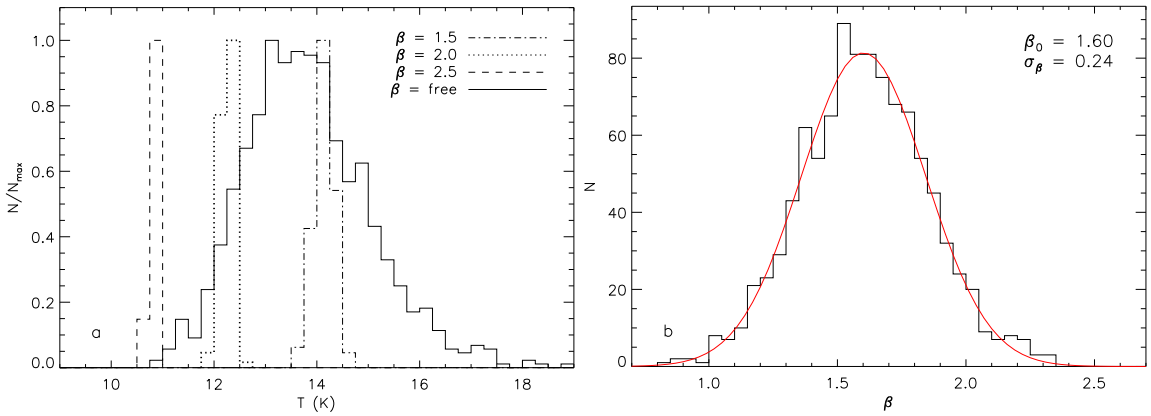

Figure 4.4: Sample results from SED-fitting towards a pixel in the B1-a core. We fit the observed SEDs after applying our colour correction factors and random calibration correction factors (see text). For each calibration correction factor, we fit the modified dust emission with a dusty black body model assuming $\beta = 1.5, 2.0, 2.5$, and free β. We show the (a) relative temperature distributions for each of these cases of β and (b) the β distribution when unrestricted. We fit the β distribution with a Gaussian (red curve).

such that the same calibration correction will be required for the three SPIRE bands.) Conversely, at longer wavelengths, the SED models are more distinct and thus, the SED parameters are much better constrained. Since we have longer wavelength data (i.e., 850 μm), we may circumvent the degeneracy between β and temperature (see Section 4.4).

4.4 Determining β

As discussed in Section 4.3.1, the SCUBA-2 observations do not recover large-scale emission and that emission can be significant. For example, the residuals between a prediction of unfiltered 850 μm emission (i.e., from SED fitting of the *Herschel* data assuming $\beta = 2$) and the observed 850 μm dust emission suggest that the observed fluxes at 850 μm could be missing $\gtrsim 30\%$ of the total emission. Therefore, direct comparisons between PACS+SPIRE and SCUBA-2 observations can be misleading.

In this Section, we explore four different techniques to determine β towards B1 using the SCUBA-2 data. In Section 4.4.1, we determined β using filtered dust emission maps and in Section 4.4.2, we determined β using unfiltered maps. Since filtered maps do not include any large-scale structure, there is no reason to expect a priori that β will be the same for filtered and unfiltered maps. For example, the extended emission may trace more of the warmer, diffuse cloud structure than the cold, dense

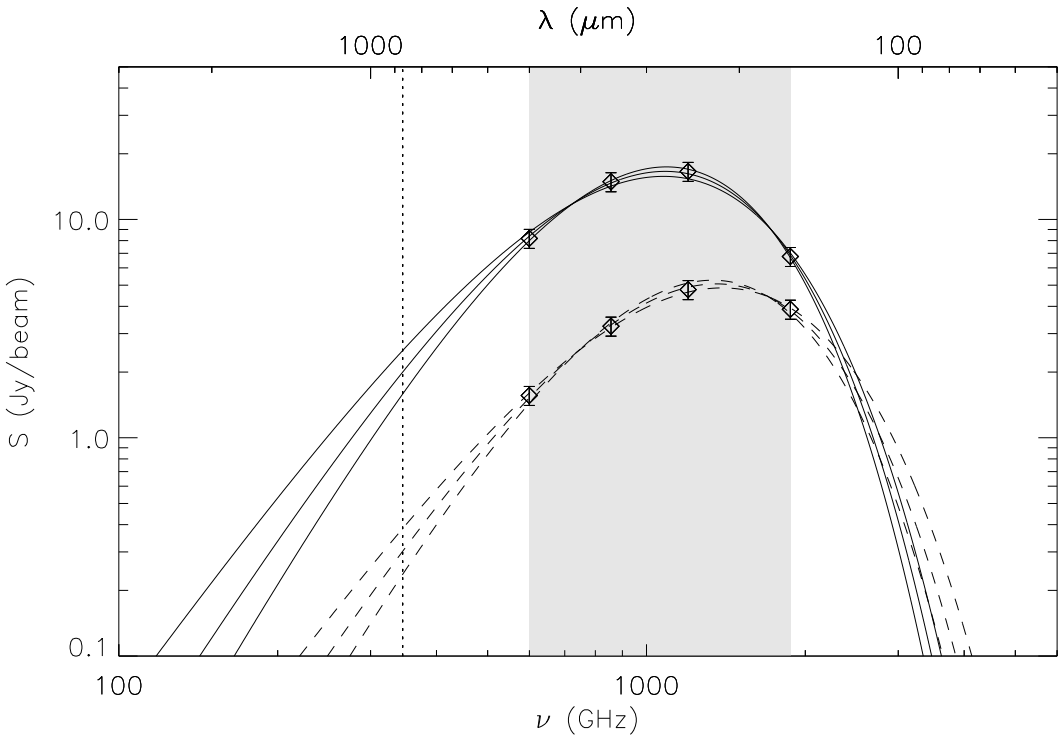

Figure 4.5: Sample modified black body profiles for dust emission corresponding to (solid) $T = 10$ K, $N(H_2) = 10^{23}$ cm^{-2}, and $\beta = 2.25$ and (dashed) $T = 14$ K, $N(H_2) = 6 \times 10^{21}$ cm^{-2}, and $\beta = 1.75$. For both cases, we fit the generated SEDs (diamonds) with (from left to right) $\beta = 1.5, 2.0$, or 2.5. The *Herschel* $160 - 500$ μm bands cover the region highlighted by the solid grey box. The dotted line corresponds to 850 μm. At short wavelengths (i.e., $\lambda \lesssim 100$ μm), the dust emission may become optically thick, and thus, the SED curves could be independent of β at these wavelengths. For simplicity, we do not consider optically thick dust emission at short wavelengths. Thus, β cannot be constrained with short wavelength observations and instead, long wavelength observations are necessary.

structures associated with cores, therefore broadening the SED and lowering β (Martin et al. 2012). If true, the absence of the large-scale structure may result in more pronounced variations in β towards the small scale features in the filtered maps than in the unfiltered maps. For all fits to the SEDs, we used the following procedure *unless stated otherwise*:

1. We applied the colour correction factors in Table 4.1 to the *Herschel* bands.

2. We adopted flux errors as the quadrature sum of the 1 σ rms errors and the uncertainty of the colour corrections (see Table 4.1).

3. We generated different sets of 1000 random calibration correction factors follow-

ing a Gaussian distribution to represent a 10% or 50% calibration uncertainty. We generated a separate set of calibration correction factors for PACS, SPIRE, SCUBA-2 at 450 μm, and SCUBA-2 at 850 μm.

4. We fit SEDs following a minimization of χ^2 routine. We used the modified black body model in Equation 4.1 and the IDL *mpfitfun* routine to minimize the χ^2 fit.

5. For the filtered maps (see Section 4.2.2), we only considered regions with ≥ 10 σ intensities at 160 - 850 μm at 36$''$ resolution (excluding the 450 μm band). The filtered maps are only well measured within the masked regions used in the reduction (see Section 4.2.2). Since the 450 μm data has a higher 1 σ rms noise level ($\sim$ 100 mJy beam^{-1}), these regions include 450 μm emission that is < 5 σ.

4.4.1 β Using Filtered Maps

For our first case (hereafter the Filtered Case), we removed the large-scale emission from the *Herschel* observations by applying the SCUBA-2 reduction pipeline to the observed *Herschel* maps as we did with the CO $(3-2)$ line data (see Appendix B for more information). This technique has the advantage of forcing all the data to include the same range of spatial scales, and thus, β and temperature can be determined from directly fitting the SEDs of the $160-850$ μm emission. Unlike with our SCUBA-2 data, we can compare the filtered and unfiltered versions of the *Herschel* maps and see how the SCUBA-2 mapmaker removes large-scale emission. Figure 4.6 compares the filtered SPIRE 250 μm map with the filtered-out large-scale emission. Note that a few artifacts remain at the locations of the brightest cores. These artifacts are very localized and thus, become negligible ($< 5\%$ of the observed emission) when the filtered maps are convolved to 36.3$''$ resolution. As of this writing, the SCUBA-2 reduction pipeline is still evolving. Thus, while some artifacts may be introduced in this version of the SCUBA-2 reduction pipeline, future versions of the pipeline should improve the filtering.

For our second case (hereafter the SCUBA-2 Ratio Case), we determined β using the 450 μm and 850 μm bands only, i.e., without *Herschel* data (e.g., see Hill et al. 2006; Hatchell et al. 2013). Using Equation 4.1, the ratio of the intensities at 450 μm and 850 μm is

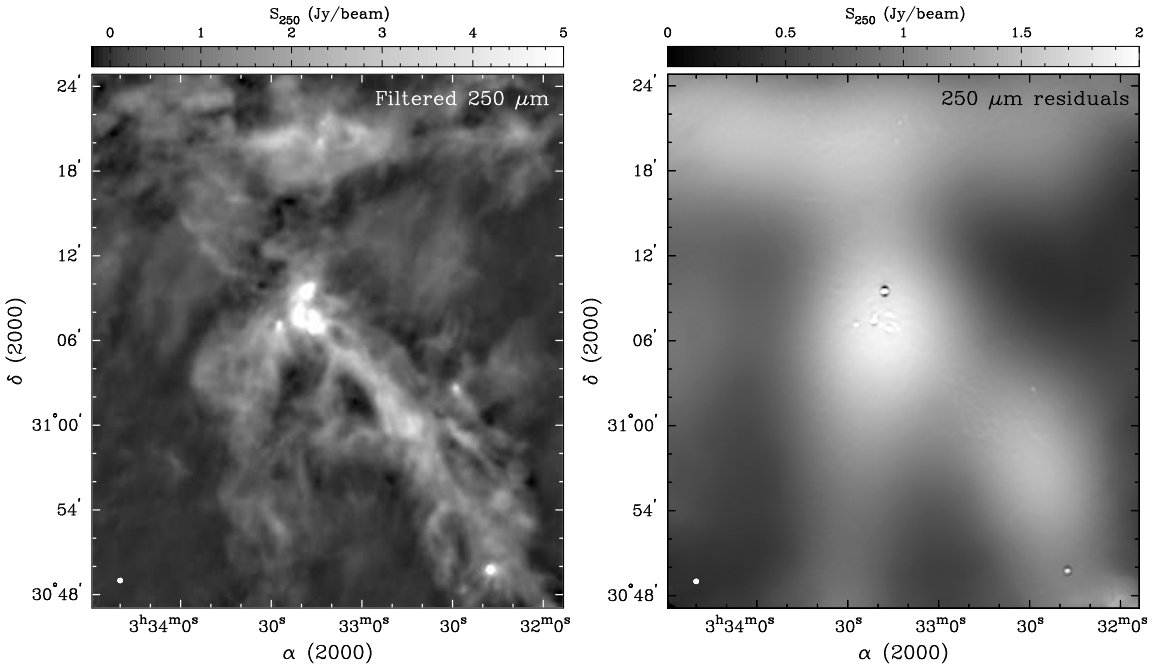

Figure 4.6: Comparison between the filtered *Herschel* map at 250 μm and the filtered-out large-scale emission (using the SCUBA-2 mapmaker; see Appendix B). Map resolutions are $18''$.

$$\frac{I_{450}}{I_{850}} = \left(\frac{\nu_{450}}{\nu_{850}}\right)^{(\beta+3)} \left[\frac{\exp\left(h\nu_{850}/kT\right) - 1.0}{\exp\left(h\nu_{450}/kT\right) - 1.0}\right]. \tag{4.2}$$

Therefore, β can be determined from the ratio of 450 μm to 850 μm emission for a given temperature. For simplicity, we find β for assumed line-of-sight temperatures. We do not naively expect the line-of-sight temperature to be constant, particularly since the B1 cluster contains known protostellar sources (i.e., B1-c, see Figure 4.3). Additionally, we also assume that the 450 μm and 850 μm maps include the same range of spatial scales.

For the Filtered Case, Figure 4.7 shows contour plots of reduced χ^2 assuming temperatures of 5 K $\leq T \leq$ 20 K and β values of $0.5 \leq \beta \leq 4.0$. These plots highlight the uncertainties from the minimization of χ^2 technique only. For clarity, we do not include the calibration uncertainties for these plots. (We note, however, that the calibration uncertainties will only increase the accepted range of beta and temperature values and would not change the behaviour of the SED fitting itself.) For simplicity, we show results for a pixel towards B1-a and a pixel towards the brightest part of the filament, though these sample pixels represent the typical behaviour for B1-a and

the filament. We compare the results from SED-fitting to the *Herschel* bands alone (H-only) and the *Herschel* bands with the 850 μm data (H+850), where the contours correspond to $2\chi_0^2$ and $4\chi_0^2$, and χ_0^2 is the reduced χ^2 measure from the best-fit SED to the corresponding data. Thus, Figure 4.7 represents the *relative* uncertainties in β and temperature from SED fits using the minimization of χ^2 technique. *By adding the 850 μm flux as a new constraint, we see significant improvements in our ability to determine β and temperature.* For example, we find improvements in the uncertainty of β by a factor of ~ 2, and improvements in the uncertainty of temperature by $\sim$ 40% with the 850 μm data.

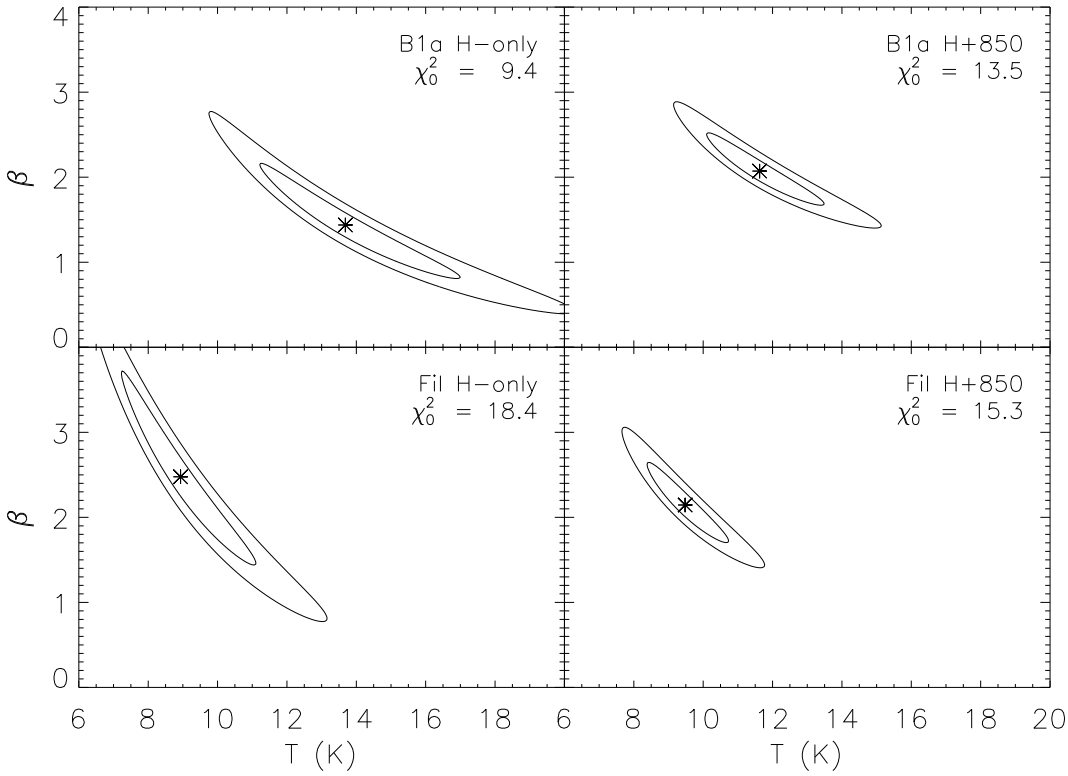

Figure 4.7: Measurements of *relative* reduced χ^2 for assumed values of temperature and β for (top) a pixel towards B1-a and (bottom) another pixel towards the brightest part of the filament (see also Figure 4.8). For these plots, we do not assume any calibration uncertainties. The central star corresponds to the best-fit temperature and β value from SED-fits to the *Herschel*-only (H-only) data or the *Herschel* with 850 μm (H+850) data. The reduced χ^2 measure associated with the best-fit SED, χ_0^2, is shown in the top right corner. The contours correspond to $2\chi_0^2$ and $4\chi_0^2$. For the H+850 data, we have four degrees of freedom and for the H-only data, we have three degrees of freedom.

In addition to temperature and β uncertainties from the fitting technique, each

instrument has a 10% flux calibration error. As in Section 4.3.2, we applied calibration correction factors within a Gaussian distribution to represent the flux calibration errors for each instrument. Figure 4.8 shows the mean β values and two example SEDs for the H-only and H+850 cases. For the H-only case, we found more extreme values of β towards the dense cores and filament. For example, the H-only fits give $\beta \approx 1.5$ towards B1-a and $\beta \approx 2.5$ towards the filament, whereas the H+850 fits give $\beta \approx 2.0$ towards both. Similarly, the H-only fits overestimated the temperature by ~ 2 K towards B1-a and underestimated the temperature by $\lesssim 1$ K towards the filament compared to the H+850 results. In the bottom panels of Figure 4.8, we show the SEDs for the sample pixels towards B1-a and the south-west filament, corresponding to the same example pixels in Figure 4.7. With the 850 μm band included, we found a significant difference in the absolute value of β (see also Figure 4.7), though the uncertainties related to the calibration correction factors are nearly identical.

Figure 4.9 shows the distributions of temperature and β for the Filtered Case. These plots highlight the change in absolute value of β between the H+850 and H-only fits. For the mean β distribution (Figure 4.9b), the H-only β distribution peaks at $\beta \approx 2.5$ and the H+850 distribution peaks at $\beta \approx 2.0$. The 1 σ standard deviation errors based on the calibration uncertainties alone are $\sigma \lesssim 1.5$ K for temperature and $\sigma < 0.3$ for β for both the H-only and H+850 fits. Note that these errors are typically less than the errors from the χ^2 fitting (Figure 4.7), suggesting that the constraints on the SED-fitting are more significant than uncertainties in the flux calibration.

Alternatively, with the SCUBA-2 Ratio Case, we can determine β if the temperature is known (see Equation 4.2). For simplicity, we assumed fixed temperatures across the entire map and for comparison with the Filtered Case, we used the 36.3″ convolved maps at 450 μm and 850 μm. Additionally, we generated 1000 random calibration correction factors within a Gaussian distribution assuming a calibration uncertainty of 50% at 450 μm and 10% at 850 μm. Figure 4.10 compares the resulting mean β distributions from the SCUBA-2 Ratio Case for the assumed temperatures of $T = 9$ K, 11 K, and 13 K. While the β distributions appear to have very similar structures, the distributions themselves are clearly shifted with respect to one another. Using a Kolmogorov-Smirnov test, the β distributions at $T = 9$ K and $T = 11$ K agree within 90% for a shift of $\Delta\beta \approx 0.4$, and the distributions at $T = 11$ K and $T = 13$ K agree within 90% for a shift of $\Delta\beta \approx 0.27$. Furthermore, the high calibration uncertainty at 450 μm results in a standard deviation error of $\sigma_\beta \approx 0.55$ across the B1 clump regardless of the temperature.

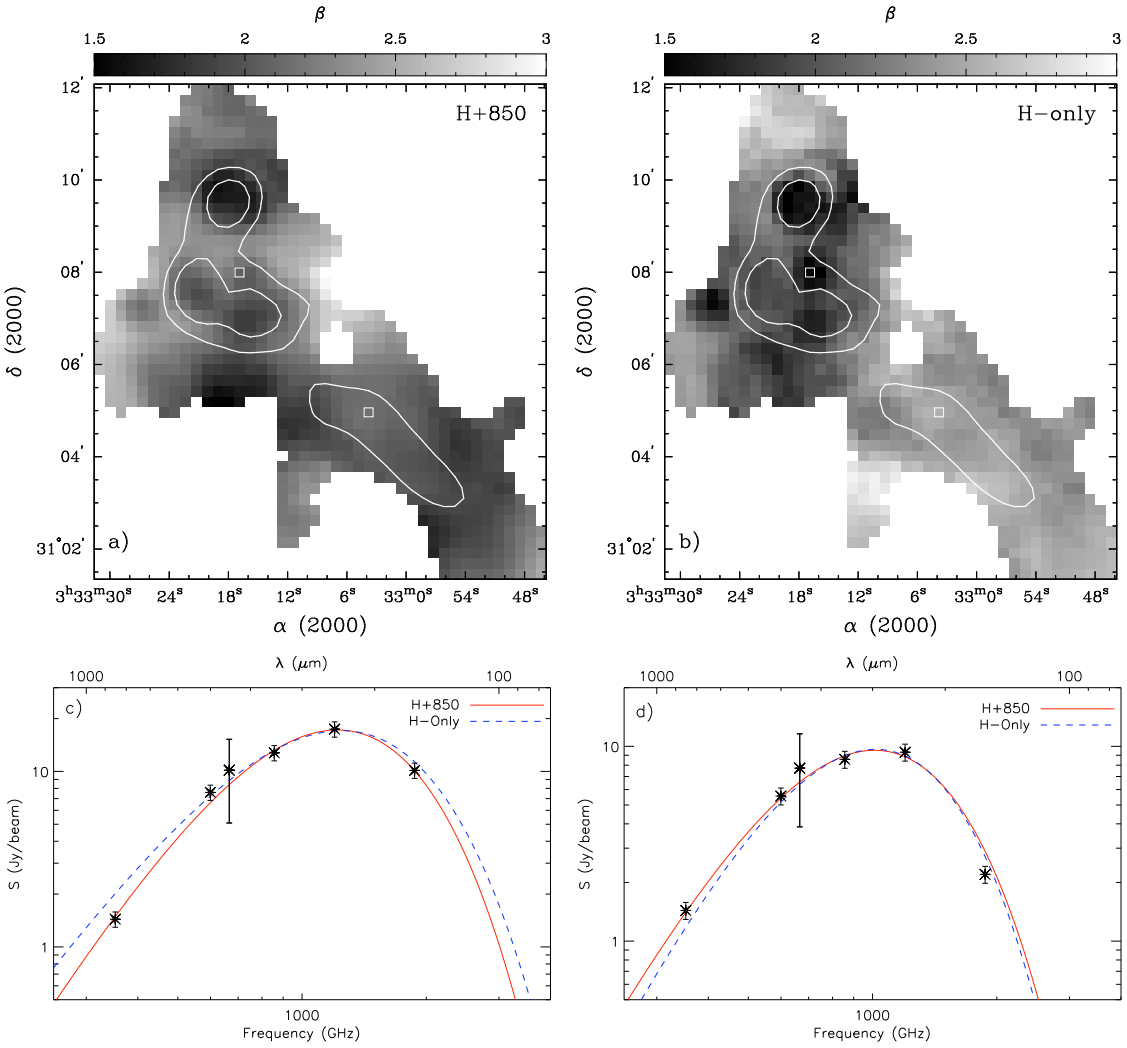

Figure 4.8: Dust emissivity maps towards the B1 main cluster for the Filtered Case. White contours show 850 μm flux levels of 1 Jy beam^{-1} and 2 Jy beam^{-1} at 36″ resolution. *Bottom:* Sample SEDs from (c) B1a and (d) the south-west filament, each marked by squares in the top panel. The curves show the best-fit SEDs. For the solid curves, we used the H+850 bands, whereas for the dashed curves, we used the H-only bands. The error bars on the data points illustrate the range in flux from the calibration uncertainties. The 450 μm band is included for comparison; it was not used in the fitting.

SCUBA-2 observations alone cannot constrain both β and temperature. If the temperature or β across a cloud is roughly constant, then we can probe relative variations using the SCUBA-2 Ratio Case. For regions with known prestellar and protostellar objects like the B1 complex, it is not ideal to assume constant temperatures or β indices, however. For example, Figure 4.9 reveals a $\sim$ 6 K variation in temperature within the central B1 region. A difference of 6 K in temperature results

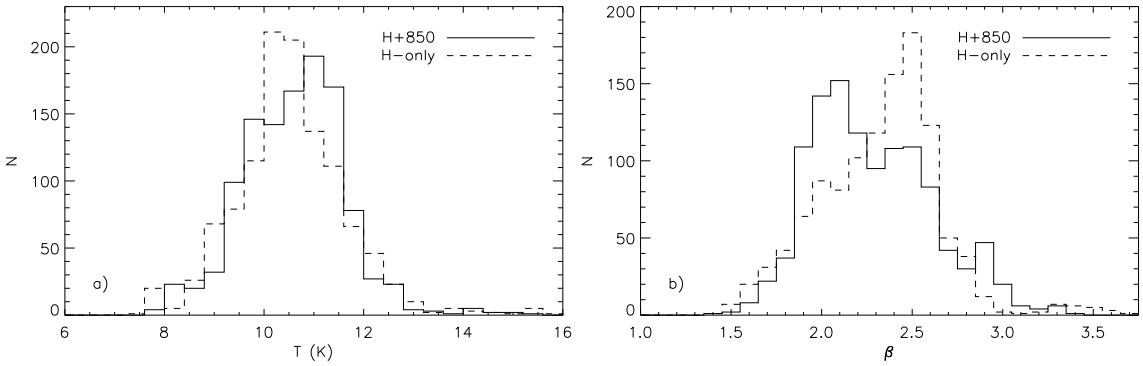

Figure 4.9: Histograms of (a) temperature and (b) β for the B1 complex. For comparison, the temperature and β values correspond to SED fits when the SCUBA-2 850 μm band is included (solid lines) or excluded (dashed lines) with the filtered *Herschel* maps (Filtered Case). In both cases, we only consider pixels with ≥ 10 σ fluxes in all five bands.

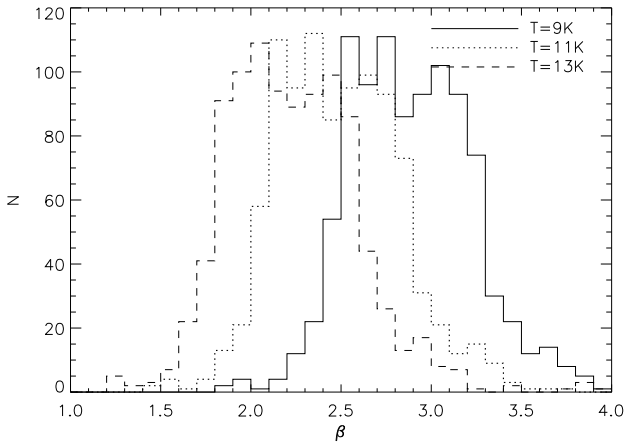

Figure 4.10: Distributions of β for fixed temperatures of 9 K, 11 K, and 13 K, and using Equation 4.2 from the SCUBA-2 Ratio Case.

in a significant uncertainty of $\Delta\beta \approx 0.86$. Similarly, when we fixed β, we found that the temperature distributions shifted by ~ 2 K between $\beta = 1.5, 2.0$, and 2.5 (see Figure 4.4). Thus, Figures 4.4 and 4.10 illustrate the caution needed for analyses which assume either a fixed β or a fixed temperature. In either case, a slight increase or decrease in the fixed parameter can result in significant differences in the determined quantity.

Additionally, in Figure 4.8 the SEDs show that the observed 450 μm fluxes are roughly 15% greater than those predicted from the SED fits, suggesting that the observed 450 μm emission towards these pixels is relatively much brighter than the filtered 500 μm emission. Figure 4.11 shows the fractional flux increase in the observed 450 μm data over the 450 μm emission predicted from the best-fit SEDs from the

Filtered Case. The ratio of observed 450 μm emission to predicted 450 μm emission peaks around 10-15%. (As described in Appendix C, we believe this "excess" at 450 μm is not due to CO (6-5) contamination.) As a test, we scaled the 450 μm emission down by 12.5% and found that β decreased by $\Delta\beta \approx 0.18$ based on a Kolmogorov-Smirnov test. These relative fractions may indicate that the 450 μm map does not trace the same material as the 850 μm map, e.g., due to different spatial scales filtered-out in the reduction or due to temperature variations along the line of sight. Alternatively, these variations could be related to uncertainties in the 450 μm fluxes themselves, e.g., from atmospheric variabilities or the beam pattern. Since we cannot assume a single line-of-sight temperature for the B1 clump and the 450 μm emission itself is very uncertain, we believe the SCUBA-2 Ratio Case method is less robust than the Filtered Case method.

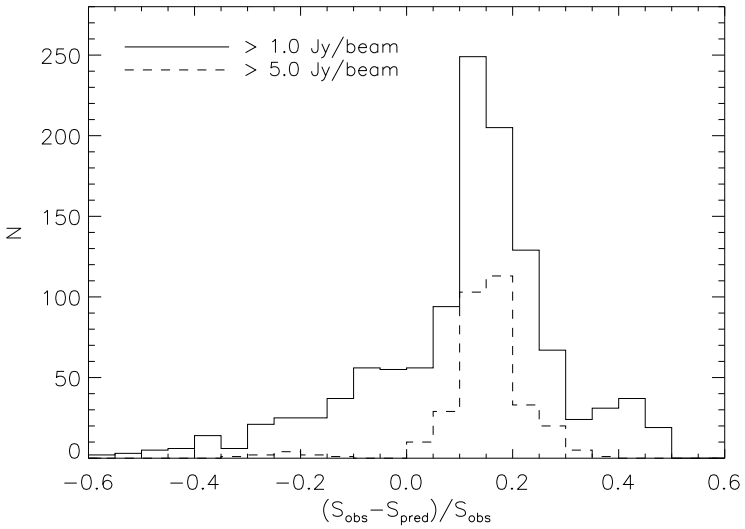

Figure 4.11: Fractional differences between the observed and predicted 450 μm emission for pixels with bright ($> 10\ \sigma$) observed 450 μm fluxes. These results correspond to the emission predicted from SED fits following the Filtered Case for the H+850 bands.

4.4.2 β Using Unfiltered Maps

For the next two techniques, we determined β after attempting to recover the missing large-scale emission filtered-out in the SCUBA-2 bands. In Figure 4.6, the median filtered-out large-scale emission at 250 μm corresponds to $\sim$ 1 Jy beam^{-1} at 18$''$ resolution (or $\sim$ 3 Jy beam^{-1} at 36.3$''$ resolution). This extended emission peaks towards the central B1 cluster, with additional emission along the south-west filament

and to the north. We could naively expect a similar large-scale distribution at 450 μm and 850 μm.

We considered two methods to recover the missing extended emission. The first method, hereafter the Offset Case, seeks to identify the missing large-scale emission at 850 μm using a grid of incremental offset values that were added to the observed 850 μm map to represent the filtered-out extended emission. We adopted the flux increment that best fit the overall SED to represent the missing emission. For more details, see Appendix E.1.

The second method, hereafter the Spatial Factor Case, assumes that the observed 450 μm and 850 μm data correspond to the same spatial scales and that both bands are missing the same fraction of extended emission. For the Spatial Factor Case, we modify the dusty black body function in Equation 4.1 as:

$$I_\nu = \kappa_{\nu_0}(\nu/\nu_0)^\beta B_\nu(T)\Sigma F_{SF} \tag{4.3}$$

where F_{SF} is a scaling factor corresponding to the fraction of recovered emission. For the *Herschel* bands, $F_{SF} = 1$ (i.e., 100% of the emission is recovered), whereas for the SCUBA-2 bands, $F_{SF} \leq 1$, and we assume F_{SF} is identical for both the 450 μm band and the 850 μm band. For more details, see Appendix E.2.

Recovering the large-scale emission is very uncertain, and we found large uncertainties in our analyses. For the Offset Case, we found uncertainties of 20-50% for the missing extended emission alone, suggesting that we cannot constrain well the diffuse emission. Thus, the Offset Case cannot be used to constrain β from SED fits. For the Spatial Factor Case, the 450 μm emission is less certain due to a larger calibration uncertainty of 50% and as Figure 4.11 demonstrates, the observed 450 μm emission tends to be 10-15% brighter than the predicted (filtered) emission. Since the scaling factor is very dependent on both the 450 μm and 850 μm fluxes, the large flux uncertainties at 450 μm will greatly affect the final results. Finally, based on the filtered *Herschel* maps (see Section 4.4.1), the fraction of emission lost in the filtering appears to vary considerably with wavelength. Therefore, F_{SF} may actually vary somewhat between the 450 μm and 850 μm bands. For the β results using these two techniques, see Appendix E.1 and Appendix E.2.

4.4.3 Comparison of the Techniques

The Filtered Case is the most robust technique to combine SCUBA-2 data with PACS and SPIRE data. For the Filtered Case, we have demonstrated that the 850 μm band makes a significant improvement to the uncertainties associated with SED fitting (see Figure 4.7) and impacts the absolute value of β. For example, we determined that the H-only results generally underestimated β towards the dense cores and overestimated β along the filament. These observations are in agreement with a recent study by Kelly et al. (2012), which suggests that SED fitting through the minimization of χ^2 may be biased towards lower β values for prestellar cores.

Using the Filtered Case technique, we find $\beta \approx 1.6-2$ for the dense cores with the lowest values towards the B1-c core. In addition, we find $\beta \approx 2$ along the filament and $\beta \gtrsim 2$ towards the moderately dense clump material. Similarly, Friesen et al. (2005) found $\beta \approx 1.3-2.1$ using a Fourier Transform Spectrograph at 350 GHz to observe several hot molecular cores. Other studies, however, have identified larger β values towards dense cores. For example, Schnee et al. (2010) found $\beta \approx 1.7-2.7$ towards a starless core using mid-infrared and (sub)millimeter continuum observations, and Shirley et al. (2011) found $\beta \approx 2.2-2.6$ towards a young protostellar core using radiative transfer models with SCUBA flux ratios and near-infrared colour excesses. Additionally, Arab et al. (2012) found $\beta \sim 2$ values towards the cooler ($\sim$ 40 K), denser regions of the Orion bar and $\beta \sim 1.1$ towards the warmer ($\sim$ 70 K) regions using *Herschel* and Spitzer observations. Thus, a larger study of dense cores and their environments with the same set of observations is necessary to understand these differences in β.

With the remaining three techniques, β is unclear. For the SCUBA-2 Ratio Case (Section 4.4.1), a minor variation in temperature greatly affects the measure of β; for the Offset Case (Section 4.4.2 and Appendix E.1), the *Herschel* calibration uncertainties result in very uncertain 850 μm offsets; and for the Spatial Factor Case (Section 4.4.2 and Appendix E.2), the 450 μm band is very uncertain, and thus, causes a wide range of plausible scale factors. Additionally, it is not clear that the 450 μm and 850 μm observations trace the same scales. Both the SCUBA-2 Ratio Case and the Spatial Factor Case require the 450 μm band.

In Section 4.5, we discuss the results for the Filtered Case only. For comparison, we will consider both the H-only and H+850 results.

4.5 Discussion

4.5.1 Submillimeter Dust Opacity and Dust Masses

We are interested in comparing the dust opacity between the dense cores and the ambient clump material. In Equation 4.1, we assumed that the dust opacity follows a power-law distribution for a reference opacity, κ_{ν_0}, at 1000 THz (300 μm). Ideally, we would want to fit κ_{ν_0} as well as β. According to Ossenkopf & Henning (1994), the dust opacity at 300 μm increases by a factor of $\lesssim 2$ for coagulated dust grains with icy mantles compared to small bare grains (this effect is more significant for grains without icy mantles). More recently, Martin et al. (2012) and Roy et al. (2013) used submillimeter dust emission and near-infrared extinction maps to constrain the submillimeter dust and gas opacity at 250 μm for $\beta = 1.8$. Both studies found a steady increase in dust opacity (by factors of $\sim 2-4$) towards colder temperatures, suggesting that the dust opacity should not be fixed at 300 μm.

Unfortunately, we cannot separate out the degeneracy of κ_{ν_0} with column density in B1 at this time. Although κ_{ν_0} can be constrained by independent measurements of column density, we are interested in changes to the dust over small scales (i.e., between dense cores), and as such we cannot utilize extinction maps (at $\sim 2'$ resolutions) as done by Martin et al. (2012) and Roy et al. (2013). Therefore, while we cannot measure absolute values of κ_ν with our observations, we can probe the variations in κ_ν due to our differences in β. Thus, we focus on the relative variations in κ_ν with the H+850 data and the significance of assuming $\beta = 2$, as with most *Herschel* analyses of molecular clouds.

Figure 4.12 shows the dust opacity at 850 μm relative to the opacity at 300 μm for the Filtered Case. This measure does not assume any prior knowledge of the dust opacity at either 300 μm or 850 μm. Thus, Figure 4.12 demonstrates that the relative dust opacity at 850 μm increases by a factor of $2-3$ between the moderately dense clump material and the dense B1-c core, which suggests the grains are evolving. Dust coagulation alone can increase the submillimeter dust opacity by factors of 4-5 at 850 μm, though this increase is enhanced for bare dust grains and suppressed with surface ices (Ossenkopf & Henning 1994). Alternatively, Ossenkopf & Henning (1994) noted that moderately elliptical dust grains or higher abundances of metal compounds can increase submillimeter dust opacities at 850 μm by factors of a few. Without an independent measure of the dust opacity or column density, however,

we cannot directly measure the absolute variations in dust opacity. Thus, further observations of the clump chemistry and dust are necessary to help determine the causes of these opacity variations.

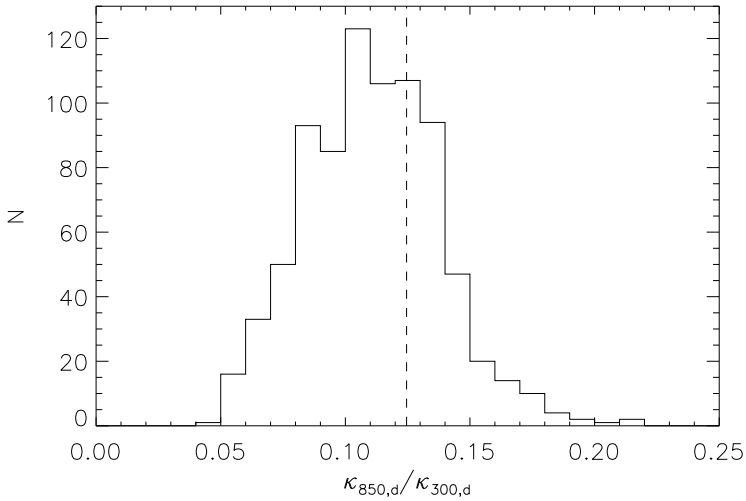

Figure 4.12: Distribution of the dust opacity at 850 μm relative to the dust opacity at 300 μm using the Filtered Case. The dashed line shows the relative dust opacities for $\beta = 2$.

To measure column densities and masses, however, we must assume a dust opacity law. Thus, we adopted a dust opacity per unit *dust* mass of $\kappa_{\nu,d} = 10\ (\nu/1\ \mathrm{THz})^{\beta}$ cm^2 g^{-1}, following our assumed dust and gas opacity, $\kappa_{\nu_0} = 0.1$ cm^2 g^{-1} at 1 THz (300 μm), and a dust-to-gas mass ratio of 100. Figure 4.13 shows the resulting map for the dust opacity at 850 μm and the distribution of best-fit temperatures from the Filtered Case using the H+850 bands. Based on our 1 σ uncertainties for β, we find that the uncertainties on $\kappa_{\nu,d}$ are $10-30\%$, where the largest errors are found towards the compact cores. These results are only valid if the dust opacity is kept fixed at 300 μm. From the temperature map, B1-a, B1-c, and B1-d show internal heating from protostellar sources. B1-b contains two first hydrostatic core candidates (see Pezzuto et al. 2012), and we see an indication of moderate heating towards these cores (at 36″ resolutions, we cannot separate the two components). The uncertainties on the dust temperatures are predominantly $\sigma < 1.5$ K with the largest errors towards B1-c. The dust temperature is ~ 10.5 K and ~ 12 K for B1-b and B1-d, respectively, which are similar to the NH_3-derived kinetic gas temperatures of ~ 11.5 K reported in Rosolowsky et al. (2008). The kinetic gas temperature of B1-c, however, is ~ 12.4 K (Rosolowsky et al. 2008), which is lower than the observed dust temperatures of ~ 15 K. This difference in temperature suggests that the NH_3 gas is tracing a different

region of the core than the dust (e.g., see Matthews et al. 2006).

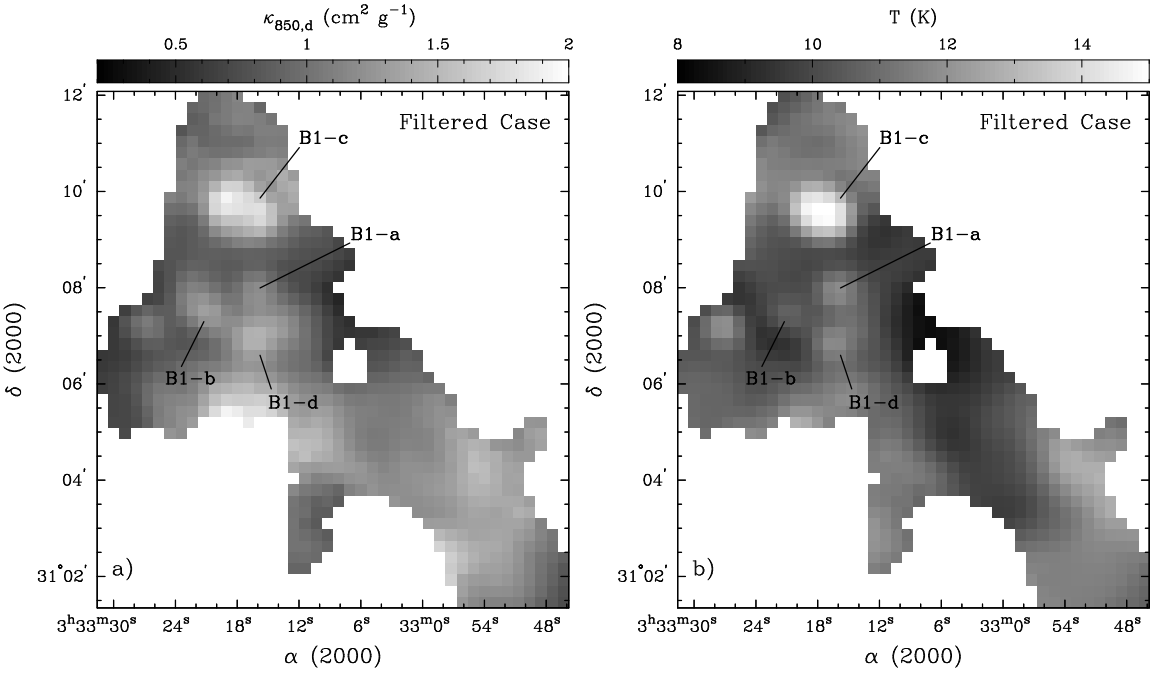

Figure 4.13: Results from the Filtered Case showing (a) the dust opacity at 850 μm and (b) the dust temperature. The dust opacity map assumes $\kappa_{\nu,d} = 10$ cm^2 g^{-1} at 300 μm and that all variations in β manifest themselves as changes in $\kappa_{\nu,d}$ at 850 μm.

Figure 4.14 compares the N(H_2) column densities measured towards the B1 cores for (a) the H+850 bands and (b) the H-only bands with $\beta = 2$ (i.e., using the method employed by most *Herschel* GBS papers). The gas column density is determined following Equation 4.1 and assuming $\kappa_\nu = 0.1$ cm^2 g^{-1} at 300 μm ($\kappa_{\nu,d} = 10$ cm^2 g^{-1} for a gas to dust ratio of 100). Table 4.2 lists the total (gas and dust) mass estimates for the B1-b, B1-c, and B1-d cores using these column density maps. For simplicity, we calculated the masses associated with 5×5 pixel boxes around the cores. For the *Herschel*-only data with $\beta = 2$, we underestimate the columns of mass towards B1-b by $\sim 10\%$ and overestimate the columns of mass towards B1-c by $\sim 30\%$ (the masses towards B1-d agree within 1%). Since we find $\beta \approx 2$ for much of the B1 clump (see Figure 4.9), assuming $\beta = 2$ with *Herschel*-only data appears to provide a decent first look at the mass distribution of dense cores and the column density of extended cloud emission. Nevertheless, for regions that deviate from $\beta = 2$, such as B1-c ($\beta \approx 1.6 - 1.7$), we find that the SED-fitting to the *Herschel*-only bands with $\beta = 2$ yields more significant mass uncertainties ($\sim 30\%$). Therefore, accurate core masses or column densities require direct measurements of β. For example, assuming

$\beta = 2$ could affect our ability to classify cores as dynamically stable or unstable, to properly compare the core mass function to the stellar initial mass function, and to calculate relative (to H_2) abundances of molecules.

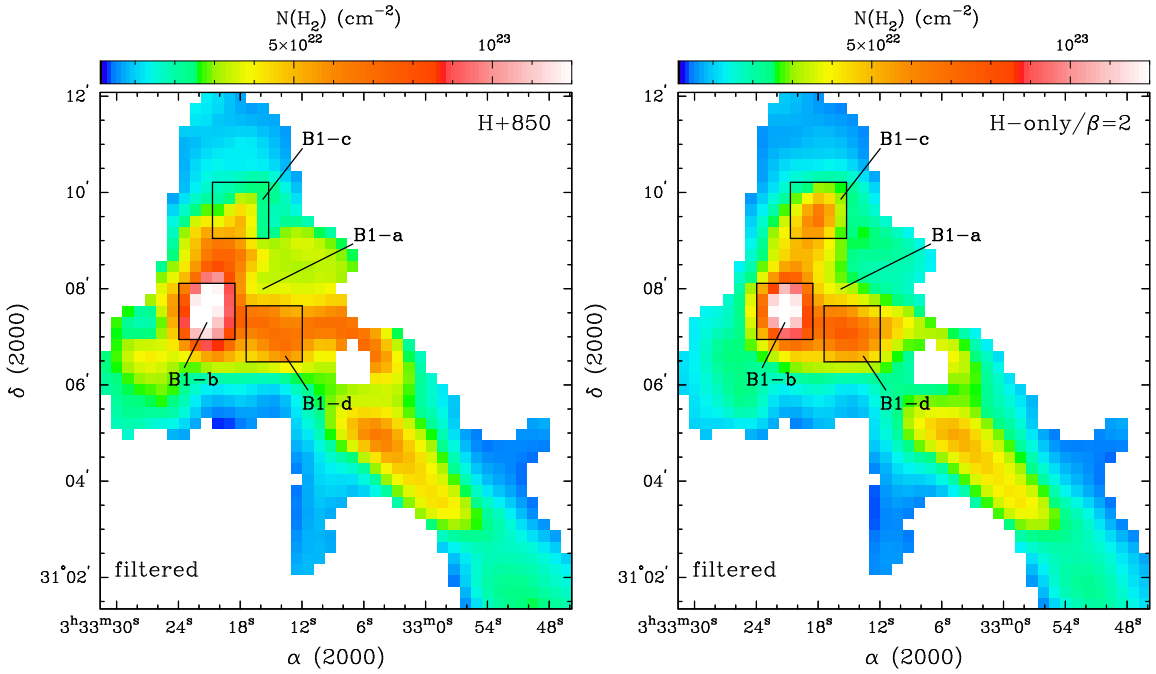

Figure 4.14: Column density maps using the filtered *Herschel* data. For panel (a), we used the H+850 bands and the β and temperature results from the Filtered Case, and for panel (b) we used the H-only bands and fixed $\beta = 2$. The black boxes correspond to our mass measurements.

Table 4.2: Core Mass Estimations[a]

Core	B1-b	B1-c	B1-d
H+850	15 $M_\odot$	5 $M_\odot$	9 $M_\odot$
H-only[b]	13 $M_\odot$	6 $M_\odot$	9 $M_\odot$

[a] Masses measured within the 5×5 pixel boxes in the column density maps (see Figure 4.14), assuming $\kappa_\nu = 0.1$ cm^2 g^{-1} at 300 μm. This fixed dust opacity at 300 μm is the greatest source of uncertainty, so these masses are only accurate within a factor of ~ 2.

[b] Masses measured from filtered H-only maps assuming $\beta = 2$ over the same 5×5 pixel boxes as with the H+850 case.

4.5.2 Temperature and β

In the literature, the dust emissivity index is often assumed to be $\beta = 2$ based on studies of the dielectric functions of graphite and silicate dust grains (e.g., Draine & Lee 1984). Deviations from $\beta = 2$ can arise from processes such as grain growth and the accumulation of icy mantles. For example, $\beta < 2$ has been attributed to the coagulation of bare dust grains (e.g., Schwartz 1982; Ossenkopf & Henning 1994; Lis et al. 1998) and Beckwith & Sargent (1991) attributed very low β values (~ 1) towards protostellar disks to grain growth. Large values of β (e.g., > 2), however, are harder to interpret. Thick icy mantles can steepen the dust opacity slope at submillimeter wavelengths, but this appears to be a lesser effect than dust coagulation (e.g., Ossenkopf & Henning 1994). Unfortunately, most dust models do not predict dust opacities with $\beta > 2$ (Shirley et al. 2011). Meny et al. (2007) found that $\beta > 2$ may arise due to complex interactions between electromagnetic radiation and the disordered mass and charge structures of amorphous dust grains. Thus, β highly reflects the dust grain properties, and it is important to understand the relationship between β and the surrounding environment.

Nevertheless, the relationship between β and temperature is not well understood. Many studies that fit submillimeter SEDs to determine β use the minimization of χ^2 technique as employed here. Several recent studies, however, have suggested that the minimization of χ^2 produces unclear results due to the degeneracy between β and temperature, especially towards the SED peak (e.g., Veneziani et al. 2010; Kelly et al. 2012). Since the *Herschel* bands span the SED peak for cold star forming regions, the method of SED fitting becomes significant. In particular, Kelly et al. (2012) demonstrated that the χ^2 minimization technique gives different temperature and emissivity values than a more detailed Bayesian approach. In addition to the fitting technique, an artificial anti-correlation between β and temperature can also be introduced by instrumental errors (e.g., Shetty et al. 2009a) or temperature variations along the line-of-sight (e.g., Shetty et al. 2009b; Schnee et al. 2010).

Despite these uncertainties, several large studies have found strong inverse relationships between β and temperature over large areas and a wide range of temperatures. These studies include the PRONAOS experiment (e.g., Dupac et al. 2003), the *Herschel* Hi-Gal project (e.g., Paradis et al. 2010), and early science results from Planck (e.g., Planck Collaboration et al. 2011b). In particular, Paradis et al. (2010) employed two techniques to their SED-fitting, a minimization of χ^2 method and a

maximum likelihood algorithm. They found an inverse β-temperature relationship with both methods.

In Figure 4.7, we find the uncertainties on our values of β and temperature are such that small degeneracies may persist between any two values determined, and so any anti-correlation seen between β and temperature may be artificial. Thus, despite our improved constraints to determine β with the 850 μm data, the SED fits may still retain some degeneracies. From our data, we believe the causes of any degeneracy are likely dominated more by our use of the χ^2 technique rather than the noise or single component line-of-sight-temperature assumption. For example, we only selected very bright emission, so issues with noise will be negligible. Additionally, our analysis used filtered observations and thus, the line-of-sight temperature is less affected by warm diffuse material. The protostellar cores, however, will have warm central objects and cool outer envelopes, and thus assuming a single line-of-sight temperature towards these objects may induce a stronger degeneracy between β and temperature. Nevertheless, with only five bands in the submillimeter domain, we cannot apply a multiple temperature component fit. Thus, with our analyses, we cannot make any robust conclusions regarding any physical β-temperature relationship.

4.5.3 The Addition of SCUBA-2 Data

Figure 4.7 demonstrates that the SED fits are much improved with the inclusion of 850 μm observations since the *Herschel* data alone are unable to constrain β for cold star-forming regions. Since the 850 μm emission is more dependent on β (see Figure 4.5), the SCUBA-2 observations have a significant influence on the best-fit SEDs and the determined values of β. Therefore, this work demonstrates that the SCUBA-2 850 μm data (or equivalent long wavelength observations) are essential for constraining SED fits.

The SCUBA-2 450 μm band has superior resolution ($\sim 9''$) to the *Herschel* data at $160 - 500$ μm presented here (see Figure 4.2), which is necessary for deblending compact sources to obtain more accurate flux measurements. Additionally, with the 450 μm band, we can measure dust properties at higher resolutions. For example, in this chapter, we convolved our data to a common resolution of $36.3''$ (corresponding to the 500 μm beam), but with the SCUBA-2 450 μm band, we could exclude the SPIRE 500 μm band and convolve to a common resolution of $25''$ (the 350 μm beam), and find the dust temperature, opacity, and column density over smaller scales, thereby

probing variations across cores themselves.

Unfortunately, the 450 μm emission has significant uncertainties. For example, in Figures 4.8 and 4.11, we see that the observed 450 μm emission is roughly $10-15\%$ brighter than the predicted emission. Additionally, the 450 μm band is more susceptible to atmospheric variability. Therefore, we do not use the 450 μm band at this time, but note that with better calibrations and atmospheric modeling, the 450 μm band will become more robust and higher resolution analyses will become possible.

4.5.4 High Resolution Extinction Maps

In Section 4.5.1, we assumed a fixed dust opacity at 300 μm to measure column densities and masses. To circumvent fixing κ_ν (300 μm), we need to measure the dust opacity or column density through an independent method, such as from extinction maps. Since we are interested in measuring changes in dust opacity over small scales, we need high resolution ($< 1'$) extinction maps. Such observations would greatly improve the analysis in this chapter.

Typically, extinction maps have resolutions of $\gtrsim 2'$, which are too coarse to probe changes in dust opacity between dense cores and the ambient clump. Nevertheless, high resolution ($\sim 20''$) extinction maps are possible with deep near-infrared observations (e.g., Román-Zúñiga et al. 2010), provided that there are sufficient background stars (dust extinction is measured via the reddening of background stars) and that the extinction is not too high. Therefore, future studies of dust opacity using *Herschel* and JCMT observations will greatly benefit from such high resolution extinction mapping.

4.6 Summary

We have presented four unique methods to measure the dust emissivity index, β, from a combination of *Herschel* PACS+SPIRE and SCUBA-2 observations. Of these methods, the Filtered Case, where the *Herschel* maps are filtered using the SCUBA-2 reduction pipeline and β is determined from SED-fitting to the filtered *Herschel*+850 bands is the most robust. Our main goal was to examine whether or not the SCUBA-2 850 μm band made significant improvements to the SED fits and the *relative* differences in β (or $\kappa_{\nu,d}$) that arise from those fits. We summarize our main findings as

follows:

1. The *Herschel*-only data do not constrain the SED fits well enough to allow simultaneous fitting of β and temperature towards cold clouds. In Figure 4.7, we demonstrated that long wavelength observations are necessary to improve SED fitting to the *Herschel* bands. The 850 μm SCUBA-2 band improves our ability to constrain β by a factor of ~ 2 and our ability to determine temperature by $\sim 40\%$. Additionally, we find significant variations in β when the 850 μm data are included, i.e., we find $\beta \sim 1.6$ towards the B1-c core and $\beta \sim 2.0$ towards the filament.

2. Based on our SED-fitting, we find the dust opacity at 850 μm varies by factors of $2-3$ relative to the dust opacity at 300 μm, with the highest opacities towards the dense cores, particularly B1-c. Therefore, the B1-c core may represent a region where the dust grains have coagulated with some icy mantles, have moderate elliptical shapes, or have higher abundances of metal compounds (Ossenkopf & Henning 1994). Our observations cannot constrain the source of the opacity variations. Future studies with high resolution extinction mapping are needed to probe the dust opacity in more detail.

3. With our analysis, we cannot make robust conclusions about the β-temperature relationship. We found that both β and temperature are constrained better with the inclusion of 850 μm observations (see Figure 4.7), yet the degeneracy between these parameters is not entirely removed. While this degeneracy likely arises from using the minimization of χ^2 technique to fit the SEDs, there can be additional degeneracies due to assuming a single component line-of-sight temperature.

4. Assuming a fixed $\beta = 2$ value with the *Herschel* bands alone affects the measured best-fit temperature by $\lesssim 2$ K if $\beta = 1.5$ or $\beta = 2.5$. We found that the core masses as measured with the *Herschel*-only bands and with $\beta = 2$ varied by $\lesssim 30\%$ compared to the results using *Herschel*+850 bands and the same assumptions for the dust opacity ($\kappa_{\nu_0} = 0.1$ cm^2 g^{-1} at 300 μm). Thus, the *Herschel*-only bands provide a decent first look at the core masses for an assumed value of $\beta = 2$. Nevertheless, to obtain more accurate core masses, i.e., to measure the dynamical stability of dense cores or the core mass function, long wavelength data and high resolution extinction maps are necessary.

This analysis of the B1 clump with PACS+SPIRE+SCUBA-2 represents the first of many future analyses with these instruments. The SCUBA-2 observations are an excellent complement to the *Herschel* bands, providing a much stronger constraint to SED-fitting and derivations of β. *Herschel* and long wavelength observations such as those from SCUBA-2 have only recently provided the wavelength and spatial coverage necessary to make these measurements. Future analyses using high resolution extinction maps are also important to probe the changes in $\kappa_{\nu,d}$ with environment.

Chapter 5

Analysis of the Perseus Molecular Cloud

In this chapter, we present the full *Herschel* observations at $70 - 500$ μm of the Perseus molecular cloud from the *Herschel* GBS. We use the *Herschel* data to sample completely the core populations. Furthermore, we use archival infrared detections from 2MASS and *Spitzer* to characterize the YSO populations. We compare and contrast the starless core and YSO populations in each of the Perseus clumps. We find that the starless cores are typically seen towards the column density peaks, in contrast to previous studies of Perseus. The NGC1333 clump has the smallest, most massive, and most dense starless cores on average. We also find that starless core temperature is anticorrelated with density for $n \lesssim 10^5$ cm^{-3} and flattens for higher densities. We measure a higher combined Class 0/I YSO lifetime of 0.8 Myr, compared to previous studies. We also find a significant population of Flat YSOs, many without well-detected emission in the submillimeter bands. Thus, some Flat YSOs may not be deeply embedded. We find that the more massive clumps have an excess of older stage YSOs, suggesting these regions contracted first. We also find a strong correlation between the fraction of Class 0 YSOs and the slope of the high column density tail. Our results suggest that the quantity of high column density material correlates with recent bursts of star formation and not the star formation history.

5.1 Introduction

Molecular clouds are highly structured, with their star-forming cores embedded within complex networks of filaments and clumps (see Chapter 1). Kainulainen et al. (2009) studied several molecular clouds and noted that the ones actively forming stars had extinction distributions with prominent power-law tails at high extinctions, whereas more quiescent clouds did not have such prominent tails (see also, Schneider et al. 2012). Similarly, Lada et al. (2010) found a tight correlation between the number of YSOs detected in a cloud and the quantity of high extinction material towards that cloud, whereas André et al. (2010) found that gravitationally bound cores were generally associated with filaments on the verge of collapse and gravitationally unbound cores were detected primarily toward subcritical filaments. These studies suggest that star formation is connected to dense, unstable material.

Dense cores collapse and form stars when their gravitational contraction overwhelms their internal supports, such as thermal pressure, turbulent (non-thermal) pressure, or magnetic pressure (Klein et al. 2007). For thermally supported cores at 10 K, core masses $\gtrsim 1$ $M_\odot$ will become unstable and form YSOs. For low-mass star formation, YSOs evolve through a variety of stages, generally classified by the shape of the observed spectral energy distribution (SED; e.g., Lada & Wilking 1984; Adams et al. 1987; André & Montmerle 1994). Broadly, these YSOs are subdivided by their SEDs into five main Classes: Class 0, Class I, Flat, Class II, and Class III (for more details, see Chapter 1).

Accurate YSO classifications are important to constraining their lifetimes. Nevertheless, these classifications are entirely empirical and the ability to place a source in one Class or another depends on available data. Thus, YSO classifications are generally completed on a best-effort basis. Fortunately, recent YSO models (e.g., Whitney et al. 2003; Robitaille et al. 2006) and large infrared surveys (e.g., with *Spitzer*) have improved classification techniques with better statistics (e.g., Evans et al. 2009). Assuming a lifetime of 2 Myr for Class II YSOs, Evans et al. (2009) estimated lifetimes for the Class 0/I and Flat YSOs of 0.44 Myr and 0.35 Myr, respectively, based on their respective number counts from multiple clouds. Unfortunately, Evans et al. (2009) were unable to distinguish Class 0 YSOs from Class I YSOs due to lack of submillimeter observations. Thus, to constrain better the earliest YSO phases, we need a better census of the submillimeter emission towards YSOs.

Fortunately, the *Herschel* has fully sampled 15 nearby (< 500 pc) clouds at 70−500

μm as part of the *Herschel* GBS (hereafter, HGBS; André & Saraceno 2005; André et al. 2010). These bands are key for cold dust emission ($T < 20$ K) associated with dense starless cores and embedded YSOs. Here, we combine *Herschel* observations with archival infrared data from 2MASS ($1.25 - 2.17$ μm) and *Spitzer* ($3.6 - 24$ μm) for the Perseus molecular cloud. The *Herschel* data for Perseus constitute the most complete census of its core populations over previous, ground-based submillimeter detectors. Since many previous studies lacked complete core statistics, they could not compare well core populations within molecular clouds and instead focused on the global star formation activity (e.g., Kirk et al. 2006; Enoch et al. 2009; Sadavoy et al. 2010). Furthermore, the archival infrared observations from 2MASS and *Spitzer* provide the most complete census of the YSO populations in Perseus. Thus, we compare and constrast the dense core and YSOs populations within the individual star-forming clumps in Perseus to determine whether there are distinct differences in the populations within a single molecular cloud.

This Chapter is organized as follows: In Section 5.2, we describe our *Herschel* observations and the archival data used in this analysis. In Section 5.3, we describe the source extraction algorithm used on the *Herschel* data. In Section 5.4, we show our results, first from the *Herschel*-only analyses of the clumps and their properties, and then from combining the information from our *Herschel* data and the archival data to classify dense cores and YSOs. In Section 5.5, we compare our techniques to previous studies and discuss the implications of our results on future studies. In Section 5.6, we summarize our results.

5.2 Data

5.2.1 Herschel Observations

As described in Chapter 2, the Perseus molecular cloud was observed with *Herschel* as part of the HGBS. For more efficient observations, the Perseus cloud was divided into two parts; (1) ~ 6 deg^2 map of the Western section, centered on the NGC 1333 clump, and (2) ~ 4 deg^2 map of the Eastern section, centered on the IC 348 clump. The Western observations were made in February, 2010 and are also highlighted in Chapter 3. The Eastern observations were completed in February, 2011. Both maps utilized parallel photometric observations with the PACS and SPIRE instruments, resulting in simultaneous mapping with the 70 μm, 160 μm, 250 μm, 350 μm, and

500 μm bands at a 60 arcsec s^{-1} scan rate. These data were reduced in the same manner as described in Chapter 4.2. Figure 5.1 shows a three-colour image of the Perseus clouds.

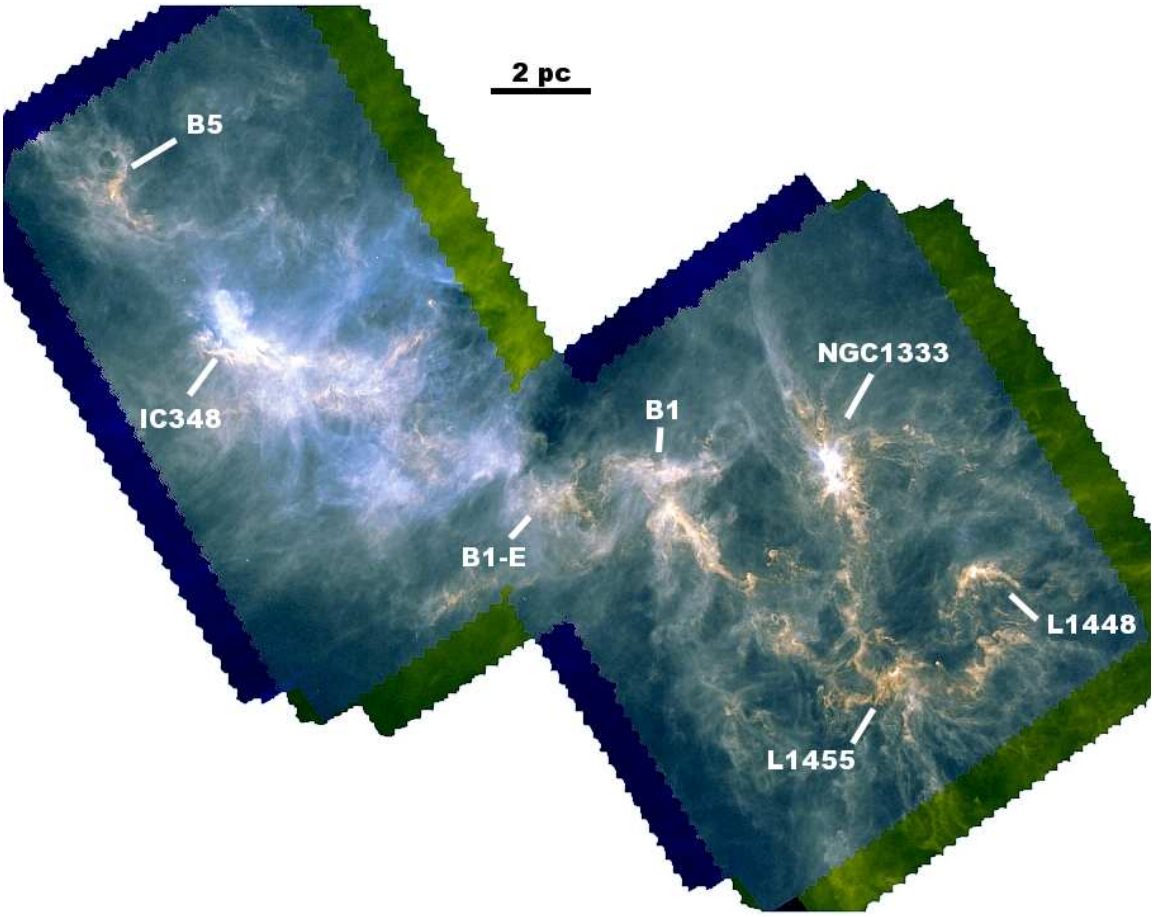

Figure 5.1: Three-colour image of the Perseus molecular cloud, where blue corresponds to 160 μm, green corresponds to 250 μm, and red corresponds to 350 μm *Herschel* observations. The main clumps are labeled.

5.2.2 Archival Data

Herschel provides excellent data for characterizing emission from cold dust ($T \lesssim 20$ K). Since we are interested in the dense core and YSO populations, we also need data that will probe warm dust. Therefore, observations from the *Spitzer* Space Telescope (Werner et al. 2004) at $3.6 - 24$ μm are an excellent complement to the far-infrared/submillimeter bands from *Herschel*. The entire *Perseus* cloud was mapped at $3.6 - 8.0$ μm with Infrared Array Camera (IRAC; Fazio et al. 2004; Jørgensen

et al. 2006) and at $24-160$ μm with the Mid-Infrared Photometer and Spectrometer (MIPS; Rieke et al. 2004; Rebull et al. 2007) detectors. While *Spitzer* also observed at 70 μm and 160 μm, the sensitivity and resolution are inferior to those of *Herschel*. Thus, we only consider the 24 μm band from MIPS.

The *Spitzer* observations of Perseus have been well studied, and the YSO populations from those data well characterized. Therefore, we used the *Spitzer* calatogues from Evans et al. (2009) and Gutermuth et al. (2009) to identify the known YSOs within the Perseus cloud. Evans et al. (2009) characterized the YSO candidates across the entire cloud for the Cores To Disks (hereafter, c2d) survey, whereas Gutermuth et al. (2009) focused on the NGC1333 and IC348 clusters as part of a young cluster study (hereafter G09). Both studies used different techniques to identify YSOs, measure source properties, and remove non-YSO contaminants (e.g., background galaxies or stars). As such, sources can be identified as YSOs in one and not the other.

In Evans et al. (2009), YSOs were identified using a combination of SED templates and colour-magnitude diagrams with near-infrared JHK ($\lambda = 1.25 - 2.17$ μm) and *Spitzer* ($\lambda = 3.6 - 24$ μm) data to identify background stars, galaxies, and YSOs. First, they used stellar templates to compare observed source SEDs with reddened stellar photospheres. Second, non-stellar templates were used to identify sources with strong characteristics that can be confused with YSOs, such as strong emission from polycyclic aromatic hydrocarbons, stellar emission with a strong dust component, or very red colours that can be associated with galaxies. Finally, YSO candidates were selected from background galaxies using three sets of colour-magnitude criteria. Since both YSOs and background galaxies can show similar colour excesses between near-infrared and far-infrared wavelengths, these colour-magnitude selection criteria are very important. Evans et al. (2009) used a blank field (from the SWIRE project) to create a control sample of unreddened background galaxies. YSOs were separated from background galaxies based on the cumulative probability of the colour-magnitude selection criteria.

Likewise, Gutermuth et al. (2009) used $1.25-24$ μm observations to identify and characterize YSOs. In their study, YSOs were identified from a complex set of colour-colour and colour-magnitude selection criteria designed to remove contaminants (see Gutermuth et al. 2008; Hatchell & Dunham 2009). Furthermore, Gutermuth et al. (2009) included a multiphase selection process that initially selected sources based on the available wavelength coverage, such as detection in all four IRAC bands, detections at the five shortest wavelengths ($1.25-4.5$ μm), and detections at 24 μm.

For each case, likely contaminants were removed using wavelength-specific colour and magnitude criteria.

For our YSO selection, we considered sources with either a "YSO" designation or a "red" designation in the publicly available c2d catalogue (650 YSOs) and all the sources in the G09 catalogue for NGC1333 and IC348 (293 YSOs). Since both catalogues used observations from the same instruments, spatial coincidences were very good. We considered a source to match in both catalogues if the positions agreed within $1''$. In total, 205 common YSOs were identified in both catalogues. If we increased the allowed position offset to $2''$, we found the same results. Above $2''$, we identified multiple coincidences for the *Spitzer* sources without adding new pairs. Thus, 88 YSOs are identified in the G09 catalogue that are not included in the c2d catalogue. One possibility for these missing c2d YSOs could be due to the detection flags. The youngest YSOs in particular were prone to being identified as contaminants (Gutermuth et al. 2009). For example, a study by Schmeja et al. (2008) found many more Class I YSOs in three large Galactic clusters than the corresponding data from the complete c2d catalogue. Alternatively, bright sources can have positional offsets based on the source fitting and aperture. For example, the well-known Class 0 source NGC1333 IRAS 2A was identified with a position offset of $\sim 5''$ between the c2d and G09 catalogues. Thus, several sources that are considered "unassociated" may have large position uncertainties.

Since the c2d and G09 studies employed different techniques to measure source properties, such as different aperture analyses, the measured fluxes can differ between these two catalogues, despite the same initial datasets. Figure 5.2 compares the fluxes across all wavebands of sources in common to the c2d catalogue and the G09 catalogue. While the extracted fluxes are mostly similar between the two catalogues, there are some clear outliers, particularly towards the brightest sources. Since choice of aperture, background subtraction, and the treatment of blended objects can greatly affect source properties, these outliers illustrate the uncertainties of source extraction from each survey. Thus, we will consider both measurements, thereby comparing and contrasting the YSO properties for objects common to both catalogues.

Several additional catalogues provide complementary data for Perseus YSOs or cores. The Wide-field Infrared Survey Explorer (WISE; Wright et al. 2010) completed an all sky survey in the near-infrared (3.4 - 22 μm), and thus covers regions of Perseus not observed by *Spitzer* entirely. Furthermore, several studies have used SCUBA (e.g., Jørgensen et al. 2007) or Bolocam (e.g., Enoch et al. 2008) to characterize dense cores

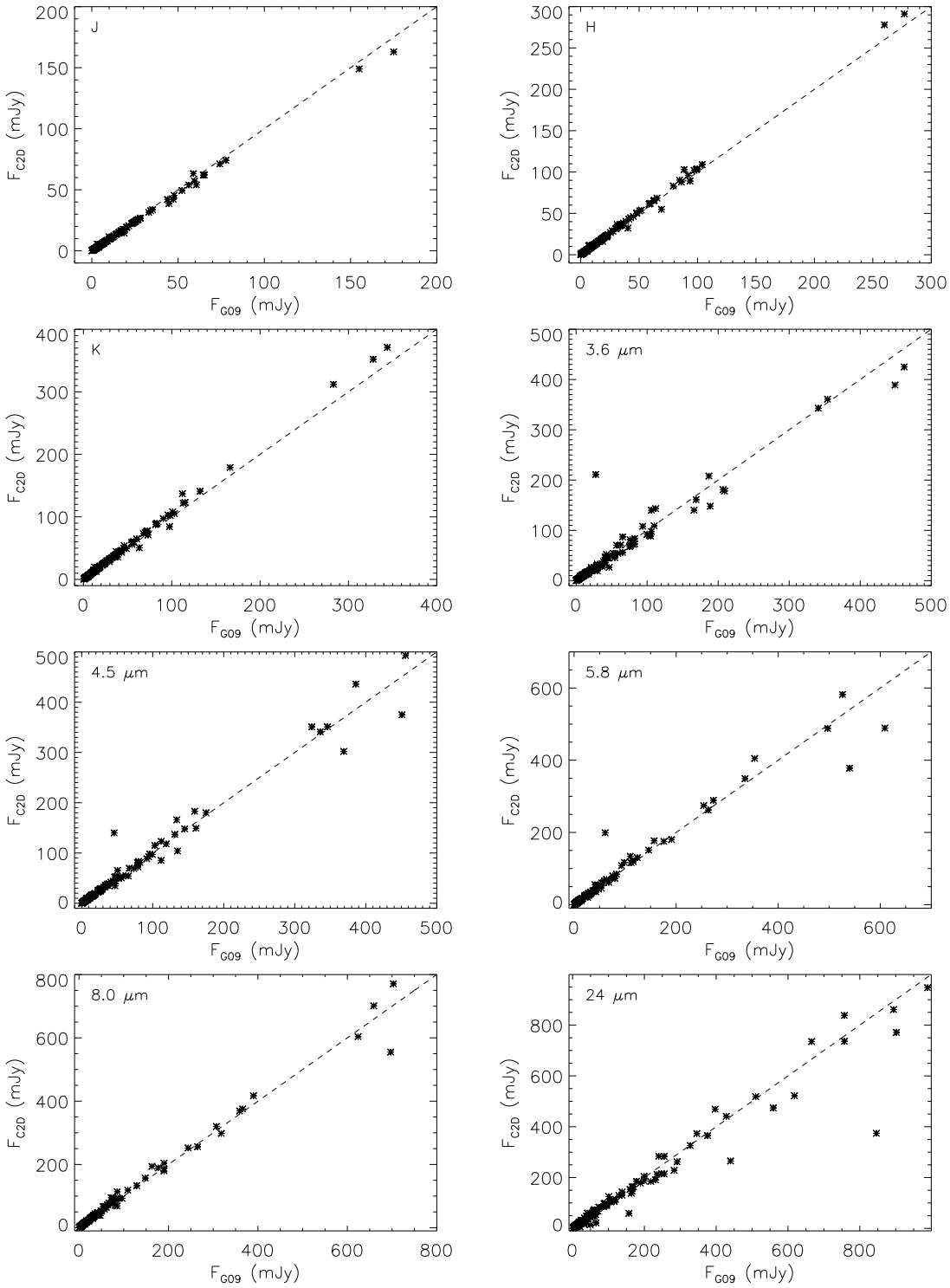

Figure 5.2: Comparison of YSO JHK, IRAC, and MIPS 24 μm fluxes for sources common to the c2d and G09 catalogues. The dashed lines correspond to perfect 1:1 relations.

with (sub)millimeter emission. Nevertheless, we do not include these data at this time. The *Spitzer* c2d data are more sensitive and have better spatial resolution than the WISE data. Furthermore, we are interested in the YSO and core populations associated with the moderately dense clumps, and *Spitzer* well observed these denser regions. Also, the *Herschel* data are much more sensitive than all previous large-scale (sub)millimeter surveys. The *Herschel* observations also provide complete coverage of Perseus, which the previous surveys with SCUBA and Bolocam were unable to do.

5.3 Herschel Sources

In this Section, we describe the source extraction process and source selection criteria for objects identified in the *Herschel* observations of Perseus. Sources were identified and analyzed for all five wave-bands in the GBS data ($70 - 500$ μm). For computational efficiency during source extraction, we considered the Western and Eastern Perseus fields separately. As such, several sources in the overlap area (see Figure 5.1) were identified twice.

5.3.1 Source Extraction

Previous submillimetre source extraction codes, such as *clumpfind* (Williams et al. 1994) or *gaussclump* (Stutzki & Guesten 1990), were designed for filtered, ground-based observations, and as such, were not designed to identify structures within complex, diffuse backgrounds. Thus, the HGBS team internally developed several techniques to localize and characterize compact sources in the *Herschel* maps. We use the most consistent of these methods, *getsources* (Men'shchikov et al. 2012) because (1) unlike the other algorithms, *getsources* conducts simultaneous multi-wave, multi-scale extractions, thereby utilizing information from the higher-resolution, shorter-wavelengths to identify and deblend structures at lower-resolution, longer-wavelengths and (2) *getsources* also extracts filamentary structure in addition to compact sources (Men'shchikov et al. 2013, in preparation).

The *getsources* algorithm is described in Men'shchikov et al. (2012). In brief, *getsources* uses spatial decompositions to identify structures at a variety of scales. First, all maps are resampled onto identical, fine resolution grids. For our data, we used the resolution at 70 μm ($3.2''$ pixels). Second, *getsources* runs a set of decompositions over a range of spatial scales separately for each wavelength in the

study. The decomposition generates a series of filtered images at various scales, which are used for the analysis and extraction. Noise and background fluctuations on spatial scales much smaller or much larger than the scale being considered are removed to improve the detectability of sources. Third, *getsources* combines information from the spatial scales from each wavelength to generate a first catalogue of sources. Sources identified at one spatial scale are followed through their subsequent detections at other spatial scales. Therefore, information obtained at higher resolutions is used to identify structure at lower resolutions.

Source properties are then measured from the original image at each wavelength. The multi-scale information provides a measure of the source mask or "footprint", allowing overlapping sources to be deblended and have their fluxes measured separately. Fluxes are extracted following a background subtraction, where the background is estimated by interpolating under the "footprint," defined by a 2-D Gaussian. Thus, source properties are extracted from filament-subtracted, flattened images. The robustness of each source is defined by the global goodness parameter, which combines the global detection significance from the monochromatic single scale extractions, the global signal-to-noise ratio (SNR), and source shape across all wavelengths. Bright, round sources detected over several monochromatic scales and several wavelengths have higher goodness. Conversely, the goodness decreases if a source becomes more elongated or the global SNR becomes lower. For more information about *getsources*, see Men'shchikov et al. (2012).

We used *getsources* version 121208, which includes a prescription for filament extraction in addition to one for source extraction. Filaments are extracted and subtracted from images before compact sources. Filaments, however, are identified using an area condition, where significantly elongated structures connect large areas in the decomposed images. Conversely, sources are generally more compact and circular. The area condition considers two parameters, one a direct measure of the elongation and the other a measure of the equivalent area. The equivalent area condition is used to identify "porous" filaments, such as spirals. Removing filaments before detecting the compact sources gives superior source identification and recovery of source properties. For example, a line-of-sight intersection of two filaments could be viewed as a compact density enhancement, resulting in an erroneously identified source. For more information about filament extraction, see Men'shchikov et al. (2013, in preparation).

Using *getsources* on our *Herschel* data alone, we identified 707 and 370 compact

structures in the Western Perseus and Eastern Perseus fields, respectively, with 23 objects common (within 8″) to both fields. These numbers are roughly a magnitude higher than the typical source counts for Perseus from previous, incomplete ground-based submillimeter surveys (e.g., Kirk et al. 2006; Enoch et al. 2009). Not all our extracted sources are actual dense cores, however. In Section 5.3.2 we list our selection criteria for well-detected sources, and in Section 5.3.3, we remove likely extragalactic contaminants. For all sources, we adopt source names as the observation field (West or East) and the *getsources* detection number.

The sources identified here correspond to a first look analysis for the Perseus cloud. A more extensive source extraction will be completed for the First Generation study from the *Herschel* Gould Belt Survey consortium (Pezzuto et al. in preparation). The complete catalogues will include the cross-section of sources identified from different extraction algorithms, such as *getsources* (Men'shchikov et al. 2012), *cutex* (Molinari et al. 2011), and *csar* (Kirk et al. 2013). Since *getsources* provides the most extensive list of sources, we only consider those results here and utilize a number of criteria to identify robust detections (see Appendix H).

5.3.2 Source Selection

We are interested in identifying dense cores and YSOs with the *Herschel* observations and archival infrared detections. Since Class II YSOs can have weak or tenuous submillimeter detections (Weintraub et al. 1989), we considered all extracted sources regardless of their detection quality. Nevertheless, we note that some sources are well-detected and others are not (see Appendix H).

In addition to the archival infrared information, 70 μm emission can be used to identify protostellar signatures. Emission at 70 μm is generally associated with warm dust (i.e., due to an embedded YSO) and can be optically thick (e.g., Pezzuto et al. 2012). Thus, compact 70 μm towards a dense core is a good indicator of a YSO (Dunham et al. 2008). For fainter protostars, such as those that are deeply embedded, 70 μm emission can be heavily confused with a bright diffuse background, e.g., the blue ring in Figure 5.1. Thus, we generated a list of compact 70 μm sources using an initial selection criteria to identify the bright objects and then we visually inspected all sources to identify the fainter compact 70 μm sources. Specifically, we initially identified bright, *compact* 70 μm sources using the following set of criteria:

1. SNR (70 μm) ≥ 3, and

2. positive peak flux and total flux, and

3. measured sizes of $a \leq 30''$ and $b \leq 30''$, and

4. $a/b \leq 2$.

To include the faint compact 70 μm sources, we visually inspected all extracted sources in the original 70 μm maps. In the Western field, we added ten compact 70 μm sources that did not meet our initial criteria (e.g., they had low SNRs, slightly larger sizes, or higher aspect ratios), but appeared compact from our visual inspection. In the Eastern field, we added only one object with $a \approx 33''$. We also removed two sources from the Western field and three sources from the Eastern field that each met our criteria. Visual inspection of these few sources suggested that a compact source was not visible, generally due to a bright diffuse background. In one case, a source coincided with a stripe artifact in the 70 μm map and was erroneously identified as compact. Figure 5.3 highlights the sizes and aspect ratios of the 70 μm emission towards all sources in Perseus.

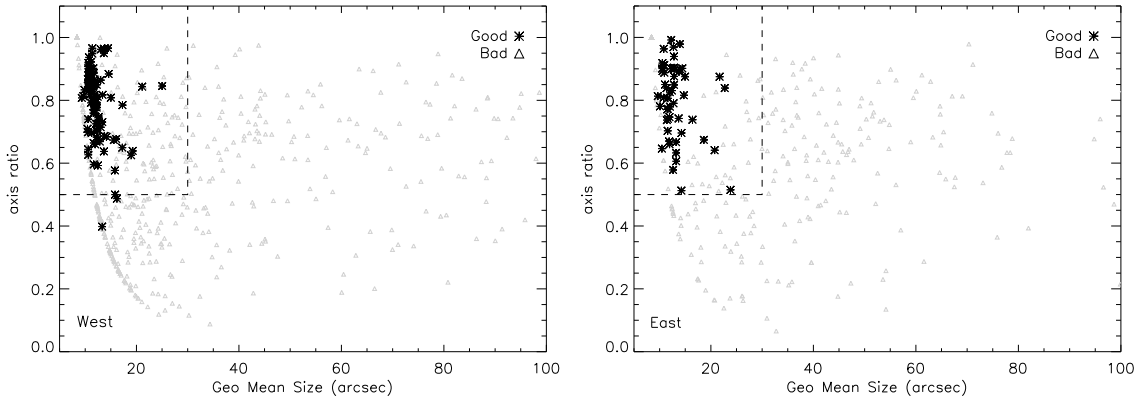

Figure 5.3: Size and aspect ratio distributions for the 70 μm detections. The grey triangles correspond to all 70 μm sources in the sample and the black stars correspond to the compact 70 μm sources that passed our criteria and visual inspection. The dashed box shows the limits for our size selection criteria. For size, we give the geometric radius, $r = \sqrt{ab}$.

We found 103 and 54 compact 70 μm sources in the Western and Eastern fields, respectively, with only one source common to both fields. Since the presence or absence of compact 70 μm emission can classify cores as protostellar or starless (Dunham et al. 2008; Bontemps et al. 2010), we will use the compact 70 μm sources in combination with the *Spitzer* catalogues (see Section 5.2.2) to identify which *Herschel* sources are protostellar and which are starless.

5.3.3 Galaxy Contamination

In addition to dense cores and YSOs, extragalactic sources, particularly those with strong dust emission, can be bright in the *Herschel* bands. Furthermore, galaxies are generally unresolved, and thus will appear as compact sources. Thus, it is important we remove such contamination from our sample if we want to obtain a clean sample of sources associated with the Perseus cloud.

Figure 5.4 shows the distribution of column density towards all the compact sources identified by *getsources*. (For an explanation of the column density measurements, see Section 5.4.1.) For comparison, we also show the distribution for just the well-detected sources (see Appendix H). Unsurprisingly, the sources associated with low column densities tend to be well-detected. Sources observed towards relatively faint diffuse emission will have greater contrast with the background and so, will be easier to extract and measure their properties. We also find a small peak in the number of detections for $N(H_2) < 2 \times 10^{21}$ cm^{-2} ($A_V < 3$). This increase occurs for both the entire sample and the well-detected only sources. Since star-forming cores are generally associated with regions of high column density (Kirk et al. 2006; Lada et al. 2010, André et al. 2010), we believe this increase is mainly due to extragalactic contamination. As such, we flagged all sources identified in regions with $N(H_2) < 2 \times 10^{21}$ cm^{-2} as galaxies. In total, 121 sources were flagged as galaxies. (We note that these extragalactic candidates do not have unique detection properties (i.e., colours, magnitudes) that distinguish them from Galactic sources.)

As a check, we measured the likelihood of an extragalactic source being detected in the relatively small areas of the sky above our assumed threshold (i.e., $N(H_2) > 2 \times 10^{21}$ cm^{-2}). For this check, we utilized the results from *Herschel* surveys of distant extragalactic sources, e.g., the *Herschel* Astrophysical Terahertz Large Area Survey (H-ATLAS; Serjeant et al. 2009) and the *Herschel* Multi-tiered Extragalactic Survey (HerMES; Oliver et al. 2012). Since these surveys cover > 100 deg^2, they provide excellent statistics for the number of contaminating galaxies we can expect in our data.

Table 5.1 summarizes the likelihood of extragalactic contamination at $160-500\,\mu$m for the $N(H_2) > 2 \times 10^{21}$ cm^{-2} region only. First, we found the minimum observed fluxes towards the high column density material at the native resolution of each wavelength. These thresholds give lower-limits to the diffuse background and consequently, upper limits to the number of galaxies we could reasonably expect at each wave-

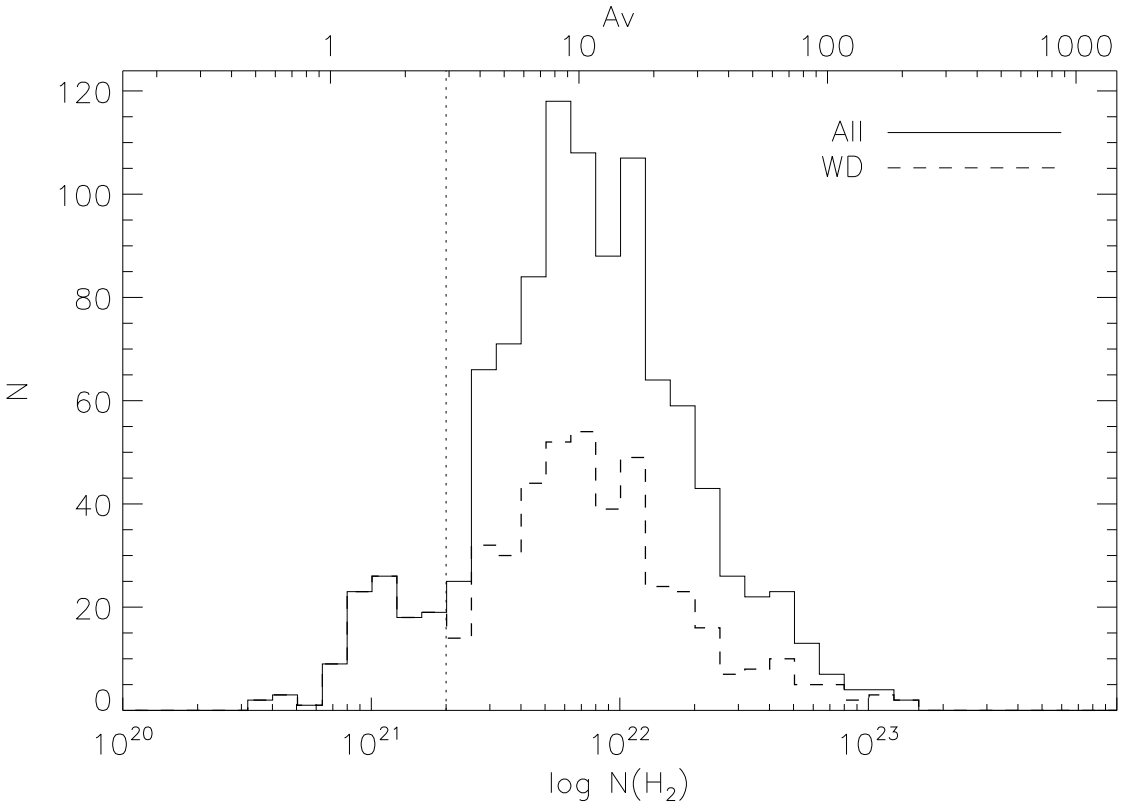

Figure 5.4: Distribution of column density for all observed compact sources (solid histogram) and the well-detected sources (dashed histogram). Well-detected sources passed the initial selection criteria outlined in Section 5.3.2. The dotted line corresponds to 2×10^{21} cm^{-2} (or $A_V \sim 3$ mag), our column density threshold for galaxy candidates.

length. Second, since extragalactic contaminants are mainly point sources, we found the equivalent (point source) flux within one beam using $S_{ps} = I_{min}\sqrt{A_{pixel}/A_{beam}}$, where I_{min} is the minimum observed intensity in the N(H_2) $> 2 \times 10^{21}$ cm^{-2} region, A_{pixel} is the pixel area, and $A_{beam} = 1.133\theta^2_{FWHM}$ is the beam area for a FWHM of θ_{FWHM}. To ensure only robust galaxy detections, we considered only extragalactic sources with $S > 3 \times S_{ps}$. Finally, we use the statistical counts of Berta et al. (2011, for PACS) and Clements et al. (2010, for SPIRE) to estimate the number of galaxies in the N(H_2) $> 2 \times 10^{21}$ cm^{-2} region.

According to Table 5.1, it is very unlikely that we detected many galaxies above N(H_2) $> 2 \times 10^{21}$ cm^{-2}. Since the diffuse emission is so bright above this threshold, extragalactic sources are obscured. Below this threshold, however, there are far more likely opportunities for extragalactic contamination. The area corresponding to N(H_2) $< 2 \times 10^{21}$ cm^{-2} covers 11.3 deg^2, and for this region we could expect < 113

Table 5.1: Extragalactic Contamination[a]

Wavelength (μm)	I_{min} (mJy beam^{-1})	pixel ($''$)	$3 \times S_{ps}$[b] (mJy)	Detection Rate[c] (gal deg^{-2})	Galaxies
160	250	4.5	235	< 2.6	< 9
250	500	6.0	460	1	< 4
350	600	10.0	680	0.5	< 2
500	600	14.0	650	0	0

[a]These results corresponding to the N(H_2) $> 2 \times 10^{21}$ cm^{-2} region of Perseus. This region covers ~ 3.5 deg^2.

[b]We consider detection rates only for galaxies with $3 \times S_{ps}$. We assume anything fainter would not be well-detected.

[c]Integrated galaxy counts, $N(> S)$. For PACS, the galaxy counts came from Berta et al. (2011). For SPIRE, the galaxy counts came from Clements et al. (2010).

galaxies at 250 μm (see Clements et al. 2010) which is of similar order to the 121 objects flagged as galaxies we find at N(H_2) $< 2 \times 10^{21}$ cm^{-2}. For PACS, Berta et al. (2011) used data taken with a scan rate of 20 arcsec s^{-1}, which resulted in better sensitivities and smaller beams than our PACS data which used scan rates of 60 arcsec s^{-1}. As such, Berta et al. (2011) are better able to detect compact sources (smaller beam) and fainter galaxies. Using their numbers suggests < 500 galaxies at 160 μm for the low column density material, which is significantly larger than the number of objects detected at these column densities. Therefore, we are confident that galaxies are only a major factor for the N(H_2) $< 2 \times 10^{21}$ cm^{-2} material and that by removing these sources, we are primarily removing extragalactic contaminants rather than star-forming cores.

5.4 Results

5.4.1 Clumps

We defined clumps as intermediate scale (~ 1 pc), moderately dense ($\sim 10^3$ cm^{-3}) structures that can form clusters (dozens to thousands) of new stars (Williams et al. 2000). Conversely, cores are the small-scale ($\lesssim 0.1$ pc) structures that form single stars or small stellar systems (e.g., Di Francesco et al. 2007). Figure 5.1 highlights the seven main clumps in the Perseus cloud and the focus of our study. In addition to probing their dense core and YSO populations, we are also interested in the relative clump properties.

As in Chapters 3 and 4, we first applied the zero-point offset correction from Planck data to our *Herschel* data. Since the Western and Eastern fields were observed at different epochs, we found the five zero-point Planck corrections separately for each field. Next, we merged the Western and Eastern fields. To merge fields, we cropped $10-20$ pixels from the map edges to remove spikes and artifacts, and then we used the *Starlink* task `wcsmosaic` to mosaic the two observations. For the overlap region, `wcsmosaic` takes the mean of the observations. For the $160-500$ μm data, the Western and Eastern fields showed excellent agreement. For the 70 μm observations, however, the background flux in the Eastern field was systematically lower than the Western field. In measuring the 70 μm offset, faint extended emission is generally lost, resulting in poor correlations with IRAS observations at 60 μm and highly uncertain 70 μm offsets (J.-P. Bernard 2013, private communication). Nevertheless, we do not use the 70 μm emission in our clump analysis. Figure 5.1 shows the resulting image combined from mosaics made at 160 μm, 250 μm, and 350 μm.

We fitted the SEDs of the entire Perseus cloud in a pixel-by-pixel in the same manner as Chapter 4 using Equation 4.1. Since we cannot directly measure the dust opacity well with *Herschel* data alone (see Section 4.5.1), we assumed that $\kappa_{\nu_0} = 0.1$ cm^2 g^{-1} at $\nu_0 = 1000$ GHz (Hildebrand 1983; André et al. 2010) with $\beta = 2$ and a mean molecular weight of $\mu = 2.8$. Finally, we also applied colour correction factors to our *Herschel* data (see Chapter 4 and Appendix D). Table 5.2 shows the adopted uncertainties in our observations. We adopt colour corrections for temperatures between $10-25$ K rather than the $10-15$ K range we assumed for B1 (see Chapter 4). The 1 σ rms noise uncertainties are the same as for B1 (see Table 4.1).

Table 5.2: Adopted Colour Corrections and Flux Uncertainties for Perseus Clumps

Band	160 μm	250 μm	350 μm	500 μm
Colour Correction[a]	1.01	1.01	1.00	1.02
Colour Uncertainty[b]	5%	2%	2%	3%

[a] Average colour corrections for each band, where $I_{corrected} = CC \times I_{obs}$. These values assume $T \approx 10-25$ K and $\beta \approx 1.5-2.5$. See Appendix D. Note that Table 4.1 assumes $T \approx 10-15$ K.

[b] Uncertainties refer to the fractional uncertainty in the average colour correction based on the range of accepted colour corrections. These uncertainties do not include the calibration uncertainties.

In Chapter 4, we applied a set of 1000 random calibration correction factors within a Gaussian distribution to the SED fits. A similar exercise for the entire Perseus cloud

would be computationally expensive, however. Furthermore, based on the analysis in Chapter 4, the calibration uncertainties are relatively minor for fixed values of β itself. Indeed, a greater source of uncertainty is the fixed value of β. For example, a difference of ± 0.5 in β resulted in $\Delta T \lesssim 2$ K, whereas the calibration errors yielded $\Delta T \lesssim 0.5$ K (see Section 4.3.2). Thus, we do not include any calibration uncertainties in our analysis here.

Figure 5.5 shows the column density map for the entire Perseus cloud. Star formation is tied to the amount of high column density material (e.g., Johnstone et al. 2004; Lada et al. 2010; André et al. 2010). Thus, we expect most dense cores and YSOs to coincide with the seven main clumps. Unfortunately, defining clump boundaries is nontrivial. We approximate the "boundary" of each clump using the extent of dense material. Lada et al. (2010) found that star formation coincided with material with $A_V \gtrsim 7$ mag. Following Evans et al. (2009), we adopt the relation between column density and extinction as proposed by Draine (2003);

$$\mathrm{N(H)}/A_V = 1.37 \times 10^{21}\ \mathrm{cm^{-2}\ mag^{-1}},$$

where N(H) is the atomic hydrogen column density and A_V is the visual extinction. For molecular clouds, where the hydrogen gas is molecular rather than atomic, $\mathrm{N(H)} = 2\mathrm{N(H_2)}$, and thus,

$$\mathrm{N(H_2)}/A_V = 6.85 \times 10^{20}\ \mathrm{cm^{-2}\ mag^{-1}}. \tag{5.1}$$

Thus, a threshold of $A_V \geq 7$ becomes $\mathrm{N(H_2)} \geq 4.8 \times 10^{21}$ cm^{-2}. The red contours in Figure 5.5 highlight such high column density material. Using these contours, we defined boxes to enclose the high column density material and correspond to the boundary of each clump. For IC348, we modified slightly the box boundary to include all sources in the IC348 cluster observed by Gutermuth et al. (2009).

Table 5.3 gives the clump properties, including the area and the mass corresponding to the $\mathrm{N(H_2)} \geq 4.8 \times 10^{21}$ cm^{-2} material within the boundaries as highlighted in Figure 5.5. Mass is measured from the column density assuming a mean molecular weight of $\mu = 2.8$. For the area and mass, we assumed a distance of 235 pc (Hirota et al. 2008). Unsurprisingly, the three most massive clumps, B1, IC348, and NGC1333, have the most star-forming activity (see also Section 5.4.2; Bally et al. 2008). These three are also the largest clumps in the sample (> 2 pc^2 of dense ma-

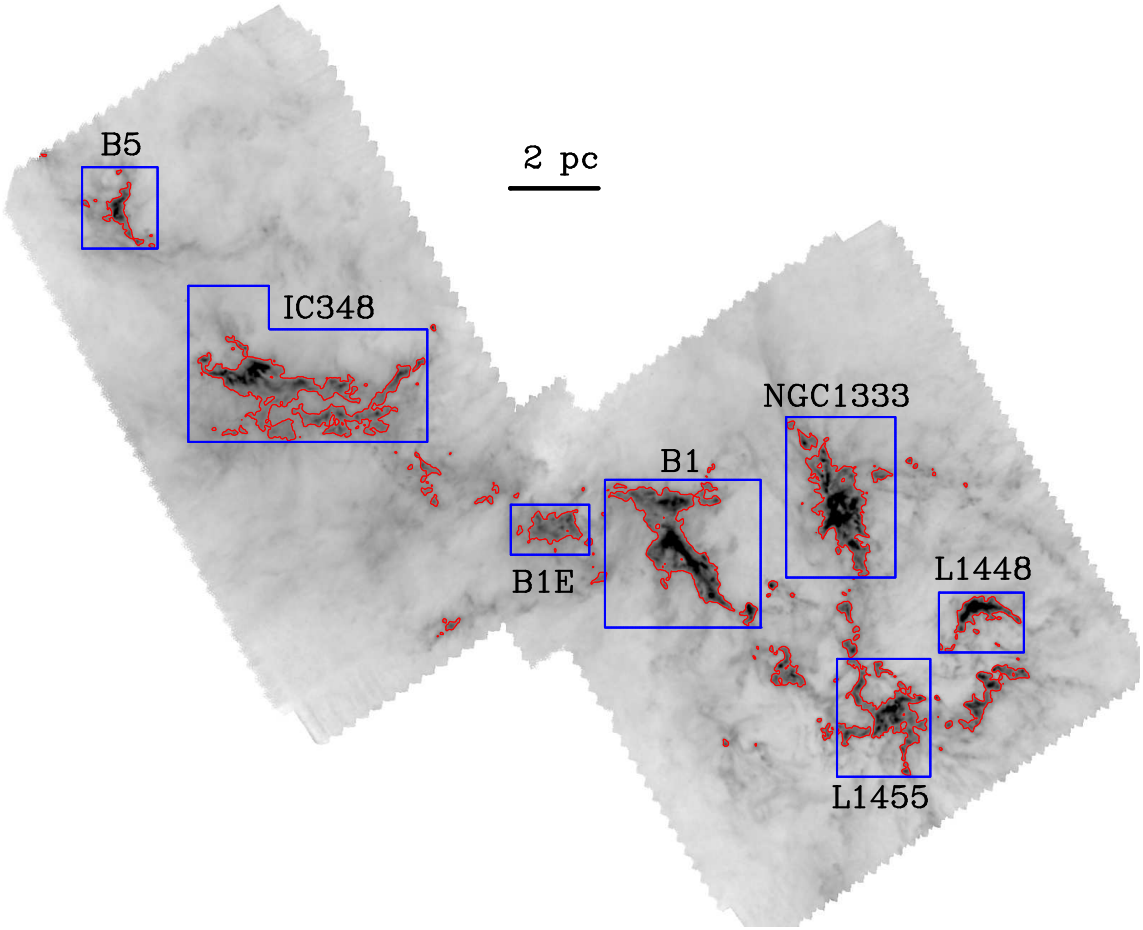

Figure 5.5: Column density map of the Perseus molecular cloud. Red contours illustrate regions with $N(H_2) > 4.8 \times 10^{21}$ cm^{-2} (or $A_V > 7$ mag). The blue boxes illustrate the boundaries selected for each clump.

terial). Table 5.3 also lists the mean and median values for temperature and column density for the $N(H_2) \geq 4.8 \times 10^{21}$ cm^{-2} material.

Figure 5.6 shows the column density distributions for all material within the boundary of each clump. As expected, the clumps with the largest mean column densities, B1, L1448, and NGC1333, do indeed show broad extensions to high column densities ($\gtrsim 5 \times 10^{22}$ cm^{-2}). Conversely, IC348 and L1455 each have moderate extensions (to $\sim 5 \times 10^{22}$ cm^{-2}). Finally, B5 shows only a slight asymmetry towards higher column densities (but $< 5 \times 10^{22}$ cm^{-2}) and B1-E shows no such asymmetric extension. We measured the slopes of the high column density tails of each clump using linear least squares fits, including only the material above 10^{22} cm^{-2}, except for L1448, where we included material above 4.8×10^{21} cm^{-2}. We remeasured these

Table 5.3: Clump Properties[a]

Clump	Area (pc^2)	Mass ($M_\odot$)	T[b] (K)	N(H_2)[b] ($10^{21} cm^{-2}$)
B1	2.6	611	13.4 / 13.5	10.5 / 7.9
B1-E	0.6	93	13.8 / 13.8	6.8 / 6.5
B5	0.4	66	13.3 / 13.5	8.3 / 6.5
IC348	3.3	548	15.6 / 15.7	7.5 / 6.0
L1448	0.5	162	12.3 / 12.5	14.2 / 8.5
L1455	1.4	260	12.2 / 12.3	8.3 / 6.7
NGC1333	2.1	581	13.4 / 13.1	12.1 / 8.0

[a]Corresponding to the $N(H_2) \geq 4.8 \times 10^{21}$ cm^{-2} material only.

[b]The mean value and median value, respectively. Based on uncertainties in fixing β (which dominates the fit uncertainties), we estimate $\Delta T \lesssim 2$ K and $\Delta N(H_2) \lesssim 40\%$ (see Chapter 4).

slopes for different bin sizes and found that our adopted slopes have uncertainties of $\lesssim 20\%$. Thus, B1, L1448, and NGC1333 have the shallowest profiles with $m \geq -2.3$, whereas B5, IC348, and L1455 have slightly steeper profiles with $m \sim -2.8$. For B1-E, the absence of a high column density tail resulted in an extremely steep profile ($m = -9.6$).

Are the high column density tails linked to clump mass or size? The two clumps with the least prominent high column density extensions, B1-E and B5, are small and have relatively low masses, whereas B1 and NGC1333 are larger and more massive. Nevertheless, L1448 is small, but has a very prominent high column density tail and L1455 is large, but has only a moderate high column density tail. Thus, additional factors beyond mass and size likely contribute to the amount of dense material observed towards clouds.

5.4.2 Source Properties

In Section 5.3.1 we identified 1054 unique *Herschel* sources. Of these, we found 121 sources were likely extragalactic contaminants (see Section 5.3.3). We characterized the remaining 933 sources using single-temperature dusty blackbody functions to their

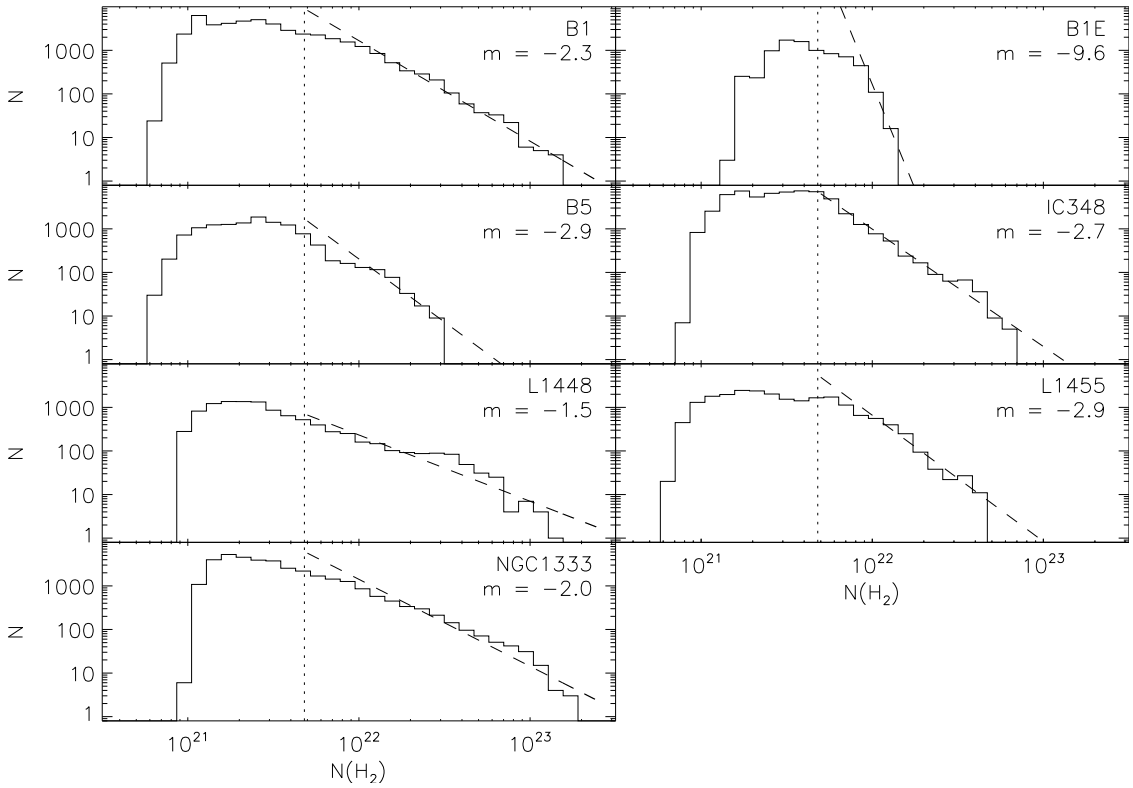

Figure 5.6: Column density distributions for each of the Perseus clumps. These plots include all column density measures within the blue boundaries shown in Figure 5.5. The dotted lines show our clump threshold column density of 4.8×10^{21} cm^{-2} and the dashed lines give the linear least squares best fit slope to the high column density end. The best fit slope is also labeled.

$160 - 500$ μm SEDs following,

$$\left(\frac{S_\nu}{1 \text{ Jy}}\right) = 3.08 \left(\frac{M}{1 \text{ M}_\odot}\right) \left(\frac{d}{100 \text{ pc}}\right)^{-2} \left(\frac{\nu}{1.0 \text{ THz}}\right)^{\beta} \left(\frac{\nu}{100 \text{ GHz}}\right)^{3} \left[\exp\left(\frac{h\nu}{kT}\right) - 1\right]^{-1}, \tag{5.2}$$

where M is the source mass, d is the distance, β is the dust emissivity index, h is the Planck constant, and k is the Boltzmann constant. As in Section 5.4.1, we used the IDL routine, *mpfitfun* to determine the best-fit source mass and temperature. For all our sources, we assumed a distance of 235 pc (Hirota et al. 2008) and $\beta = 2$. Although we expect $\beta \lesssim 2$ for dense cores and embedded YSOs (e.g., see Chapter 4), we do not yet have complete coverage at long wavelengths (i.e., 850 μm) for the entire Perseus field, and thus, we cannot constrain β well.

For the compact sources, we required a new set of colour corrections for the $160 - 500$ μm bands. In particular, the SPIRE colour corrections vary between extended emission (that uniformly fills the beam) and compact structures (that do not uniformly fill the beam). For more information, see the SPIRE Observers' Manual[1] and Appendix D. (The PACS colour corrections do not distinguish between extended and compact emission). Thus, we computed new colour corrections for all bands associated with compact sources with $T = 10 - 30$ K and $\beta = 2$. For an explanation of the temperature range, see Appendix F. Table 5.4 gives the colour corrections for our assumed profiles. We also include the 70 μm corrections, though these data are not included in the SED fitting. Unlike the longer wavelengths, emission at 70 μm may include optically thick emission from a central protostellar source or non-equilibrium emission from very small dust grains due to stochastic heating or shocks (Li & Draine 2001; van Dishoeck 2004; Martin et al. 2012). Furthermore, the colour corrections at 70 μm are very uncertain. As such, emission at 70 μm is less robust than the other bands.

Table 5.4: Colour Corrections for the Compact Sources

Band (μm)	70	160	250	350	500
CC	0.70	1.01	0.97	0.96	0.92
ΔCC	33%	5%	5%	4%	4%

Finally, we only fit the SEDs for all 933 galactic sources, ignoring the extragalactic contaminants. For each source, we fitted the 160 μm $- 500$ μm SEDs using a minimization of χ^2 technique with Equation 5.2 and $\beta = 2$. Flux errors were taken as the quadrature sum of the colour correction uncertainties and the intrinsic flux errors from the extraction. Thus, we ignored bands with SNR < 1 and whole sources with more than three bands with SNR < 3. Additionally, for cold sources, the 160 μm extraction may not be robust despite robust detections in the SPIRE bands. In these cases, the associated 160 μm emission was either very large (i.e., larger than the 250 μm source) or very elongated. Since the 160 μm beam is smaller than the 250 μm beam, the source size should be smaller at 160 μm. Thus, we only included the 160 μm point in the SED fit only if the 160 μm detection had $a/b < 2$ and $R_{eff,160} < R_{eff,250}$, for $R_{eff} = \sqrt{ab}$.

Figure 5.7 shows a sample of good SED fits for sources located in the IC348

[1] http://herschel.esac.esa.int/Docs/SPIRE/html/spire_om.html

clump. Figure 5.7 also lists the best-fit mass, temperature and reduced χ^2 value. For the reduced χ^2, we assume $n-2$ degrees of freedom where n is the number of bands used in the fitting. The 70 μm point was not used in the SED fitting, and is only included for comparison.

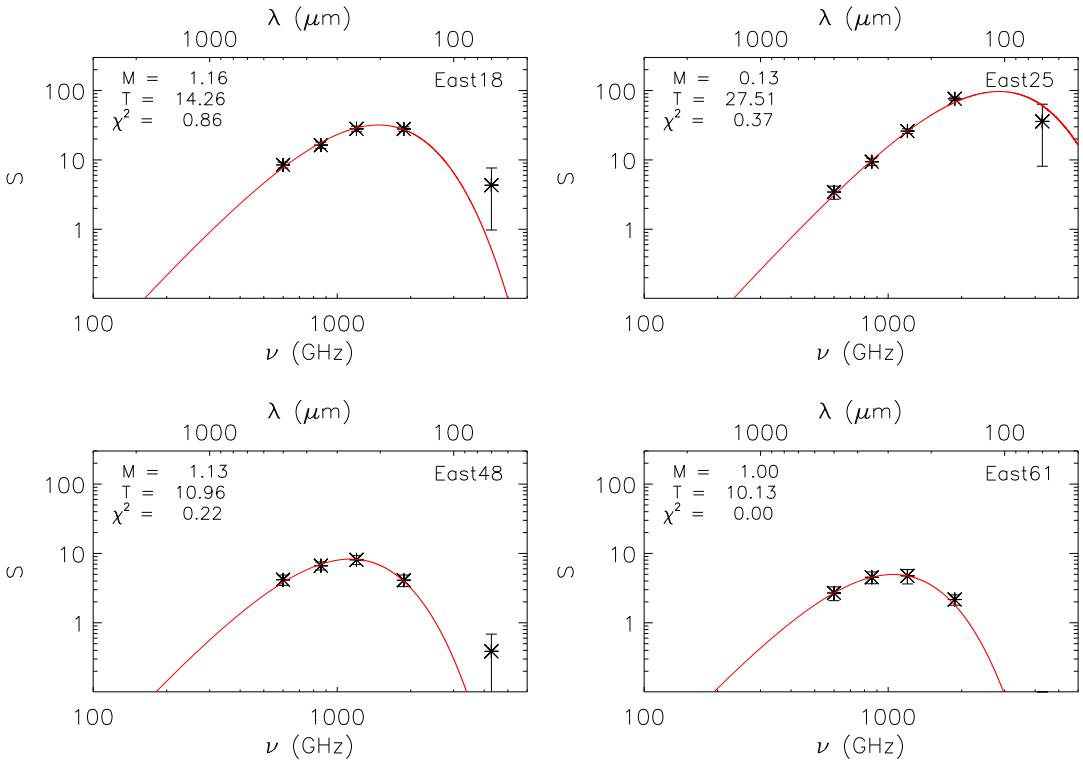

Figure 5.7: Sample SEDs for well-detected sources in the Perseus cloud. All four sources are located in the IC348 clump. The 70 μm point was not used in the fit. The best fit mass, temperature, and reduced χ^2 are given.

Table 5.5 gives sample results from the SED-fitting, including the best-fit mass, temperature, and reduced χ^2, and the effective source size as measured from the 250 μm band. For a complete list see Appendix H. Table 5.5 also includes a flag for good (G) and bad (B) SED fits, where a good (G) flag indicates the source can be well described by a single-temperature dusty blackbody function and a bad (B) flag indicates the source cannot be described by a single-temperature dusty blackbody function. We identified good SED fits as having the following;

1. $T < 100$ K, and

2. $M > 0$ M$_\odot$, and

3. reduced $\chi^2 \leq 1.5$ for well-detected sources or reduced $\chi^2 \leq 1$ for poorly-detected sources.

Since poorly-detected sources generally have larger flux errors, the best-fit χ^2 was generally lower (χ^2 is weighted by the inverse square of the observation uncertainties). Therefore, we used a stricter reduced χ^2 criterion for these sources. Sources with bad-fit flags are still very interesting. For example, cores that require multiple temperature components (i.e., due to a central protostar) may not be well-fit by a single-temperature blackbody model.

Table 5.5: Example SED-fit Properties[a]

Location	Source Name	Fit[b]	M ($M_\odot$)	T (K)	R_d (pc)[c]	χ^2
Off Clump	West483	G	0.5	11.7	0.04	0.9
Off Clump	West689	G	0.1	18.0	0.04	0.2
Off Clump	West460	B	2.9	10.5	0.07	3.9
B1	West256	G	0.5	10.6	0.02	0.0
B1	West489	B	0.6	10.7	0.03	7.0
B1	West274	G	1.9	7.9	0.01	0.0
B1	West17	B	0.9	14.3	0.00	17.3
B1	West670	B	-9.0	-9.0	0.02	9.0

[a]Sources that were not fit (i.e., due to insufficient bands) are given values of -9.0 for mass and temperature and 9.0 for the reduced χ^2.

[b]Fits are good (G) if they pass the criteria enumerated above and are bad (B) otherwise.

[c]Deconvolved geometric size based on the 250 μm observations, where $R_d = 0.5\sqrt{(ab)^2 - (18.2)^2}$ for a beam size of $18.2''$.

Table 5.6 summarizes the statistics from the SED-fitting for each clump. We found that most of the well-detected sources were fit by a single-temperature dusty blackbody function, whereas most of the poorly-detected sources required more complicated SED fits (i.e., multiple temperature components). Most sources in the smaller, lower-mass clumps (B1-E, B5, L1448, and L1455) were well-fit by a single-temperature model, whereas most sources in the larger, higher-mass clumps (B1, IC348, NGC1333) gave bad fits with single-temperature models. Since the NGC1333 and IC348 regions contain large clusters (Bally et al. 2008), external heating by nearby cluster members could be influencing the SEDs (see Section 5.5.4). Alternatively, the sources in these regions may be more evolved and simply require more complex SED models.

Hereafter, we identify all sources with good fits to single-temperature blackbody models as compact cores. Thus, we obtained 477 cores (51% of all galactic sources),

Table 5.6: SED-Fitting Statistics for Each Clump

Fit	B1	B1-E	B5	IC348	L1448	L1455	NGC1333	Off
Good	55	11	21	94	27	53	54	162
Bad	66	2	6	119	19	24	143	77

where 65% are well-detected cores and 35% are poorly-detected cores (see Appendix H). The remaining 456 sources are called "non-cores" and had poor fits to single-temperature blackbody models. Since these sources may correspond to YSOs, this emission may correspond to weak envelopes or excesses from disks.

5.4.3 Source Classification

We used the 477 cores and the 456 non-cores from the previous section for source classification. We matched each of these sources with protostellar signatures. Protostellar signatures are identified as either (1) a compact 70 μm detection, (2) a YSO from the c2d catalogue within $8''$, or (3) a YSO from the G09 catalogue within $8''$. A distance of $8''$ corresponds to the radius of the 160 μm beam[2]. Sources with a corresponding protostellar signature were classified as YSOs, whereas the sources without protostellar signatures were classified as starless.

Table 5.7 gives sample classifications for the sources in Table 5.5. For a complete list of source classifications, see Table H.2. We denoted starless cores with an "S", questionably starless cores with a "Q", and protostellar sources with a "P". Starless cores (S) were defined as sources without YSO signatures that were well-fit by a single temperature dusty blackbody function. Questionably starless cores (Q) are also without YSO signatures, but these sources deviated from a single-temperature dust blackbody function. Thus, the nature of these objects is unclear. Finally, protostellar sources (P) are *Herschel* sources that have associated YSO signatures. Table 5.7 also lists the corresponding protostellar sources in the c2d or G09 catalogues, if applicable.

Table 5.8 highlights the statistics from our classification. In total, we found 458 starless cores, 126 protostellar sources, and 349 questionable starless objects in all of Perseus. The protostellar objects listed in Table 5.8, however, do not include YSOs without envelopes. Since the *Herschel* bands at $160 - 500$ μm primarily trace envelopes, we are insensitive to unembedded YSOs. Of our 126 protostellar sources,

[2]The 160 μm beam has a FWHM of $\sim 13.5''$. Thus, the beam size is $\Omega = 1.133\theta^2_{FWHM} = 206.5$ arcsec^2 with an effective radius of $R_{eff} \sim 8''$.

Table 5.7: Source Classification

Location	Source	Class	70 μm	c2d catalogue	G09 catalogue
Off Clump	West483	S	N	none	none
Off Clump	West689	S	N	none	none
Off Clump	West460	Q	N	none	none
B1	West256	S	N	none	none
B1	West489	Q	N	none	none
B1	West274	S	N	none	none
B1	West17	P	Y	J033121.0+304530	none
B1	West670	Q	N	none	none

we found fourteen sources with multiple (two) YSO signatures. Table H.2 gives the identifications for both YSOs in the multiple cases. In general, these sources were poorly-fit by single-temperature blackbody functions. West39 and East25, however, could be described by a single-temperature component. West39 had two corresponding YSOs within 6″, whereas East25 had one source within 1″ and another within 5.2″. For all multiple sources, we count the protostars only once in Table 5.8, but we consider each YSO in later analyses.

Table 5.8: Source Classification Statistics for Each Clump

Class	B1	B1-E	B5	IC348	L1448	L1455	NGC1333	Off
S	54	11	21	87	27	53	44	161
P	13	0	2	35	5	5	51	15
Q	54	2	4	91	14	19	102	62

5.4.4 Bound and Unbound Starless Cores

For the starless cores, it is important to distinguish gravitationally bound objects from unbound objects. A gravitationally bound core (or prestellar core) is more likely to contract and form stars, whereas a gravitationally unbound starless core could dissipate before collapse. Unfortunately, identifying cores as bound or unbound requires a plethora of additional data. In particular, we require accurate kinematic diagnostics of the internal motions within cores. For example, in Section 3.4.3, we used NH_3 emission to demonstrate that several sources in B1-E were gravitationally unbound

with only one source (B1-E2) having the potential to be gravitationally bound. Unfortunately, such information is unavailable for most of our *Herschel* detections.

To quantify the internal motions within dense cores, we supplemented our nine NH_3 pointings from Chapter 3 with archival single-pointing NH_3 observations from Rosolowsky et al. (2008) for a total of 177 NH_3 detections. With these data, we compared the observed core mass to the virial mass (see Chapter 3),

$$M_{virial} = \frac{5\sigma_v^2 R}{G} = 1162.2 \left(\frac{\sigma_v}{1 \text{ km s}^{-1}}\right)^2 \left(\frac{R}{1 \text{ pc}}\right), \tag{5.3}$$

For simplicity, we assumed other energy terms, such as magnetic energies or surface pressures, are negligible. For each NH_3 detection, we calculated σ_v from the observed line widths assuming a mean molecular weight of $\mu = 2.8$ and the observed kinetic temperature, T_K. If the kinetic temperature was not measured, we assumed $T_K = 11$ K, the average kinetic temperature from Rosolowsky et al. (2008).

We found 113 *Herschel* sources with NH_3 detections within 16.5″ (half the GBT beam). Thus, only 12% of our *Herschel* sources had NH_3 detections. Of those sources, only 51 had good SED fits and thus, good mass measurements to obtain the virial parameter, α_V. Therefore, we were only able to measure the virial parameter, α_V, for 5% of our *Herschel* sources. Table H.3 lists the virial properties of these 51 sources, including the average density, virial mass, and α_V. (Note that these 51 objects include seven protostellar cores, one point source, and two cores with double NH_3 measurements for the same pointing).

Figure 5.8 compares core density with virial parameter for the 44 starless cores in Table H.3. In Figure 5.8, well-detected cores are in blue, poorly detected cores are in grey, bound cores ($\alpha_V \leq 2$) are diamonds, and unbound cores ($\alpha_V > 2$) are stars. Ideally, we would want virial measurements for all cores in our sample. Based on our subsample, we find that sources with high densities ($n > 10^5$ cm^{-3}) tend to be bound, whereas sources with low densities ($n < 10^5$ cm^{-3}) tend to be unbound. This density threshold corresponds well to the critical density associated with a dynamical stable core with $M \sim 1$ M$_\odot$, $T \sim 10$ K, and subsonic internal motions. Furthermore, $n \sim 10^5$ cm^{-3} corresponds to a transition in dense core cooling. For lower densities, cores are primarily cooled from molecular line emission, whereas for higher densities, cores are primarily cooled via collisional cooling (Keto & Field 2005). Thus, in the absence of wider NH_3 detections, we will use the average density to determine the likely virial state.

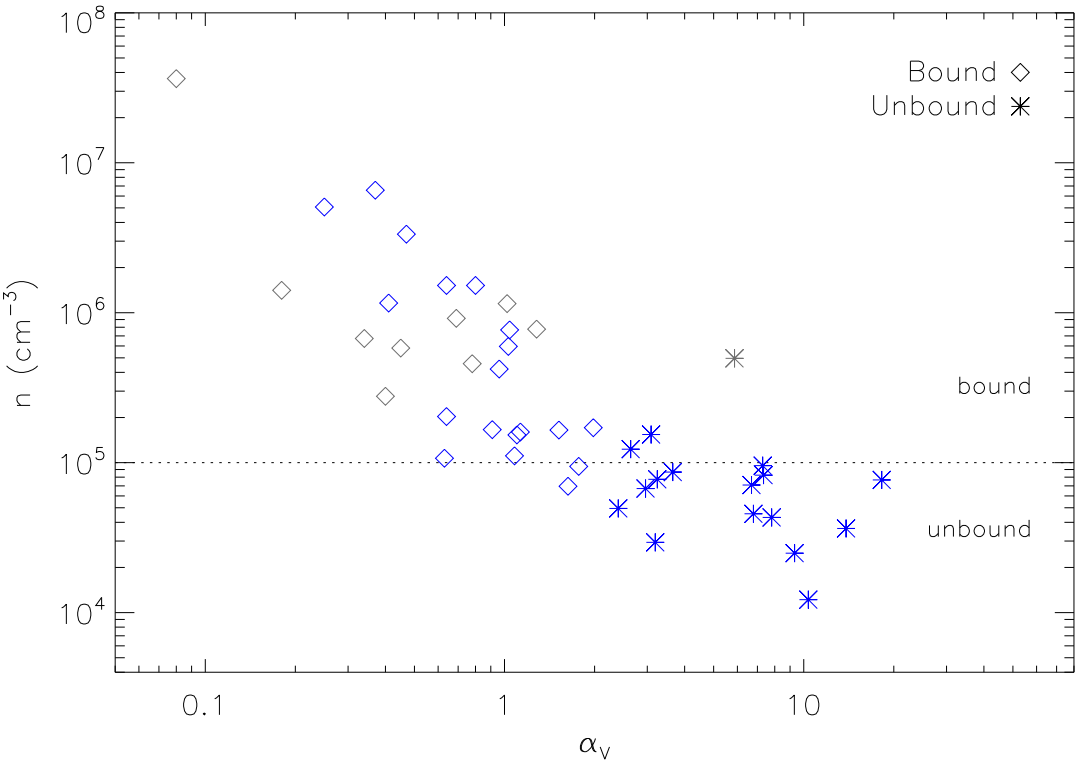

Figure 5.8: Comparison of average source density with virial parameter for starless cores with NH_3 detections (see Table H.3). Bound cores ($\alpha_V \leq 2$) are shown with diamonds and unbound cores ($\alpha_V > 2$) are shown with stars. Blue symbols represent well-detected (WD) cores and grey symbols represent poorly-detected (PD) cores. The dotted lines illustrate our virial classification for subsequent objects. We consider starless cores with $n > 1 \times 10^5$ cm^{-3} likely to be bound and starless cores with $n < 1 \times 10^5$ cm^{-3} likely to be unbound.

Table 5.9 shows the statistics for bound and unbound starless cores for each clump determined using the NH_3 data and our density threshold of $n_{th} = 1 \times 10^5$ cm^{-3}. The majority of NH_3-detected starless cores were bound, including both well-detected and poorly-detected sources. With small numbers, however, it is difficult to compare the clumps. Conversely, we find the majority of all starless cores towards the clumps have $n < 10^5$ cm^{-3} and thus, are more likely to be unbound. Only NGC1333 yielded more higher density cores. Since Rosolowsky et al. (2008) used SCUBA (850 μm) and Bolocam (1.1 mm) observations to select pointings for their NH_3 survey, they were likely biased to high density, bound objects. Additionally, *Herschel* is very sensitive to low-density structures. Thus, many of our "starless" cores are likely unbound objects. Without direct measurements, however, we can only indicate whether a source is likely to be bound or unbound.

Table 5.9: Virial Classification Statistics of Starless Cores for Each Clump

State	B1	B1-E	B5	IC348	L1448	L1455	NGC1333	Off
bound[a]	5	1	1	5	2	2	6	5
unbound[a]	2	5	0	6	1	1	0	2
$n \geq n_{th}$[b]	15	1	6	22	10	13	27	24
$n < n_{th}$[b]	39	10	15	65	17	40	17	137

[a] As identified using NH_3 observations.
[b] For $n_{th} = 1.0 \times 10^5$ cm^{-3}.

Many previous *Herschel* studies used either the critical Jeans mass (critical mass for a thermally supported sphere) or the Bonnor-Ebert mass (critical mass under hydrostatic equilibrium) to estimate boundedness (e.g., André et al. 2010; Könyves et al. 2010). This assumption breaks down for highly turbulent sources. For example, in Chapter 3 we demonstrated that most of the B1-E sources had significant non-thermal motions and that only one source was likely to be bound. Had we used a Jeans analysis or a Bonnor-Ebert analysis to classify the B1-E sources, we would have classified $2 - 4$ substructures as bound. Conversely, using the average density as a proxy for boundedness, we matched our virial results from Chapter 3 for B1-E. While complete NH_3 observations are necessary to classify our starless cores better, in the absence of that information, comparing the average density may be a better test for boundedness than either the critical Jeans mass or the Bonnor-Ebert mass.

5.4.5 YSO Classification

YSOs are generally classified using infrared observations. The first classifications used the slope of the SED at infrared wavelengths (Lada & Wilking 1984; Lada 1987), where younger YSOs had broad blackbody profiles and more evolved YSOs had little infrared excesses (Lada 1987). The spectral shape was determined by the spectral index, α, which corresponds to the slope at infrared wavelengths. The spectral index is defined by;

$$\alpha = \frac{d \log (\lambda F_\lambda)}{d \log \lambda}, \tag{5.4}$$

where younger YSOs have positive slopes and more evolved YSOs have negative slopes. Another common classification technique uses the bolometric temperature, T_{bol}, which corresponds to the temperature of a blackbody with the same mean frequency as the observed SED (see Myers & Ladd 1993). The bolometric temperature

is defined by;

$$\mathrm{T}_{bol} = 1.25 \times 10^{11}\ \mathrm{K\ Hz^{-1}} \frac{\int \nu S_\nu d\nu}{\int S_\nu d\nu}. \tag{5.5}$$

Thus, cooler sources that peak towards lower frequencies will have lower T_{bol} values than warmer sources that include higher frequencies (see Myers & Ladd 1993). Additional YSO classification schemes include the luminosity at submillimeter wavelengths to identify envelope-dominated YSOs (André et al. 1993), specific infrared colours (e.g., Gutermuth et al. 2008), and comparisons to protostellar models (e.g., Whitney et al. 2003; Robitaille et al. 2006).

Each of these techniques assign rough boundaries for the different Classes. Nevertheless, these boundaries are entirely empirical and the ability to place a source in one Class or another depends on available data. Thus, YSO classifications are generally completed on a best-effort basis. Fortunately, recent large infrared surveys (e.g., with *Spitzer*) have improved classification techniques with better statistics (e.g., Evans et al. 2009) and YSO modeling (e.g., Whitney et al. 2003; Robitaille et al. 2006).

For the 126 protostellar sources (see Section 5.4.3), we are interested in the evolutionary stage of the YSO. Typically, YSOs are classified by the shape of their SED, and in the literature, several diagnostics have been developed for protostellar classification. For this study, we selected three common methods. First, we used the infrared spectral index (Lada & Wilking 1984), or the slope at infrared wavelengths, as defined Equation 5.4. Following Evans et al. (2009), we assumed the following slopes for each Class:

Class 0/I: $\alpha \geq 0.3$

Flat: $-0.3 \leq \alpha < 0.3$

Class II: $-1.6 \leq \alpha < -0.3$

Class III: $\alpha < -1.6$

We measured the infrared spectral index using a linear-least squares fit for all available data from $2 - 24$ μm, weighting each point by the uncertainty in $\log \lambda F_\lambda$. Since this technique uses $\lambda \leq 24$ μm only, α is difficult to measure for young, highly embedded protostars (i.e., Class 0) where short wavelength emission may be undetected.

Second, we used the bolometric temperature (Myers & Ladd 1993), as defined by Equation 5.5. Unlike the spectral index, T_{bol} is measured across the entire observed

SED. Following Evans et al. (2009), we assumed the following T_{bol} ranges for each Class:

Class 0: $T_{bol} < 70$ K

Class I: 70 K $\leq T_{bol} \leq 650$ K

Class II: 650 K $< T_{bol} \leq 2800$ K

Class III: $T_{bol} > 2800$ K

We measured T_{bol} for each protostellar source using the trapezoidal integration technique between detections in our SED. We included all observed bands between 1.25 μm and 500 μm, using the data from the c2d catalogue or G09 catalogue for $\lambda \leq 24$ μm data. For consistency, we do not include IRAS observations or (sub)millimeter observations from SCUBA, Bolocam, or MAMBO which may be available only for some sources. We also added $T_{bol} > 2800$ K for Class III sources. Evans et al. (2009) found that Class II and III YSOs can have similar T_{bol} values. Therefore, we caution that our assumed Class II/III boundary for T_{bol} may not result in accurate Class III YSO classifications.

Finally, we also used the ratio of the bolometric luminosity (L_{bol}) to the submillimeter luminosity (L_{smm}), where L_{bol} is the luminosity obtained from the entire observed SED and L_{smm} is the luminosity obtained from only the submillimeter bands (André et al. 1993). For very young objects embedded in thick envelopes, L_{smm} contributes a larger fraction of the total luminosity than for older, less embedded YSOs, and using L_{bol}/L_{smm}, André et al. (1993) proposed the Class 0 classification for the first time. We classified YSOs with $L_{smm}/L_{bol} \geq 0.5\%$ as Class 0 (André et al. 2000). More evolved YSOs, however, cannot be classified with this technique. The bolometric luminosity is given by,

$$L_{bol} = 4\pi d^2 \int S_\nu d\nu = 3.038 \times 10^{-15}\ L_\odot \left(\frac{d}{100\ \mathrm{pc}}\right)^2 \int \left(\frac{S_\nu}{1\ \mathrm{Jy}}\right) d\nu. \qquad (5.6)$$

Following Stutz et al. (2013), we defined L_{smm} as the integrated luminosity (Equation 5.6) for $\lambda \geq 350$ μm. For our analysis, this L_{smm} includes, at most, 2 detections in the submillimeter regime, and thus, we do not sample well the submillimeter luminosity. Nevertheless, this measure will provide a good consistency check for Class 0 YSOs we identified from the other two methods. The lifetime of Class 0 sources is unclear

(e.g., André et al. 1993; Enoch et al. 2009; Evans et al. 2009; Schnee et al. 2012), and thus, we need a significant number of these sources to estimate their lifetimes.

With the addition of *Herschel* data, classifications with T_{bol}, L_{bol}, and protostellar models become more robust, as the SED is better sampled, particularly at younger stages when the SED is dominated by the PACS and SPIRE bands. Nevertheless, complex protostellar models are still degenerate with our data. Since these models contain a large variety of parameters, such as mass accretion rate, inclination, stellar mass, stellar age, and disk mass, a wide variety of models can still fit our data. Thus, we do not consider protostellar models at this time.

We note that the spectral index classifications cannot distinguish between Class 0 and Class I sources, whereas T_{bol} classifications cannot identify well the Flat YSOs. Additionally, the ratio of L_{bol}/L_{smm} can only identify Class 0 YSOs. Thus, each technique has strengths and weakness.

Table H.4 lists the YSO Classes from each technique for the 126 YSOs identified here. Many of these YSOs are found in both the c2d and G09 catalogues. We treated each of these YSOs separately. Table H.4 also lists the interstellar extinction adopted towards each YSO. Since dust preferentially obscures shorter (bluer) wavelengths (e.g., Figure 1.2), fluxes at $\lambda \leq 24$ μm will be biased towards redder colours. (Note that extinction effects are negligible at far-infrared and submillimeter wavelengths.) Foreground extinction can greatly affect the observed fluxes at infrared wavelengths such that T_{bol} and L_{bol} can be underestimated and α can be biased to positive slopes. Thus, we corrected the observed $\lambda \leq 24$ μm fluxes as outlined in Appendix G.

Figure 5.9 shows example SEDs for the five YSO classes: Class 0, Class I, Flat, Class II, and Class III. For these examples, we selected YSOs where the classifications matched between the infrared spectral index and T_{bol} classification techniques, when applicable. These SEDs can be compared to the ideal cases shown in Figure 1.6. As expected, the Class 0 phase is dominated by cold blackbody emission from the envelope. At the Class I phase, the SED is still dominated by the envelope, but near-infrared emission is more prominent. During the Flat YSO phase, the envelope has begun to dissipate, revealing the YSO and disk (e.g., Calvet et al. 1994). Thus, Flat YSOs are expected to have weak submillimeter emission, though whether this submillimeter "excess" is related to remnants of an envelope or the disk is unclear (e.g., see Gregorio-Hetem & Hetem 2002). Class II YSOs have strong infrared emission from the exposed YSO with a slowly declining SED, suggesting far-infrared excesses due to a thick accretion disk. Conversely, Class III YSOs have little to no excess emission

from their disks, which are expected to be optically thick (for more details of each YSO stage, see Chapter 1).

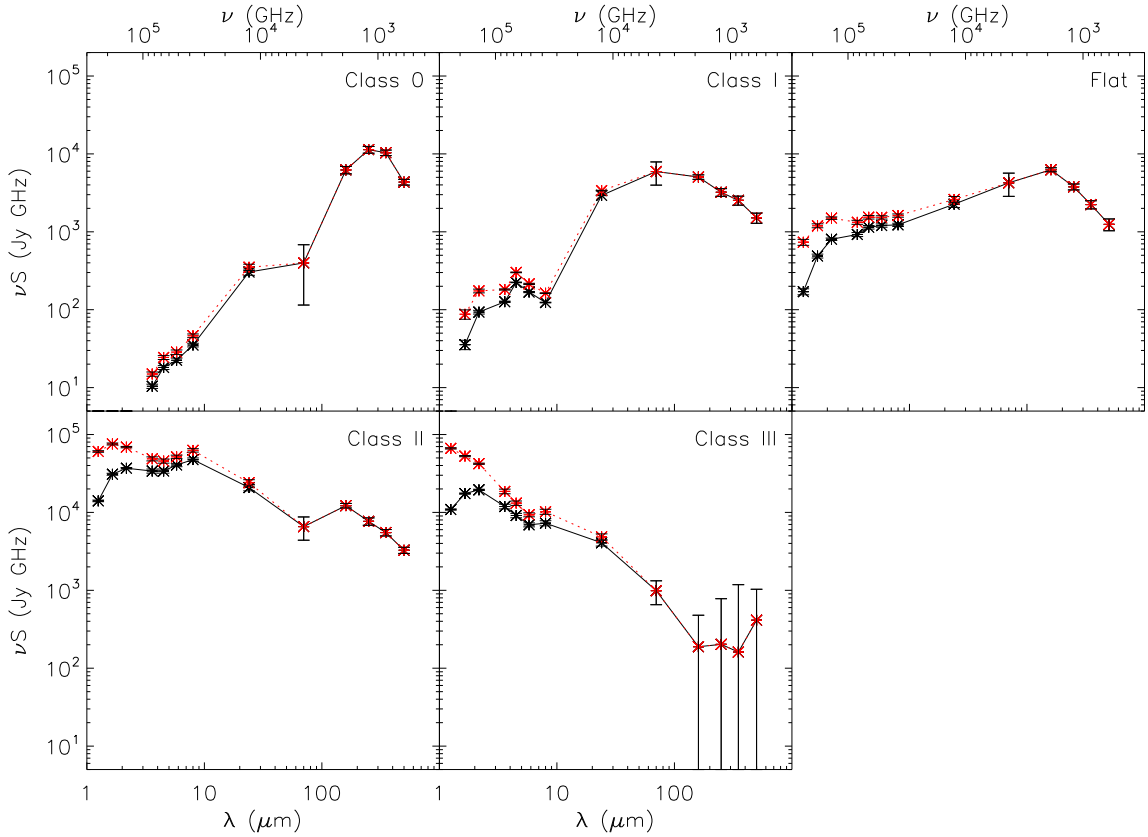

Figure 5.9: Sample SEDs for YSOs at each stage. Black points correspond to the observed fluxes, red points correspond to the fluxes corrected for interstellar extinction.

5.4.6 YSO Coincidences

Accurate YSO classifications are necessary to measure the ages and lifetime of observed YSOs. In Section 5.4.3, we classified 126 YSOs based on the spectral index (α), bolometric temperature (T_{bol}), and the ratio of submillimeter luminosity to bolometric luminosity (L_{smm}/L_{bol}). For our infrared sources, we considered (1) sources with position offsets of $\leq 2''$ between the c2d and G09 catalogues to represent the same source, and (2) sources with position offsets of $\geq 2''$ but within $8''$ of a *Herschel* source associated with the *Herschel* source.

With the first condition, we have classifications for the same infrared source using fluxes from different catalogues. For these infrared sources, we took an average of

the values measured for α, T_{bol}, and L_{smm}/L_{bol} to determine the final classification from each method. We found that there were six infrared sources with either very low or very high extinction values (i.e., $A_V = 0$ mag or $A_V > 20$ mag, respectively) in either the c2d or G09 catalogues (see Table H.4). We excluded sources likely to be mis-identified due to the reddening correction, and did not measure an average in these cases.

With the second condition, we identified separate infrared source associated with the same *Herschel* source. We found 14 *Herschel* sources with multiple infrared detections at separations $> 2''$. Each of these detections are listed separately in Table H.4. We visually inspected these 14 YSOs using IRAC maps of Perseus from the c2d delivery products[3]. We found that 12 YSO pairs had very clear, distinct sources, one pair was ambiguous, and one pair appeared as a single bright YSO. For the distinct YSO pairs, we treated both infrared sources separately, since such cases may correspond with wide binary systems (e.g., Jørgensen et al. 2006; Chen et al. 2013). For example, L1448-N (West 4) is a known binary system with a separation of $\sim 7''$ (Looney et al. 2000; Jørgensen et al. 2006). The one misidentified YSO "pair" is a well-known, bright Class 0 YSO, NGC1333 IRAS 2A, associated with the *Herschel* source, West1. In the case of NGC1333 IRAS 2A, the c2d catalogue and G09 catalogue each determined a different source position (by $4.9''$), where the source position in the G09 catalogue is in better agreement with high resolution observations from Looney et al. (2000).

Table 5.10 compares the YSO classifications from the infrared spectral index and T_{bol} methods, only (for a comparison with L_{smm}/L_{bol} see Section 5.5.7). We include all *unique* infrared detections as described above. For the most part, classification of YSOs by these different methods agreed within their broad definitions. For example, the sources identified as Class II using the spectral index are mostly also identified as Class II with T_{bol}. The spectral index, however, cannot distinguish between Class 0 and Class I sources. We find that the Class 0/I sources from the spectral index technique generally match with Class 0 or Class I YSOs from the T_{bol} classification, with a slight bias towards Class 0 YSOs. Similarly, the T_{bol} method cannot easily distinguish Flat spectral sources. We find that the Flat spectral sources identified by the spectral index generally align with Class I objects identified by T_{bol}.

We also found several outliers of evolved YSOs identified with young envelopes. For example, we found 13 YSOs classified as Class II/III using the infrared spectral

[3]http://irsa.ipac.caltech.edu/data/SPITZER/C2D/images/PER/

Table 5.10: Comparison of YSO Classifications[a]

α-Class \ T_{bol}-Class	Class 0	Class I	Class II	Class III
Class 0/I	33	24	0	0
Flat	3	10	1	0
Class II	5	6	34	0
Class III	0	2	4	0

[a]For each unique infrared detection. For infrared sources identified in both catalogues, we used the average infrared spectral index and average T_{bol} for classification. We considered the two infrared detections towards West1 to correspond to the same source.

index that also have prominent envelopes when classified with T_{bol} (i.e., Class 0/I). Figure 5.10 shows an example SED for these discrepant classifications, where the long wavelength end resembles Class 0 YSOs and the short wavelength end resembles Class II YSOs. For YSOs with prominent envelopes, the *Herschel* bands will dominate the SEDs and the measure of T_{bol} irrespective of the infrared spectral index classification. For example, the East25 has fluxes ~ 10 mJy for $\lambda \leq 8$ μm and fluxes > 1 Jy at $70 - 500$ μm (see Figure 5.10). Since Class II YSOs do not have such prominent envelopes and Class 0 YSOs do not have such bright near-infrared fluxes (see Figure 1.6; Figure 5.9), these SEDs are not expected.

Most of our outliers are found in IC348 and NGC1333, which are rich, young stellar clusters. Thus, we can expect some chance coincidences, where a more evolved YSO (i.e., Class II or Class III) coincides with a younger core along the same line-of-sight. Gutermuth et al. (2009) report peak surface densities of 1000 YSOs per pc^2 for NGC1333 and 300 YSOs per pc^2 for IC348. Using these peak surface densities as an upper limit (and correcting the surface densities for Class II sources), we found a 6% probability of a coincidence within a radius of $8''$ of any given core in NGC1333 and a 4% probability of a coincidence in IC348. For the number of sources we detect in both regions, this amounts to a maximum number of 12 coincidences in NGC1333 and 9 coincidences in IC348. These numbers are consistent with the number of outliers we identified in Perseus.

Alternatively, some discrepancy may arise from the extinction correction or misclassifications due to inclination affects. Most YSOs in our sample did not have direct extinction measurements, and thus, we assumed $A_V = 5.9$ in the absence of a measurement. If we overestimate the extinction, we bias the SED to include brighter near-infrared emission, particularly for the bluer infrared bands. Additionally, sev-

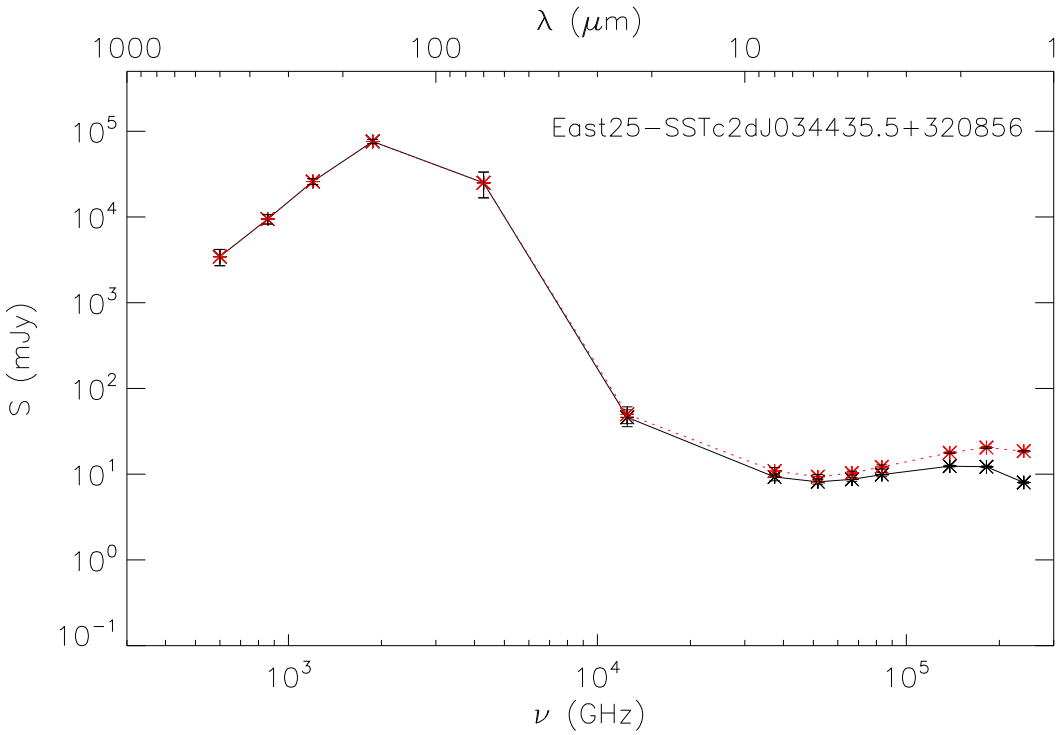

Figure 5.10: SED of *Herschel* source East25 with c2d infrared source J034435.5+320856. The near-infrared ($\lambda \leq 8$ μm) section appears similar to Class II YSOs whereas the far-infrared and submillimeter end ($\lambda \geq 70$ μm) appears similar to Class 0 YSOs. The red points correspond to fluxes corrected for interstellar extinction.

eral YSOs had different extinction measures between the c2d catalogue and G09 catalogue. For example, the c2d catalogue gives an extinction of $A_V = 3.4$ towards one YSO, resulting in a Class II designation, whereas the G09 catalogue gives an extinction of $A_V = 2.9$ resulting in a Flat designation (see West493 in Table H.4). Additionally, several YSOs had very high extinctions ($A_V > 20$ mag), which can greatly affect the assumed classification from the spectral index. To correct source misclassification due to the inclination, we require more complete wavelength coverage to constrain better different YSO models (e.g., Robitaille et al. 2006). We cannot remove misclassifications due to source inclination at this time.

We flagged any source likely to be a chance coincidence in Table H.4. Chance coincidences were based on the presence of a second source with a younger classification or an unusual SED (e.g., Figure 5.10). We also flagged all YSOs with $A_V \gtrsim 20$ or $A_V = 0$ as possible misclassifications due to a possibly erroneous reddening correction. (Sources with such reddening flags were not used for Table 5.10). An $A_V \gtrsim 20$ is very

large. Typically, we measure extinctions that high towards dense cores and filaments. Thus, such high line-of-sight extinctions imply the infrared source is background to a core or filament. Instead, these objects could be younger sources embedded in an envelope, and thus, appear to be highly reddened older objects. Conversely, an $A_V = 0$ implies the source is foreground to the cloud. Since YSOs generally form in regions of high column density, no line-of-sight extinction is unlikely.

For our final YSO classifications, we used the T_{bol} method to identify younger YSOs (Class 0 and Class I) and the infrared spectral index method for older YSOs (Flat, Class II, and Class III). YSOs identified by their T_{bol} as Class 0 or Class I are designated as such, regardless of the classification from the infrared spectral index or L_{smm}/L_{bol}. For the remaining YSOs, we use the infrared spectral index to classify them. Sources with likely coincident YSOs must have a compact 70 μm detection to be classified as protostellar; otherwise, these objects may be starless (see Section 5.5.5). We do not use the L_{smm}/L_{bol} classification at this time (see Section 5.5.7).

5.4.7 Source Classification Summary

In Section 5.3.1, we identified 1077 sources in the Perseus cloud, of which 1054 were unique. We classified all sources located towards low column density ($N(H_2) < 2 \times 10^{21}$ cm^{-2}) emission as extragalactic contaminants, resulting in 933 Galactic sources. Using our clump boundaries (see Figure 5.5), we determined the location of each Galactic source within the Perseus cloud. We considered all sources outside of the clump boundaries to be "Off Clump".

We fit all 933 Galactic sources with single-temperature dusty blackbody functions using Equation 5.2. We found that 477 sources (51%) were well fit by single-temperature profiles and 456 sources (49%) were not. The 456 poorly-fit sources likely require more complex SED models than a single-temperature profile.

We used absence or presence of a compact 70 μm source or *Spitzer* source from the c2d catalogue or G09 catalogue within 8″ to classify sources as starless or protostellar, respectively. A starless source that was well fit by a single temperature dusty blackbody function was called a "starless core", whereas a starless source that was not well fit by such a model was called a "questionably starless core". We found 458 starless cores (49%), 349 questionably starless cores (37%), and 126 protostellar sources (14%). Of the 126 protostellar sources, 13 had two unique infrared sources within 8″.

For the starless cores, we used archival NH_3 observations to estimate which sources are likely to be gravitationally bound and which gravitationally unbound. With NH_3 detections for 44 starless cores, we determined that starless cores with $n \geq 10^5$ cm^{-3} are likely to be bound, whereas starless cores with $n < 10^5$ cm^{-3} are likely to be unbound. Using the average core density as a proxy, we classified the remaining starless cores, finding that 118 starless cores (26%) are likely to be bound whereas 340 starless cores (74%) are unbound.

Finally, we classified the YSOs using the infrared spectral index (α) for the older YSOs (Flat, Class II, and Class III) and the bolometric temperature (T_{bol}) for the younger YSOs (Class 0 and Class I). For infrared sources listed in both the c2d catalogue and the G09 catalogue, we classified the sources using the average value of α or T_{bol}. For the *Herschel* sources with multiple unique infrared detections, we considered each detection as a separate YSO. Table 5.10 shows that there is general agreement between the different classification, though several outliers exist, likely due to chance coincidences between older YSOs (i.e., Class II sources) and cores (see also, Section 5.5.5). We discuss the YSO classifications in more detail in Section 5.5.8.

5.5 Discussion

5.5.1 Robustness of Source Selections

Unlike previous ground-based submillimeter instruments, PACS and SPIRE recover large-scale emission, which makes source extractions more complex. Thus, several techniques have been utilized to select robust *Herschel* objects from a variety of source extractions. With the *getsources* algorithm, we performed simultaneous extractions of filaments and cores at all wavelengths, thereby removing the filamentary structure from the compact source properties. Separating out the filamentary structure from the compact sources results in more robust fluxes (Men'shchikov et al., in preparation).

Nevertheless, not all extracted objects will represent dense cores or protostellar envelopes. As such, several studies have employed different sets of criteria to identify well-detected objects. For example, many studies imposed a combined significance limit in selected bands to identify robust sources, e.g., in Aquila (Könyves et al. 2010), Chamaeleon (Winston et al. 2012), and Lupus (Rygl et al. 2013). Alternatively, Nguyen Luong et al. (2011) used complementary data at other wavelengths to weight the detection significance in addition to a size and significance cut for sources in

W48, whereas Di Francesco et al. (2010) used all identified objects in the Rosette for simplicity and completeness.

For our *Herschel* objects, we found that most well-detected sources were found towards regions of lower column density. About half of the well-detected sources (51%) were found "off clump". Since the diffuse background was generally less significant off the main clumps, the sources in these regions are easier to identify. Figure 5.4 also demonstrates that sources associated with less diffuse emission are generally well-detected (see Appendix H). Nevertheless, dense cores and protostars are generally associated with regions of high column density (e.g., Kirk et al. 2006). For the clumps, 85% of the *Herschel* sources are poorly-detected.

Therefore, selecting cores via the robustness of the detection will bias results in favour of low density (column density and source density) environments compared to higher density environments. Caution is necessary when selecting objects over a range of environments.

5.5.2 Column Density and Extinction

In their study of Perseus, Kirk et al. (2006) found that the dense, submillimeter cores were found in regions with $A_V \geq 5$ mag ($N(H_2) > 3.4{\times}10^{21}$ cm^{-2}), indicating that star formation occurs towards high column density material (see also Kainulainen et al. 2009; Lada et al. 2010). Furthermore, André et al. (2010) found that gravitationally bound cores were generally associated with filaments on the verge of collapse, whereas gravitationally unbound cores were detected primarily toward subcritical filaments. Therefore, core occurrence and dynamical state appears to be greatly tied to its surrounding material.

Figure 5.11 shows the center-position line-of-sight column density distribution of the 458 starless cores identified in Perseus. We split the populations into "On Clump", corresponding to the starless cores within the seven main clumps (see Figure 5.5, and "Off Clump" for the starless cores outside of these clumps. Figure 5.11 also compares the column density distributions for the starless cores likely to be gravitationally bound and unbound (see Section 5.4.4). For reference, we included the threshold column density associated with $A_V = 5$. Recall that we set used a lower limit column density of 2×10^{21} cm^{-2} to identify extragalactic contaminants (see Section 5.3.3).

Similar to André et al. (2010), we find that the gravitationally bound starless cores are generally found towards regions with higher column densities than the grav-

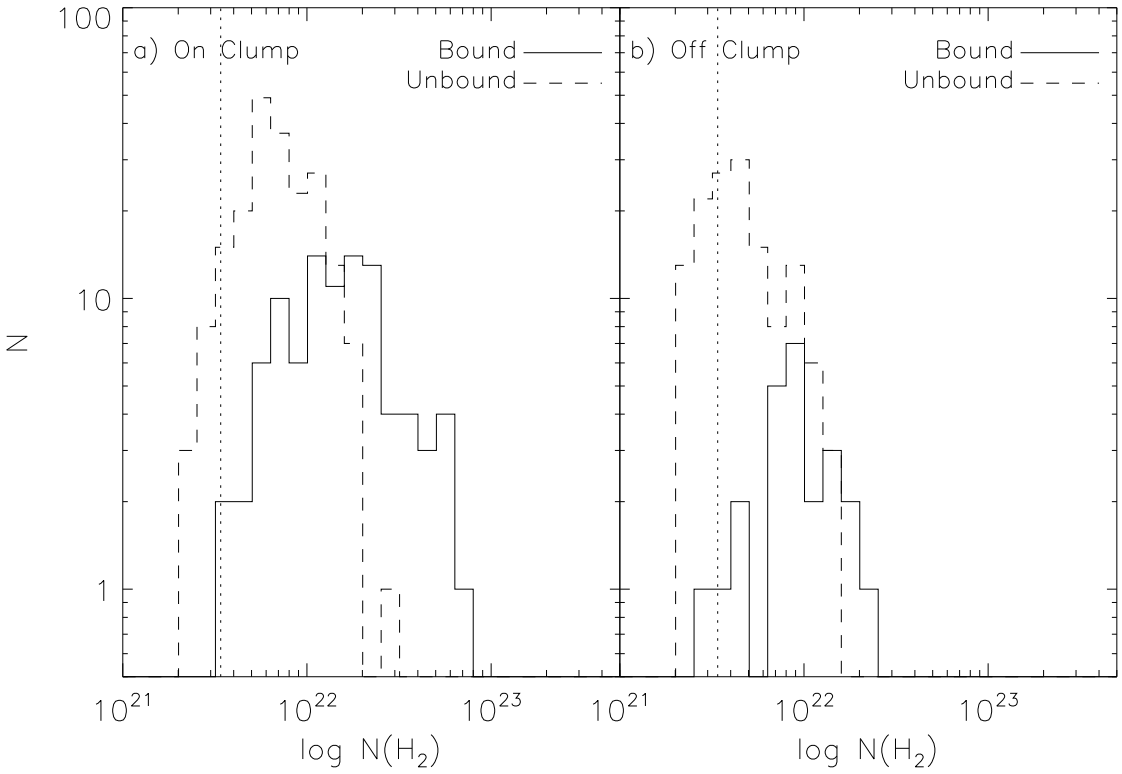

Figure 5.11: Line-of-sight column density measured towards starless cores (a) associated with the clumps and (b) unassociated with the clumps. For clump boundaries, see Figure 5.5. The solid histograms correspond to cores most likely to be bound ($n \geq 1 \times 10^5$ cm^{-3}), whereas the dashed histograms correspond to the cores most likely to be unbound ($n < 1 \times 10^5$ cm^{-3}). The dotted line represents a column density of N(H_2) = 3.4×10^{21} cm^{-2}, which corresponds to the extinction threshold of Kirk et al. (2006).

itationally unbound cores. Furthermore, most cores are located towards regions with N(H_2) $> 3.4 \times 10^{21}$ cm^{-2} ($A_V > 5$ mag), the threshold in Perseus noted by Kirk et al. (2006). Many gravitationally unbound "off clump" starless cores (Figure 5.11b), however, have lower line-of-sight column densities.

Figure 5.12 compares the average density (boundedness) with the line-of-sight column density of our starless cores with their average density. Starless cores located in regions of higher column density generally have higher average densities and thus, are more likely to be gravitationally bound. Conversely, cores detected in regions of lower column density have lower average densities and thus, are more likely to be gravitationally unbound. This relation appears to hold for all starless cores found within the star-forming clumps and those found "off clump". On average, we find that the "off clump" starless cores have lower column densities and lower average

densities than their "on clump" counterparts (see also Figure 5.11).

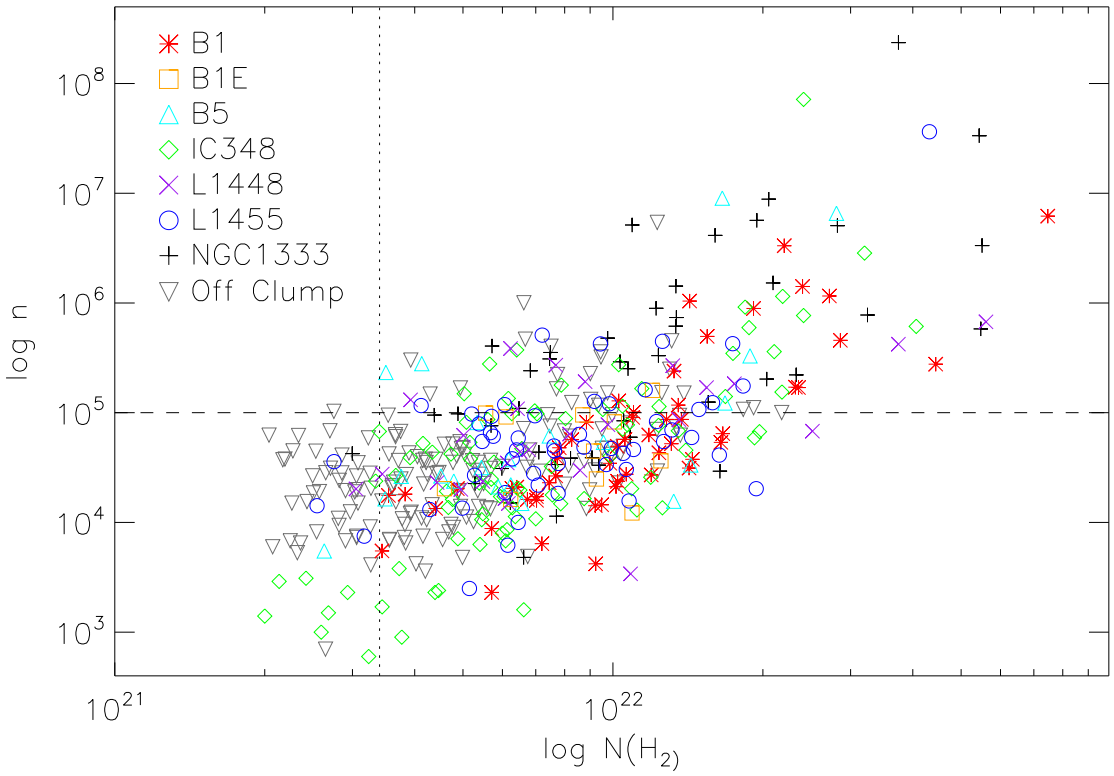

Figure 5.12: Comparison of the line-of-sight column density measured towards starless cores and their average density. The dotted line represents a column density of $N(H_2) = 3.4 \times 10^{21}$ cm^{-2}, which corresponds to the extinction threshold of Kirk et al. (2006), and the dashed line represents our density threshold for bound and unbound sources.

We find that the starless cores are located towards the peaks in the column density distribution. In contrast, Kirk et al. (2006) found offsets between their submillimeter cores and the extinction peaks from low spatial resolution extinction maps. Figure 5.13 compares equivalent measures of column density and extinction towards IC348. The red contours represent our *Herschel*-derived column density levels of $N(H_2) = 5.4 \times 10^{21}$ cm^{-2} at 36.3″ resolution and the green contours represent an equivalent extinction level of $A_V = 8$ mag from a 300″ resolution extinction map derived by the COMPLETE survey (Ridge et al. 2006a). At $A_V \gtrsim 8$ mag, the two maps do not agree well, suggesting that the near-infrared extinction did not probe well the regions with $A_V \gtrsim 8$ mag. At lower extinction levels (i.e., $A_V \sim 5$ mag), however, the two maps show much better agreement.

The COMPLETE extinction map has a resolution of 300″, which is nearly an

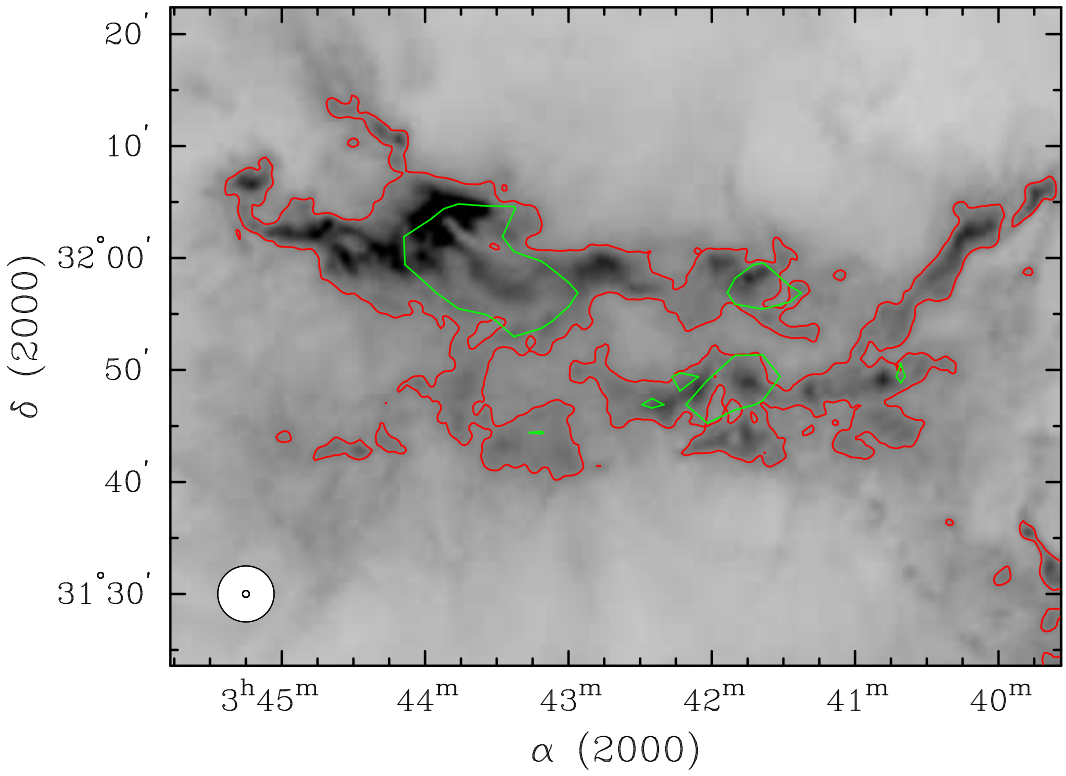

Figure 5.13: The *Herschel*-derived line-of-sight column density towards IC348. The red contours represent column density of 5.4×10^{21} cm^{-2} (at $\sim 36''$ resolution) and the green contours show the corresponding visual extinction of $A_V = 8$ mag (at $\sim 300''$ resolution). The visual extinction data were taken from the COMPLETE survey (Ridge et al. 2006a). Both map resolutions are shown in the bottom left corner.

order of magnitude coarser than our *Herschel*-derived column density map at $36''$. Thus, the dense cores, which correspond to the column density peaks, are washed out by the large beam in the extinction map. As such, the dense cores are not associated with the correct material. We note that the *Spitzer*-derived extinction map of Perseus at $180''$ resolution shows better agreement with the *Herschel*-derived column density map at $A_V \sim 8$ mag than the COMPLETE extinction map. The *Spitzer*-derived extinction map is able to probe more deeply into the higher extinction regions than the COMPETE extinction map. Additionally, deeper near-infrared extinction maps show a much better correspondence with *Herschel* column density maps (Johnstone et al., in preparation). Thus, dense cores correspond to the peaks in dust extinction, provided that the extinction data have sufficient spatial resolution and depth.

5.5.3 Starless Core Properties

Table 5.11 shows the mean and median values for temperature, density, mass, and deconvolved radius at 250 μm for the starless cores in each clump. Mass and temperature were determined from SED fitting to the $160 - 500$ μm bands, whereas density was calculated from the mass and source size at 250 μm, assuming spherical geometry. We note, that Table 5.3 gives the average clump properties whereas Table 5.11 gives the average starless core properties for each clump.

Table 5.11: Average Starless Core Properties

Clump	Cores	T[a] (K)	n[a] (10^5 cm^{-3})	M[a] ($M_\odot$)	R_d[a] (10^{-2} pc)
B1	54	12.7 / 12.6	3.2 / 0.48	0.8 / 0.4	3.1 / 2.8
B1-E	11	12.7 / 12.6	0.62 / 0.45	0.6 / 0.5	3.3 / 3.0
B5	21	11.6 / 11.2	8.1 / 0.33	0.6 / 0.4	3.1 / 3.0
IC348	87	16.4 / 14.5	9.6 / 0.36	0.5 / 0.2	3.1 / 2.8
L1448	27	12.4 / 12.0	1.3 / 0.64	0.5 / 0.3	2.6 / 2.7
L1455	53	12.0 / 11.4	7.7 / 0.50	0.7 / 0.3	3.0 / 2.7
NGC1333	44	11.0 / 10.6	71. / 2.5	1.0 / 0.5	2.2 / 1.8
Off Clump	161	13.3 / 12.9	0.96 / 0.31	0.6 / 0.2	3.2 / 2.8

[a]The mean value and median value, respectively.

We find similar average starless core temperatures of $11 - 12$ K for most clumps. The starless cores in IC348, however, are warmer than in the other clumps ($\sim 15 - 16$ K). Since the temperature uncertainties are $\lesssim 2$ K, from assuming $\beta = 2$, this difference in temperature is significant. One cause for the higher core temperature could be a higher local interstellar radiation field. Tibbs et al. (2011) measured a factor of ~ 4 higher interstellar radiation field towards IC348 compared to the rest of the cloud. This high interstellar radiation field has been attributed mostly the IC348 young stellar cluster, which include several B-stars, with possible influences from the Per OB2 association[4] (see also, Bachiller et al. 1987; Preibisch et al. 2003; Herbst 2008). Furthermore, in Table 5.3, we found that the average dust temperature in IC348 was ~ 16 K, similar to the average dust temperature of its starless cores and higher than the average dust temperatures in the other clumps. Thus, local

[4]The Per OB2 association is the second closest collection of OB stars and is situated behind the Perseus cloud. In particular, HD 278942, a B0 V star, is relatively near to IC348 and may be the cause of the gas and dust shell seen between IC348 and B1-E (see the blue ring in Figure 5.1; Tibbs et al. 2011).

environmental factors can affect the embedded starless core populations. We will explore the relationship between the young stellar cluster and core temperature more in Section 5.5.4.

We also find a large range of average starless core densities for the different clumps. The "off clump" and B1-E cores have the lowest densities, with mean and median values $< 10^5$ cm^{-3}. Since the B1-E region is very young, likely condensing into a first generation of dense cores, such low densities are not unsurprising (see Chapter 3). Similarly, the off clump sources are typically seen towards lower column densities (see Figure 5.12) and subsequently lower pressure environments, resulting in fluffier starless cores. Conversely, NGC1333 has the highest core densities, with a mean value of 7×10^6 cm^{-3}, which is roughly an order of magnitude higher than the other clumps. Since NGC1333 is a highly energetic region (Hatchell & Dunham 2009), it may also be relatively more turbulent, and as such, its cores may be compressed due to higher external pressures.

Higher core densities should shield the core from external heating, causing lower average temperatures. Figure 5.14 compares core density and temperature for all starless cores. We find that core density and temperature are anti-correlated, such that $T \sim n^{-0.18}$ for $n < 10^5$ cm^{-3}, regardless of location or dynamical state. Furthermore, the IC348 cores also follow this trend despite their higher average core temperatures. Recall, that we found starless cores with densities above 1×10^5 cm^{-3} more likely to be gravitationally bound and those below 1×10^5 cm^{-3} more likely to be gravitationally unbound. At high densities ($> 10^5$ cm^{-3}), the density-temperature relationship appears to flatten ($T \sim n^{-0.05}$ for $n > 10^5$ cm^{-3}). Dense starless cores are primarily heated by Galactic cosmic rays and the interstellar radiation field and primarily cooled by molecular line emission or long wavelength emission from dust. At densities of $n > 10^5$ cm^{-3}, the dust and gas are generally coupled, such that the molecular gas primarily cools via collisions with dust (Goldreich & Kwan 1974; Galli et al. 2002). At even higher densities (i.e., $> 10^6$ cm^{-3}), Keto & Field (2005) found relatively uniform central temperatures of $T \gtrsim 5$ K in starless cores due to compressive heating. Therefore, the flattening in the temperature-density relation at $n > 10^6$ cm^{-3} may reflect the transition where dense cores reach their minimum temperatures.

NGC1333 has the smallest, most massive, and densest cores on average. For the other clumps, we find similar average starless core masses and sizes of $\lesssim 0.5$ M$_\odot$ and ~ 0.03 pc, respectively, assuming distances of 235 pc. Hirota et al. (2008) and Hirota et al. (2011) derived distances of 235 pc to NGC1333 and L1448, respectively, using

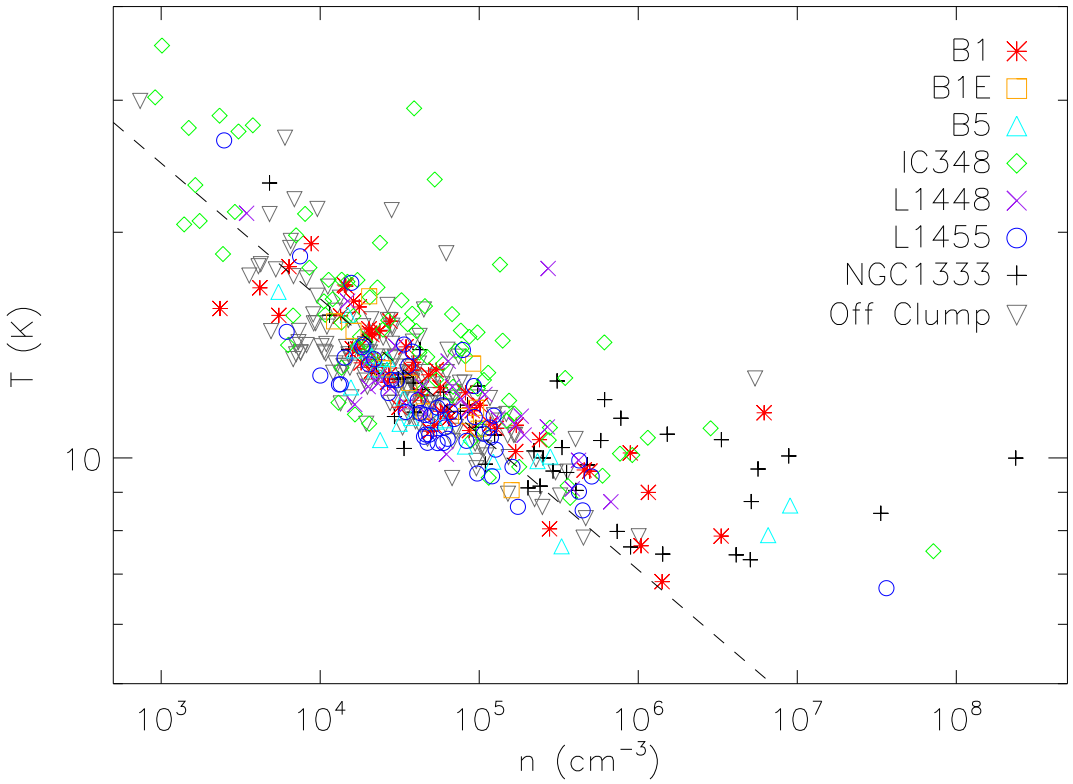

Figure 5.14: Comparison of starless core density and temperature with clump. The dashed line shows a linear least squares fit to the data for $n < 10^5$ cm^{-3}, with a slope of -0.18. At $n > 10^5$ the relation appears to flatten to -0.05.

very long baseline interferometers to observe the proper motions of water masers. While these measurements provide excellent distances for the Western clumps in Perseus, several studies have suggested that the Eastern IC348 clump may lie at a greater distance (e.g., Cernicharo et al. 1985; Herbig 1998; Ridge et al. 2006a). If the IC348 clump is more distant, its starless core population would appear smaller and with lower masses for the same starless core population at 235 pc. Table 5.11, however, demonstrates that the starless cores in IC348 have comparable masses and sizes to the rest of the Perseus clumps. Thus, we cannot conclude that IC348 is necessarily more distant than the other clumps in Perseus.

5.5.4 Starless Cores and Questionably Starless Cores

Since starless cores lack internal luminous sources, they are generally assumed to be isothermal. In general, cores are not perfect isothermal structures; they have warm

outer surfaces from external heating and cool inner envelopes due to shielding (e.g., Evans et al. 2001). (A protostellar core will have additional internal heating, which complicates the observed SED further, e.g., Launhardt et al. 2013). Thus, many cores will require multiple temperature components or models to fit such complex SEDs. With only five far-infared and submillimeter bands ($70-500$ μm), however, we could only measure the broad properties of our starless sources through single-temperature SED-fitting. Thus, we defined two distinct subcategories of starless objects; (1) starless cores which could be fit by a single-temperature blackbody function and (2) questionably starless cores which deviated from single-temperature dusty blackbody function.

Roughly 43% of all the starless *Herschel* objects were classified as questionable, with the highest fractions of questionable sources in IC348 and NGC1333 (see Table 5.8). Figures 5.15 and 5.16 show the distribution of all starless cores, questionably starless cores, and protostellar cores towards IC348 and NGC1333, respectively. For both clumps, the protostellar and questionably starless sources are generally clustered together. Thus, their excesses of questionably starless cores could be the result of confused emission from such complex environments. For example, in Section 5.5.3, we noted that the starless cores in IC348 have higher temperatures than the other clumps on average likely due to a higher local interstellar radiation field (Tibbs et al. 2011). Thus, the questionably starless cores could represent a population of cores with more complex SED profiles due to external heating. Nevertheless, NGC1333 also contains a rich young stellar cluster, including several late-type B-stars (Walawender et al. 2008), yet its starless cores have much lower average temperatures than the cores in IC348.

If the questionably starless cores represent populations of starless cores with more complex SED profiles due to external heating, we would expect to see warmer starless core temperatures towards the regions with large fractions of questionable starless cores. Figure 5.17 compares the distribution of all starless core temperatures in IC348 and NGC1333 with the distribution for the cores in the crowded regions of these clumps. We selected the crowded regions as follows; the section of IC348 with $3^h43^m \leq \mathrm{RA} \leq 3^h46^m$ and $31°55' \leq \mathrm{Dec} \leq 32°22'$ and the section of NGC1333 with $3^h28.5^m \leq \mathrm{RA} \leq 3^h29.5^m$ and $31°10' \leq \mathrm{Dec} \leq 31°30'$. These areas were selected to encompass the largest surface density of sources. For IC348, most of the high temperature starless cores are located within the crowded environment associated with the young stellar cluster, hinting that external heating from the cluster may

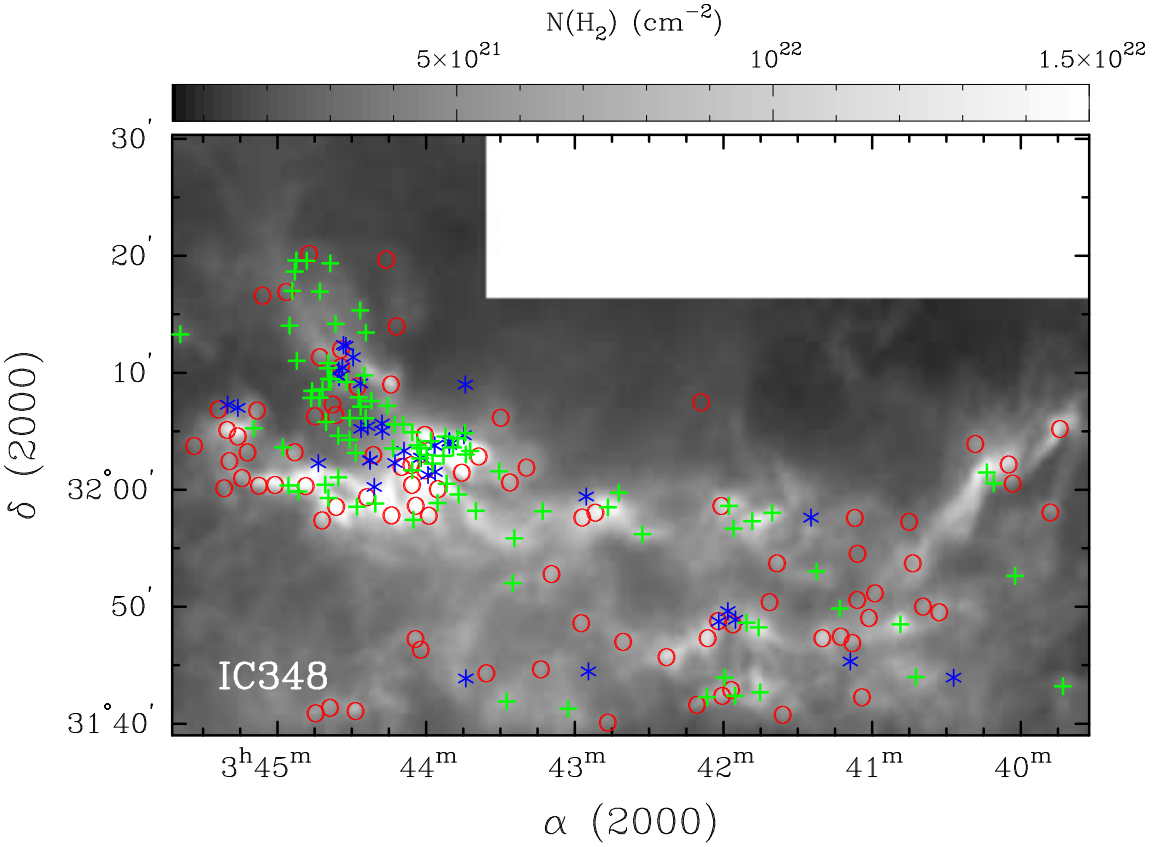

Figure 5.15: Locations of starless cores (red circles), questionably starless cores (green pluses), and protostellar cores (blue stars) towards IC348. The background image shows the column density map for the clump.

have affected the SEDs of the questionably starless cores. For NGC1333, however, we do not find a significant difference in temperature between the starless cores within the crowded region and the entire sample. Since the interstellar radiation field is relatively moderate for NGC1333 (Tibbs et al. 2011), the starless cores in NGC1333 may not have significant external heating.

Only the questionably starless cores in IC348 arguably have more complex SEDs due to external heating. For the other clumps, their questionably starless cores do not appear to be due to significantly increased external heating and their nature remains unclear. One possibility is that the questionably starless cores may correspond to line-of-sight blending of separate objects at different temperatures. Since most questionably starless cores are generally located in more crowded regions, emission from multiple overlapping sources will be more common. Alternatively, some questionably starless cores may correspond to line-of-sight artifacts or tentative sources, which we

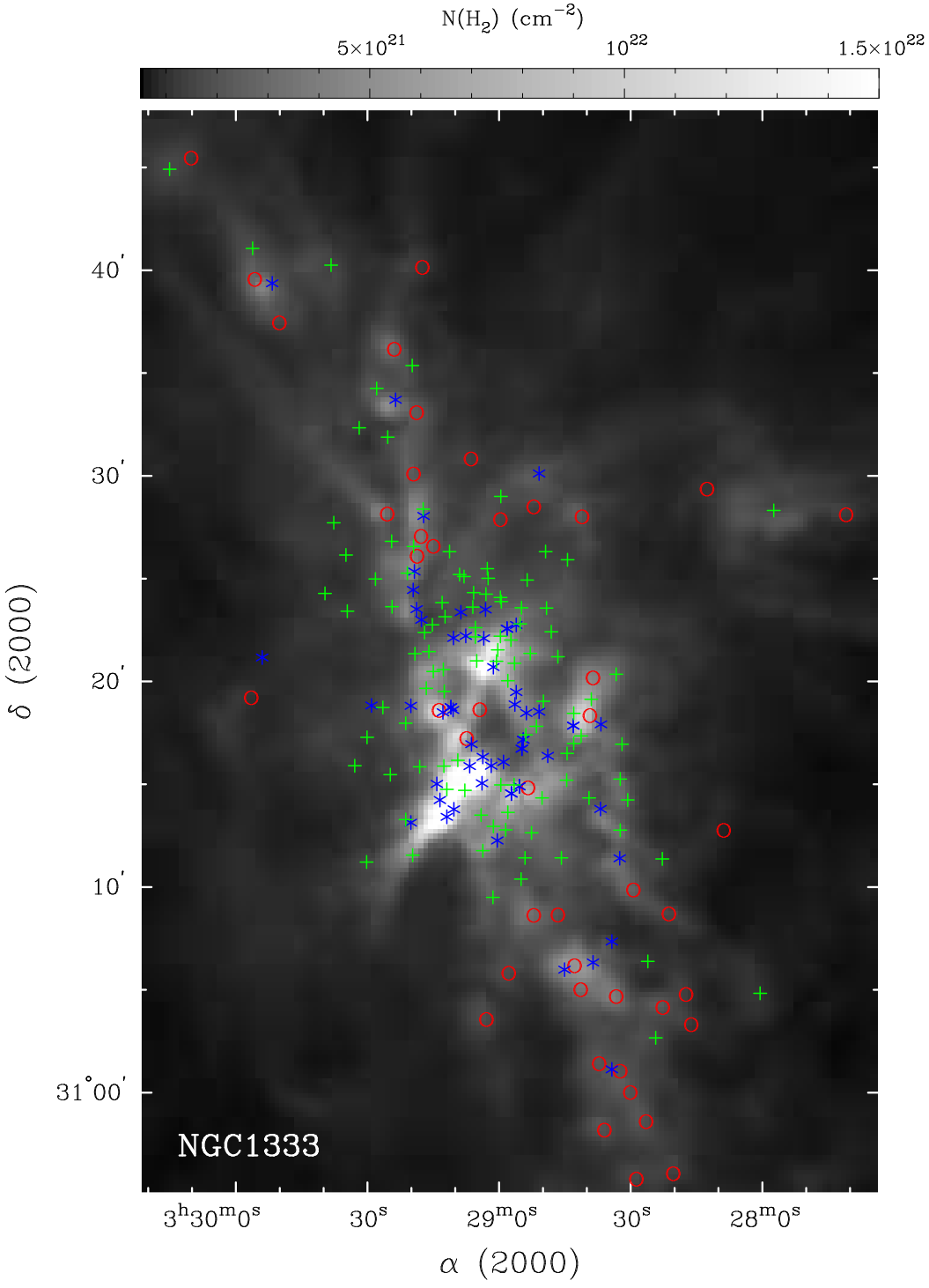

Figure 5.16: Same as Figure 5.15, but for the NGC1333 clump.

included for completeness. Ideally, we want to discard the unrelated fluffy aggregates or line-of-sight artifacts. A more conservative analysis of the core populations will be

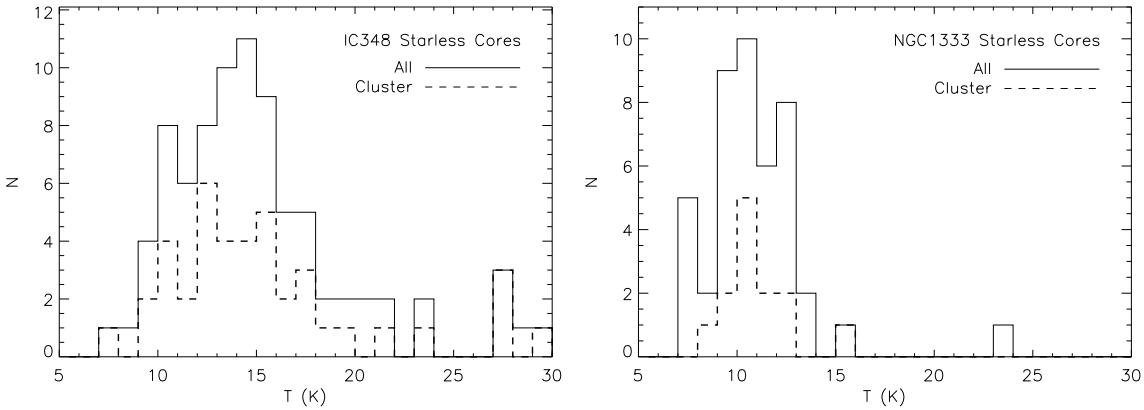

Figure 5.17: Distributions of starless core temperatures for IC348 (left) and NGC1333 (right). Core temperatures were measured from fitting the $160 - 500$ μm SED with single-temperature dusty blackbody functions. The dashed histograms correspond to the starless cores within the crowded areas in each clump (see text).

made for the first generation HGBS papers (Pezzuto et al., in preparation).

5.5.5 Protostellar Cores

We identified cores as starless or protostellar using the absence or presence of a compact 70 μm source or *Spitzer*-identified YSO. Since emission at 70 μm traces warm (internally heated) envelopes, it is a relatively good tracer of protostellar sources (Dunham et al. 2008). Diffuse emission, however, can contaminate the extraction at 70 μm, particularly for faint protostellar signatures (Bontemps et al. 2010). Since *getsources* uses information from all wavelengths to identify structures, the algorithm will seek to identify a source at 70 μm for all sources with strong detections at $\lambda = 160 - 500$ μm. Cold cores or faint protostars associated with diffuse emission will not have robust detections at 70 μm.

Since true protostellar signatures at 70 μm should be compact, we employed a separate set of criteria to identify compact 70 μm sources (see Section 5.4.2) and found good agreement between our criteria and a visual inspection of the 70 μm data. We added ten visually compact 70 μm sources by hand and removed five sources as non-compact 70 μm detections. Generally, we excluded compact 70 μm sources that were faint and failed to meet our signal-to-noise cut. With the combination of our criteria and visual inspection, we identified 112 Galactic compact 70 μm objects.

For comparison, other studies identified protostellar signatures through a signal-to-noise cut on the detected 70 μm emission or associated 24 μm emission (e.g.,

Könyves et al. 2010; Rygl et al. 2013). Had we imposed a similar signal-to-noise cut as these studies (SNR > 5 at 70 μm), we would identify 253 "protostellar signatures." Even with a higher threshold of SNR > 7 at 70 μm, we would measure 213 "protostellar signatures." These SNR thresholds include many sources associated with bright, diffuse 70 μm emission which are unlikely to be protostellar sources. Thus, one should be cautious when employing a SNR cut at 70 μm (see also Section 5.5.7).

In addition to the presence of compact 70 μm emission, we also identified protostellar cores using coincidences with infrared-selected YSOs from either the c2d catalogue or G09 catalogue, for a total of 126 *Herschel* objects associated with YSOs. Thus, 14 protostellar sources did not have compact 70 μm emission. These 14 sources are associated with NGC1333 and IC348, and most coincide with regions of bright diffuse emission at 70 μm that may confuse any faint protostellar sources. Furthermore, three of these YSOs are likely chance coincidences between Class II/III sources and dense cores (see Section 5.4.6). Figure 5.18 shows the observed SEDs for these three coincident YSOs. (Note that their 70 μm emission is not compact.) For comparison, we also show the observed SED for a Class 0 YSO and the expected SEDs of two starless cores. Two of the coincident YSOs resemble the warmer (22 K) starless core for $\lambda \geq 70$ μm; we have reclassified these sources as starless cores. The third coincident YSO resembles the Class 0 SED for $\lambda \geq 70$ μm, and may correspond to a protostellar core. Thus, out of all the likely early-stage YSOs in our sample, only one was not identified by compact 70 μm emission due to significant diffuse 70 μm emission.

Of the 112 YSOs identified by compact 70 μm emission, 19 did not have associated *Spitzer* detections. A *Spitzer* source could have been missed if it is (1) displaced from its natal core by more than ~ 0.01 pc ($8''$ at 235 pc), (2) was misclassified by either the c2d or G09 catalogues, or (3) is deeply embedded and thus, not detected with *Spitzer*. Generally, YSOs are found close to the submillimeter emission peak of the parent core (Jørgensen et al. 2007). Therefore, we do not expect large displacements, particularly for younger YSOs with well-detected envelopes. Of these 19 YSOs, we found that ten sources had no *Spitzer* objects of any designation within $8''$ in the c2d catalogue, and most of the remaining YSOs had *Spitzer* sources with "star" or "galaxy" designations. Since our *Herschel* objects were mostly associated with the highest column densities (see Section 5.5.2), we would not expect much background contamination (see Section 5.3.3). Only one source had a *Spitzer* object within $8''$ with a possible YSO-like designation of "rising" (see Table H.4).

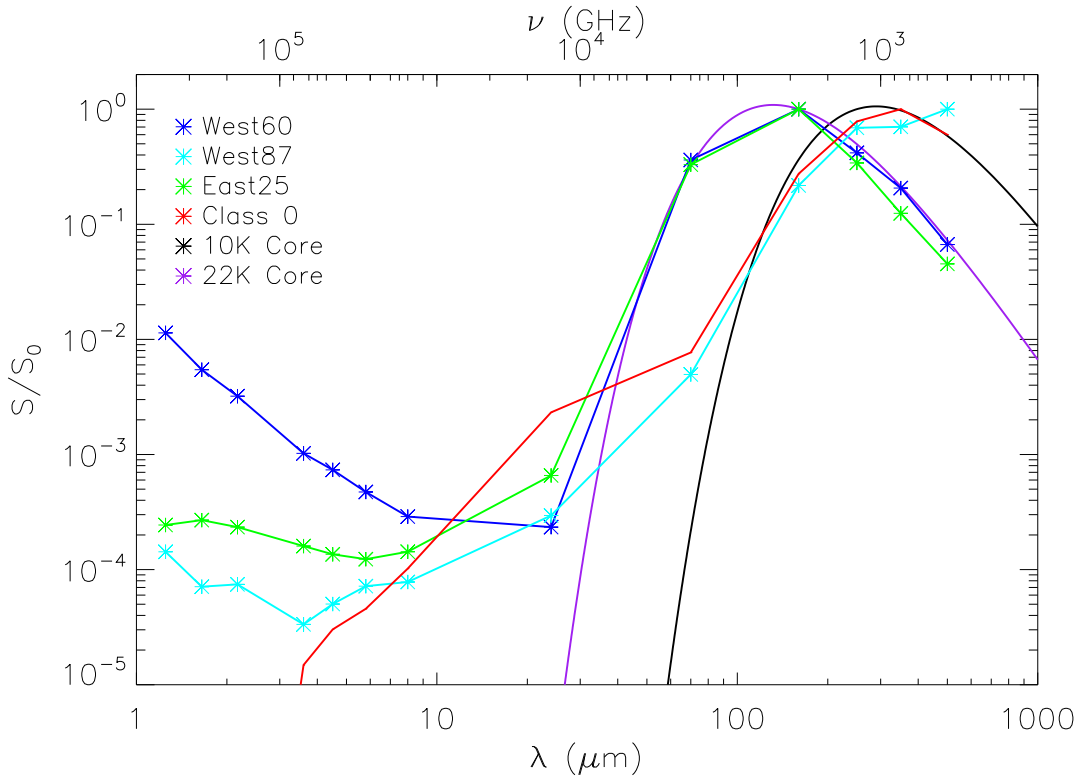

Figure 5.18: The SEDs of three YSOs likely to be coincident with dense cores that lack compact 70 μm emission. The three profiles are West60 (blue), West87 (cyan) and East25 (green). For reference, we include a Class 0 SED (red) associated with West162 (see also Figure 5.9a) and two dusty blackbody profiles representing starless cores at 10 K (black) and 22 K (purple). For the starless cores, we assume $\beta = 2$. All SED profiles have been normalized by the peak flux.

We have identified 18 YSOs based on compact 70 μm emission without corresponding *Spitzer* detections. Have we detected new, deeply embedded YSOs? Not all these objects have well-detected submillimeter emission indicative of envelopes, however. Of these 18 YSOs, 11 have undetected or noisy fluxes between $250 - 500$ μm. Half of these sources are in IC348, where the core population has higher temperatures on average (see Section 5.5.3). Since 70 μm emission from YSOs still originates primarily from the envelope, we consider compact 70 μm sources without well-detected envelopes or corresponding *Spitzer* sources to be unclear and require follow-up study. These objects are highlighted in Table H.4.

5.5.6 T_{bol} with Herschel

With *Herschel*, we are able to probe the peak of the SED for cold cores and younger YSOs. For example, Figure 5.7 shows peak emission of $\sim$ 300 μm for cores (or envelopes) at T $\sim$ 10 K, whereas Figure 5.9 demonstrates that far-infrared and submillimeter dust emission can exceed near-infrared emission by several orders of magnitude for Class 0 and Class I YSOs. Thus, the *Herschel* bands are key in measuring T_{bol} and L_{bol} for young objects.

We measured both T_{bol} and L_{bol} using 2MASS near-infrared (1.25 - 2.17 μm), *Spitzer* infrared (3.6 - 24 μm), and *Herschel* far-infrared and submillimeter (70 - 500 μm) wavelengths, taking the $\lambda \leq 24$ μm fluxes from either the c2d catalogue or the G09 catalogue. Despite the range in wavelength, we do not fully sample the SED of YSOs. In particular, we lack important long-wavelength emission ($\lambda > 500$ μm) for the young YSOs with envelopes (e.g., André et al. 1993; Visser et al. 2002). Additionally, we have a significant gaps between 8 μm and 160 μm. Depending on the SED shape, additional fluxes between $8 - 160$ μm would improve our ability to determine T_{bol} and L_{bol}.

Evans et al. (2009) included archival optical to millimeter wavelength data for their YSOs. For example, they supplemented their near-infrared and *Spitzer* data with observations from IRAS (25 μm, 60 μm, and 100 μm), SCUBA (450 μm and 850 μm), and Bolocam (1100 μm), when applicable. Thus, objects sampled with these additional detectors have excellent SED coverage. Unfortunately, detections with these other facilities were sparse. The IRAS instrument had poor resolution and sensitivity, and thus, was insensitive to faint, embedded sources. Conversely, the SCUBA and Bolocam instruments had good resolution and reasonable sensitivities, but these detectors only mapped key regions of Perseus. Thus, inclusions of IRAS, SCUBA, or Bolocam data to our *Herschel* observations will be incomplete. Since we are interested in the broad differences across Perseus, we need to compare regions in a uniform manner. Thus, we do not include archival data from other facilities here.

Figure 5.19 compares T_{bol} as measured here with the corresponding value given in the c2d catalogue. For the c2d data, we used updated T_{bol} measurements provided by M. Dunham (2013, private communication; see also Dunham et al. 2013). We typically obtain lower T_{bol} values by $\lesssim$ 100 K due to non-zero emission in the *Herschel* bands. Nevertheless, several YSOs have lower T_{bol} values by $\gtrsim$ 300 K. Most of these sources lacked (sub)millimeter from previous surveys (i.e., with Bolocam or SCUBA),

but were observed in all five *Herschel* bands. In particular, two of these sources had submillimeter emission > 10 Jy that dominated their SEDs. Conversely, we found a small fraction of sources with higher T_{bol} values (> 100 K) with the *Herschel* data due to different 70 μm measurements from *Herschel* than from *Spitzer*. Therefore, we found the *Herschel* data to be very significant to the measurement of T_{bol}.

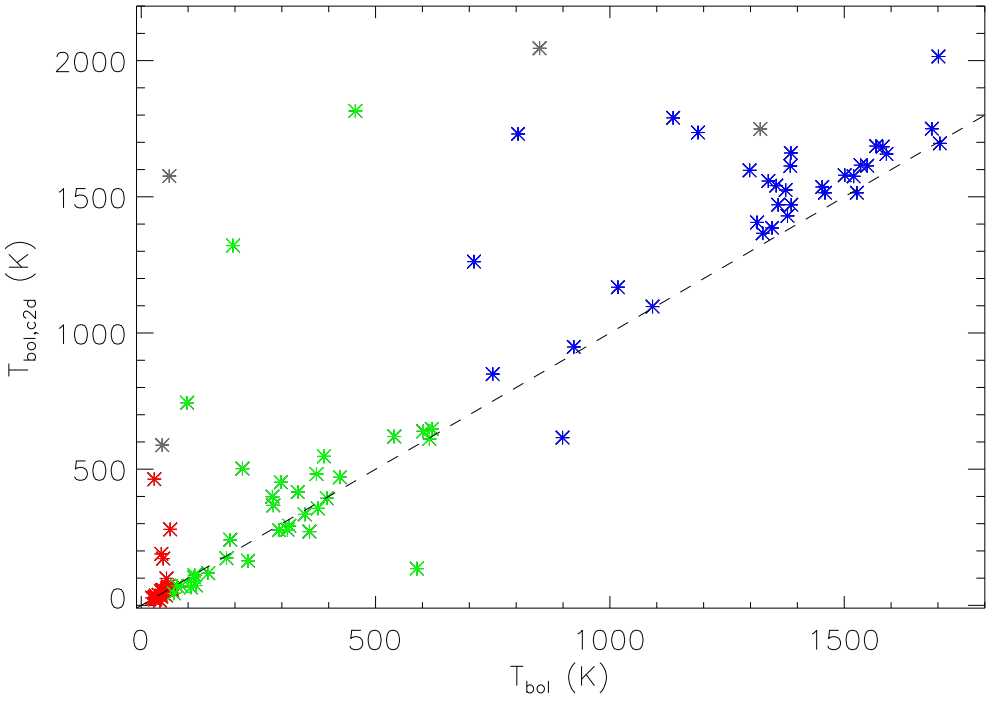

Figure 5.19: Comparison of T_{bol} from our analysis and from the c2d catalogue. A one-to-one correlation is shown as the dashed line. We show Class 0 YSOs in red, Class I YSOs in green, and Class II YSOs in blue based on our determination of T_{bol}. Sources in grey correspond to likely chance coincidences (see Section 5.4.6). Upper and Lower limits for T_{bol} are as indicated in the c2d catalogue.

5.5.7 L_{bol} with Herschel

In Section 5.4.6, we compared the YSO classifications from the infrared spectral index and T_{bol}. Here, we compare the classifications from T_{bol} and L_{smm}/L_{bol}, which is specifically aimed at identifying Class 0 YSOs (see Section 5.4.5). Most YSOs with *Herschel* detections were found to be young (Class 0 or Class I) using T_{bol}, yet relatively few Class 0 YSOs were identified as such by both T_{bol} and L_{smm}/L_{bol}. Table 5.12 compares the classifications from T_{bol} with those based on L_{smm}/L_{bol}. Of all the

Class 0 objects identified by T_{bol}, only 26% were also identified as Class 0 with the ratio of L_{smm}/L_{bol}. Thus, either T_{bol} overestimates the number of Class 0 objects or we are underestimating the Class 0 objects with L_{smm}/L_{bol}. Since our analysis includes data from $\lambda = 1.25 - 500$ μm, we may not measure well L_{smm} using just the 350 μm band and 500 μm band. Thus, our L_{smm}/L_{bol} ratios are likely lower-limits. With more complete observations at long wavelengths, we can obtain a better measure of L_{smm}.

Table 5.12: Comparison of YSO Classifications[a]

T_{bol}-Classification	Class 0	Class I	Class II
$L_{smm}/L_{bol} \geq 0.05$	16	3	0
$L_{smm}/L_{bol} < 0.05$	45	37	39

[a]For each infrared detection. Several *Herschel* sources have multiple detections.

The ratio of L_{smm}/L_{bol} is often used to identify very young objects (e.g., Stutz et al. 2013), which are often more deeply embedded. Thus, YSO signatures for these objects may be dominated by emission from external heating of the envelope rather than the central luminous source (Dunham et al. 2008) or not detected due to a thick envelope. Such faint sources may include FHSCs, which are at a theoretical, short-lived stage between prestellar core and Class 0 protostars (e.g., Larson 1969; Bate 2011). Recent theoretical studies suggest that FHSCs should have faint signatures at ~ 70 μm, but no detections for $\lambda \leq 30$ μm (Omukai 2007; Commerçon et al. 2012). Pezzuto et al. (2012) used *Herschel* observations to characterize two FHSC candidates, B1-bN and B1-bS, in Perseus. Figure 5.20 shows the 70 μm emission towards these FHSC candidates, B1-bN and B1-bS, with 450 μm data from SCUBA-2 (see Chapter 4) to highlight the dense cores. Neither B1-bN nor B1-bS have a compact 70 μm source, though, we do detect faint 70 μm excess towards B1-bS, though this emission may be confused by the nearby YSO, J033320.3+310721 (Pezzuto et al. 2012). (We note that this nearby YSO did not have an associated *Herschel* object.)

Pezzuto et al. (2012) included 100 μm PACS observations from PACS-only observations[5] in their study. Both B1-bN and B1-bS are detected at 100 μm. At $\lambda \geq 160$ μm, these two objects become blended. Since we lack the observations at 100 μm, the B1-bN and B1-bS FHSC candidates are combined into one core in our *getsources* extraction. Furthermore, since we did not identify a compact 70 μm source, B1-bN

[5]High extinction regions of the Gould Belt clouds were observed by *Herschel* in PACS-only mode to obtain higher resolution imaging at 100 μm and 160 μm.

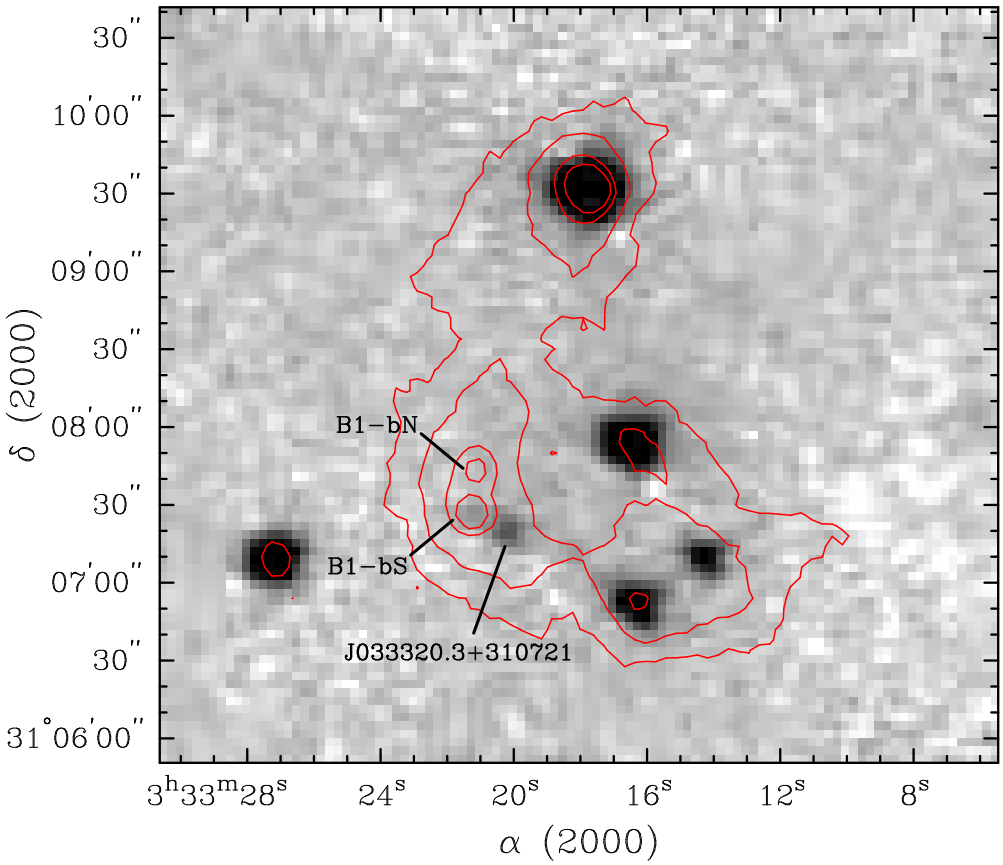

Figure 5.20: The central region of B1. The background image shows 70 μm emission. The red contours correspond to SCUBA-2 450 μm observations at 0.6, 1.0, 2.0, and 3.0 Jy beam^{-1}. The PACS data at 70 μm and SCUBA-2 observations at 450 μm have similar resolutions $\sim 8 - 9''$, and are able to separate out the two sources. The B1-bN and B1-bS cores are blended in the three SPIRE bands. The nearby YSO J033320.3+310721 is also labeled.

and B1-bS were classified as a single questionably starless core. Other FHSC candidates in Perseus are identified as either starless cores or questionably starless cores (see Chen et al. 2010; Enoch et al. 2010; Pineda et al. 2011; Schnee et al. 2012). Thus, FHSCs may be too faint to detect well with *Herschel* observations.

As in the previous Section, we are also interested in the influence of *Herschel* observations on L_{bol}. Figure 5.21 compares L_{bol} between this study and the c2d values (Dunham 2013, private communication; see also Dunham et al. 2013). We find that the older YSOs show the best agreement. These sources are likely dominated by the short ($\lambda < 24$ μm) wavelengths, thus the *Herschel* bands do not greatly affect the measured L_{bol}. For the Class 0 YSOs, however, we typically measure much higher (orders of magnitude) bolometric luminosities than the c2d catalogue. Since

the $160 - 500$ μm dominate the SED for embedded YSOs (e.g., see Figure 5.9a), the *Herschel* data are key to measuring L_{bol}. The c2d catalogue generally estimated L_{bol} for sources that lacked observations in these key bands, and thus, did not sample the SED peak. By excluding the peak emission, L_{bol} is greatly underestimated.

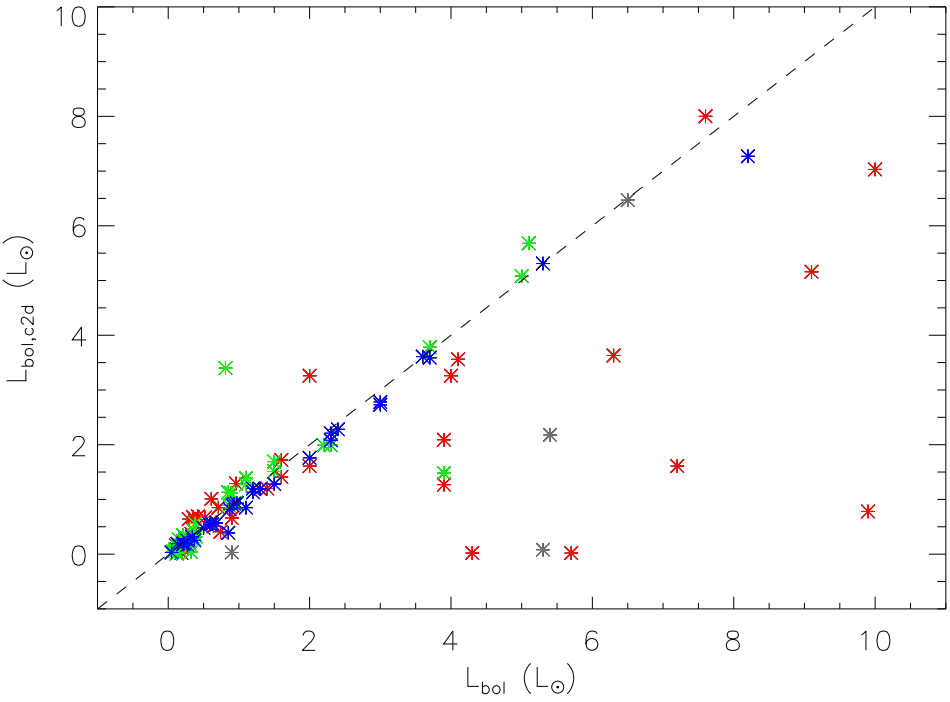

Figure 5.21: Comparison of L_{bol} from our analysis and from the c2d catalogue. Symbols are the same as Figure 5.19. The dashed line shows a one-to-one relation.

5.5.8 Global YSO Populations

Generally YSO and core lifetimes are determined by the number of objects detected in each group, where longer-lived stages will have more associated objects assuming a constant star formation rate. Nevertheless, one must assume all regions in question are similar, such that individual clump or cloud properties do not affect the ages or properties of the core and YSO populations. For example, an older region may contain an excess of Class II/III YSOs, whereas a younger region may contain an excess of starless cores or Class 0 YSOs.

We identified *Herschel*-associated YSOs as Class 0 or Class I using the T_{bol} classification method, regardless of the YSO classification from the infrared spectral index.

For all of Perseus, we identified 53 cores as Class 0 and 41 cores as Class I by their bolometric temperatures. Several of these cores contained multiple *Spitzer* detections. For simplicity, we count each core once. Furthermore, two Class 0/I YSOs were reclassified as starless due to likely chance coincidences between young envelopes and more evolved YSOs (see Section 5.5.5), for a total count of 92 Class 0/I YSOs.

We used the spectral index classification method to identify Flat, Class II, and Class III sources. We took the entire YSO sample from the c2d catalogue (651 objects) and the G09 catalogue (293 objects), for a total of 740 YSO candidates. We calculated the infrared spectral index for each YSO, correcting the fluxes for line-of-sight-extinction (see Appendix G). If a YSO was identified in both catalogues (204 YSOs in common), we took the average spectral index between both samples. For the most part, the spectral indices between the two catalogues agreed well. In most cases, discrepant spectral indices arose due to different adopted extinction measurements. Those YSOs identified towards regions with $N(H_2) < 2 \times 10^{21}$ cm^{-2} were excluded. The YSO catalogues may still include contamination, such as extragalactic sources or shock emission (M. Dunham 2013, private communication). While it is difficult to disentangle shock emission from protostellar signatures, we assume that faint extragalactic sources will be undetected towards the higher column densities associated with the clumps.

We found that only $\sim 25\%$ of our previously identified Flat spectral sources had associated *Herschel* emission. While Class 0 and Class I YSOs are in the most deeply embedded stages, Flat spectral sources are also generally considered embedded (e.g., Greene et al. 1994; van Kempen et al. 2009). The low *Herschel* detection rate suggests the Flat spectral stage may not be embedded in an envelope. Alternatively, extinction may be an issue. Most of our Flat spectral sources do not have direct measurements of the dust extinction. For these sources, we assumed $A_V = 5.9$. If the line-of-sight interstellar extinction is higher, the spectral index would decrease (and possibly reach Class II designations; see Forbrich et al. 2010). At this time, we cannot determine whether some Flat spectral sources are devoid of envelopes or are have been misclassified due to our assumed extinctions.

Similarly, we find 19% ($\sim$ 15% after removing likely line-of-sight coincidences) of our Class II sources are within $8''$ of a *Herschel* source. Moreover, only 7% (2% after removing likely line-of-sight coincdences) of our Class III sources are within $8''$ of a *Herschel* source. For both Class II and Class III objects, most of these *Herschel* sources are poorly detected, mostly due to low signal-to-noise values over most

Herschel bands (e..g., see Figure 5.9d). Since Class II objects can have prominent circumstellar disks, excesses at submillimeter wavelengths are not unexpected (e.g., Weintraub et al. 1989). Class III YSOs, however, are expected to have relatively little submillimeter excess from circumstellar disks. Likewise, we find that Class III sources are mostly unassociated with *Herschel* objects, though we do find several line-of-sight coincidences, whereas some Class II YSOs appear associated with *Herschel* detections.

Table 5.13 compares our YSO counts to those of Evans et al. (2009) and Gutermuth et al. (2009). As in these studies, we find significantly more Class II YSOs than sources in the other classes. In contrast, however, we find many more Class 0 and Class I objects. We find a combined Class 0/I count of 92 objects, whereas the previous studies found 75 and 29, respectively. (Recall that the G09 catalogue only included NGC1333 and IC348, and thus their counts will be intrinsically lower.) Thus, we find 16 additional (17%) Class 0/I YSOs compared to the c2d study. We note that this increase is similar to the number of YSOs identified with compact 70 μm that had no corresponding *Spitzer* detections (see Section 5.5.5).

Table 5.13: Comparison of YSO counts for Perseus[a]

YSO	Present Study	c2d	G09[b]
Class 0/I	92	75	29
Flat	66	34	32
Class II	232	232	168
Class III	80	41	35

[a]YSOs were defined from the extinction-corrected spectral index values using the boundaries given in Section 5.4.3. For the c2d measures, we used the updated results from Dunham (2013, private communication). We require all YSOs to be associated with material at $N(H_2) > 2 \times 10^{21}$ cm^{-2}.
[b]Includes NGC1333 and IC348 only.

With our number counts, we estimated a new combined Class 0/I lifetime of 0.8 Myr, assuming a Class II lifetime of 2 Myr. For comparison, Evans et al. (2009) found a Class 0/I lifetime of 0.62 Myr for just the Perseus sources (0.54 Myr for their entire sample). Using the updated extinction-corrected data (see Table 5.13, this lifetime becomes 0.64 Myr. Therefore, our results suggest $\sim 25\%$ increase in the lifetime of the Class 0/I YSOs. Previous measurements suggest shorter lifetimes (e.g., Wilking et al. 1989; Greene et al. 1994; Evans et al. 2009). For the Class 0/I lifetimes, we detected more sources due to improved sensitivity with *Herschel*. If we discard the 11 unusual YSOs with compact 70 μm emission but not significant submillimeter detections or

Spitzer YSOs (see Section 5.5.5), we have a much smaller increase in detected Class 0/I sources over the c2d results, and our estimated combined Class 0/I lifetime agrees better with the results from Evans et al. (2009). Thus, the longer lifetimes may be a real effect, but first we must verify the classification of our compact 70 μm sources.

More significantly, we measured a Flat spectrum lifetime of 0.57 Myr, which is a factor of 2 increase over the value given in Evans et al. (2009). The Flat spectrum sources, however, are more uncertain due to unmeasured extinction corrections; most of our identified Flat YSOs did not have direct measurements of the dust extinction, and thus, we assumed a mean value of $A_V = 5.9$ mag. This mean value may not apply well to all sources, however. For example, using the extinction values from Evans et al. (2009), we find a much higher mean extinction of $A_V \approx 6.7$ for NGC1333 using 54 YSOs, and much lower mean extinction values of $A_V \approx 2.9$ and $A_V \approx 3.9$ for B5 and L1455, respectively, based on only two YSOs each. With different extinction corrections, many of our Flat YSOs could be identified as Class I or Class II YSOs. Therefore, the increased lifetime for this stage is less certain. Improved interstellar extinction estimates are necessary to classify better the unembedded YSOs. We caution that the lifetimes measured here depend greatly on the number of Class II sources and the assumed lifetime of 2 Myr.

5.5.9 Core and YSO Populations with Clump

With *Herschel*, we now have the statistics to conduct a complete and uniform study of the starless core population in Perseus, and with complementary *Spitzer* observations, we expanded that study to include the YSO population. In Section 5.5.8, we characterized the YSO populations across all of Perseus. Here, we compare the starless core and YSO populations between the main clumps of our study.

Table 5.14 gives the high column density slope (see Figure 5.6) and the number counts for starless cores and the YSOs for each of the clumps. For the starless cores, we determined which cores were likely to be gravitationally bound based on our density threshold (see Section 5.4.3). For the YSOs, we list the number counts for each Class separately (see Section 5.4.5), considering only those sources coincident with material at $N(H_2) > 2 \times 10^{21}$ cm^{-2} ($A_V \gtrsim 3$). All source counts have been corrected for chance coincidences (see Sections 5.4.6 and 5.5.5). Figure 5.22 illustrates the population distribution for each of the clumps.

Figure 5.23 shows the fractional occurrence of starless cores and YSOs within each

Table 5.14: Core and YSO Populations in Perseus Clumps

Clump	slope[a]	Starless Cores		Young Stellar Objects				
		unbound[b]	bound[b]	0	I	Flat	II	III
B1	-2.3	39	15	6	4	8	10	3
B1-E	-9.6	10	1	0	0	0	0	0
B5	-2.9	15	6	0	2	1	0	0
IC348	-2.7	66	22	12	11	18	119	61
L1448	-1.5	17	10	5	0	2	0	0
L1455	-2.9	40	13	2	2	1	5	0
NGC1333	-2.0	18	27	22	16	22	85	15
Off Clump	···	137	24	5	5	14	13	1

[a]Slope for the high column density tail from the column density distributions shown in Figure 5.6.

[b]We use the average density to determine which objects are likely to be bound and which are not. Bound cores have $n \geq 1 \times 10^5$ cm^{-3}, whereas unbound cores have $n < 1 \times 10^5$ cm^{-3}.

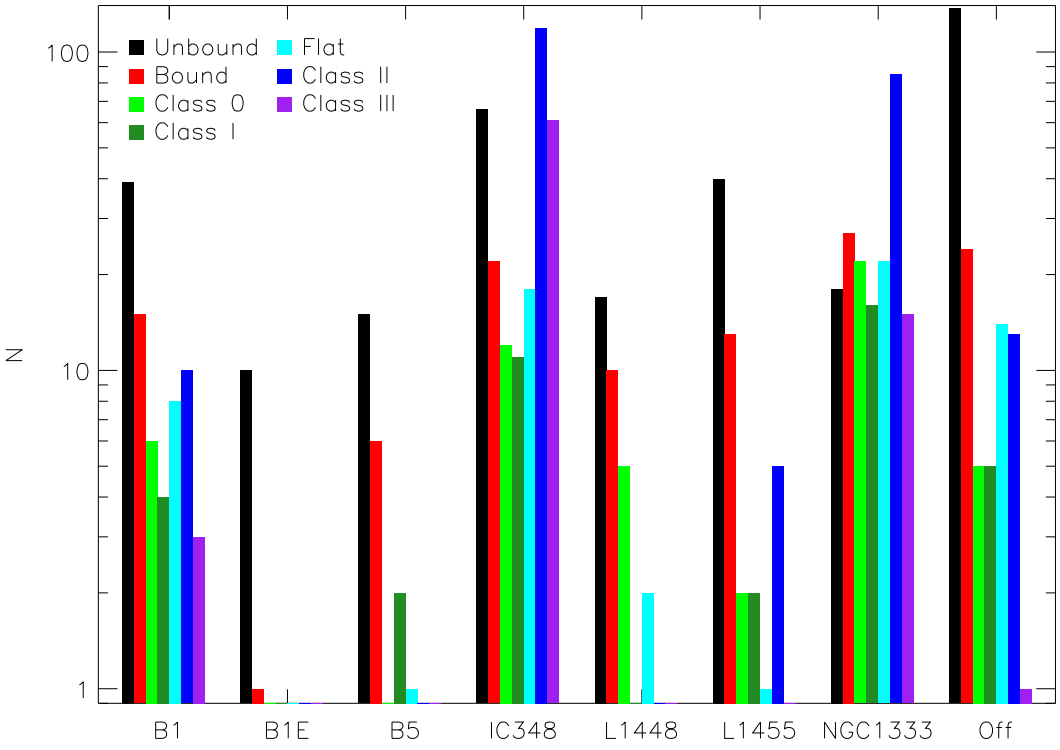

Figure 5.22: Core and YSO populations in the Perseus clumps and "off clump". Starless cores are divided into unbound (black) and bound (red) according to their average density (see Section 5.4.4). The YSO populations are divided into their separate Classes in order of Class 0, Class I, Flat, Class II, and Class III. For clarity, the populations are arranged by evolutionary state.

clump using the number counts from Table 5.14. B1-E contains a clear overabundance of unbound starless cores compared to the other clumps. Furthermore, B1-E is the only clump without a YSO population, which supports the view that the B1-E region is very young and likely fragmenting into a first generation of dense cores (see also Chapter 3). For example, the B1-E clump is most similar in mass and size to B5 and L1448, which are both actively forming stars. If B1-E had the same core and YSO populations as B5 or L1448, we would expect it to have $1-2$ YSOs. B1-E has the lowest average column density (see Table 5.3) and the steepest high column density slope of all clumps. Since many studies have shown that bound cores and YSOs are generally associated with supercritical filaments or high extinction regions (e.g., Kirk et al. 2006; André et al. 2010; Lada et al. 2010), B1-E may lack the dense material necessary to form stars.

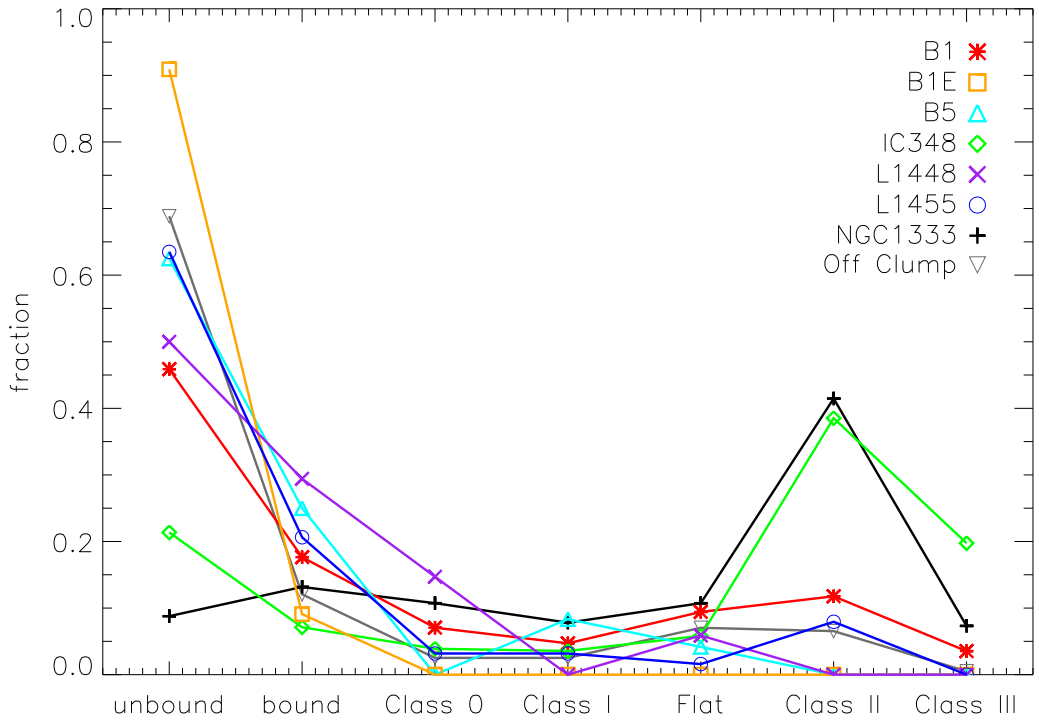

Figure 5.23: Fractional occurrence of source classifications in each Perseus clump. We consider starless cores (bound or unbound) and YSOs only. Fractional occurrence is measured as the instances for a given classification normalized by the number of detections for each clump.

Both IC348 and NGC1333 have a clear spike in Class II sources compared to the rest of Perseus. IC348 and NGC1333 also have the highest YSO number counts and

both large, high-mass clumps (see Table 5.3). Furthermore, IC348 has an overabundance of Class III objects compared to the other clumps. Thus, high-mass clumps are most likely the first to contract and form stars, whereas smaller, less massive clumps may be delayed. Smaller clumps such as B1-E, B5, and L1455 each have relatively large fractions of starless cores, suggesting that these regions have only begun to form their YSO populations. In contrast, B1, IC348, and NGC1333 have the smallest fractions of starless cores. Thus, star formation towards these clumps may be ramping down, whereas star formation towards B1-E, B5, and L1455 may be ramping up.

The B1-E, B5, and L1455 clumps each have the steepest slopes in their column density distributions, indicating that these clumps have less high column density material. Conversely, L1448 and NGC1333 have more shallow slopes at high column densities. L1448 and NGC1333 also have the highest fractions of bound starless cores and Class 0 YSOs. Figure 5.24 compares the high column density slope for each clump with the fraction of Class 0 YSOs. We find a good correlation, where the fraction of Class 0 YSOs drops with steeper slopes. (We note that this broad trend does not change if we included bound starless cores, though the correlation becomes less tight). We found a linear least squares best-fit slope of ~ 0.1 for our data (excluding B1-E). Since most studies use the global YSO properties, different age populations are mixed. Thus, we demonstrate a strong trend between the fraction of young (Class 0) sources and the high column density slope for the first time.

Previously, the high column density tail was used as a measure for star formation activity. Regions that had column density distributions that resemble log-normal functions were thought to be relatively inactive, whereas regions with prominent column density tails (i.e., those that deviate from a log-normal distribution), were actively forming stars (e.g., Kainulainen et al. 2009; Kainulainen et al. 2011; Schneider et al. 2012). Recent simulations by Ballesteros-Paredes et al. (2011) demonstrated that as molecular clouds evolve, their column density distributions broadened due to gravitational contraction, eventually forming power-law tails.

We suggest that the high column density tail reflects more recent star formation activity rather than the star formation history of the clump, where clumps with recent bursts of young YSOs have shallower slopes. For example, IC348 has the most YSOs detected of all clumps, but its slope was relatively steep. IC348 also has a lower fraction of Class 0 sources than most other clumps. Thus, clumps require significant fractions of high column density material to form additional generations of YSOs. Extrapolating our linear relation suggests that column density slopes of $\gtrsim -3$ are

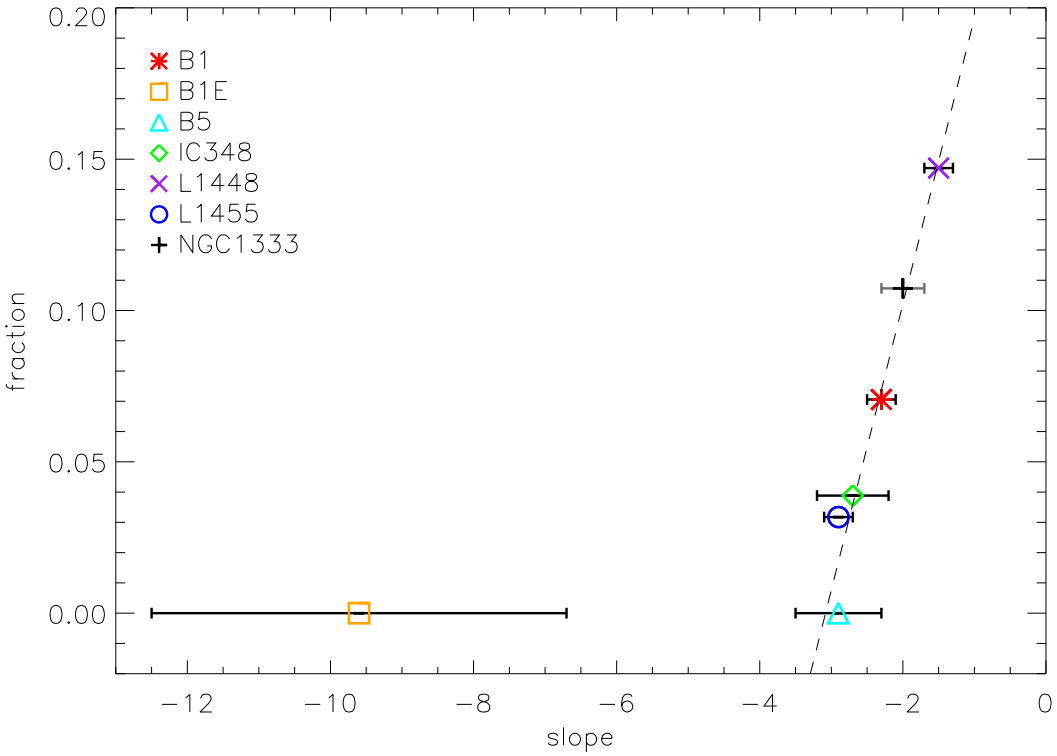

Figure 5.24: Comparison of high column density slope from Figure 5.6 with the fraction of Class 0 YSOs in each clump. The dashed line corresponds to a linear least squares best fit to the data (excluding B1-E). We find a best-fit slope of ~ 0.1. The error bars indicate the robustness of the high column density slope (see Section 5.4.1).

necessary to promote new star formation. This concordance excludes systems such as B1-E, however. In Figure 5.24, B1-E is a clear outlier. Although B1-E is arguably young, it has a very steep slope, suggesting that there is little material at high column densities and thus, it cannot form new stars at this time. Whether the formation of a first YSOs leads to enhanced compression (thereby forming a high column density tail) or whether the compression and formation of a high column density tail promotes the first YSOs is unclear. It is possible that both processes happen concurrently.

Finally, we caution that some of our clumps have small number statistics. In particular, B1-E and B5 each have less than 30 sources, and L1448 has only 34 sources. Conversely, the NGC1333 and IC348 clumps have > 200 objects, each. The trend in Figure 5.24 agrees with clumps containing many and relatively few objects, and thus appears relatively robust. Nevertheless, some of the fractional comparisons in Figure 5.23 may be biased due to small numbers.

5.6 Summary

We have analyzed the relationship between star-forming clumps and their embedded populations using *Herschel* observations at $70 - 500$ μm of the Perseus molecular cloud. These data constitute the most complete submillimeter observations of the Perseus cloud to date. We used *getsources* to identify sources in the *Herschel* data and measure their properties. Furthermore, we used archival *Spitzer* catalogues to characterize the YSO populations. We used the presence or absence of either a compact 70 μm source or an associated *Spitzer* source to classify our *Herschel* sources as protostellar or starless, respectively.

Our analysis indicates that the clumps in Perseus have different core and YSO populations. The core properties appear to relate directly to the clump properties, such as the local interstellar radiation field of the quantity of dense material, whereas the YSO populations appear to depend more on the quantity of dense material and when the clump first formed stars. We summarize our main findings as follows:

1. Most *Herschel* starless cores are coincident with material above a column density threshold of $N(H_2) > 3.4 \times 10^{21}$ cm^{-2} ($A_V > 5$; see also Kirk et al. 2006). Furthermore, the cores are associated with peaks in their local column density distribution, where bound starless cores are typically found towards higher column densities than the unbound starless objects. Similarly, cores found in clumps typically have higher column densities than those found "off clump." In the "off clump" regions, the unbound starless cores outnumber bound starless cores by a factor of 6, which is much more significant than for the "on clump" populations.

2. Starless cores associated with regions of higher column density are generally denser, suggesting that they are compressed due to higher external pressures (Kainulainen et al. 2009). For example, the starless cores in NGC1333 were the smallest and densest on average, and the NGC1333 clump is also very turbulent possibly due to many large-scale outflows (i.e., Hatchell & Dunham 2009). Furthermore, we found that the denser starless cores were cooler than the less dense cores. We interpreted this relationship as evidence of increased shielding with density. Conversely, IC348 appears to be influenced by a high, localized interstellar radiation field, which causes higher starless core temperatures.

3. Overall, the presence of a *compact* 70 μm source is a good indication of a

protostellar core. We found that using a SNR cut at 70 μm often identified diffuse emission as a protostellar signature and missed visually compact sources with lower SNRs. Using compact 70 μm sources will likely miss FHSCs, however, due to their expectedly very weak 70 μm emission. Compact 70 μm sources may also be missed towards regions of bright, diffuse 70 μm emission. Therefore, caution is needed when classifying *Herschel* cores towards clouds with warmer ambient material.

4. We measure a Class 0/I combined lifetime of 0.8 Myr, assuming a Class II lifetime of 2 Myr. This lifetime is $\sim 25\%$ larger than the Class 0/I lifetime given by Evans et al. (2009). We also found a very significant fraction of Flat spectral sources, resulting in a factor of 2 increase for the Flat Class lifetime. Furthermore, most Flat YSOs did not have associated *Herschel* objects, suggesting that Flat YSOs may not be embedded. Since most of our Flat YSOs did not have direct interstellar extinction measurements, these objects may instead be misclassified due to poor extinction corrections.

5. Clump mass and size appears to determine when the star formation process begins. We find that the largest, most massive clumps have the highest fractions of older YSOs (i.e., Class II sources) and relatively low fractions of starless cores, whereas the smallest, least massive clumps have the highest fractions of unbound cores. Clumps with shallow high column density tails (i.e., more high column density material) have high fractions of Class 0 YSOs, whereas those with steep tails have lower fractions or no detected Class 0 YSOs. Thus, the quantity of high column density material in a clump reflects the recent star formation activity rather than the star formation history of the clump.

Due to a lack of available kinematic data, we classified starless cores as bound or unbound using an estimated boundedness threshold density of $n_{th} = 1 \times 10^5$ cm^{-3}, where cores with $n \geq n_{th}$ were likely bound and those with $n < n_{th}$ were likely unbound. In the absence of molecular line data, this limit appears to provide a good estimate of core states. Nevertheless, a complete sampling of the kinematic and temperature information for all starless cores would improve our analysis. Our analysis also lacks observations at $\lambda > 500$ μm, which are crucial for determining the dust properties from cold, dust emission. In the absence of such information for all cores, we assumed a fixed dust opacity law. Sources that deviate from this dust

opacity law will have inaccurate mass measurements. Thus, both kinematic data and long wavelength data are necessary to obtain the physical properties and dynamic states of starless cores.

We also included the complete source extractions from *getsources*, whereas future source catalogues will only include the robust source detections. Detection quality, however, varies with the diffuse background such that sources located towards bright diffuse backgrounds are more difficult to detect well. By including the less robust objects, we were able to trace which YSOs had submillimeter excesses and which did not. The more evolved YSO Classes in particular were associated with only poorly-detected (low significance) *Herschel* sources except in cases of likely coincidence. We also identified a number of interesting sources for follow-up studies, such as the "questionably starless cores" and the compact 70 μm sources with neither corresponding submillimeter emission (envelopes) nor *Spitzer* YSOs. Since many of our questionable cores are not robust detections, we expect them to be discarded with future analyses for the First Generation study that compares the extraction results from *getsources* and other algorithms (i.e., *cutex* and *csar*). Nevertheless, the correlation between the questionably starless cores and the crowded environments of IC348 and NGC1333, suggest that these may objects reflect their environment and thus, are interesting for follow-up study.

The YSO populations suggest a significant fraction of Flat spectral sources. Since most of these YSOs did not have direct extinction measurements, we assumed an average extinction of $A_V = 5.9$ and thus, may have misclassified these sources if the true interstellar extinction varies from this value. In Appendix G, we demonstrate a significant scatter from $A_V = 5.9$. Furthermore, the mean A_V varies from clump to clump. Thus, improved extinction measurements and statistics for our YSOs are necessary to determine the interstellar extinction for the YSOs in each clump.

We also need to expand this study to determine if the trends between YSO and core populations with clump properties we observe for Perseus are common. Notably, Perseus is not forming high-mass stars. Therefore, it is important to survey other clouds with different environments and star formation histories. While the Perseus clumps constitute different environments themselves, several have small samples of cores and YSOs. For these clumps, it is difficult to conclude that the trends we observe are robust or are a product of small number statistics. With the full *Herschel* Gould Belt Survey, we will be able to explore the relationship between source populations and clumps in a large variety of clouds and environments.

Chapter 6

Conclusions

Herschel provides an unique opportunity to probe simultaneously the complete dense core populations and the extended cloud structure for the Perseus molecular cloud. This thesis utilized such observations from *Herschel* to generate the most complete catalogue of its starless cores in Perseus to date. These data also allowed us to compare and contrast how star formation is proceeding in its seven main clumps. We outline the results of this thesis and their impact in the field of star formation here.

1. Catalogues of Starless Cores and Young Stellar Objects

We classified the *Herschel* sources identified by *getsources* as starless or protostellar based on the absence or presence of protostellar signatures (see Section 5.4.3). For the starless cores, we further classified them as bound or unbound. In Chapter 3, we demonstrated that the sources in the B1-E clump were mainly turbulent and should not be identified as bound structures. Unfortunately, we lacked dynamical information for most of the remaining *Herschel* sources, and required a different diagnostic to estimate boundedness. In Section 5.4.4, we used the average density to characterize boundedness in the absence of kinematic measurements. Conversely, many previous *Herschel* studies without dynamical information used either the critical Jeans mass or critical Bonnor-Ebert mass to estimate boundedness (e.g., André et al. 2010; Könyves et al. 2010). These critical masses do not strictly apply to turbulent cores, however. Had we used either the Jeans mass or Bonnor-Ebert mass to determine boundedness for the B1-E sources, we would have misidentified several as being bound objects. The average density, however, matched our results from kinematic measurements. Thus, the average density may be a better diagnostic for boundedness than either the Jeans

mass or the Bonnor-Ebert mass.

For the protostellar sources, we used compact 70 μm emission and associations with *Spitzer*-identified YSOs to classify our sources. We found that compact 70 μm emission was an excellent signature of protostellar activity, whereas a simple signal-to-noise ratio cut at 70 μm greatly overestimated the number of protostellar sources. Furthermore, we identified 18 sources of compact 70 μm emission without corresponding *Spitzer* detections. These sources may be deeply embedded YSOs or very young sources, indicating that *Herschel* detections can identify YSOs missed by *Spitzer*. Nevertheless, faint compact 70 μm emission can be obscured towards regions of bright diffuse 70 μm emission. Indeed, 14 YSOs had *Spitzer* detections without compact 70 μm emission. Thus, the combination of compact 70 μm sources and *Spitzer* sources can better establish the evolutionary state of dense cores than either method alone. For very young sources, such as FHSCs, however, we were unable to use either compact 70 μm emission or *Spitzer*-selected YSOs to identify these objects. Other diagnostics, such as 100 μm emission (Pezzuto et al. 2012) are needed to classify these sources. Furthermore, care is needed when classifying sources in clustered environments. We found several cases of chance coincidences between more evolved YSOs and younger envelopes. Therefore, SED shapes also need to be considered.

We used the bolometric temperature to identify early-stage YSOs (Class 0, Class I) and the infrared spectral index to identify later-stage YSOs (Flat, Class II, Class III). Using these classifications, we generated new number counts for each YSO class and found new lifetimes (see Section 5.5.8). Assuming a lifetime of 2 Myr for the Class II YSOs, we find a combined Class 0/I lifetime of 0.8 Myr, which is 25 % longer than previous estimates by Evans et al. (2009). We also find a longer (factor of two) Flat and Class III YSO lifetime. Nevertheless, Flat, Class II, and Class III YSO classifications are greatly affected by their interstellar extinction corrections. (Class 0 and Class I SEDs are dominated by emission in the far-infrared and submillimeter and for their bolometric temperatures extinction is negligible; whereas for Flat, Class II, and Class III YSOs, identifications by the infrared spectral index can have vary significantly with extinction corrections.) Since we did not have extinction measurements for most YSOs, the longer Flat and Class III lifetimes are uncertain. For the Class 0/I lifetime, however, our results suggest that previous studies missed many sources, and subsequently underestimated their lifetimes.

The sources identified here correspond to a first-look analysis for the Perseus cloud.

A more extensive source extraction will be completed for the First Generation study from the HGBS consortium (Pezzuto et al., in preparation), and will include only robust sources. Indeed, most core population studies with *Herschel* focus on robust detections (e.g., Könyves et al. 2010; Winston et al. 2012; Rygl et al. 2013). Conversely, we considered all extracted *Herschel* sources irrespective of their detection quality (see Chapter 5). As such, we were able to test which YSOs had associated submillimeter excesses. We found that all early-stage YSOs had prominent submillimeter detections, whereas later-stage YSOs had little to no submillimeter emission, as expected. Nevertheless, only a quarter of our Flat YSOs had *Herschel* detections. Since Flat YSOs are often considered embedded, our results suggest that this stage is less embedded than expected. Had we only selected the well-detected *Herschel* sources, we would have found no submillimeter excesses for later-stage YSOs, except in cases of likely coincidences, and would be unable to make any conclusions about the envelopes of Flat YSOs. Certainly, for source catalogues robust detections are ideal, nevertheless, less robust objects can still be interesting.

2. Comparisons of Core and YSO Populations with Host Clump

The second goal of this dissertation was to compare and contrast the starless core and YSO populations in each clump to determine if star formation was proceeding differently between them. First, we identified the B1-E clump as a very young region likely fragmenting into a first generation of dense cores in relative isolation (Chapter 3). Such a region has not been identified before and offers the unique opportunity to study core formation without influences from stars or outflows, which may otherwise change the turbulent motions in the region. Based on our observations, we suspect B1-E may be influenced by a strong, localized magnetic field, but future observations are needed explore this possibility. Thus, Chapter 3 reveals an excellent target to understand how ambient clump material condenses into cores. In particular, follow-up observations of the turbulent velocities and magnetic field in B1-E can provide valuable comparisons and constraints to core formation models.

Second, we tested the common assumption of a fixed dust opacity law as used in *Herschel* studies of star-forming regions using complementary long wavelength data (Chapter 4). We found that such long wavelength data constrained better the model fits to the dust emission than just the *Herschel* data alone. Furthermore, we demonstrated that the dust properties varied towards the dense cores compared to the

ambient clump material, suggesting that dust grains have evolved between the clumps and cores. Thus, long wavelength data are critical to obtain the physical properties and dynamic states of dense cores. Nevertheless, such information is unavailable for all of Perseus. We found that in the absence of long wavelength data, assuming a reasonable dust opacity law provides a decent first estimate of source properties. Thus, Chapter 4 demonstrates that dust models with an assumed fixed dust opacity law still provide meaningful results. Since most *Herschel* studies in the literature (and other sections of this thesis) make these assumptions, this study is critical. Furthermore, Chapter 4 demonstrates a new method to combine filtered ground-based long wavelength observations with unfiltered *Herschel* data, and this method can be utilized in future studies.

Finally, using the results from Chapters 3 and 4, we characterized the seven main Perseus clumps and their source populations in a uniform manner, linking source populations to their parent clump properties for the first time. Previous studies either lacked the ability to resolve dense cores or could not recover the diffuse emission associated with the clump. Thus, Chapter 5 represents the first case where clumps and cores were characterized with the same observations in an uniform manner. Chapter 5 also includes the most complete sampling of starless cores in Perseus to date.

In Chapter 5, we found that several localized clump properties could affect their embedded source properties. We outline these differences below:

1. The IC348 clump is influenced by a high local interstellar radiation field (Tibbs et al. 2011), which in turn has raised the temperature of the clump and its core populations. Thus, the young stellar cluster of IC348 (and perhaps the nearby B0 star, HD 278942) are influencing both the clump and the starless core properties in IC348.

2. The starless cores in NGC1333 were the smallest and densest on average. The NGC1333 clump is also very turbulent possibly due to many large-scale outflows (i.e., Hatchell & Dunham 2009). The resulting higher pressure may be the cause of the highly compressed starless cores in this clump compared to the other clumps.

3. Both IC348 and NGC1333 have high fractions of questionably starless cores towards their clustered regions, suggesting that the temperature structure of sources in clustered environments be more complicated than for the other clumps.

For example, sources with cool interiors and warm exteriors may not be well-fit by the single-temperature models employed here. For IC348, these objects may be complicated by external heating from the local interstellar radiation field, but we find no evidence of external heating for the cores in NGC1333, however.

4. IC348 and NGC1333 contain the highest fractions of Class II and Class III YSOs. The B1 clump had the next highest Class II fraction, but at a factor of two lower than IC348 and NGC1333. These three clumps are also the largest and most massive in Perseus. As such, it appears that the first YSOs formed towards the larger and more massive clumps.

5. IC348 and NGC1333 also have the lowest fractions of starless cores, suggesting that their star formation is likely slowing down. Conversely, B1-E, B5, L1448, and L1455, which are small lower-mass clumps, each have high fractions of starless cores, suggesting that their star formation has only begun.

6. B1-E is an unusually young region that has yet to form a single YSO. For example, B1-E clump has a similar mass and size to B5 and L1448, whereas the latter two are actively forming stars. If B1-E had the same type of populations as B5 or L1448, we would expect it to have $1-2$ YSOs. We propose that star formation in B1-E is delayed by a strong, localized magnetic field (see Chapter 3).

7. The L1448 clump has the highest fractions of bound starless cores and Class 0 YSOs. This clump also had the shallowest slope at high column densities in its column density distribution (see Figure 5.6). Clumps with shallow high column density tails have higher fractions of Class 0 YSOs, whereas those with steep tails have lower fractions or no detected Class 0 YSOs. Thus, the quantity of high column density material in a clump reflects the recent star formation activity.

These results suggest that the amount of high column density material, overall clump mass, and local influences such as a high interstellar radiation field or a strong local magnetic field can all affect the the observed properties of dense cores with clumps and the population types (i.e., onset of star formation) within the clump. Furthermore, we found a clear trend between the fraction of young sources and the high column density tail. While several previous studies showed that most clouds and

clumps have prominent high column density tails, where those with more prominent tails have more active star formation (Kainulainen et al. 2009; Kainulainen et al. 2011; Schneider et al. 2012), this work demonstrates that the relation does not reflect the star formation history of a clump. The IC348 clump has a prominent late-stage YSO population, but its high column density tail is relatively steep indicating it has relatively less high column density material. Conversely, L1448 is a smaller clump with few YSOs but high fractions of early-stage YSOs and a very shallow high column density tail.

We also found many similarities between the clumps and their populations. We outline these similarities below:

1. Starless cores were typically coincident with the peaks in the column density, with cores found "on clump" at higher column densities than those found "off clump" on average. Furthermore, bound starless cores were generally associated with higher column densities than unbound starless cores.

2. Starless cores associated with regions of higher column densities were generally denser. Thus, the density of the starless clumps depends on how material is distributed within their parent clump. For example, cores located towards higher column densities may be more compressed due to higher external pressures.

3. Denser starless cores are better shielded from their local interstellar radiation field, which lowers the overall core temperature. For very dense cores ($\gtrsim 10^6$ cm^{-3}), this density-temperature relationship flattens, suggesting that a minimum core temperature is achieved. These trends appear consistent across all clumps, regardless of the local interstellar radiation field.

4. Most clumps had very similar average core sizes. While it has been suggested that IC348 is more distant (e.g., Cernicharo et al. 1985; Herbig 1998; Ridge et al. 2006a), we find no evidence of a greater distance based on the average apparent core size.

Thus, we found a common thread between core density (boundness) and temperature with clump column density, where cores associated with high density environments are generally denser and colder. These relationships also agree well for all sources regardless of clump properties or localized influences (i.e., the local interstellar radiation field), and for sources identified as "off clump". These results agree well

with previous studies that associated star formation with dense material (i.e., Kainulainen et al. 2009; André et al. 2010; Lada et al. 2010), and yet, these results also suggest that the connection is relatively consistent throughout different environments (clump properties, localized influences) and evolutionary stages (older and younger populations). For example, while the starless cores in IC348 are warmer on average, we find the same trends where cores at higher column densities are themselves denser and colder in a similar manner as the other clumps.

Additionally, we found that the *Herschel* sources were associated with the column density peaks. In contrast, Kirk et al. (2006) found that SCUBA-identified cores in Perseus were offset from the extinction peaks in their low resolution extinction map. This disparity suggests that caution is needed when using low-resolution extinction mapping to estimate the column of material associated with small-scale objects. Low resolution extinction maps can estimate the bulk properties of clouds, however. We found better agreement at lower column densities between the lower-resolution extinction map and our higher-resolution column density map.

3. Future Work

We focused on *Herschel* observations of the Perseus molecular cloud with complementary observations from other facilities (i.e., the GBT, JCMT, *Spitzer*, 2MASS). Our analysis, however, lacks complete dynamical information and complete observations at $\lambda > 500$ μm our sources. Complete dynamical information is necessary to determine boundedness for our starless cores (see Chapter 3), and without this information we can only estimate which cores are likely or unlikely to be bound. Complete observations at $\lambda > 500$ μm are crucial to determine the dust properties from cold, dust emission (see Chapter 4). In the absence of such information for all cores, we assumed a fixed dust opacity law. Nevertheless, sources that deviate from this dust opacity law will have inaccurate mass measurements, and thus, their physical properties and their dynamic states will be correspondingly uncertain. There are several surveys of molecular clouds at long wavelengths (i.e., 850 μm observations from the SCUBA-2 Gould Belt Survey; Ward-Thompson et al. 2007b), and these data can be used to improve the SED fitting and determine the dust emissivity index.

Additionally, we lacked interstellar extinction estimates for most of our YSOs. These corrections are most significant for the classification of later-stage YSOs, such as Flat, Class II, and Class III YSOs compared to the early-stage YSOs (i.e., Class

0 and Class I). As such, our classifications of YSOs as Flat, Class II, or Class III is less certain due to these extinction corrections. Therefore, complete interstellar extinction corrections for unembedded YSOs are necessary to classify these sources better. For example, if we significantly over- or under-estimate the extinction towards the sources in one clump, we may bias the YSO populations towards older or younger populations, respectively.

Finally, this study focused on only the Perseus molecular cloud. We need to expand this study to determine whether the trends between YSO and core populations with clump properties we observe for Perseus are common. Notably, Perseus is not forming high-mass stars. Therefore, it is important to survey other clouds with different environments and star formation histories. While the Perseus clumps constitute different environments themselves, several have small samples of cores and YSOs. For these clumps, it is difficult to conclude that the trends we observe are robust or are a product of relatively small number statistics.

With the full *Herschel* Gould Belt Survey, we will be able to explore the relationship between source populations and clumps in a large variety of clouds, thereby improving the number statistics. Many of the *Herschel* Gould Belt clouds also have complementary infrared observations with *Spitzer*, which samples their YSO populations. This study of the Perseus molecular cloud is the first of many detailed studies to fully combine data from *Herschel*, *Spitzer*, and SCUBA-2 (for B1) to characterize the full star formation activity in a molecular cloud. This work demonstrates the type of analysis that can be achieved by combining such datasets.

Appendix A

Acronyms and Symbols

Table A.1: Common Acronyms

GBS	Gould Belt Survey
HGBS	*Herschel* Gould Belt Survey
SED	spectral energy distribution
YSO	young stellar object
FHSC	first hydrostatic core
SPIRE	Spectral and Photometric Imaging Receiver (*Herschel* detector)
PACS	Photodetector Array Camera and Spectrometer (*Herschel* detector)
IRAC	Infrared Array Camera (*Spitzer* detector)
MIPS	Mid-Infrared Photometer and Spectrometer (*Spitzer* detector)
HIPE	*Herschel* Interactive Processing Environment
GBT	Green Bank Telescope
KFPA	K-band Focal Plane Array (GBT detector)
JCMT	James Clerk Maxwell Telescope
SCUBA	Submillimeter Common-User Bolometer Array (JCMT detector)
SCUBA-2	Submillimeter Common-User Bolometer Array 2 (JCMT detector)
S2SV	SCUBA-2 Science Verification
HARP	Heterodyne Array Receiver Program (JCMT detector)
H+850	*Herschel* 160 μm $-$ 500 μm bands with the SCUBA-2 850 μm band
H-only	*Herschel* 160 μm $-$ 500 μm bands only
c2d	cores to disks survey
G09	Gutermuth et al. (2009) survey
IRAS	Infrared Astronomical Satelitte
2MASS	2 Micron All Sky Survey
IDL	Interactive Data Language
FWHM	full width at half maximum
SNR	signal-to-noise-ratio

Table A.2: Common Symbols and Constants

$B_\nu(T)$	blackbody function
h	Planck constant
k	Boltzmann constant
c	speed of light
c_s	sound speed
ν	frequency, typically given in GHz
λ	wavelength, typically given in μm
A_V	visual extinction, measured in magnitudes
A_λ	extinction at wavelength λ, measured in magnitudes
S_ν	flux density at frequency ν, measured in Jy (1 Jy = 10^{-26} W m^{-2})
I_ν	intensity at frequency ν, typically given as W m^{-2} sr^{-1}
T	dust temperature, measured in Kelvin
T_K	kinetic temperature, measured in Kelvin
d	distance, typically measured in parsec
R_{eff}	effective radius, typically measured in pc
R_d	deconvolved radius, typically measured in pc
a, b	semi-major, semi-minor axis, typically measured in arcsec ($''$)
N(H_2)	molecular hydrogen column density, measured in cm^{-2}
μ	mean molecular weight, unitless
m_H	hydrogen mass, measured in grams
Σ	gas mass column density, measured in g cm^{-2}
n	density, measured in cm^{-3}
β	dust emissivity index, unitless
κ_ν	dust opacity per unit dust and gas mass, measured in cm^2 g^{-1}
$\kappa_{\nu,d}$	dust opacity per unit dust mass, measured in cm^2 g^{-1}
τ_ν or τ_λ	optical depth with frequency or wavelength, unitless
σ	standard deviation
σ_v	velocity dispersion, measured in km s^{-1}
σ_T	thermal velocity dispersion, measured in km s^{-1}
σ_{NT}	non-thermal velocity dispersion, measured in km s^{-1}
M_{virial}	virial mass, measured in $M_\odot$
α_v	virial parameter, unitless
F_{SF}	spatial filtering factor, unitless
α	infrared spectral index
T_{bol}	bolometric temperature, measured in Kelvin
L_{bol}	bolometric luminosity, measured in $L_\odot$
L_{smm}	submillimeter luminosity (for $\lambda \geq 350$ μm), measured in $L_\odot$
$L_\odot$	solar luminosity, $\sim 3.84 \times 10^{26}$ W or 3.84×10^{33} erg s^{-1}
$M_\odot$	solar mass, $\sim 2 \times 10^{33}$ g

Appendix B

SCUBA-2 Filtering

Since SCUBA-2 is a ground-based detector, we filter out large-scale astronomical emission in the process of removing the emission from a bright and variable atmosphere. Thus, SCUBA-2 is sensitive only to spatial scales where emission is fully recovered. To determine the largest such spatial scale, we introduced artificial Gaussian sources of various sizes ranging from $1'$ to $7.5'$ FWHM to the original SCUBA-2 data, and then ran these modified maps through the pipeline. Since the SCUBA-2 pipeline determines which map pixel is covered by which bolometer at any given time, the extra signal corresponding to the Gaussian sources is simply added to the bolometer timeseries. Following our reduction process from Section 4.2.2, the smaller Gaussians were fully recovered, e.g., Gaussians of $1'$ or $2.5'$ sizes. Larger Gaussians, however, were only partially recovered or fully filtered out. For example, peak fluxes for $\sim 5'$ Gaussians were only 70% recovered. Based on these tests, the SCUBA-2 observations appear to fully recover objects on size scales $\lesssim 2.5'$.

Conversely, *Herschel* is a space-based observatory, and thus, the PACS+SPIRE data are unaffected by atmospheric emission. For our HARP CO $(3-2)$ line observations, we used an emission-free off position to remove the atmospheric contributions. Thus, both PACS+SPIRE and HARP observations are unfiltered, and such data cannot be directly compared to the SCUBA-2 maps. One simple solution is to filter out these large-scale structures, such that the *Herschel* continuum and HARP line observations are sensitive to the same spatial scales as the SCUBA-2 data.

We filtered out the large-scale emission from the CO $(3-2)$ and *Herschel* maps using the SCUBA-2 reduction pipeline in the same manner as the artificial Gaussian sources. We created "artificial maps" by adding the unfiltered CO $(3-2)$ integrated intensity map (in Jy beam^{-1}) or the *Herschel* data to the SCUBA-2 bolometer time-

series by adjusting the original signal observed at every bolometer to include the emission observed by HARP, PACS, or SPIRE. Using these artificial signals, we repeated the SCUBA-2 reduction as given in Section 4.2.2 four times, once for each of the four Grade 1 observations. Finally, we combined the products into a single mosaic. Since this mosaic also includes the original 850 μm data, we subtracted out the reduced 850 μm map to leave behind the filtered version of the other data (see Figure 4.6).

Appendix C

CO Line Contamination

The CO (3-2) line transition coincides with the 850 μm SCUBA-2 band, and thus, will contaminate the continuum emission. Significant CO $(3-2)$ contamination is mostly identified towards outflows and highly energetic regions such as HII regions, where the contamination levels can dominate ($> 50\%$) the total continuum emission (e.g., Davis et al. 2000; Tothill et al. 2002; Drabek et al. 2012). Although B1 is a low-mass star-forming complex, and such regions generally contain weaker CO $(3-2)$ line emission (Drabek et al. 2012), this clump contains several protostellar sources driving outflows (Bally et al. 2008).

To evaluate the CO $(3-2)$ contamination, we determined the contribution from the line flux over the entire SCUBA-2 850 μm passband. Following Drabek et al. (2012), the line flux at frequency ν_0 across the continuum band is,

$$\frac{S_{\nu_0}}{\text{mJy beam}^{-1}} = \frac{2k\nu_0^3}{c^3}\frac{g_{\nu_0,line}}{\int g_{\nu,cont}d\nu}\,\Omega\int T_{MB}dv, \tag{C.1}$$

where k is the Boltzmann constant, c is the speed of light, Ω is the telescope beam, T_{MB} is the main beam temperature of the line, $g_{\nu_0,line}$ is the transmission of the submillimeter filter at the frequency of the molecular line (ν_0), and $g_{\nu,cont}$ is the transmission profile of the entire submillimeter filter. Drabek et al. (2012) adopted a "conversion factor" as,

$$\frac{C}{\text{mJy beam}^{-1}\ (\text{K km s}^{-1})^{-1}} = \frac{2k\nu_0^3}{c^3}\frac{g_{\nu_0,line}}{\int g_{\nu,cont}d\nu}\,\Omega. \tag{C.2}$$

The SCUBA-2 filter profile, $g_{\nu,cont}$, varies significantly with atmospheric conditions.

For example, the filter response is best for dry conditions ($\tau_{225} < 0.05$) and can drop by more than 50% in wet conditions ($\tau_{225} > 0.12$). We used the S2SV observations made in very dry conditions, $\tau_{225} < 0.05$, resulting in $C \approx 0.63$ mJy beam^{-1} (K km s^{-1})$^{-1}$ (Drabek et al. 2012). This factor, however, assumes that the beam of SCUBA-2 at 850 μm is 13.8$''$. We have adopted here an effective beam of 14.2$''$ (see Section 4.2.2), which considers the larger error beam. Thus, our conversion factor should be modified by $\Omega_{eff}/\Omega = 1.06$. Therefore, we use

$$C = 0.67 \text{ mJy beam}^{-1} \text{ (K km s}^{-1})^{-1}. \tag{C.3}$$

In addition to CO $(3-2)$ line contamination, other (weaker) molecular line emission will contaminate the continuum bands (Drabek et al. 2012). For example, CO $(6-5)$ at 691.473 GHz coincides with the 450 μm SCUBA-2 band and CO $(7-6)$ at 806.652 GHz coincides with the SPIRE 350 μm band. Nevertheless, Drabek et al. demonstrated that such high excitation line transitions are generally negligible compared to the dust emission. For example, the dust emission rises towards shorter wavelengths as $\nu^{\beta+2}$ whereas the emission from higher transitions of CO does not rise as steeply. For example, we do not believe the excess brightness at 450 μm relative to the filtered 500 μm emission (see Figures 4.8 and Figure 4.11) is due to CO (6-5) contamination at 450 μm. Since the CO $(3-2)$ line contamination is relatively minor, we can also assume that the contamination from less abundant molecules (i.e., ^{13}CO or C^{18}O) should be negligible.

Appendix D

Herschel Colour Corrections

The PACS and SPIRE fluxes from HIPE[1] contain several sources of uncertainty. First, both instruments have a 10% flux error based on the uncertainties in the calibration. For PACS, flux calibrations are mainly based on stellar sources and bright asteroids (Poglitsch et al. 2010), whereas for SPIRE, flux calibrations primarily use Neptune (Griffin et al. 2010). Second, both PACS and SPIRE calibrations assume that the observed spectral profile follows a ν^{-1} power-law such that νS_ν is flat (Poglitsch et al. 2010; Griffin et al. 2010). For cold molecular clouds ($T \sim 10$ K), emission in the PACS and SPIRE bands will not follow a ν^{-1} power-law, and thus, colour corrections are necessary (e.g., see Pezzuto et al. 2012). Furthermore, the spectral colour corrections are not systematic, and they depend on the SED shape and thus, will vary with frequency, temperature, and opacity.

Calculating the spectral colour corrections is nontrivial. First, these correction factors require foreknowledge of the SED profiles. Second, the colour corrections compare the flux from the true SED profile to the assumed SED profile, both weighted by the filter response function. For SPIRE, the beam solid angle varies with wavelength, resulting in more power at longer wavelengths. While this effect is insignificant for point sources, extended sources (i.e., objects that uniformly fill the entire beam) will be biased towards longer wavelengths. Thus, colour corrections vary between point sources and extended objects[2]. PACS calibration does not differentiate between point sources and extended sources. Since we are interested in the extended *Herschel* map

[1]The *Herschel* Interactive Processing Environment (HIPE) is a joint development software by the *Herschel* Science Ground Segment Consortium, consisting of ESA, the NASA *Herschel* Science Center, and the HIFI, PACS, and SPIRE consortia.

[2]For additional information, see the SPIRE Observers' Manual (2011), HERSCHEL-DOC-0798, v2.4, http://herschel.esac.esa.int/Docs/SPIRE/pdf/spire_om.pdf

structures, we will adopt the extended colour corrections for SPIRE. We caution that these structures likely do not fill the filter beam uniformly at all wavelengths, and that these colour corrections represent our best estimate. For SPIRE, these extended source corrections are generally minor (few percent) and should not greatly affect our results (Griffin et al. 2010). For PACS, however, the colour corrections of cold objects can be more significant, particularly at 70 μm (Poglitsch et al. 2010). We do not include 70 μm emission in the SED fits in this paper, however.

Since the SED profiles are unknown a priori, to determine the colour correction, we assumed the observed dust has temperatures between 10 K and 15 K and dust emissivity indices between 1.5 and 2.5. For PACS, the colour corrections for cold and dusty environments are given in Müller et al. (2011)[3], and we extrapolated those tabulated values to identify the colour corrections associated with our adopted ranges of temperature and beta. For SPIRE, we calculated the colour corrections by integrating model SEDs weighted by the relative spectral response function (RSRF) of each band (see Pezzuto et al. 2012). We scaled the RSRF profiles[4] such that a fixed $S_\nu \sim \nu^{-1}$ SED would yield colour corrections of 1.0 (i.e., what was initially assumed in the calibration). Assuming various power-law profiles, our colour corrections agree with the corrections in the SPIRE Observers' Manual to within a few percent. For both PACS and SPIRE, we adopted the midpoint between the maximum and minimum colour correction, taking the difference of the average value with respect to the range of accepted values are our uncertainty. Table 4.1 lists our adopted colour corrections for each wavelength. We caution that these values are only valid for $T \approx 10 - 15$ K and $\beta \approx 1.5 - 2.5$.

[3]PACS Photometer Passbands and Colour Correction Factors for Various Source SEDs, http://herschel.esac.esa.int/twiki/pub/Public/PacsCalibrationWeb/cc_report_v1.pdf

[4]For extended emission, the RSRF profile is multiplied by λ^2 to account for the differences in the beam size between the short wavelength end and the long wavelength end of the filter. For more details, see the SPIRE Observers' Manual.

Appendix E

Measuring β from Unfiltered Maps

In this Appendix, we outline the techniques for measuring β while recovering the missing large-scale structure in the SCUBA-2 maps. These techniques are the Offset Case (Appendix E.1) and the Spatial Factor Case (Appendix E.2). We highlight the method and discuss the uncertainties in the determined values of β.

E.1 Offset Case

We use the *Herschel* data to recover the large-scale structure at 850 μm. We assume that the missing large-scale emission corresponds to scales $> 2.5'$, and thus, we do not expect large variations in the extended structure for scales $< 2.5'$. The method is outlined below and in Figure E.1:

1. For each pixel, we select a 9×9 pixel subregion (corresponding to $\sim 2.1'$ for $14''$ pixels). The extended emission should not vary over this subregion. See the top panels of Figure E.1.

2. We create a grid of 850 μm flux offsets ranging from $0 - 1.5$ Jy beam^{-1} in increments of 0.03 Jy beam^{-1} to represent the filtered-out emission at 850 μm.

3. For each 850 μm offset, we fit the $160 - 850$ μm emission from all pixels within the 9×9 pixel subregion.

4. We total the individual χ^2 measures across the entire subregion for each estimation of the 850 μm offset. If the 850 μm offset is close to the filtered-out extended emission, the total χ^2 will be low, and if the 850 μm offset differs from the true extended emission, then the total χ^2 will be high.

5. For the central pixel in the subregion, we adopt the 850 μm offset value that corresponds to the minimum total χ^2. For simplicity, we fit a parabolic function to the distribution of total χ^2 with offset. See the bottom panels of Figure E.1.

Figure E.1 illustrates our technique. The top panels show two example subregions with 9×9 pixel boxes used to measure the offset at the marked positions towards a pixel in B1-a and the south-west filament. For each estimate of the 850 μm offset ranging from 0 Jy beam^{-1} to 1.5 Jy beam^{-1}, we found the best-fit SEDs across these subregions, and then summed the χ^2 values from all 81 pixels. The bottom panels show the distributions of total χ^2 with 850 μm offsets for our two example subregions. As expected, when the 850 μm offset is greatly underestimated or overestimated, the total χ^2 is large. We used parabolic fits to identify the offset corresponding to the minima. For simplicity, Figure E.1 does not include the 10% calibration uncertainties for each instrument.

Figure E.2 shows the range of best-fit 850 μm offsets within the 10% calibration uncertainties for the two pixels highlighted in Figure E.1. The range of acceptable offsets appears fairly broad, suggesting that this technique does not constrain well the missing 850 μm large-scale emission and these uncertainties overwhelm the uncertainties of the observed 850 μm data (10%). Applying 1000 random calibration correction factors to each subregion (effectively 81 SEDs per increment) and each estimated 850 μm offset (50 possible increments) is computationally expensive. Therefore, we sampled a subset of 10 pixels and found that the 1 σ standard deviation errors in the mean offsets are $20 - 50\%$ of the respective offset measures.

Figure E.3 shows the "recovered" 850 μm large-scale emission. The black contours show the 10 σ flux level from Section 4.4.1. The recovered 850 μm extended emission shows some similarities and yet some variations with the filtered-out large-scale emission at 250 μm shown in Figure 4.6. For example, we see the recovered 850 μm large-scale emission peak towards the central B1 region at both wavelengths. Conversely, the recovered 850 μm large-scale emission map appears more structured, with less extended emission towards the main filament and B1-c. Since the 850 μm emission traces very cold dust, these differences could reflect differences in dust temperature. Similar differences, however, are not seen between the *Herschel* bands at 250 μm and 500 μm.

Figure E.4 shows the β maps determined from SED fitting with the *Herschel*+850 bands, where the 850 μm emission includes the recovered extended structure from

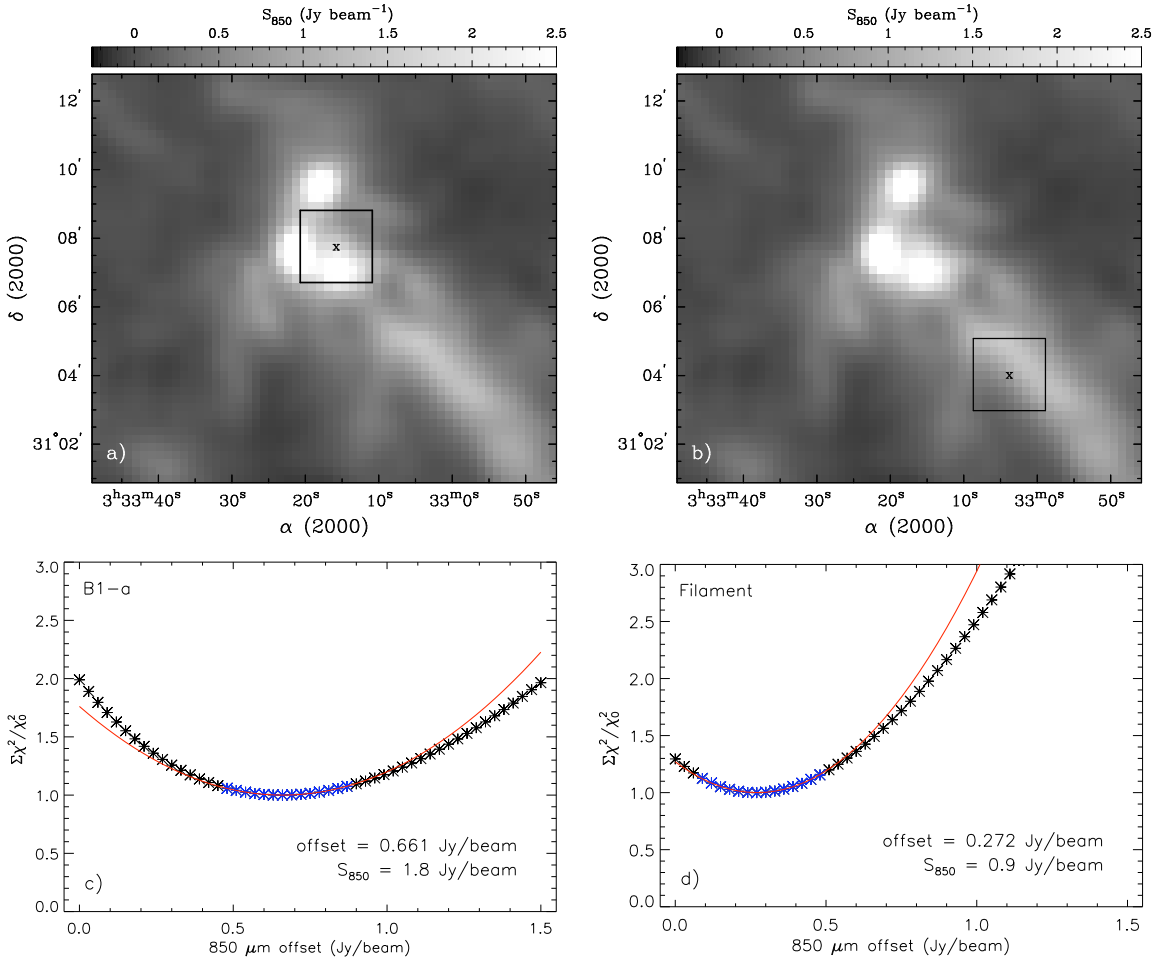

Figure E.1: Technique to measure the missing 850 μm emission. *Top:* Two examples of 9×9 pixel subregions centered on (a) B1-a and (b) the filament. For a given subregion, the SEDs of each pixel are fit for a range of 850 μm offset values from $0 - 1.5$ Jy beam^{-1}. Then, for each offset estimate, we sum the individual χ^2 measurements from every best-fit SED in the subregion. *Bottom:* The *relative* total χ^2 measure at each offset for the two example subregions. The lowest χ^2 value (χ_0) is determined from a parabolic fit to a set of values (shown in blue) near the distribution minimum. The 850 μm offsets corresponding with these minima are given in the bottom right corners along with the observed emission at 850 μm (S_{850}).

Figure E.3. We measured β assuming two extremes, i.e., (a) no uncertainties in the extended emission and (b) 50% uncertainties in the extended emission. In the bottom panels, we compare the derived β distributions with the equivalent H-only distribution. Most noticeably, there is a spike at $\beta \approx 1.8 - 1.9$ in Figure E.4c, which is similar to the $\beta \approx 2$ peak seen in Figure 4.9. Nevertheless, as shown in Figure E.4d, this spike disappears if we assume 50% errors for the 850 μm extended emission, likely

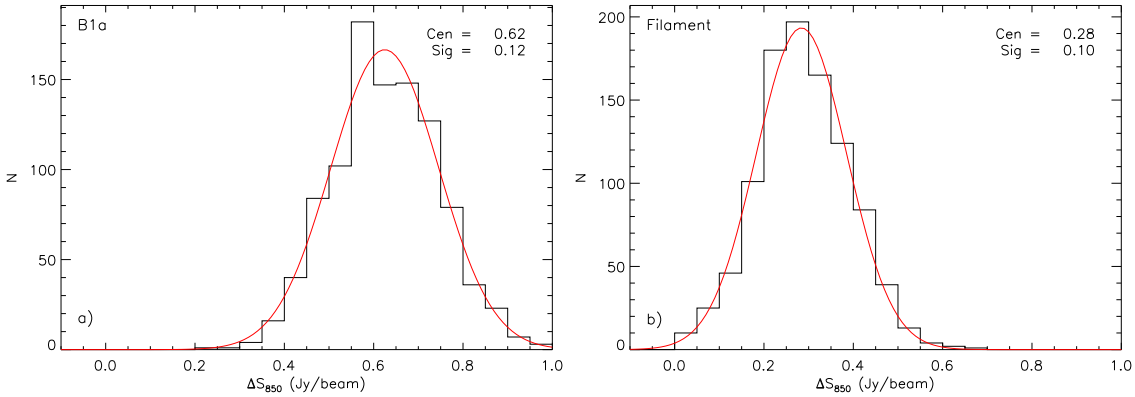

Figure E.2: Range of best-fit 850 μm offsets. We generated 1000 random calibration correction factors as described in Section 4.4, and then found the best-fit 850 μm offset for each set of correction factors according to our technique (see text and Figure E.1). The red curves show a Gaussian fit to the histograms.

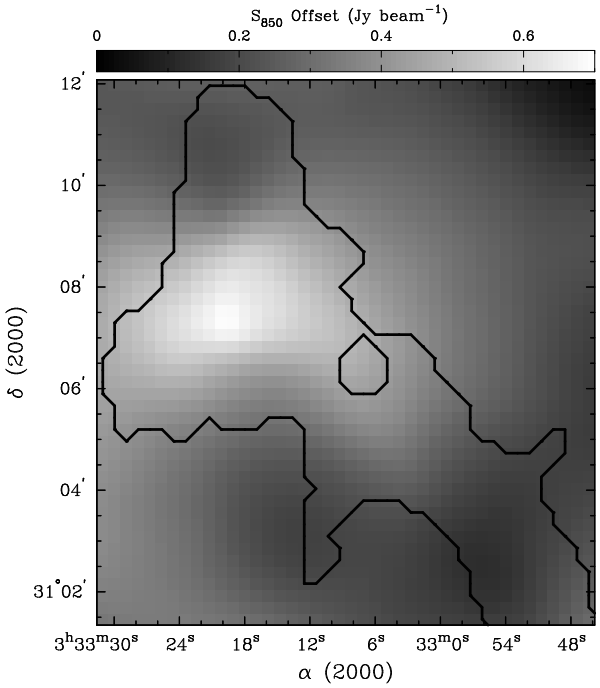

Figure E.3: The recovered diffuse emission at 850 μm obtained with our technique. The black contours correspond to the 10 σ region in Section 4.4.1.

due to the 850 μm data being too uncertain to constrain well the SEDs. Indeed, the β distribution with 50% flux errors in the 850 μm extended structure appears more similar to the H-only distribution, with a slight offset towards lower β values. Therefore, the Offset Case approach to recover the filtered-out, large-scale 850 μm emission makes the 850 μm data too uncertain to be an effective constraint.

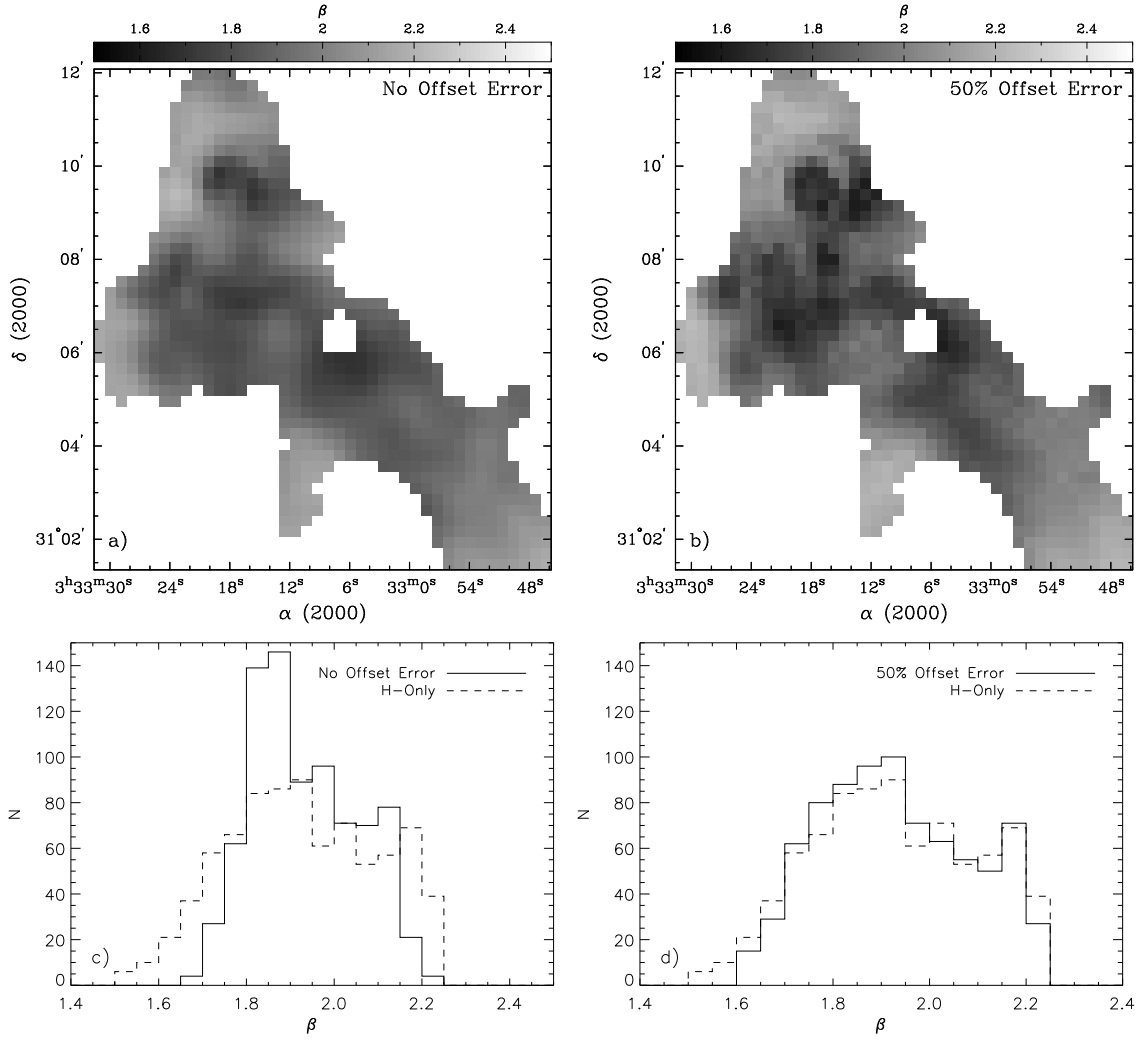

Figure E.4: *Top:* Dust emissivity maps assuming (a) no errors for the 850 μm offsets or (b) 50% errors for the 850 μm offsets (see Appendix E.1). The black contours indicate the region correspond to > 10 σ from Section 4.4.1. *Bottom:* Histograms comparing β distributions from the 850 μm offset analyses and the distribution obtained from H-only data. We assume no 850 μm offset uncertainties in (c) and 50% offset uncertainties in (d).

E.2 Spatial Factor Case

For the Spatial Factor Case, we attempt to recover the missing large-scale emission by scaling the 450 μm and 850 μm emission by a spatial filtering factor to account for the missing extended flux. We assume that the 450 μm and 850 μm observations are missing the same fraction of extended emission, and then fit the SEDs according to Equation 4.3, solving for the SED parameters and the spatial filtering factor, F_{SF}. Since Figure 4.11 demonstrates that the observed 450 μm emission tends to be 10-15%

brighter than the predicted emission, we adjusted the 450 μm emission downward by 12.5%. This adjustment appears most reasonable for the brightest parts of the B1 clump (i.e., $I_{450} > 5$ Jy beam^{-1}), however, and may cause erroneous results outside of these locations.

The top panels of Figure E.5 shows the β values and spatial filtering factors derived using Equation 4.3. The contours correspond to the regions with $I_{450} > 5$ Jy beam^{-1}, and where a scaling of -12.5% is more reasonable (see Figure 4.11). Similar to the previous measures of β, we find that β is lowest towards B1-c. On the other hand, we find $\beta \sim 2.3$ towards B1-a and $\beta \sim 1.6$ towards B1-b. Additionally, we obtain $\beta \sim 1.7$ along the filament. For the spatial filtering factor, we find $F_{SF} \sim 0.8 - 0.9$ towards the dense, compact cores and $F_{SF} \sim 0.7$ towards the filament. Towards the edges of the 10 σ region, however, the spatial filtering factor drops to $\lesssim 0.4$, suggesting that most of that emission was removed by the SCUBA-2 reduction pipeline. Figure E.5 also shows the distributions of β and F_{SF} for the > 1 Jy beam^{-1} and > 5 Jy beam^{-1} regions. Unsurprisingly, the brightest regions (i.e., the locations of the compact objects) correspond with the highest fraction of recovered emission. Nevertheless, we find a wide range of β values even for the > 5 Jy beam^{-1} region. Within the calibration uncertainties, we find $\sigma \lesssim 1.0$. Therefore, the Spatial Filtering Case is not a robust method to determine β.

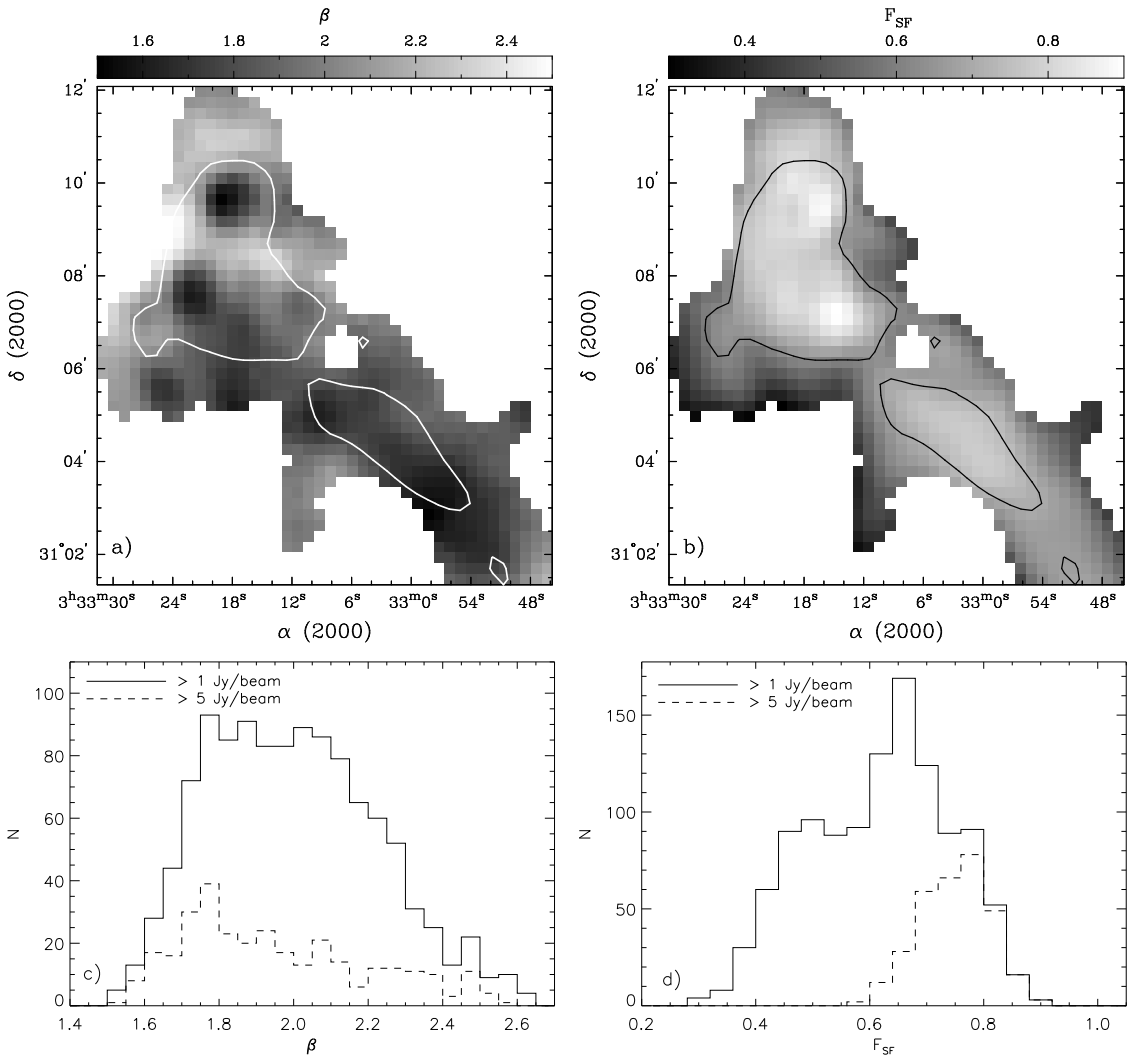

Figure E.5: *Top:* Results from the Spatial Factor Case highlighting (a) the dust emissivity and (b) spatial filtering factor (F_{SF}). The dust emission was fit using Equation 4.3, assuming an equal scaling factor, F_{SF} for the 450 μm band and the 850 μm band. The contours indicate the region with $I_{450} > 5$ Jy beam^{-1}. *Bottom:* Histograms for β and spatial filtering factor. The solid lines show the histograms for the entire region in the upper panels, and the dashed lines show the histograms for the $I_{450} > 5$ Jy beam^{-1} regions, only. For these analyses, the 450 μm data were scaled by 12.5% to account for the fractional increase in brightness in the observed maps over the predicted maps (see Figure 4.11).

Appendix F

Source Temperatures

We fitted source SEDs at 160 -500 μm using Equation 5.2. Since we have limited wavelength coverage, our ability to fit the SEDs varies with temperature. For example, at $T \sim 40$ K and $\beta = 2$, the SED peaks around 70 μm, which is beyond the range of our fitting (we do not include the 70 μm observations in our fits). As such, the 160 μm $-$ 500 μm SED fit does not constrain the temperature well for such warm material. Conversely, a source with $T \sim 10$ K and $\beta = 2$ will peak around 290 μm, which is bounded by our observations. Thus, the $160 - 500$ μm SED will result in a better constrained fit.

To test the degeneracy of the SED fitting with temperature, we generated model fluxes for 1 $M_\odot$ sources at temperatures of $T = 10 - 50$ K with $\beta = 2$. For each value of temperature, we divided the model flux in each band by the appropriate colour correction for that temperature and then multiplied the result by our assumed colour corrections. This modification simulates the fluxes we would obtain using our technique. Additionally, we split the colour corrections into two bins. For temperatures of $10 - 30$ K, we used the colour corrections given in Table 5.4. For the sources with $T > 30$ K, we calculated new colour corrections appropriate for that temperature range (following the same procedure as for Table 5.4). Finally, we applied 1000 randomly generated errors within $\pm 1\sigma$ to each band to represent observational noise. For simplicity, we assumed each band was observed at a SNR = 7.

From the procedure outlined above, we obtained 1000 modified SEDs for each estimate of temperature. Since we know the true SED, we can test the accuracy of the SED-fitting. For each temperature, we fitted the 1000 modified SEDs following Equation 5.2 using the IDL program *mpfitfun*. We took the quadrature sum of the simulated noise and the colour correction uncertainties for the flux error in each band.

Figure F.1 shows the range in best-fit temperature and mass for our 1000 modified model SEDs. To highlight the differences between the best-fit values and the true results, Figure F.1 shows the relative values, corresponding the fractional difference between the observed fit and the true value, i.e., $(fit - true)/true$. For temperature, we find that the uncertainty in the fitting increases significantly between 10 K and 50 K. For example, at 10 K, we have a standard deviation for temperature of $\sigma = 2\%$, whereas at 50 K, the standard deviation becomes $\sigma \sim 20\%$. Surprisingly, the source mass has a large uncertainty at every temperature ($\sigma > 10\%$), but the uncertainty doubles between 10 K and 50 K.

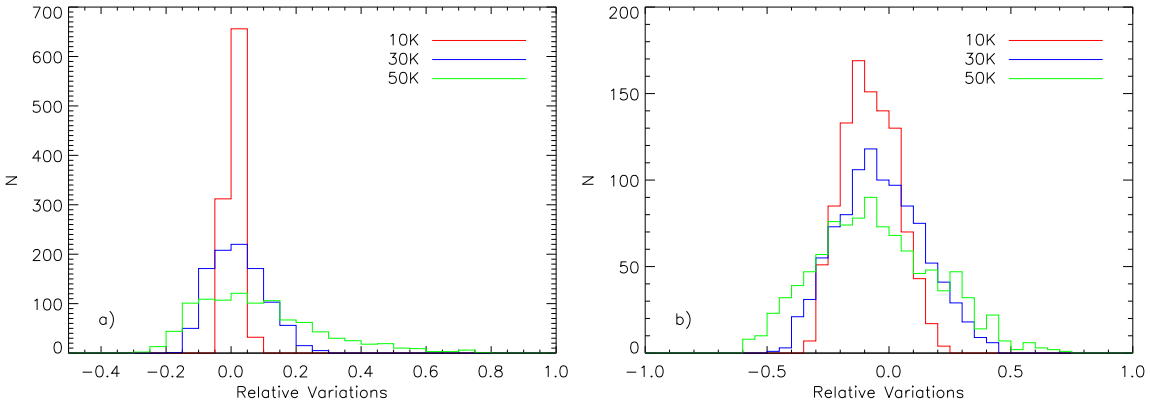

Figure F.1: Relative variations between the best-fit values and the true values for (a) temperature and (b) mass. For clarity, we only show the results for 10 K, 30 K, and 50 K.

For $T > 30$ K, the relative variations between the best-fit temperatures and the true temperature becomes non-Gaussian with high temperature tails (see Figure F.1a). Since the 160 μm band is longward of the SED peak at these temperatures, it is unsurprising that the SED fits cannot constrain well the higher temperatures from 160 -500 μm data only. Since the 70 μm data are themselves too uncertain, we cannot use these data to help constrain the SED peak and the temperature. Thus, sources with best-fit temperatures of $T > 30$ K are unreliable.

For the colour correction, we also set a lower-limit of $T = 10$ K. For SPIRE, the colour corrections do not vary significantly at this temperature range (we recover the same absolute colour correction). For PACS, however, colder sources have more significant colour corrections. Nevertheless, such cold sources are unlikely to have strong 160 μm emission. For example, a 1 $M_\odot$ source at 8 K will have $S_{160} < 0.2$ Jy. Such a source will not be well detected within an $N(H_2) \geq 2.0 \times 10^{21}$ cm^{-2} region (see Section 5.3.3).

Appendix G

YSO Extinction

Molecular clouds have higher optical depths at short wavelengths than long wavelengths (see Figure 1.2). As such, YSOs will appear fainter, particularly at $\lambda \lesssim 24$ μm. For accurate SEDs from 1.25 μm to 500 μm, we must correct the fluxes at the shorter wavelengths. The change in the amount of emission is given by

$$\frac{dI_\lambda}{I_\lambda} = -d\tau_\lambda,$$

where dI_λ is the loss in emission due to dust with an optical depth of τ_λ. Thus, we find that for a source with a given intensity of $I_\lambda(0)$, the emission detected by an observer would be,

$$I_\lambda = I_\lambda(0)e^{-\tau_\lambda}.$$

Thus, to measure $I_\lambda(0)$, we must first obtain τ_λ.

Typically, the measure for reddening is given by the interstellar extinction rather than optical depth. The interstellar extinction corresponds to the loss in magnitudes (brightness) at a given wavelength due to intervening material (i.e., dust). By definition, the magnitude is given by,

$$m_\lambda = -2.5 \log F_\lambda + C,$$

where m is the magnitude, $S_\lambda \sim I/d^2$ is the flux density, and C is a constant for unit coversion. Thus, the difference in magnitude between the observed emission and the

true emission is given by,

$$\begin{aligned} m_{\lambda,obs} - m_{\lambda,true} &= -2.5 \log S_{\lambda,obs}/S_{\lambda,true} \\ A_\lambda &= -2.5 \log I/I_\lambda(0), \end{aligned}$$

where A_λ is the change in magnitude brightness due to interstellar extinction, for $m_{obs} \geq m_{true}$. For the same source, the flux, S, can be written by the intensity (distance independent). Thus, we can write A_λ as,

$$\begin{aligned} A_\lambda &= -2.5 \log e^{-\tau_\lambda}, \text{or} \\ A_\lambda &= 1.086 \tau_\lambda \end{aligned}$$

Thus, to correct our observed emission, we use the following relation;

$$S_{true} = S_{obs} e^{A_\lambda / 1.086}. \tag{G.1}$$

For Perseus, we can estimate the visual extinction (A_V) from our column density map (Figure 5.5) using Equation 5.1. To measure A_λ, however, we relied on theoretical extinction curves (e.g., Weingartner & Draine 2001), which vary depending on dust grain properties. Thus, we follow the c2d catalogue and adopt the following A_λ/A_V ratios (M. Dunham 2013, private communication);

Table G.1: Adopted Ratios of Extinction with Wavelength

Band	J	H	K	IRAC1	IRAC2	IRAC3	IRAC4	MIPS1
λ (μm)	1.25	1.65	2.17	3.6	4.5	5.8	8.0	24
A_λ/A_V	0.2688	0.1647	0.1149	0.0664	0.0544	0.0443	0.0505	0.0260

For the c2d catalogue, visual extinction (A_V) was measured using optical surveys of YSO populations in the literature. Since embedded sources are not detected at such short wavelengths, visual extinction could only be measured for older YSOs (i.e., Class II/III sources). The mean extinction was $A_V = 5.9$. Similarly, the G09 catalogue uses expected colours for Class II YSOs (classical T-Tauri stars) or low-mass dwarf stars to measure the line-of-sight extinction towards the sources. Gutermuth et al. (2009) reports source extinction in K-band, assuming $A_K = 0.112 A_V$. The mean extinction was $A_V = 5.1$. For the younger YSOs, such as Class 0/I objects, neither survey could directly measure the line-of-sight extinction. For these, we assumed the mean value

from the c2d catalogue of $A_V = 5.9$ mag. The c2d catalogue is larger and samples the entire Perseus cloud, whereas the G09 catalogue only sampled NGC1333 and IC348.

Figures G.1 and G.2 compare the extinction measured for the older YSOs from the c2d catalogue and G09 catalogue, respectively, with the total line-of-sight extinction from the maps. The extinction map from *Spitzer* data is provided by the c2d survey[1] at 180″ resolution. Furthermore, we produced two *Herschel* extinction maps. The first used the column density for the whole cloud, the second used the column density from the background only. We measured the background column density by removing the objects detected by getsources from the individual flux maps. In both cases, we converted our *Herschel* column density maps to extinction using Equation 5.1, and then convolved these maps to 180″ resolution. The relation for a fixed source extinction of $A_V = 5.9$ is shown by the dashed curve.

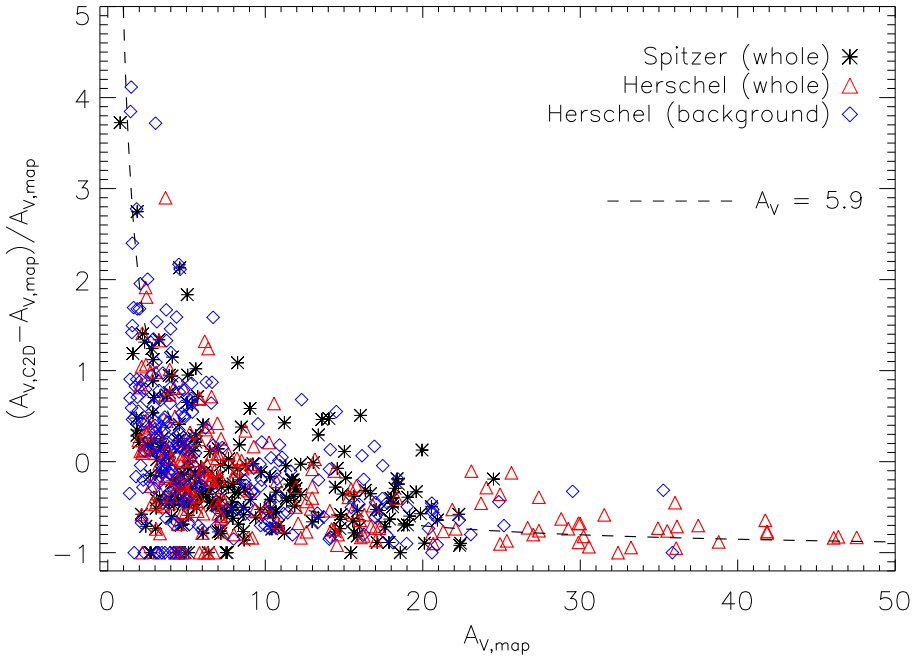

Figure G.1: Relative variations between the visual extinction (A_V) for the YSOs from the c2d catalogue. We only include the YSOs where foreground extinction was determined. For comparison, we give the relative differences between the determined extinction for each YSO with the extinction measured towards the Perseus field from *Spitzer* (black stars), *Herschel* (red triangles), and *Herschel* background (blue diamonds). The distribution for $A_V = 5.9$ is shown with a dashed curve.

For both Figure G.1 and Figure G.2, the extinction is scattered about the $A_V = 5.9$ curve. We do not find any systematic offsets from this curve. Thus, in the absence

[1] http://irsa.ipac.caltech.edu/data/SPITZER/C2D/images/PER/

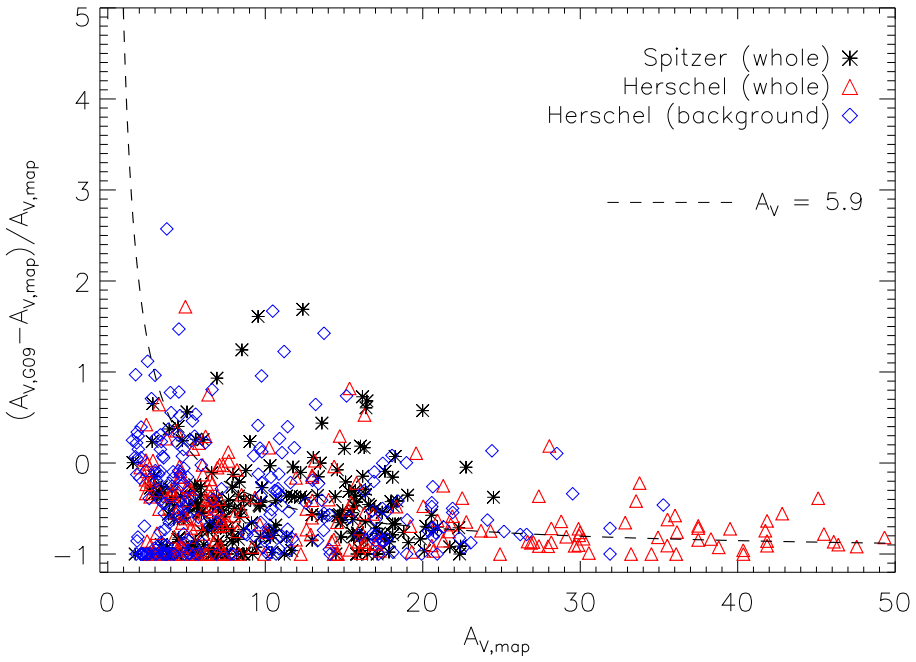

Figure G.2: Same as Figure G.1 but for the YSOs from the G09 catalogue.

of a measured extinction value, assuming $A_V = 5.9$ provides a reasonable estimation of the line-of-sight extinction to any given source.

Appendix H

Source Tables

In this Section, we provide complete source tables. We caution that these catalogues correspond to a preliminary extraction for the Perseus cloud. As such, we will not publish source positions or fluxes at this time. Source positions and fluxes will be provided with the First Generation paper (see explanation in Section 5.3.2).

Table H.1 gives the results from fitting single-temperature dusty blackbody models to the observed SEDs. Column 1 gives the source location as defined by the boundaries in Figure 5.5. For sources outside of the clumps, we use the designation "Off Clump". Column 2 gives the source name. We use the observation field (West or East) and the extraction number to define unique names for all our sources. Column 3 gives the detection quality (see below), where "WD" corresponds to well-detected sources and "PD" corresponds to poorly-detected sources. See Section 5.3.2 for more details. Column 4 gives the SED fit quality, where "G"' corresponds to a good fit and "B" corresponds to a bad fit. We outlined the details for the fit quality in Section 5.4.2. Columns 5-7 give the best-fit SED parameters of mass, temperature, and the reduced χ^2. Column 8 gives the effective source radius, as measured from the 250 μm extraction and for a distance of 235 pc. The effective radius has been deconvolved with an 18.2$''$ beam. Column 9 gives the average density, assuming a spherical source and a mean molecular weight of $\mu = 2.8$.

We characterized each *Herschel* source identified by *getsources* as either "well-detected" (WD) or "poorly-detected" (PD) according to the significance of the detection and the robustness of the flux measurements obtained by *getsources*. A well-detected source met each of the following criteria;

1. a *getsources* global goodness parameter > 1 (see Section 5.3.1),

2. a semi-major axis at 500 μm $< 180''$,

3. a low aspect ratio ($a/b \leq 2$) in at least three bands between 160 $-$ 500 μm,

4. a SNR ≥ 5 in at least two *Herschel* bands and a SNR ≥ 3 in at least one other *Herschel* band between 160 μm $-$ 500 μm.

The first condition generally removes unreliable or spurious detections. From experience, sources with *good* < 1 are unreliable. The second condition removes large, fluffy sources unlikely to be dense cores. Since cores are generally < 0.1 pc in size, we imposed a very conservative upper limit for the detected size of $180''$ (~ 0.2 pc at a distance of 235 pc). We selected only the 500 μm band for this condition since it has the coarsest resolution. The third condition ensures we are selecting cores rather than small fragments of filaments. While cores themselves can be elongated, most have aspect ratios of $a/b \lesssim 2$ (Jijina et al. 1999; Offner & Krumholz 2009). The final condition selects objects that have well-measured fluxes in at least three wavebands. Objects that fail this condition could be due to poor signal (faint) or high noise (source is associated with a bright, diffuse background). We flag all well-detected sources with "WD" and all poorly-detected sources with "PD".

Table H.1. Results From SED Fitting

Location	Name	Quality[a]	Fit[b]	M ($M_\odot$)	T (K)	red χ^2	R (10^{-2} pc)	n (10^5 cm^{-3})
Off Clump	West1255	WD	B	0.7	12.6	4.4	6.8	0.1
Off Clump	West1136	WD	B	0.7	14.0	2.3	8.6	0.0
Off Clump	West829	WD	G	0.3	12.0	5.5×10^{-1}	3.9	0.2
Off Clump	West1091	WD	G	0.4	14.3	5.1×10^{-1}	5.7	0.1
Off Clump	West791	WD	G	0.0	12.7	2.5×10^{-2}	1.6	0.4
Off Clump	West716	WD	G	0.1	13.1	1.2	2.1	0.2
Off Clump	West740	WD	G	0.0	26.7	3.6×10^{-2}	1.3	0.1
Off Clump	West869	WD	G	0.1	14.2	2.1×10^{-4}	2.1	0.2
Off Clump	West413	WD	G	0.2	12.6	6.1×10^{-2}	2.6	0.4
Off Clump	West788	WD	G	1.1	11.4	1.8×10^{-2}	4.8	0.4
Off Clump	West263	WD	G	1.4	10.7	2.6×10^{-1}	3.2	1.5
Off Clump	West884	WD	G	0.6	13.2	1.1×10^{-1}	5.1	0.2
Off Clump	West272	WD	G	0.2	12.0	2.8×10^{-2}	1.8	1.2
L1448	West334	PD	G	0.7	12.0	4.1×10^{-4}	3.1	0.8
Off Clump	West454	WD	G	0.1	12.7	3.0×10^{-3}	2.2	0.4
Off Clump	West509	PD	G	0.5	8.9	7.1×10^{-2}	1.8	3.2
Off Clump	West663	PD	G	0.0	14.9	1.6×10^{-2}	1.6	0.3
L1448	West457	WD	G	0.1	21.2	6.3×10^{-2}	3.7	0.0
Off Clump	West789	WD	G	1.3	11.8	2.8×10^{-1}	6.9	0.1
L1448	West609	PD	B	-9.0	-9.0	9.0	1.8	-9.0
Off Clump	West705	WD	G	0.9	8.8	1.2×10^{-1}	2.4	2.2
Off Clump	West417	WD	G	1.5	9.0	4.0×10^{-1}	3.2	1.5
Off Clump	West662	WD	B	0.3	12.1	2.3	4.2	0.1
L1448	West437	WD	G	0.4	12.9	2.9×10^{-2}	3.9	0.2
Off Clump	West284	WD	G	2.6	8.6	1.2×10^{-1}	3.3	2.5
L1448	West639	PD	G	0.5	12.5	3.1×10^{-1}	4.5	0.2
Off Clump	West859	WD	G	1.5	11.8	9.9×10^{-2}	5.0	0.4
L1448	West714	PD	B	0.0	400.0	2.2×10^{1}	8.2	0.0
L1448	West146	PD	G	0.0	17.9	1.4×10^{-1}	0.7	2.7
L1448	West32	PD	B	-9.0	-9.0	9.0	0.2	-9.0
Off Clump	West160	WD	B	2.3	7.8	2.9	1.4	26.7
L1448	West612	PD	G	0.1	10.7	8.9×10^{-2}	1.4	1.9
L1448	West458	WD	G	0.3	14.1	6.7×10^{-2}	3.3	0.3
L1448	West238	PD	G	0.4	11.1	8.3×10^{-2}	2.1	1.7
Off Clump	West909	WD	B	0.3	11.9	9.1	4.2	0.1
Off Clump	West243	WD	G	4.9	10.8	5.2×10^{-3}	5.5	1.0
Off Clump	West616	WD	G	0.5	13.8	5.1×10^{-2}	5.6	0.1
L1448	West264	PD	B	-9.0	-9.0	9.0	1.7	-9.0
L1448	West375	PD	B	-9.0	-9.0	9.0	2.2	-9.0
L1448	West9	WD	B	0.8	16.5	6.8	0.0	-9.0
Off Clump	West637	WD	B	0.2	13.4	3.2	2.4	0.4
Off Clump	West875	PD	G	0.1	12.9	1.0×10^{-2}	1.6	0.5
L1448	West1049	PD	B	-9.0	-9.0	9.0	3.6	-9.0

Table H.1 (cont'd)

Location	Name	Quality[a]	Fit[b]	M ($M_\odot$)	T (K)	red χ^2	R (10^{-2} pc)	n (10^5 cm^{-3})
L1448	West99	PD	B	3.3	8.4	1.3	0.8	216.0
Off Clump	West279	WD	G	1.4	10.1	1.4×10^{-2}	3.5	1.1
Off Clump	West804	WD	G	0.2	13.8	1.1×10^{-2}	3.7	0.2
L1448	West223	PD	B	-9.0	-9.0	9.0	1.3	-9.0
Off Clump	West280	WD	B	2.7	11.0	3.2	5.4	0.6
Off Clump	West310	WD	G	0.1	10.6	2.3×10^{-1}	1.0	4.0
L1448	West230	WD	B	1.1	11.2	4.5	4.4	0.4
L1448	West25	WD	B	1.6	13.9	7.5	0.2	6417.0
Off Clump	West753	WD	G	0.1	14.2	1.0×10^{-1}	2.2	0.3
L1448	West8	WD	B	3.7	14.7	8.5	0.2	10521.0
Off Clump	West453	PD	G	23.5	7.8	4.1×10^{-1}	5.6	4.5
Off Clump	West452	WD	G	3.0	10.5	7.0×10^{-1}	4.8	0.9
Off Clump	West278	WD	G	0.6	10.0	8.1×10^{-2}	2.1	2.3
L1448	West397	WD	G	0.2	12.5	2.1×10^{-2}	2.4	0.4
Off Clump	West351	WD	B	0.3	11.3	1.5	2.0	1.2
L1448	West4	WD	B	1.5	17.6	4.3	0.1	40163.3
L1448	West629	PD	B	-9.0	-9.0	-9.0	2.1	-9.0
Off Clump	West349	WD	G	0.5	12.4	1.1	3.7	0.4
Off Clump	West636	PD	G	0.1	13.0	1.6×10^{-1}	1.6	0.6
L1448	West584	PD	G	0.5	11.8	1.7×10^{-1}	4.7	0.2
L1448	West613	PD	B	-9.0	-9.0	9.0	1.7	-9.0
Off Clump	West954	WD	G	0.6	11.1	7.1×10^{-2}	4.6	0.2
Off Clump	West451	WD	G	0.1	13.9	9.5×10^{-2}	2.4	0.2
Off Clump	West920	WD	G	0.1	13.2	2.0×10^{-2}	1.9	0.3
Off Clump	West907	PD	G	0.4	8.3	9.9×10^{-2}	1.4	4.7
Off Clump	West617	WD	G	0.1	13.0	6.1×10^{-2}	1.8	0.4
Off Clump	West574	WD	B	0.4	13.1	7.0	5.1	0.1
L1448	West251	PD	B	-9.0	-9.0	9.0	1.9	-9.0
Off Clump	West692	WD	G	0.7	12.5	5.2×10^{-4}	4.2	0.3
L1448	West1047	WD	G	0.2	12.4	1.7×10^{-1}	2.8	0.3
Off Clump	West416	WD	G	1.9	10.0	3.3×10^{-2}	3.5	1.5
L1448	West197	PD	G	4.2	8.7	3.0×10^{-3}	2.8	6.7
L1448	West191	WD	G	1.2	9.9	1.3×10^{-1}	2.1	4.2
L1448	West353	PD	B	-9.0	-9.0	9.0	2.0	-9.0
L1448	West382	PD	B	-9.0	-9.0	9.0	1.0	-9.0
Off Clump	West463	WD	G	0.2	13.8	2.1×10^{-1}	3.1	0.2
Off Clump	West332	PD	B	0.6	11.2	1.0×10^{1}	3.0	0.8
L1448	West1148	PD	G	0.0	16.2	4.7×10^{-1}	1.9	0.1
Off Clump	West635	WD	G	0.0	14.4	9.7×10^{-3}	1.9	0.2
Off Clump	West906	PD	G	0.5	13.8	2.1×10^{-1}	6.0	0.1
L1448	West213	WD	G	0.2	11.4	1.5×10^{-1}	1.6	1.8
L1448	West287	WD	G	1.3	12.4	6.0×10^{-1}	4.0	0.7
Off Clump	West111	PD	B	-9.0	-9.0	9.0	0.0	-9.0

Table H.1 (cont'd)

Location	Name	Quality[a]	Fit[b]	M ($M_\odot$)	T (K)	red χ^2	R (10^{-2} pc)	n (10^5 cm^{-3})
Off Clump	West659	PD	B	-9.0	-9.0	9.0	0.0	-9.0
L1448	West244	WD	G	0.8	11.6	1.4×10^{-1}	3.1	0.9
L1448	West265	WD	G	0.3	11.0	4.6×10^{-1}	1.6	2.7
Off Clump	West870	WD	G	0.1	14.8	8.3×10^{-1}	4.0	0.0
L1448	West641	PD	G	0.1	13.5	9.6×10^{-2}	1.5	0.6
L1448	West608	PD	G	0.1	11.3	3.8×10^{-2}	1.2	1.3
L1448	West327	WD	G	0.2	12.2	2.0×10^{-2}	1.7	1.1
Off Clump	West604	WD	G	0.2	12.7	7.5×10^{-2}	3.1	0.3
L1448	West583	PD	B	0.1	15.3	1.6	3.7	0.0
Off Clump	West605	WD	G	0.1	12.7	4.7×10^{-3}	2.5	0.2
L1448	West668	PD	G	0.3	10.1	7.6×10^{-1}	2.5	0.6
Off Clump	West481	PD	G	0.1	11.7	1.8×10^{-1}	1.8	0.6
Off Clump	West1141	WD	G	0.2	13.8	6.1×10^{-1}	4.4	0.1
L1448	West312	PD	G	0.5	9.1	3.1×10^{-1}	1.6	3.9
L1448	West399	PD	G	0.1	13.5	1.1×10^{-3}	2.8	0.2
L1448	West396	WD	G	0.2	11.8	2.0×10^{-2}	2.7	0.3
Off Clump	West857	WD	G	1.7	11.1	1.4×10^{-2}	5.2	0.4
L1448	West582	WD	G	0.1	12.6	1.4×10^{-1}	2.7	0.2
L1448	West325	WD	G	0.6	11.5	8.5×10^{-3}	3.6	0.5
Off Clump	West1093	WD	B	0.6	14.2	2.8	7.9	0.0
Off Clump	West873	WD	G	0.0	14.1	1.6×10^{-3}	2.2	0.1
Off Clump	West721	WD	G	0.6	12.9	3.4×10^{-1}	4.5	0.2
Off Clump	West863	WD	G	0.1	13.6	3.0×10^{-3}	2.6	0.2
Off Clump	West761	WD	G	0.3	13.7	5.2×10^{-3}	3.6	0.2
Off Clump	West20	WD	B	0.4	13.9	2.3×10^{1}	0.0	-9.0
Off Clump	West886	PD	G	0.0	15.0	2.8×10^{-1}	1.7	0.3
Off Clump	West760	WD	G	0.1	12.0	4.7×10^{-1}	2.4	0.4
Off Clump	West658	WD	G	0.5	14.1	1.0	6.2	0.1
L1455	West1097	WD	B	0.3	9.8	1.9	2.9	0.4
L1455	West958	WD	G	0.9	14.7	8.2×10^{-1}	8.0	0.1
Off Clump	West840	PD	G	0.0	18.8	9.1×10^{-2}	0.6	0.6
L1455	West226	WD	G	1.4	11.3	1.1×10^{-1}	4.1	0.7
Off Clump	West268	WD	G	0.5	12.6	1.2×10^{-1}	2.8	0.8
Off Clump	West488	WD	G	0.2	13.7	1.3×10^{-1}	3.1	0.3
Off Clump	West855	WD	G	0.1	13.7	3.0×10^{-1}	2.5	0.2
L1455	West1054	PD	G	0.0	26.5	5.0×10^{-2}	2.5	0.0
L1455	West580	PD	G	0.2	11.0	1.8×10^{-2}	2.1	0.6
Off Clump	West216	WD	G	1.1	12.6	3.1×10^{-3}	3.6	0.8
L1455	West688	PD	G	1.3	10.7	4.5×10^{-1}	4.5	0.5
L1455	West935	WD	G	0.2	14.1	1.3×10^{-1}	3.2	0.2
L1455	West323	WD	B	0.7	13.5	1.5	4.1	0.4
L1455	West254	WD	G	0.2	14.2	4.1×10^{-1}	2.9	0.3
L1455	West708	PD	G	0.0	13.9	1.4×10^{-1}	1.0	0.8

Table H.1 (cont'd)

Location	Name	Quality[a]	Fit[b]	M ($M_\odot$)	T (K)	red χ^2	R (10^{-2} pc)	n (10^5 cm^{-3})
L1455	West352	WD	G	0.7	12.7	7.2×10^{-2}	4.2	0.3
L1455	West537	PD	B	-9.0	-9.0	9.0	1.5	-9.0
L1455	West575	WD	G	0.3	12.7	3.1×10^{-1}	3.4	0.3
L1455	West745	PD	B	0.6	9.6	2.2	3.2	0.6
L1455	West373	WD	B	3.1	10.9	8.1	5.1	0.8
L1455	West374	WD	G	0.1	13.9	4.8×10^{-4}	2.3	0.4
L1455	West419	WD	G	0.8	10.5	7.6×10^{-2}	3.2	0.8
L1455	West412	WD	G	0.5	9.0	1.9×10^{-1}	1.5	4.3
L1455	West567	WD	G	0.3	11.5	5.0×10^{-3}	3.0	0.3
L1455	West350	PD	G	1.5	9.7	4.3×10^{-3}	3.2	1.6
L1455	West880	WD	G	0.8	12.9	3.8×10^{-1}	6.4	0.1
L1455	West638	PD	B	-9.0	-9.0	-9.0	1.9	-9.0
L1455	West239	PD	G	0.6	9.9	2.5×10^{-1}	1.6	4.3
L1455	West792	PD	B	-9.0	-9.0	9.0	1.3	-9.0
L1455	West910	WD	G	0.1	11.4	6.5×10^{-3}	2.2	0.5
L1455	West607	PD	B	-9.0	-9.0	9.0	1.4	-9.0
L1455	West35	WD	B	0.4	13.5	3.5	0.3	299.8
L1455	West395	WD	G	0.3	11.8	9.6×10^{-3}	2.7	0.6
L1455	West285	WD	B	8.7	8.4	3.1	5.2	2.2
L1455	West5	WD	B	0.5	18.7	1.1×10^{1}	0.0	-9.0
L1455	West772	WD	G	0.2	12.2	3.2×10^{-3}	2.8	0.3
L1455	West394	WD	G	0.2	11.3	1.0	2.0	0.9
L1455	West161	PD	G	7.7	6.7	7.3×10^{-1}	0.9	363.9
NGC1333	West365	WD	G	0.4	9.1	3.4×10^{-1}	1.5	4.0
L1455	West435	PD	G	0.1	12.5	4.4×10^{-1}	1.4	0.9
L1455	West18	WD	B	0.6	13.9	3.8×10^{1}	0.0	-9.0
L1455	West540	WD	G	0.1	17.1	1.0×10^{-2}	2.4	0.2
L1455	West311	PD	B	-9.0	-9.0	9.0	0.6	-9.0
L1455	West611	PD	B	0.2	12.6	2.9	3.3	0.2
L1455	West478	PD	G	1.0	8.5	3.9×10^{-2}	2.0	4.5
L1455	West36	WD	B	0.8	12.1	1.9×10^{1}	0.5	239.1
L1455	West606	PD	B	-9.0	-9.0	9.0	1.5	-9.0
L1455	West793	PD	B	-9.0	-9.0	9.0	1.0	-9.0
L1455	West860	WD	G	0.2	12.5	4.9×10^{-1}	3.8	0.1
L1455	West286	PD	B	-9.0	-9.0	9.0	1.1	-9.0
L1455	West237	PD	G	0.5	9.4	1.4×10^{-1}	1.5	5.1
L1455	West418	WD	G	0.6	10.8	2.4×10^{-2}	2.6	1.1
L1455	West568	WD	G	0.5	10.3	2.5×10^{-2}	2.4	1.3
L1455	West1142	PD	B	-9.0	-9.0	-9.0	2.1	-9.0
NGC1333	West725	PD	B	2.6	12.8	8.4×10^{1}	12.0	0.1
L1455	West1144	PD	B	-9.0	-9.0	9.0	1.6	-9.0
L1455	West456	PD	G	0.2	13.3	5.3×10^{-2}	3.4	0.2
L1455	West577	PD	G	0.1	11.0	5.6×10^{-2}	1.5	1.2

Table H.1 (cont'd)

Location	Name	Quality[a]	Fit[b]	M ($M_\odot$)	T (K)	red χ^2	R (10^{-2} pc)	n (10^5 cm^{-3})
Off Clump	West948	WD	G	0.1	15.1	3.0×10^{-5}	3.0	0.1
L1455	West821	PD	G	0.0	18.6	1.8×10^{-1}	2.3	0.1
L1455	West82	WD	B	0.1	10.9	7.8	0.4	97.8
NGC1333	West1065	PD	B	1.4	10.8	3.6	5.0	0.4
L1455	West664	PD	G	0.1	10.7	2.8×10^{-3}	1.6	1.2
Off Clump	West1094	WD	G	0.7	13.4	1.2	5.8	0.1
L1455	West748	WD	G	2.7	10.5	1.1	5.8	0.5
L1455	West477	WD	G	0.3	11.5	1.7×10^{-5}	2.5	0.7
L1455	West541	PD	G	2.0	8.6	3.2×10^{-1}	3.4	1.8
L1455	West480	WD	G	0.6	11.9	1.6×10^{-2}	3.6	0.4
NGC1333	West1205	PD	G	0.0	13.9	5.7×10^{-4}	1.3	0.4
L1455	West794	WD	G	0.2	11.4	3.5×10^{-3}	2.6	0.5
NGC1333	West897	PD	G	0.1	11.0	6.0×10^{-2}	1.5	1.0
NGC1333	West589	WD	G	0.2	11.5	1.1×10^{-1}	2.2	0.8
NGC1333	West718	WD	G	0.3	9.8	2.2×10^{-1}	2.2	1.1
L1455	West915	PD	G	0.2	9.5	5.4×10^{-2}	2.0	1.0
Off Clump	West1151	WD	G	0.2	13.0	1.4×10^{-1}	3.9	0.1
NGC1333	West919	WD	G	0.3	12.7	4.0×10^{-2}	3.2	0.3
L1455	West742	WD	G	0.2	13.6	2.5×10^{-1}	3.5	0.1
NGC1333	West384	PD	G	0.3	9.6	1.7×10^{-2}	1.4	3.5
NGC1333	West339	WD	G	0.5	10.0	4.3×10^{-1}	1.9	2.5
NGC1333	West644	PD	B	-9.0	-9.0	9.0	1.5	-9.0
NGC1333	West1032	PD	B	0.1	17.2	1.4	4.5	0.0
NGC1333	West835	PD	B	-9.0	-9.0	-9.0	2.5	-9.0
NGC1333	West834	WD	G	0.8	11.5	8.0×10^{-4}	4.1	0.4
L1455	West542	PD	G	0.5	11.5	3.4×10^{-4}	3.4	0.4
NGC1333	West549	WD	G	0.3	12.3	8.2×10^{-2}	2.9	0.4
L1455	West586	WD	G	0.3	10.6	1.9×10^{-1}	2.5	0.6
NGC1333	West362	PD	G	1.8	7.4	2.0×10^{-1}	1.6	14.1
NGC1333	West377	PD	G	0.4	9.6	2.6×10^{-1}	1.7	2.9
L1455	West383	WD	G	0.4	11.7	3.3×10^{-2}	3.0	0.5
NGC1333	West222	PD	B	-9.0	-9.0	9.0	1.1	-9.0
L1455	West333	WD	G	0.1	13.3	2.1×10^{-1}	2.2	0.4
NGC1333	West425	PD	B	-9.0	-9.0	9.0	3.3	-9.0
NGC1333	West363	PD	B	-9.0	-9.0	9.0	1.4	-9.0
NGC1333	West464	PD	G	0.3	8.7	1.7×10^{-1}	0.6	51.4
NGC1333	West198	PD	B	-9.0	-9.0	9.0	1.2	-9.0
NGC1333	West86	WD	B	0.2	12.6	6.0	0.3	277.2
NGC1333	West809	WD	B	0.2	13.2	2.0	3.0	0.3
NGC1333	West420	WD	G	3.3	9.1	4.0×10^{-4}	3.9	2.0
L1455	West245	WD	G	0.5	11.4	5.2×10^{-1}	2.3	1.2
NGC1333	West31	WD	B	0.1	16.3	4.6	0.3	66.7
NGC1333	West96	WD	G	0.2	11.4	8.6×10^{-1}	0.0	-9.0

Table H.1 (cont'd)

Location	Name	Quality[a]	Fit[b]	M ($M_\odot$)	T (K)	red χ^2	R (10^{-2} pc)	n (10^5 cm^{-3})
NGC1333	West361	WD	G	0.5	12.8	2.1×10^{-2}	3.8	0.3
Off Clump	West486	WD	G	0.2	14.3	2.3×10^{-1}	2.4	0.4
NGC1333	West129	PD	B	0.1	12.6	1.4	0.3	167.7
NGC1333	West3	WD	B	0.4	19.7	9.2	0.2	2706.7
L1455	West747	PD	B	0.3	13.2	2.1	6.0	0.1
NGC1333	West414	PD	G	0.4	9.8	2.3×10^{-2}	1.4	4.8
Off Clump	West328	PD	B	-9.0	-9.0	9.0	0.5	-9.0
NGC1333	West162	WD	G	3.4	9.4	1.0	2.9	4.8
NGC1333	West366	WD	G	2.0	10.2	4.0×10^{-5}	3.2	2.2
NGC1333	West209	PD	B	-9.0	-9.0	9.0	1.0	-9.0
NGC1333	West149	PD	G	5.2	10.6	2.3×10^{-1}	3.1	5.8
NGC1333	West722	PD	B	-9.0	-9.0	9.0	0.8	-9.0
Off Clump	West348	WD	G	0.1	12.0	1.0×10^{-1}	1.8	0.7
Off Clump	West968	WD	G	0.1	13.3	2.3×10^{-1}	3.3	0.1
L1455	West547	WD	G	0.1	13.5	9.4×10^{-3}	2.5	0.2
NGC1333	West371	WD	G	1.0	12.2	2.2×10^{-1}	3.9	0.6
NGC1333	West133	WD	B	0.2	13.9	1.7	0.7	24.7
NGC1333	West757	PD	G	1.8	7.4	2.9×10^{-1}	1.2	41.3
Off Clump	West338	WD	B	3.9	10.7	7.1	6.0	0.6
NGC1333	West281	WD	G	3.1	7.3	5.0×10^{-1}	1.3	50.9
NGC1333	West228	PD	B	-9.0	-9.0	-9.0	0.8	-9.0
NGC1333	West330	PD	B	-9.0	-9.0	9.0	0.4	-9.0
NGC1333	West39	WD	G	0.2	14.1	1.1	0.5	63.2
L1455	West455	WD	G	0.5	9.5	2.1×10^{-3}	2.5	1.2
NGC1333	West1210	PD	B	-9.0	-9.0	9.0	1.6	-9.0
NGC1333	West559	PD	B	-9.0	-9.0	9.0	1.1	-9.0
NGC1333	West314	PD	B	-9.0	-9.0	9.0	3.0	-9.0
NGC1333	West38	WD	B	0.2	12.6	1.2×10^{1}	0.4	124.2
NGC1333	West441	PD	B	-9.0	-9.0	-9.0	5.2	-9.0
Off Clump	West1152	WD	B	0.1	19.0	5.0	5.5	0.0
NGC1333	West591	PD	G	0.1	11.8	1.6×10^{-2}	1.8	0.8
NGC1333	West276	PD	B	-9.0	-9.0	9.0	1.6	-9.0
L1455	West485	WD	G	0.2	14.2	4.9×10^{-1}	3.4	0.2
NGC1333	West894	PD	B	-9.0	-9.0	9.0	1.0	-9.0
L1455	West667	PD	B	-9.0	-9.0	-9.0	1.0	-9.0
NGC1333	West200	PD	B	-9.0	-9.0	9.0	1.5	-9.0
NGC1333	West494	PD	B	-9.0	-9.0	9.0	1.4	-9.0
NGC1333	West898	PD	B	-9.0	-9.0	9.0	1.4	-9.0
NGC1333	West282	PD	B	-9.0	-9.0	9.0	1.1	-9.0
NGC1333	West140	PD	B	-9.0	-9.0	9.0	0.9	-9.0
Off Clump	West67	PD	G	0.4	13.6	3.4×10^{-1}	2.6	0.7
NGC1333	West258	PD	B	-9.0	-9.0	9.0	0.2	-9.0
NGC1333	West387	WD	G	1.3	12.4	1.2×10^{-2}	5.6	0.3

Table H.1 (cont'd)

Location	Name	Quality[a]	Fit[b]	M ($M_\odot$)	T (K)	red χ^2	R (10^{-2} pc)	n (10^5 cm^{-3})
Off Clump	West255	PD	B	0.2	12.1	1.3×10^{1}	2.2	0.6
Off Clump	West439	WD	G	1.3	13.0	8.2×10^{-2}	5.8	0.2
NGC1333	West150	PD	B	-9.0	-9.0	9.0	1.4	-9.0
NGC1333	West247	WD	G	1.8	10.7	4.7×10^{-1}	3.7	1.2
NGC1333	West270	PD	G	0.1	12.7	8.0×10^{-3}	1.0	3.1
L1455	West862	PD	G	0.4	10.5	3.2×10^{-2}	2.8	0.5
NGC1333	West329	PD	B	-9.0	-9.0	9.0	1.4	-9.0
NGC1333	West173	PD	B	-9.0	-9.0	9.0	1.3	-9.0
NGC1333	West75	PD	G	2.2	10.0	7.1×10^{-2}	0.3	2360.5
L1455	West381	WD	G	2.9	10.5	1.5×10^{-2}	5.5	0.6
NGC1333	West495	PD	B	-9.0	-9.0	9.0	1.2	-9.0
NGC1333	West78	PD	B	-9.0	-9.0	9.0	0.4	-9.0
NGC1333	West407	PD	B	-9.0	-9.0	9.0	0.6	-9.0
NGC1333	West887	PD	B	-9.0	-9.0	9.0	1.3	-9.0
NGC1333	West493	PD	B	-9.0	-9.0	9.0	0.4	-9.0
NGC1333	West208	PD	B	-9.0	-9.0	9.0	0.0	-9.0
NGC1333	West210	PD	B	-9.0	-9.0	9.0	0.7	-9.0
NGC1333	West838	PD	B	-9.0	-9.0	9.0	0.9	-9.0
NGC1333	West141	PD	B	-9.0	-9.0	9.0	1.5	-9.0
NGC1333	West1	WD	B	1.7	21.1	5.3	0.2	11309.7
L1455	West666	WD	G	1.0	10.7	4.0×10^{-3}	4.2	0.5
Off Clump	West691	WD	G	0.6	12.4	2.0×10^{-1}	3.8	0.4
NGC1333	West206	PD	B	-9.0	-9.0	9.0	0.4	-9.0
NGC1333	West121	PD	B	-9.0	-9.0	9.0	1.3	-9.0
NGC1333	West91	PD	B	-9.0	-9.0	9.0	0.7	-9.0
NGC1333	West290	PD	B	-9.0	-9.0	9.0	0.5	-9.0
NGC1333	West104	PD	B	-9.0	-9.0	9.0	0.0	-9.0
L1455	West511	WD	G	0.8	10.7	5.3×10^{-1}	3.9	0.5
NGC1333	West10	WD	B	0.4	16.8	6.7	0.4	202.5
NGC1333	West88	PD	B	-9.0	-9.0	9.0	0.5	-9.0
NGC1333	West720	PD	G	0.7	10.3	4.2×10^{-1}	4.1	0.3
NGC1333	West119	PD	B	-9.0	-9.0	9.0	0.7	-9.0
NGC1333	West492	PD	B	-9.0	-9.0	9.0	0.6	-9.0
NGC1333	West43	PD	B	-9.0	-9.0	9.0	0.3	-9.0
NGC1333	West267	PD	B	-9.0	-9.0	9.0	0.9	-9.0
Off Clump	West631	PD	B	0.0	400.0	9.9	7.2	0.0
NGC1333	West53	PD	B	-9.0	-9.0	9.0	0.7	-9.0
NGC1333	West211	PD	B	-9.0	-9.0	9.0	1.4	-9.0
NGC1333	West426	PD	B	-9.0	-9.0	9.0	1.9	-9.0
NGC1333	West148	PD	B	-9.0	-9.0	9.0	0.7	-9.0
NGC1333	West190	PD	B	-9.0	-9.0	9.0	0.4	-9.0
NGC1333	West471	WD	G	0.3	15.5	3.8×10^{-1}	4.6	0.1
NGC1333	West130	PD	B	-9.0	-9.0	9.0	0.4	-9.0

Table H.1 (cont'd)

Location	Name	Quality[a]	Fit[b]	M ($M_\odot$)	T (K)	red χ^2	R (10^{-2} pc)	n (10^5 cm^{-3})
NGC1333	West63	WD	B	10.9	8.8	1.8	1.7	75.2
NGC1333	West33	PD	B	0.4	13.6	1.3	0.2	1253.2
NGC1333	West164	PD	B	-9.0	-9.0	9.0	0.8	-9.0
NGC1333	West15	WD	B	3.0	14.2	2.8×10^{1}	0.4	1500.8
NGC1333	West340	PD	B	-9.0	-9.0	9.0	0.5	-9.0
NGC1333	West558	PD	B	0.2	15.9	5.3	4.8	0.1
NGC1333	West19	WD	B	5.9	11.1	2.4	0.5	1285.9
NGC1333	West217	PD	B	-9.0	-9.0	9.0	1.1	-9.0
NGC1333	West165	PD	B	-9.0	-9.0	9.0	1.7	-9.0
NGC1333	West553	WD	G	0.8	12.6	1.0×10^{-2}	4.1	0.4
NGC1333	West199	PD	B	-9.0	-9.0	9.0	1.0	-9.0
NGC1333	West68	PD	B	-9.0	-9.0	9.0	0.1	-9.0
NGC1333	West77	PD	B	-9.0	-9.0	9.0	0.6	-9.0
NGC1333	West2	WD	B	2.5	17.6	2.1	0.4	1856.1
NGC1333	West266	PD	B	-9.0	-9.0	9.0	1.0	-9.0
L1455	West711	WD	B	0.4	10.0	9.5	3.1	0.5
NGC1333	West40	PD	G	13.3	7.1	9.9×10^{-2}	0.6	2237.5
NGC1333	West232	PD	B	-9.0	-9.0	9.0	0.8	-9.0
NGC1333	West124	PD	G	1.7	11.3	6.0×10^{-2}	2.0	7.8
NGC1333	West48	WD	B	6.3	9.6	1.6	0.9	313.3
NGC1333	West120	PD	B	-9.0	-9.0	9.0	0.7	-9.0
NGC1333	West47	PD	B	2.6	10.3	3.8	0.4	1391.2
NGC1333	West291	PD	B	-9.0	-9.0	9.0	0.7	-9.0
NGC1333	West155	PD	B	-9.0	-9.0	9.0	0.3	-9.0
NGC1333	West125	PD	B	-9.0	-9.0	9.0	0.4	-9.0
NGC1333	West922	PD	G	0.1	14.0	2.1×10^{-2}	3.0	0.2
NGC1333	West87	PD	B	20.6	6.7	3.2	0.8	1437.8
L1455	West1167	WD	G	0.1	12.5	1.4×10^{-2}	3.3	0.1
NGC1333	West92	WD	G	2.5	10.6	1.1×10^{-2}	1.4	33.4
NGC1333	West7	WD	B	0.5	19.3	7.2	0.5	131.1
NGC1333	West201	PD	B	-9.0	-9.0	9.0	0.8	-9.0
NGC1333	West194	PD	B	-9.0	-9.0	9.0	0.6	-9.0
Off Clump	West961	WD	G	0.2	11.2	2.9×10^{-1}	2.5	0.4
NGC1333	West42	PD	B	-9.0	-9.0	9.0	0.7	-9.0
NGC1333	West212	PD	B	-9.0	-9.0	9.0	1.8	-9.0
Off Clump	West614	WD	G	1.4	11.8	5.7×10^{-1}	5.6	0.3
Off Clump	West832	PD	G	0.1	12.0	9.7×10^{-2}	1.3	0.9
NGC1333	West890	PD	B	-9.0	-9.0	9.0	1.3	-9.0
Off Clump	West532	WD	G	0.1	15.0	6.0×10^{-3}	2.4	0.2
NGC1333	West6	WD	B	5.0	14.4	1.0×10^{1}	0.0	-9.0
Off Clump	West669	WD	G	0.1	15.3	5.1×10^{-1}	2.1	0.2
NGC1333	West11	WD	B	0.3	30.2	1.0×10^{1}	1.2	6.0
NGC1333	West16	WD	G	0.2	19.1	2.2×10^{-1}	0.3	195.1

Table H.1 (cont'd)

Location	Name	Quality[a]	Fit[b]	M ($M_\odot$)	T (K)	red χ^2	R (10^{-2} pc)	n (10^5 cm^{-3})
NGC1333	West14	WD	B	1.2	15.3	2.4	0.4	816.9
NGC1333	West180	PD	B	-9.0	-9.0	9.0	0.9	-9.0
NGC1333	West13	WD	B	3.2	14.3	2.6	0.1	46869.2
NGC1333	West215	PD	B	-9.0	-9.0	9.0	0.6	-9.0
NGC1333	West317	PD	B	-9.0	-9.0	9.0	1.0	-9.0
NGC1333	West154	PD	B	-9.0	-9.0	9.0	1.0	-9.0
NGC1333	West315	PD	B	-9.0	-9.0	9.0	1.1	-9.0
NGC1333	West110	PD	B	-9.0	-9.0	9.0	1.0	-9.0
NGC1333	West49	PD	B	-9.0	-9.0	9.0	0.1	-9.0
NGC1333	West83	PD	B	-9.0	-9.0	9.0	1.4	-9.0
NGC1333	West30	PD	B	0.5	14.2	4.8	0.0	-9.0
NGC1333	West143	PD	G	3.3	8.4	1.7×10^{-8}	0.7	334.0
NGC1333	West205	PD	B	-9.0	-9.0	9.0	1.2	-9.0
NGC1333	West81	PD	B	-9.0	-9.0	9.0	1.4	-9.0
NGC1333	West181	PD	G	0.3	12.0	1.0×10^{-1}	1.2	6.2
NGC1333	West122	PD	B	-9.0	-9.0	9.0	0.3	-9.0
Off Clump	West787	WD	G	0.3	14.2	3.5×10^{-1}	4.6	0.1
Off Clump	West581	WD	G	0.0	13.4	1.1×10^{-1}	1.5	0.4
NGC1333	West131	PD	B	-9.0	-9.0	9.0	0.8	-9.0
NGC1333	West203	PD	B	-9.0	-9.0	9.0	0.9	-9.0
NGC1333	West94	PD	B	-9.0	-9.0	9.0	1.2	-9.0
NGC1333	West23	WD	G	0.4	14.7	5.5×10^{-1}	0.3	447.9
NGC1333	West260	PD	B	-9.0	-9.0	9.0	1.0	-9.0
NGC1333	West561	WD	G	0.4	13.0	8.3×10^{-1}	4.0	0.2
NGC1333	West116	PD	B	-9.0	-9.0	9.0	0.6	-9.0
NGC1333	West341	PD	G	0.6	9.7	8.8×10^{-3}	0.7	56.7
NGC1333	West409	PD	B	-9.0	-9.0	9.0	1.5	-9.0
NGC1333	West195	PD	G	0.6	10.1	3.3×10^{-1}	0.6	88.4
NGC1333	West473	PD	G	0.8	7.6	4.0×10^{-2}	1.5	9.0
NGC1333	West37	PD	G	0.6	13.2	2.7×10^{-1}	0.2	4236.9
NGC1333	West229	PD	B	-9.0	-9.0	9.0	0.0	-9.0
NGC1333	West60	WD	G	0.9	20.0	4.3×10^{-1}	3.5	0.7
NGC1333	West259	PD	G	0.2	10.3	8.0×10^{-3}	1.3	3.3
NGC1333	West182	PD	B	-9.0	-9.0	9.0	0.6	-9.0
NGC1333	West55	WD	G	0.1	39.4	1.3×10^{-1}	2.5	0.3
NGC1333	West171	PD	B	-9.0	-9.0	9.0	2.4	-9.0
NGC1333	West560	PD	B	-9.0	-9.0	9.0	1.7	-9.0
NGC1333	West973	PD	B	-9.0	-9.0	9.0	1.2	-9.0
NGC1333	West157	PD	B	-9.0	-9.0	9.0	0.6	-9.0
NGC1333	West123	PD	B	-9.0	-9.0	9.0	0.9	-9.0
NGC1333	West592	PD	B	-9.0	-9.0	9.0	2.2	-9.0
NGC1333	West224	PD	B	-9.0	-9.0	9.0	1.2	-9.0
Off Clump	West436	WD	G	0.4	9.9	1.2×10^{-1}	2.4	1.0

Table H.1 (cont'd)

Location	Name	Quality[a]	Fit[b]	M ($M_\odot$)	T (K)	red χ^2	R (10^{-2} pc)	n (10^5 cm^{-3})
Off Clump	West861	PD	B	0.4	10.6	2.7	4.0	0.2
NGC1333	West44	WD	B	0.8	10.8	2.1×10^{1}	0.4	417.3
NGC1333	West319	WD	G	1.3	11.4	3.0×10^{-1}	5.4	0.3
NGC1333	West207	PD	B	-9.0	-9.0	9.0	0.9	-9.0
NGC1333	West726	PD	B	-9.0	-9.0	9.0	1.2	-9.0
NGC1333	West891	PD	B	-9.0	-9.0	9.0	2.1	-9.0
NGC1333	West522	PD	B	-9.0	-9.0	9.0	1.2	-9.0
NGC1333	West108	WD	G	0.7	10.8	2.3×10^{-2}	1.2	15.1
NGC1333	West1071	PD	B	-9.0	-9.0	9.0	2.1	-9.0
Off Clump	West628	WD	G	0.6	9.7	8.6×10^{-2}	2.8	1.0
NGC1333	West622	PD	B	0.6	8.0	1.7	1.4	6.8
Off Clump	West746	WD	G	0.1	13.5	1.2×10^{-1}	2.7	0.2
NGC1333	West697	PD	B	-9.0	-9.0	9.0	1.2	-9.0
NGC1333	West137	PD	B	-9.0	-9.0	9.0	0.0	-9.0
Off Clump	West324	WD	G	0.3	10.5	1.0×10^{-3}	2.4	0.7
NGC1333	West1008	PD	B	-9.0	-9.0	9.0	1.7	-9.0
NGC1333	West807	PD	B	-9.0	-9.0	9.0	2.2	-9.0
Off Clump	West702	PD	G	0.0	15.3	5.1×10^{-2}	1.7	0.1
NGC1333	West844	PD	B	-9.0	-9.0	9.0	1.9	-9.0
Off Clump	West336	WD	G	0.2	11.6	2.3×10^{-3}	2.4	0.5
NGC1333	West763	PD	B	-9.0	-9.0	9.0	2.5	-9.0
NGC1333	West620	PD	B	-9.0	-9.0	9.0	2.9	-9.0
NGC1333	West940	PD	B	-9.0	-9.0	9.0	2.3	-9.0
Off Clump	West739	WD	G	0.0	17.9	1.1×10^{-2}	2.7	0.1
Off Clump	West300	WD	G	0.9	12.0	9.9×10^{-2}	4.4	0.4
NGC1333	West977	PD	B	-9.0	-9.0	9.0	1.0	-9.0
NGC1333	West768	WD	B	1.4	11.8	3.1	6.1	0.2
Off Clump	West640	PD	G	0.1	11.7	7.5×10^{-2}	1.4	0.6
Off Clump	West749	PD	G	0.2	10.3	2.3×10^{-1}	1.8	1.0
NGC1333	West444	PD	B	-9.0	-9.0	9.0	2.4	-9.0
NGC1333	West649	PD	G	0.4	9.2	3.4×10^{-1}	1.9	2.4
NGC1333	West28	WD	B	0.6	13.0	2.8×10^{1}	0.0	-9.0
NGC1333	West283	PD	B	-9.0	-9.0	9.0	0.0	-9.0
NGC1333	West730	PD	G	0.8	8.0	3.0×10^{-1}	1.6	7.4
NGC1333	West1012	PD	B	0.1	15.2	1.4×10^{1}	5.1	0.0
NGC1333	West292	WD	G	0.1	12.5	3.4×10^{-3}	1.6	1.0
Off Clump	West401	WD	G	0.0	13.9	1.4×10^{-2}	1.3	0.6
Off Clump	West1015	PD	B	0.5	13.2	1.5	6.6	0.1
Off Clump	West865	WD	G	0.1	13.2	5.1×10^{-2}	1.7	0.4
NGC1333	West573	WD	G	0.0	23.3	1.1	2.9	0.0
Off Clump	West885	WD	B	0.3	14.8	1.7×10^{1}	5.7	0.0
Off Clump	West1027	PD	G	0.4	11.0	1.8×10^{-1}	3.4	0.3
Off Clump	West175	PD	B	0.9	9.0	2.3	1.1	27.4

Table H.1 (cont'd)

Location	Name	Quality[a]	Fit[b]	M ($M_\odot$)	T (K)	red χ^2	R (10^{-2} pc)	n (10^5 cm^{-3})
Off Clump	West516	WD	G	0.7	12.3	8.5×10^{-1}	4.3	0.3
Off Clump	West833	WD	B	0.0	18.9	4.4	3.7	0.0
Off Clump	West21	WD	B	0.2	15.6	1.1×10^{1}	0.4	77.9
NGC1333	West682	WD	B	4.5	10.5	3.1	6.2	0.6
Off Clump	West252	WD	G	0.1	12.8	7.5×10^{-1}	0.4	54.5
Off Clump	West1106	WD	B	0.0	12.7	2.7	1.9	0.3
Off Clump	West62	PD	B	0.0	34.9	1.5	0.0	-9.0
Off Clump	West752	PD	G	0.1	12.9	4.9×10^{-2}	2.4	0.3
Off Clump	West717	WD	G	0.1	12.8	1.7×10^{-5}	1.6	0.4
Off Clump	West588	PD	B	0.1	14.4	2.6	2.9	0.2
Off Clump	West302	PD	G	0.2	11.2	4.3×10^{-2}	1.6	1.3
Off Clump	West400	PD	G	0.1	11.4	1.8×10^{-2}	1.5	1.2
Off Clump	West246	WD	G	0.5	13.6	6.5×10^{-1}	3.9	0.3
Off Clump	West51	PD	B	-9.0	-9.0	9.0	0.0	-9.0
Off Clump	West76	WD	B	0.8	9.5	1.9×10^{1}	0.3	682.6
Off Clump	West422	PD	G	0.2	9.6	9.9×10^{-2}	1.4	3.0
Off Clump	West1197	PD	B	-9.0	-9.0	9.0	1.6	-9.0
Off Clump	West402	WD	G	0.1	10.7	5.4×10^{-2}	1.3	1.7
Off Clump	West156	PD	B	-9.0	-9.0	9.0	0.0	-9.0
Off Clump	West587	WD	G	0.8	11.0	4.0×10^{-3}	3.4	0.7
Off Clump	West798	WD	G	0.6	11.9	1.4×10^{-2}	4.0	0.3
Off Clump	West690	WD	G	0.4	12.9	2.4×10^{-1}	4.1	0.2
Off Clump	West693	PD	G	0.1	12.4	3.8×10^{-2}	1.7	0.4
Off Clump	West52	PD	B	-9.0	-9.0	-9.0	0.0	-9.0
Off Clump	West515	WD	G	0.4	11.1	9.4×10^{-4}	2.9	0.6
Off Clump	West167	WD	G	4.8	10.3	1.0	5.4	1.1
Off Clump	West273	PD	B	0.2	13.4	1.7	2.2	0.6
Off Clump	West221	WD	G	0.6	10.7	3.6×10^{-4}	2.4	1.6
Off Clump	West170	WD	B	0.2	9.1	6.5	0.4	114.3
Off Clump	West918	WD	G	0.1	17.5	3.5×10^{-1}	4.6	0.0
Off Clump	West557	WD	G	0.1	12.3	5.6×10^{-3}	1.9	0.4
Off Clump	West483	WD	G	0.4	11.7	9.4×10^{-1}	3.5	0.4
Off Clump	West689	WD	G	0.1	18.0	1.6×10^{-1}	3.8	0.0
Off Clump	West460	WD	B	2.9	10.5	3.9	6.6	0.4
B1	West256	PD	G	0.5	10.6	3.9×10^{-4}	2.0	2.4
B1	West489	WD	B	0.6	10.7	7.0	3.3	0.6
B1	West274	PD	G	1.9	7.9	4.0×10^{-3}	1.2	33.6
B1	West17	WD	B	0.9	14.2	1.7×10^{1}	0.0	-9.0
B1	West670	PD	B	-9.0	-9.0	9.0	1.6	-9.0
Off Clump	West499	WD	G	0.1	13.0	4.6×10^{-1}	2.4	0.3
Off Clump	West128	WD	G	0.0	15.5	1.3	0.0	-9.0
B1	West1003	WD	G	0.1	15.8	3.7×10^{-1}	5.3	0.0
Off Clump	West1086	WD	B	2.4	9.2	1.5×10^{1}	4.8	0.8

Table H.1 (cont'd)

Location	Name	Quality[a]	Fit[b]	M ($M_\odot$)	T (K)	red χ^2	R (10^{-2} pc)	n (10^5 cm^{-3})
Off Clump	West484	PD	G	0.1	11.4	2.6×10^{-2}	1.1	1.5
Off Clump	West1221	PD	B	-9.0	-9.0	-9.0	1.1	-9.0
B1	West928	WD	G	0.1	15.5	1.4×10^{-1}	4.3	0.1
Off Clump	West354	WD	G	1.1	11.9	1.1×10^{-1}	4.3	0.5
Off Clump	West514	WD	G	0.2	13.0	7.3×10^{-2}	2.3	0.5
B1	West355	WD	G	0.9	11.7	1.3×10^{-1}	4.6	0.3
B1	West235	PD	B	-9.0	-9.0	9.0	0.6	-9.0
B1	West368	WD	G	0.5	12.2	1.4×10^{-2}	2.7	0.8
B1	West504	WD	G	0.0	14.9	3.9×10^{-1}	2.0	0.2
B1	West841	PD	B	-9.0	-9.0	9.0	2.1	-9.0
B1	West321	WD	B	2.1	11.8	1.7	5.3	0.5
B1	West700	PD	G	0.3	13.4	1.5×10^{-2}	3.9	0.2
B1	West895	WD	G	0.1	18.0	1.1×10^{-1}	4.1	0.1
B1	West723	PD	B	-9.0	-9.0	9.0	1.7	-9.0
Off Clump	West236	WD	G	0.8	13.0	6.5×10^{-1}	6.0	0.1
B1	West415	WD	G	0.6	13.1	1.3×10^{-3}	3.4	0.5
Off Clump	West432	PD	G	0.1	12.5	1.1×10^{-1}	1.7	0.6
B1	West632	WD	G	0.3	12.4	1.8×10^{-2}	2.6	0.6
B1	West406	PD	B	-9.0	-9.0	9.0	0.8	-9.0
B1	West430	PD	G	0.1	14.7	3.9×10^{-1}	2.7	0.2
B1	West597	WD	B	0.1	12.2	2.4	1.3	1.7
B1	West26	WD	B	1.6	12.4	1.6×10^{1}	0.0	-9.0
B1	West443	PD	G	0.2	11.3	4.8×10^{-2}	2.3	0.6
Off Clump	West308	WD	G	0.4	10.9	3.9×10^{-1}	2.7	0.7
B1	West839	PD	B	-9.0	-9.0	9.0	0.8	-9.0
B1	West695	PD	B	-9.0	-9.0	9.0	1.7	-9.0
B1	West900	PD	B	0.1	13.2	1.0	1.3	0.8
B1	West389	PD	B	1.9	12.0	1.1×10^{1}	5.8	0.3
Off Clump	West565	WD	G	0.2	12.1	4.8×10^{-1}	2.4	0.5
B1	West779	WD	G	0.3	13.1	4.8×10^{-2}	3.8	0.2
B1	West764	WD	G	0.3	11.6	4.3×10^{-1}	2.2	0.9
B1	West519	PD	G	2.6	7.6	7.6×10^{-3}	2.1	10.4
B1	West496	WD	G	0.3	13.5	5.5×10^{-2}	3.7	0.2
B1	West241	PD	G	1.7	9.6	1.0	2.4	4.5
B1	West674	PD	G	0.1	13.1	3.1×10^{-2}	2.3	0.4
B1	West202	PD	B	-9.0	-9.0	9.0	1.0	-9.0
B1	West899	PD	G	0.1	11.8	1.0×10^{-1}	1.7	1.0
B1	West46	WD	B	0.2	13.8	6.6	0.4	79.6
B1	West525	WD	G	0.6	14.0	9.3×10^{-1}	5.1	0.2
B1	West297	PD	B	0.1	12.4	3.7	1.4	1.6
Off Clump	West917	PD	B	-9.0	-9.0	-9.0	1.3	-9.0
B1	West369	WD	G	0.5	11.5	1.2×10^{-1}	3.1	0.6
B1	West647	PD	B	-9.0	-9.0	9.0	2.1	-9.0

Table H.1 (cont'd)

Location	Name	Quality[a]	Fit[b]	M ($M_\odot$)	T (K)	red χ^2	R (10^{-2} pc)	n (10^5 cm^{-3})
B1	West370	WD	B	-9.0	-9.0	-9.0	2.2	-9.0
B1	West132	PD	B	-9.0	-9.0	9.0	0.0	-9.0
B1	West1128	WD	G	0.2	15.5	1.6×10^{-3}	3.7	0.1
B1	West385	WD	G	0.2	14.1	7.9×10^{-2}	2.5	0.3
Off Clump	West851	PD	B	-9.0	-9.0	9.0	1.1	-9.0
B1	West1036	PD	B	-9.0	-9.0	9.0	1.5	-9.0
B1	West780	PD	B	-9.0	-9.0	9.0	2.3	-9.0
B1	West593	WD	B	1.2	13.5	4.8	6.8	0.1
Off Clump	West529	WD	G	0.3	13.6	1.6×10^{-1}	5.4	0.1
B1	West813	PD	B	-9.0	-9.0	9.0	1.7	-9.0
B1	West318	WD	B	7.2	10.3	1.2×10^{1}	6.5	0.9
B1	West686	PD	B	-9.0	-9.0	9.0	2.5	-9.0
B1	West1010	PD	B	-9.0	-9.0	9.0	2.3	-9.0
B1	West595	PD	G	0.6	10.9	1.8×10^{-2}	3.4	0.5
B1	West929	PD	B	-9.0	-9.0	9.0	1.3	-9.0
B1	West812	WD	G	0.1	14.6	7.4×10^{-1}	2.7	0.2
B1	West1216	PD	B	-9.0	-9.0	9.0	1.9	-9.0
B1	West342	PD	G	0.2	10.2	2.6×10^{-2}	0.9	8.9
B1	West733	PD	G	0.5	10.9	1.9×10^{-1}	2.8	0.9
B1	West520	PD	B	0.8	13.5	1.2×10^{1}	5.3	0.2
B1	West562	WD	G	0.8	12.1	2.6×10^{-1}	4.0	0.4
B1	West924	PD	B	-9.0	-9.0	9.0	1.1	-9.0
B1	West978	PD	B	-9.0	-9.0	9.0	1.1	-9.0
B1	West571	WD	B	0.9	11.7	5.2	4.5	0.3
B1	West925	PD	B	-9.0	-9.0	9.0	0.9	-9.0
B1	West249	WD	G	1.8	11.1	7.8×10^{-2}	3.3	1.7
B1	West307	PD	G	5.9	8.0	2.3×10^{-2}	4.2	2.8
B1	West261	PD	B	-9.0	-9.0	9.0	2.2	-9.0
B1	West1112	PD	B	0.0	400.0	1.3	3.9	0.0
B1	West271	PD	B	-9.0	-9.0	9.0	1.9	-9.0
B1	West301	PD	B	-9.0	-9.0	9.0	1.8	-9.0
B1	West727	WD	G	0.8	11.5	6.1×10^{-3}	3.5	0.6
B1	West379	PD	B	-9.0	-9.0	9.0	2.4	-9.0
B1	West250	PD	G	0.4	9.6	5.9×10^{-3}	1.4	5.0
B1	West503	PD	G	0.1	13.4	2.8×10^{-4}	2.1	0.4
B1	West698	PD	B	0.0	400.0	2.4×10^{1}	6.0	0.0
B1	West29	PD	B	-9.0	-9.0	9.0	0.0	-9.0
B1	West135	PD	B	0.8	10.4	1.1	0.6	101.5
B1	West136	WD	G	2.1	9.0	1.8×10^{-1}	1.8	11.5
B1	West650	PD	B	-9.0	-9.0	9.0	3.0	-9.0
B1	West50	WD	B	0.9	10.6	5.8	0.4	460.1
B1	West34	WD	B	0.9	12.6	1.3×10^{1}	0.4	609.8
B1	West24	PD	B	0.1	15.8	6.2	0.3	175.8

Table H.1 (cont'd)

Location	Name	Quality[a]	Fit[b]	M ($M_\odot$)	T (K)	red χ^2	R (10^{-2} pc)	n (10^5 cm^{-3})
B1	West845	PD	B	-9.0	-9.0	9.0	2.0	-9.0
B1	West769	PD	B	-9.0	-9.0	9.0	1.1	-9.0
B1	West729	PD	B	-9.0	-9.0	9.0	1.0	-9.0
B1	West12	WD	B	1.6	15.1	8.9	0.0	-9.0
B1	West234	PD	G	0.3	11.5	2.2×10^{-1}	0.5	61.7
B1	West41	WD	B	4.1	10.6	2.2×10^{1}	0.7	414.9
B1	West847	PD	B	-9.0	-9.0	9.0	1.3	-9.0
B1	West624	PD	B	-9.0	-9.0	-9.0	2.3	-9.0
B1	West248	PD	B	-9.0	-9.0	9.0	0.8	-9.0
B1	West1078	PD	B	-9.0	-9.0	9.0	1.9	-9.0
B1	West1161	PD	B	-9.0	-9.0	9.0	2.0	-9.0
B1	West934	PD	B	-9.0	-9.0	9.0	3.0	-9.0
B1	West500	WD	G	0.4	16.2	5.7×10^{-2}	4.3	0.2
B1	West295	PD	G	6.3	6.8	2.1×10^{-2}	2.5	14.0
B1	West526	PD	B	-9.0	-9.0	9.0	2.1	-9.0
B1	West27	PD	G	0.1	17.1	7.4×10^{-1}	0.3	142.7
B1	West427	WD	G	0.3	12.9	1.9×10^{-2}	2.8	0.5
B1	West505	PD	G	5.1	10.2	1.4×10^{-2}	4.7	1.7
B1	West498	WD	G	0.8	11.7	3.8×10^{-2}	3.2	0.9
B1	West410	PD	G	0.5	11.1	2.2×10^{-2}	2.5	1.2
B1	West84	PD	B	-9.0	-9.0	9.0	0.0	-9.0
B1	West429	PD	B	0.0	400.0	4.7	4.4	0.0
B1	West731	PD	B	-9.0	-9.0	9.0	0.8	-9.0
B1	West447	WD	G	0.7	11.0	1.1×10^{-1}	3.6	0.5
B1	West343	WD	G	0.1	17.0	4.3×10^{-1}	3.2	0.1
B1	West474	PD	B	-9.0	-9.0	9.0	0.2	-9.0
B1	West345	PD	G	0.7	10.9	9.4×10^{-2}	2.6	1.3
B1	West431	WD	G	0.1	15.2	1.3×10^{-1}	2.5	0.3
B1	West572	PD	B	0.3	13.2	1.1	4.2	0.1
B1	West501	WD	G	0.1	19.3	8.3×10^{-2}	2.9	0.1
B1	West626	WD	G	1.1	12.9	7.2×10^{-3}	5.2	0.3
B1	West784	PD	G	0.0	15.9	1.6×10^{-3}	2.0	0.2
B1	West633	WD	G	0.4	16.9	2.7×10^{-1}	6.8	0.0
B1	East460	PD	G	0.0	17.0	2.7×10^{-3}	1.9	0.1
B1	West684	WD	G	0.1	14.8	3.9×10^{-2}	2.6	0.2
B1	West736	PD	B	0.0	18.5	1.2	2.7	0.1
B1	West816	PD	B	120.6	5.2	2.2	3.9	72.8
B1	West1080	WD	G	0.3	14.0	4.6×10^{-2}	3.9	0.2
B1	West356	WD	G	0.5	12.6	8.6×10^{-2}	4.0	0.3
B1	East421	PD	B	-9.0	-9.0	9.0	2.5	-9.0
Off Clump	East494	PD	B	0.7	19.9	1.6×10^{1}	11.0	0.0
Off Clump	East476	WD	G	0.2	15.5	5.1×10^{-4}	4.3	0.1
Off Clump	West449	WD	G	1.5	11.8	1.3	4.7	0.5

Table H.1 (cont'd)

Location	Name	Quality[a]	Fit[b]	M ($M_\odot$)	T (K)	red χ^2	R (10^{-2} pc)	n (10^5 cm^{-3})
B1E	West391	PD	G	0.1	13.4	2.1×10^{-2}	1.3	0.9
Off Clump	East462	WD	G	0.2	13.9	3.0×10^{-3}	4.2	0.1
Off Clump	West854	WD	B	2.9	10.2	8.9	5.9	0.5
Off Clump	East423	WD	G	1.3	13.7	7.0×10^{-2}	8.5	0.1
B1E	West309	PD	G	0.3	10.9	4.8×10^{-1}	2.1	1.0
B1E	East336	PD	B	2.9	7.2	2.6	3.2	3.1
B1E	West346	WD	G	0.7	15.2	7.2×10^{-3}	5.9	0.1
B1E	West507	WD	G	0.7	12.6	4.3×10^{-3}	4.1	0.4
B1E	West531	WD	G	1.2	9.1	1.9×10^{-1}	3.0	1.6
B1E	West737	WD	G	0.4	13.2	2.3×10^{-1}	3.7	0.2
Off Clump	East612	WD	G	0.4	15.0	2.4×10^{-1}	5.0	0.1
B1E	West656	WD	G	1.8	11.5	7.8×10^{-2}	5.2	0.4
B1E	West450	WD	G	0.5	11.7	7.0×10^{-1}	2.5	1.0
B1E	West942	WD	G	0.1	14.8	7.9×10^{-3}	2.9	0.2
B1E	East325	WD	G	0.1	16.4	5.4×10^{-4}	2.1	0.2
B1E	East222	PD	B	13.2	9.0	6.8	6.3	1.8
B1E	East170	WD	G	0.9	11.4	8.8×10^{-1}	3.4	0.8
Off Clump	West903	PD	B	-9.0	-9.0	9.0	1.5	-9.0
Off Clump	West1227	PD	B	-9.0	-9.0	-9.0	1.4	-9.0
Off Clump	East380	PD	B	0.4	19.7	1.9×10^{1}	10.6	0.0
Off Clump	West1293	PD	G	1.3	18.1	3.1×10^{-1}	10.2	0.0
Off Clump	East497	PD	B	27.5	6.9	7.2	5.0	7.7
Off Clump	West1085	WD	B	1.3	14.2	4.2×10^{1}	7.9	0.1
Off Clump	West1084	WD	G	0.1	19.1	2.5×10^{-2}	3.4	0.1
Off Clump	East642	WD	G	0.3	15.1	1.1×10^{-2}	4.8	0.1
Off Clump	West1333	PD	B	-9.0	-9.0	9.0	0.0	-9.0
Off Clump	East402	WD	G	0.1	16.5	2.6×10^{-2}	3.5	0.1
Off Clump	West984	PD	B	-9.0	-9.0	9.0	0.0	-9.0
Off Clump	East758	PD	B	104.6	5.3	3.8×10^{2}	3.5	85.3
Off Clump	East591	WD	B	0.8	13.8	5.2	8.2	0.0
Off Clump	West1325	PD	B	-9.0	-9.0	9.0	0.0	-9.0
Off Clump	East537	WD	G	0.0	21.2	1.2×10^{-1}	3.2	0.0
Off Clump	East385	WD	G	0.2	13.0	4.7×10^{-2}	2.9	0.2
Off Clump	West1052	PD	B	-9.0	-9.0	9.0	0.0	-9.0
Off Clump	East410	PD	B	-9.0	-9.0	9.0	3.1	-9.0
Off Clump	East356	WD	G	0.0	14.5	1.3×10^{-3}	1.5	0.4
Off Clump	East355	WD	G	1.1	12.6	3.4×10^{-1}	4.9	0.3
Off Clump	East561	PD	G	0.0	22.1	2.0×10^{-6}	2.0	0.1
Off Clump	West1166	PD	B	-9.0	-9.0	9.0	0.0	-9.0
Off Clump	East313	WD	B	0.5	13.4	4.9	3.8	0.3
Off Clump	East345	WD	G	0.3	16.9	3.6×10^{-1}	4.5	0.1
Off Clump	West1332	PD	B	-9.0	-9.0	9.0	0.0	-9.0
Off Clump	East246	PD	B	0.1	19.7	3.5×10^{1}	8.0	0.0

Table H.1 (cont'd)

Location	Name	Quality[a]	Fit[b]	M ($M_\odot$)	T (K)	red χ^2	R (10^{-2} pc)	n (10^5 cm^{-3})
Off Clump	East441	WD	G	0.4	13.3	2.8×10^{-2}	4.6	0.1
Off Clump	West1367	PD	B	-9.0	-9.0	9.0	0.0	-9.0
Off Clump	East382	WD	G	1.8	12.4	7.9×10^{-1}	6.8	0.2
Off Clump	East258	WD	G	0.5	11.8	3.8×10^{-1}	3.3	0.5
Off Clump	East256	WD	G	0.1	16.4	5.6×10^{-1}	2.9	0.1
Off Clump	West1228	PD	B	-9.0	-9.0	9.0	0.0	-9.0
Off Clump	East291	WD	B	0.6	13.9	2.2	4.8	0.2
Off Clump	West1229	PD	B	-9.0	-9.0	9.0	0.0	-9.0
Off Clump	East371	WD	G	0.1	14.1	5.0×10^{-2}	3.4	0.1
Off Clump	East383	WD	G	0.4	14.1	5.1×10^{-1}	5.7	0.1
Off Clump	East351	PD	G	0.1	12.2	7.6×10^{-2}	1.4	0.7
Off Clump	East414	PD	B	-9.0	-9.0	9.0	1.2	-9.0
Off Clump	East464	WD	G	1.3	12.8	5.6×10^{-2}	5.9	0.2
Off Clump	East316	WD	G	1.4	7.9	1.1	1.7	10.1
Off Clump	East479	PD	G	0.1	11.7	3.1×10^{-1}	2.2	0.4
Off Clump	East255	WD	G	0.0	17.4	1.5×10^{-2}	2.2	0.1
Off Clump	East625	WD	G	0.1	17.5	6.0×10^{-2}	3.4	0.1
Off Clump	East6	WD	B	0.4	13.3	2.8×10^{1}	0.2	4010.8
Off Clump	East443	PD	B	-9.0	-9.0	-9.0	1.7	-9.0
Off Clump	East328	WD	G	0.1	14.8	5.7×10^{-3}	3.1	0.1
Off Clump	East465	PD	G	0.3	10.6	8.8×10^{-1}	2.7	0.5
Off Clump	East373	PD	B	0.3	17.3	4.7×10^{1}	7.9	0.0
Off Clump	East280	WD	G	0.9	11.0	1.1×10^{-1}	4.1	0.5
IC348	East347	WD	B	0.4	14.0	3.8	5.6	0.1
IC348	East152	PD	G	2.3	9.4	7.8×10^{-3}	4.1	1.1
Off Clump	East124	WD	G	0.7	9.6	2.1×10^{-2}	1.8	3.6
IC348	East168	WD	G	0.3	15.5	1.8×10^{-2}	4.1	0.2
Off Clump	East599	PD	B	0.0	61.4	2.3×10^{1}	4.8	0.0
Off Clump	East499	PD	G	0.2	9.4	1.3×10^{-6}	2.3	0.7
IC348	East650	WD	B	0.0	32.2	4.9	4.4	0.0
IC348	East327	PD	G	0.1	12.3	2.6×10^{-1}	1.8	0.4
IC348	East340	WD	G	0.5	11.9	1.0×10^{-2}	5.1	0.1
Off Clump	East412	PD	B	0.1	17.8	4.7	5.1	0.0
IC348	East569	PD	B	-9.0	-9.0	9.0	1.2	-9.0
IC348	East201	PD	B	15.0	7.6	3.6×10^{1}	4.9	4.4
Off Clump	East828	PD	B	5.7	10.4	1.1×10^{2}	12.0	0.1
IC348	East570	WD	G	0.1	16.2	7.8×10^{-2}	3.4	0.1
Off Clump	East178	WD	G	0.2	13.6	1.4×10^{-1}	2.8	0.3
Off Clump	East563	PD	G	0.0	21.4	1.3×10^{-2}	0.9	0.3
Off Clump	East721	PD	B	1.2	14.0	1.0×10^{2}	12.3	0.0
Off Clump	East150	WD	G	0.0	21.5	1.1×10^{-1}	2.2	0.1
IC348	East58	PD	B	0.0	23.1	1.0	0.2	20.7
IC348	East348	PD	G	0.3	10.9	3.2×10^{-1}	2.2	1.0

Table H.1 (cont'd)

Location	Name	Quality[a]	Fit[b]	M ($M_\odot$)	T (K)	red χ^2	R (10^{-2} pc)	n (10^5 cm^{-3})
Off Clump	East326	WD	G	0.1	14.5	2.3×10^{-2}	2.6	0.2
IC348	East282	WD	G	0.1	15.1	8.8×10^{-1}	1.8	0.4
Off Clump	East830	PD	B	0.8	14.6	2.8×10^{1}	9.5	0.0
IC348	East293	PD	B	0.3	29.3	2.4×10^{1}	11.8	0.0
IC348	East626	WD	G	0.4	23.1	1.0×10^{-1}	9.4	0.0
IC348	East891	WD	G	0.1	20.7	9.1×10^{-3}	4.8	0.0
Off Clump	East706	WD	G	0.0	29.9	1.0×10^{-1}	2.9	0.0
IC348	East114	WD	B	2.0	11.9	2.8	4.9	0.6
Off Clump	East273	WD	G	0.2	12.7	5.1×10^{-2}	2.7	0.4
IC348	East428	WD	G	0.1	16.3	4.1×10^{-1}	3.0	0.1
IC348	East405	PD	G	0.0	17.3	4.1×10^{-2}	2.2	0.1
Off Clump	East597	PD	B	-9.0	-9.0	-9.0	1.5	-9.0
IC348	East480	WD	G	0.8	14.1	6.7×10^{-1}	7.6	0.1
IC348	East799	PD	G	0.0	30.3	1.7×10^{-2}	2.7	0.0
IC348	East745	PD	G	0.0	28.6	3.4×10^{-3}	2.3	0.0
IC348	East173	WD	G	0.4	12.7	1.1	3.0	0.5
IC348	East283	PD	G	0.0	17.3	3.3×10^{-3}	2.0	0.2
IC348	East10	WD	G	0.0	19.2	7.4×10^{-1}	0.0	-9.0
IC348	East172	PD	G	0.0	16.2	5.1×10^{-2}	1.7	0.3
IC348	East726	PD	B	0.1	18.0	1.8	4.4	0.0
IC348	East128	WD	G	0.5	13.9	1.4	2.8	0.7
Off Clump	East457	WD	B	0.9	14.0	2.2	5.8	0.2
IC348	East262	PD	B	0.0	400.0	2.7×10^{1}	12.4	0.0
IC348	East53	PD	G	0.0	19.5	1.7×10^{-1}	0.3	6.0
IC348	East281	PD	G	0.1	11.2	4.0×10^{-2}	1.4	1.5
Off Clump	East512	PD	B	-9.0	-9.0	9.0	0.9	-9.0
IC348	East357	WD	G	1.1	8.8	4.2×10^{-1}	2.2	3.7
IC348	East202	WD	B	1.7	10.0	4.7	3.3	1.6
IC348	East448	WD	G	0.1	19.8	1.0×10^{-1}	3.0	0.1
IC348	East179	WD	B	8.7	8.8	1.2×10^{1}	5.6	1.7
IC348	East180	WD	B	5.0	11.3	6.8	6.4	0.7
IC348	East183	PD	B	1.7	16.5	1.0×10^{2}	11.5	0.0
IC348	East329	PD	B	-9.0	-9.0	9.0	2.1	-9.0
IC348	East136	PD	B	-9.0	-9.0	9.0	0.0	-9.0
IC348	East231	PD	B	-9.0	-9.0	-9.0	1.1	-9.0
IC348	East573	PD	B	-9.0	-9.0	9.0	1.7	-9.0
IC348	East78	WD	G	0.0	18.1	5.1×10^{-1}	0.8	1.3
IC348	East339	WD	G	0.8	11.4	3.4×10^{-1}	5.5	0.2
IC348	East391	PD	B	-9.0	-9.0	9.0	2.2	-9.0
IC348	East57	PD	B	-9.0	-9.0	9.0	1.1	-9.0
IC348	East653	PD	B	-9.0	-9.0	9.0	2.2	-9.0
IC348	East306	WD	G	0.7	9.7	8.3×10^{-1}	2.4	1.8
IC348	East308	WD	G	2.2	11.1	4.9×10^{-1}	7.2	0.2

Table H.1 (cont'd)

Location	Name	Quality[a]	Fit[b]	M ($M_\odot$)	T (K)	red χ^2	R (10^{-2} pc)	n (10^5 cm^{-3})
IC348	East153	PD	B	-9.0	-9.0	9.0	0.2	-9.0
IC348	East115	PD	G	0.0	14.7	3.7×10^{-1}	1.2	1.0
IC348	East224	WD	G	1.6	13.5	5.8×10^{-1}	6.0	0.3
IC348	East307	WD	B	1.7	8.7	3.5	3.3	1.6
IC348	East950	WD	G	0.1	20.5	1.1	6.9	0.0
IC348	East151	PD	G	0.1	11.0	7.9×10^{-2}	1.1	2.8
IC348	East182	WD	G	0.2	10.6	2.2×10^{-3}	1.4	2.7
IC348	East184	PD	B	-9.0	-9.0	9.0	1.3	-9.0
IC348	East388	WD	G	1.0	13.6	5.6×10^{-1}	5.6	0.2
IC348	East941	PD	B	-9.0	-9.0	9.0	5.8	-9.0
IC348	East275	WD	B	1.6	12.8	2.1	5.1	0.4
IC348	East294	WD	G	0.2	14.3	7.3×10^{-4}	3.1	0.2
IC348	East81	WD	G	0.6	15.9	4.5×10^{-2}	3.5	0.5
IC348	East205	PD	B	-9.0	-9.0	9.0	0.2	-9.0
IC348	East23	PD	B	-9.0	-9.0	9.0	1.0	-9.0
IC348	East191	WD	G	0.3	14.8	1.4×10^{-2}	2.4	0.8
IC348	East274	WD	G	0.4	14.1	2.7×10^{-2}	4.2	0.2
IC348	East544	PD	B	9.1	9.1	3.2×10^{1}	5.3	2.1
Off Clump	East528	WD	G	0.0	19.5	2.3×10^{-2}	2.1	0.1
IC348	East190	PD	G	0.4	14.5	1.7×10^{-2}	4.3	0.2
Off Clump	East505	PD	G	0.1	15.7	7.3×10^{-1}	2.4	0.1
IC348	East452	WD	B	0.9	12.7	1.8	4.9	0.2
IC348	East358	WD	G	0.0	21.2	1.4×10^{-2}	2.4	0.1
Off Clump	East169	WD	G	0.1	16.0	9.3×10^{-1}	2.1	0.3
IC348	East509	PD	G	1.2	15.2	5.0×10^{-2}	6.8	0.1
IC348	East526	PD	B	1.6	12.2	2.0	5.1	0.4
IC348	East416	PD	B	0.0	25.7	4.8	4.4	0.0
IC348	East142	PD	G	0.3	17.2	8.6×10^{-2}	4.3	0.1
Off Clump	East148	WD	G	0.1	15.3	3.5×10^{-1}	2.0	0.3
IC348	East413	WD	B	0.1	46.9	1.4×10^{1}	10.2	0.0
IC348	East862	WD	G	0.2	18.7	6.8×10^{-1}	6.9	0.0
IC348	East235	PD	B	-9.0	-9.0	9.0	1.8	-9.0
Off Clump	East515	WD	B	0.0	105.5	1.2×10^{1}	7.9	0.0
IC348	East450	WD	G	0.2	14.8	2.1×10^{-1}	2.8	0.2
IC348	East64	WD	G	2.1	11.9	4.7×10^{-1}	3.6	1.5
IC348	East375	PD	B	0.3	19.2	1.4×10^{1}	5.1	0.1
IC348	East104	PD	B	1.0	9.8	1.2	1.2	22.2
IC348	East103	PD	B	12.6	6.8	1.4	1.5	123.1
IC348	East54	PD	B	-9.0	-9.0	9.0	0.2	-9.0
IC348	East408	PD	B	-9.0	-9.0	9.0	0.4	-9.0
IC348	East471	PD	B	-9.0	-9.0	9.0	1.3	-9.0
IC348	East12	PD	B	-9.0	-9.0	9.0	0.2	-9.0
IC348	East86	PD	G	1.7	10.1	1.8×10^{-1}	1.9	9.1

Table H.1 (cont'd)

Location	Name	Quality[a]	Fit[b]	M ($M_\odot$)	T (K)	red χ^2	R (10^{-2} pc)	n (10^5 cm^{-3})
IC348	East132	PD	B	-9.0	-9.0	9.0	1.6	-9.0
IC348	East407	PD	B	-9.0	-9.0	9.0	1.0	-9.0
Off Clump	East155	WD	G	0.2	15.3	5.0×10^{-1}	3.0	0.3
IC348	East93	PD	B	-9.0	-9.0	9.0	0.6	-9.0
IC348	East11	WD	B	0.7	12.1	5.9	0.3	1419.3
IC348	East9	WD	B	0.4	14.5	5.0	0.3	671.7
IC348	East63	PD	B	-9.0	-9.0	9.0	1.2	-9.0
IC348	East97	PD	B	-9.0	-9.0	9.0	1.4	-9.0
IC348	East118	PD	B	-9.0	-9.0	9.0	0.9	-9.0
Off Clump	East584	PD	G	0.0	15.8	6.0×10^{-2}	1.0	0.4
IC348	East137	PD	G	3.9	7.5	1.1×10^{-1}	0.6	718.2
IC348	East453	PD	B	-9.0	-9.0	9.0	1.2	-9.0
IC348	East4	WD	B	1.9	13.6	1.6×10^{1}	0.0	-9.0
IC348	East5	WD	B	1.3	13.7	2.3×10^{1}	0.3	2410.8
IC348	East79	PD	B	-9.0	-9.0	9.0	0.4	-9.0
Off Clump	East482	PD	B	-9.0	-9.0	-9.0	1.2	-9.0
IC348	East55	WD	B	10.4	6.9	9.3	1.2	222.0
IC348	East193	PD	G	0.5	12.4	7.6×10^{-3}	3.0	0.7
IC348	East26	PD	B	-9.0	-9.0	9.0	0.4	-9.0
IC348	East62	WD	B	4.5	8.2	2.6	0.8	277.4
IC348	East18	WD	G	1.2	14.3	8.6×10^{-1}	1.9	6.2
IC348	East100	PD	G	0.3	14.3	7.6×10^{-1}	2.0	1.4
IC348	East17	PD	B	2.9	7.8	3.4	0.1	42655.0
IC348	East486	PD	G	0.0	13.7	2.7×10^{-2}	1.2	0.8
IC348	East208	PD	B	-9.0	-9.0	9.0	1.4	-9.0
IC348	East89	WD	B	1.3	11.4	7.5	1.7	9.5
IC348	East632	PD	B	-9.0	-9.0	9.0	1.4	-9.0
IC348	East185	WD	G	0.6	13.3	1.4	3.3	0.6
IC348	East206	WD	G	0.1	13.6	2.1×10^{-2}	2.1	0.5
IC348	East250	PD	B	-9.0	-9.0	9.0	1.8	-9.0
IC348	East67	WD	B	3.1	8.7	2.3	1.0	95.5
IC348	East98	PD	B	0.1	27.7	6.1	4.3	0.0
IC348	East107	WD	G	1.9	9.5	8.6×10^{-1}	2.2	5.9
IC348	East48	WD	G	1.1	11.0	2.2×10^{-1}	1.1	28.7
IC348	East30	PD	B	-9.0	-9.0	9.0	0.5	-9.0
IC348	East252	PD	B	-9.0	-9.0	9.0	0.6	-9.0
IC348	East121	PD	G	0.2	12.8	3.3×10^{-1}	1.3	3.5
IC348	East253	WD	G	0.1	27.3	6.8×10^{-3}	4.0	0.0
IC348	East7	PD	G	0.0	24.7	7.8×10^{-5}	0.0	-9.0
IC348	East771	PD	B	-9.0	-9.0	9.0	1.7	-9.0
IC348	East82	PD	B	-9.0	-9.0	-9.0	1.8	-9.0
IC348	East157	WD	G	0.5	12.1	3.7×10^{-2}	3.0	0.7
IC348	East92	WD	G	0.6	14.0	6.6×10^{-2}	3.0	0.8

Table H.1 (cont'd)

Location	Name	Quality[a]	Fit[b]	M ($M_\odot$)	T (K)	red χ^2	R (10^{-2} pc)	n (10^5 cm^{-3})
IC348	East187	PD	B	-9.0	-9.0	9.0	2.1	-9.0
IC348	East436	WD	G	0.1	21.3	2.8×10^{-2}	4.3	0.0
IC348	East363	PD	B	-9.0	-9.0	9.0	1.0	-9.0
IC348	East16	PD	B	-9.0	-9.0	9.0	0.2	-9.0
IC348	East120	PD	B	-9.0	-9.0	9.0	0.9	-9.0
IC348	East13	WD	G	0.1	14.6	1.3	0.4	39.0
IC348	East236	PD	G	0.1	17.9	6.0×10^{-1}	3.0	0.1
IC348	East126	PD	B	-9.0	-9.0	9.0	1.0	-9.0
IC348	East362	PD	B	-9.0	-9.0	9.0	1.1	-9.0
IC348	East122	PD	B	-9.0	-9.0	9.0	0.9	-9.0
IC348	East207	PD	G	0.6	9.2	7.2×10^{-2}	1.8	3.6
IC348	East303	PD	B	-9.0	-9.0	9.0	2.4	-9.0
IC348	East154	PD	B	-9.0	-9.0	9.0	1.6	-9.0
IC348	East29	PD	B	0.2	15.2	1.4	2.2	0.6
IC348	East76	PD	B	-9.0	-9.0	9.0	1.0	-9.0
IC348	East394	PD	B	-9.0	-9.0	9.0	0.0	-9.0
IC348	East265	PD	B	-9.0	-9.0	9.0	0.7	-9.0
IC348	East310	PD	B	-9.0	-9.0	9.0	2.2	-9.0
IC348	East319	PD	B	-9.0	-9.0	9.0	1.2	-9.0
IC348	East27	PD	G	0.0	29.3	2.3×10^{-1}	0.8	0.4
IC348	East219	PD	B	-9.0	-9.0	9.0	2.3	-9.0
IC348	East317	PD	B	-9.0	-9.0	9.0	1.7	-9.0
IC348	East218	WD	G	0.6	10.5	1.0	2.8	0.9
IC348	East110	PD	G	0.1	21.8	4.3×10^{-2}	2.4	0.1
IC348	East158	PD	B	-9.0	-9.0	9.0	2.3	-9.0
IC348	East238	PD	B	-9.0	-9.0	9.0	5.8	-9.0
IC348	East165	PD	B	-9.0	-9.0	9.0	0.0	-9.0
IC348	East36	PD	B	-9.0	-9.0	9.0	0.0	-9.0
IC348	East45	PD	G	0.0	17.8	1.3×10^{-1}	1.3	0.8
IC348	East40	PD	B	-9.0	-9.0	9.0	0.0	-9.0
IC348	East579	PD	G	0.0	23.5	5.2×10^{-1}	1.4	0.5
IC348	East176	PD	G	0.2	14.5	3.5×10^{-2}	1.8	0.9
IC348	East25	WD	G	0.1	27.5	3.7×10^{-1}	3.5	0.1
IC348	East15	PD	B	-9.0	-9.0	9.0	0.0	-9.0
IC348	East101	PD	B	-9.0	-9.0	9.0	1.9	-9.0
IC348	East365	PD	B	-9.0	-9.0	9.0	2.6	-9.0
IC348	East61	WD	G	1.0	10.1	4.2×10^{-5}	1.6	7.7
IC348	East269	PD	B	-9.0	-9.0	9.0	1.8	-9.0
IC348	East211	PD	G	0.0	56.3	1.9×10^{-1}	3.6	0.0
IC348	East195	PD	G	0.0	41.7	8.2×10^{-3}	2.6	0.0
IC348	East43	PD	B	-9.0	-9.0	9.0	0.0	-9.0
IC348	East134	PD	B	-9.0	-9.0	9.0	1.2	-9.0
IC348	East432	WD	G	0.4	15.5	9.8×10^{-2}	5.9	0.1

Table H.1 (cont'd)

Location	Name	Quality[a]	Fit[b]	M ($M_\odot$)	T (K)	red χ^2	R (10^{-2} pc)	n (10^5 cm^{-3})
IC348	East50	PD	B	-9.0	-9.0	9.0	1.8	-9.0
IC348	East175	PD	B	-9.0	-9.0	9.0	2.5	-9.0
IC348	East111	PD	B	0.0	24.1	2.7	1.6	0.2
IC348	East66	PD	B	-9.0	-9.0	9.0	0.2	-9.0
IC348	East634	PD	B	-9.0	-9.0	9.0	1.4	-9.0
IC348	East225	PD	B	-9.0	-9.0	9.0	1.4	-9.0
IC348	East166	PD	B	-9.0	-9.0	9.0	1.0	-9.0
IC348	East125	PD	G	0.1	14.8	5.8×10^{-3}	2.3	0.4
IC348	East131	PD	G	0.5	16.9	4.0×10^{-2}	4.1	0.2
IC348	East254	PD	B	-9.0	-9.0	9.0	2.2	-9.0
IC348	East127	PD	B	-9.0	-9.0	9.0	1.3	-9.0
IC348	East2	WD	B	0.4	17.5	1.6	0.2	4020.3
IC348	East309	WD	G	0.1	13.7	6.1×10^{-1}	2.5	0.2
IC348	East94	PD	G	0.0	19.4	4.8×10^{-2}	1.9	0.2
IC348	East80	PD	B	-9.0	-9.0	9.0	1.9	-9.0
IC348	East96	PD	B	-9.0	-9.0	9.0	0.8	-9.0
IC348	East84	WD	G	0.0	35.5	1.3×10^{-1}	5.1	0.0
IC348	East71	PD	B	-9.0	-9.0	9.0	1.6	-9.0
IC348	East68	PD	G	0.6	10.6	8.1×10^{-2}	1.2	11.5
IC348	East510	PD	B	-9.0	-9.0	9.0	0.8	-9.0
IC348	East604	PD	B	-9.0	-9.0	9.0	1.9	-9.0
IC348	East130	WD	B	0.0	79.9	3.8	5.8	0.0
IC348	East140	WD	B	0.1	24.7	6.6	3.7	0.0
IC348	East105	WD	G	0.6	16.4	6.7×10^{-2}	4.7	0.2
IC348	East270	PD	B	-9.0	-9.0	9.0	1.6	-9.0
IC348	East580	PD	B	-9.0	-9.0	9.0	3.0	-9.0
IC348	East139	PD	B	-9.0	-9.0	9.0	1.2	-9.0
IC348	East278	PD	G	0.0	27.8	3.3×10^{-1}	2.8	0.0
IC348	East109	PD	B	-9.0	-9.0	9.0	1.5	-9.0
IC348	East209	WD	G	1.0	13.2	5.7×10^{-1}	6.3	0.1
IC348	East805	PD	G	0.0	27.6	4.0×10^{-2}	3.6	0.0
IC348	East119	PD	G	0.2	12.7	2.1×10^{-1}	1.8	1.1
IC348	East147	WD	G	0.6	17.3	2.7×10^{-1}	5.2	0.1
IC348	East213	WD	B	0.3	14.3	1.6	2.6	0.6
IC348	East454	PD	G	0.1	15.6	6.0×10^{-1}	1.9	0.4
IC348	East210	WD	G	0.1	15.5	5.0×10^{-1}	3.1	0.1
IC348	East159	PD	B	-9.0	-9.0	9.0	0.3	-9.0
IC348	East116	WD	G	1.6	11.5	2.7×10^{-1}	3.2	1.7
IC348	East266	PD	G	0.1	12.4	1.5×10^{-1}	1.3	1.0
IC348	East267	PD	B	-9.0	-9.0	9.0	0.7	-9.0
IC348	East102	PD	G	0.6	13.0	9.4×10^{-1}	2.7	1.1
IC348	East318	PD	G	0.1	13.8	1.4×10^{-2}	1.7	0.4
IC348	East240	PD	G	0.0	15.6	2.5×10^{-2}	1.3	0.7

Table H.1 (cont'd)

Location	Name	Quality[a]	Fit[b]	M ($M_\odot$)	T (K)	red χ^2	R (10^{-2} pc)	n (10^5 cm^{-3})
IC348	East455	PD	G	0.0	15.3	2.3×10^{-3}	1.8	0.3
IC348	East473	WD	B	0.6	13.9	8.3	5.4	0.1
Off Clump	East3	WD	B	0.1	17.8	1.8×10^{1}	0.0	-9.0
B5	East271	WD	G	0.2	10.0	1.2×10^{-1}	1.3	2.8
B5	East304	WD	G	0.6	13.7	3.3×10^{-1}	4.6	0.2
B5	East284	WD	G	0.4	10.4	1.0	2.5	0.8
B5	East661	PD	B	0.0	22.8	2.4	2.1	0.0
B5	East242	WD	G	0.2	13.9	6.0×10^{-2}	3.4	0.2
B5	East14	WD	B	0.2	12.1	2.9×10^{1}	0.3	249.8
B5	East323	WD	G	0.1	16.7	3.0×10^{-2}	3.9	0.1
B5	East285	PD	G	0.6	11.2	7.2×10^{-1}	3.5	0.5
B5	East215	WD	G	0.1	13.6	1.4×10^{-2}	2.6	0.3
B5	East229	WD	G	0.1	15.5	2.9×10^{-2}	2.9	0.1
B5	East589	PD	B	-9.0	-9.0	9.0	1.2	-9.0
B5	East189	WD	G	0.5	12.0	1.4×10^{-1}	3.6	0.3
B5	East519	PD	B	-9.0	-9.0	9.0	1.0	-9.0
B5	East305	WD	G	0.6	12.4	1.8×10^{-1}	5.1	0.2
B5	East286	PD	G	0.7	9.9	1.7×10^{-3}	2.7	1.2
B5	East75	WD	G	1.8	7.9	3.7×10^{-1}	1.0	65.5
B5	East244	WD	G	0.4	13.1	4.9×10^{-3}	3.8	0.2
B5	East321	PD	G	2.2	7.6	5.0×10^{-1}	2.9	3.3
B5	East1	WD	B	0.3	16.0	9.3	0.3	646.1
B5	East197	PD	G	0.6	8.6	9.5×10^{-5}	0.6	90.4
B5	East439	PD	G	0.2	11.2	3.5×10^{-3}	2.3	0.6
B5	East367	PD	G	0.4	10.6	1.5×10^{-1}	3.8	0.2
B5	East530	PD	B	0.1	14.9	2.1	3.5	0.1
B5	East379	PD	G	1.0	11.1	9.6×10^{-1}	4.7	0.3
B5	East288	WD	G	0.2	9.9	4.8×10^{-2}	1.4	2.3
B5	East398	PD	G	0.1	13.1	1.3×10^{-1}	2.2	0.3
B5	East243	WD	G	1.6	11.3	4.9×10^{-1}	5.3	0.4
Off Clump	East162	WD	G	-9.0	-9.0	9.0	0.0	-9.0

[a] *Herschel* source detection quality; WD is well-detected and PD is poorly-detected. See Section 5.3.2.

[b] SED fit quality; G is a good fit and B is a bad fit. See Section 5.4.2.

Table H.2 gives the initial results from source classification. Columns 1-2 gives the source location and name. Column 3 gives the classification, where "S" corresponds to starless cores, "Q" corresponds to questionably starless cores, and "P" corresponds to protostellar cores. Column 3 indicates whether a compact 70 μm source was identified. Columns 4-5 give infrared source names from the c2d catalogue or G09 catalogue, respectively. We defined the G09 source names by the source location (i.e., NGC1333 or IC348) and the running source number.

Table H.2. Classification of *Herschel* Objects

Location	Source Name	Class[a]	70 μm[b]	C2D Source	G09 Source
Off Clump	West1255	Q	N	none	none
Off Clump	West1136	Q	N	none	none
Off Clump	West829	S	N	none	none
Off Clump	West1091	S	N	none	none
Off Clump	West791	S	N	none	none
Off Clump	West716	S	N	none	none
Off Clump	West740	S	N	none	none
Off Clump	West869	S	N	none	none
Off Clump	West413	S	N	none	none
Off Clump	West788	S	N	none	none
Off Clump	West263	S	N	none	none
Off Clump	West884	S	N	none	none
Off Clump	West272	S	N	none	none
L1448	West334	S	N	none	none
Off Clump	West454	S	N	none	none
Off Clump	West509	S	N	none	none
Off Clump	West663	S	N	none	none
L1448	West457	S	N	none	none
Off Clump	West789	S	N	none	none
L1448	West609	Q	N	none	none
Off Clump	West705	S	N	none	none
Off Clump	West417	S	N	none	none
Off Clump	West662	Q	N	none	none
L1448	West437	S	N	none	none
Off Clump	West284	S	N	none	none
L1448	West639	S	N	none	none
Off Clump	West859	S	N	none	none
L1448	West714	Q	N	none	none
L1448	West146	S	N	none	none
L1448	West32	P	Y	none	none
Off Clump	West160	Q	N	none	none
L1448	West612	S	N	none	none
L1448	West458	S	N	none	none
L1448	West238	S	N	none	none
Off Clump	West909	Q	N	none	none
Off Clump	West243	S	N	none	none
Off Clump	West616	S	N	none	none
L1448	West264	Q	N	none	none
L1448	West375	Q	N	none	none
L1448	West9	P	Y	SSTc2dJ032522.3+304514	none
Off Clump	West637	Q	N	none	none
Off Clump	West875	S	N	none	none
L1448	West1049	Q	N	none	none
L1448	West99	Q	N	none	none

Table H.2 (cont'd)

Location	Source Name	Class[a]	70 μm[b]	C2D Source	G09 Source
Off Clump	West279	S	N	none	none
Off Clump	West804	S	N	none	none
L1448	West223	Q	N	none	none
Off Clump	West280	Q	N	none	none
Off Clump	West310	S	N	none	none
L1448	West230	Q	N	none	none
L1448	West25	P	Y	none	none
Off Clump	West753	S	N	none	none
L1448	West8	P	Y	SSTc2dJ032536.5+304522	none
Off Clump	West453	S	N	none	none
Off Clump	West452	S	N	none	none
Off Clump	West278	S	N	none	none
L1448	West397	S	N	none	none
Off Clump	West351	Q	N	none	none
L1448	West4	P	Y	SSTc2dJ032538.8+304406	none
L1448	West4	P	Y	SSTc2dJ032539.1+304358	none
L1448	West629	Q	N	none	none
Off Clump	West349	S	N	none	none
Off Clump	West636	S	N	none	none
L1448	West584	S	N	none	none
L1448	West613	Q	N	none	none
Off Clump	West954	S	N	none	none
Off Clump	West451	S	N	none	none
Off Clump	West920	S	N	none	none
Off Clump	West907	S	N	none	none
Off Clump	West617	S	N	none	none
Off Clump	West574	Q	N	none	none
L1448	West251	Q	N	none	none
Off Clump	West692	S	N	none	none
L1448	West1047	S	N	none	none
Off Clump	West416	S	N	none	none
L1448	West197	S	N	none	none
L1448	West191	S	N	none	none
L1448	West353	Q	N	none	none
L1448	West382	Q	N	none	none
Off Clump	West463	S	N	none	none
Off Clump	West332	Q	N	none	none
L1448	West1148	S	N	none	none
Off Clump	West635	S	N	none	none
Off Clump	West906	S	N	none	none
L1448	West213	S	N	none	none
L1448	West287	S	N	none	none
Off Clump	West111	Q	N	none	none
Off Clump	West659	Q	N	none	none

Table H.2 (cont'd)

Location	Source Name	Class[a]	70 μm[b]	C2D Source	G09 Source
L1448	West244	S	N	none	none
L1448	West265	S	N	none	none
Off Clump	West870	S	N	none	none
L1448	West641	S	N	none	none
L1448	West608	S	N	none	none
L1448	West327	S	N	none	none
Off Clump	West604	S	N	none	none
L1448	West583	Q	N	none	none
Off Clump	West605	S	N	none	none
L1448	West668	S	N	none	none
Off Clump	West481	S	N	none	none
Off Clump	West1141	S	N	none	none
L1448	West312	S	N	none	none
L1448	West399	S	N	none	none
L1448	West396	S	N	none	none
Off Clump	West857	S	N	none	none
L1448	West582	S	N	none	none
L1448	West325	S	N	none	none
Off Clump	West1093	Q	N	none	none
Off Clump	West873	S	N	none	none
Off Clump	West721	S	N	none	none
Off Clump	West863	S	N	none	none
Off Clump	West761	S	N	none	none
Off Clump	West20	P	Y	SSTc2dJ032637.5+301528	none
Off Clump	West886	S	N	none	none
Off Clump	West760	S	N	none	none
Off Clump	West658	S	N	none	none
L1455	West1097	Q	N	none	none
L1455	West958	S	N	none	none
Off Clump	West840	S	N	none	none
L1455	West226	S	N	none	none
Off Clump	West268	S	N	none	none
Off Clump	West488	S	N	none	none
Off Clump	West855	S	N	none	none
L1455	West1054	S	N	none	none
L1455	West580	S	N	none	none
Off Clump	West216	S	N	none	none
L1455	West688	S	N	none	none
L1455	West935	S	N	none	none
L1455	West323	Q	N	none	none
L1455	West254	S	N	none	none
L1455	West708	S	N	none	none
L1455	West352	S	N	none	none
L1455	West537	Q	N	none	none

Table H.2 (cont'd)

Location	Source Name	Class[a]	70 μm[b]	C2D Source	G09 Source
L1455	West575	S	N	none	none
L1455	West745	Q	N	none	none
L1455	West373	Q	N	none	none
L1455	West374	S	N	none	none
L1455	West419	S	N	none	none
L1455	West412	S	N	none	none
L1455	West567	S	N	none	none
L1455	West350	S	N	none	none
L1455	West880	S	N	none	none
L1455	West638	Q	N	none	none
L1455	West239	S	N	none	none
L1455	West792	Q	N	none	none
L1455	West910	S	N	none	none
L1455	West607	Q	N	none	none
L1455	West35	P	Y	SSTc2dJ032738.2+301359	none
L1455	West395	S	N	none	none
L1455	West285	Q	N	none	none
L1455	West5	P	Y	SSTc2dJ032738.8+301258	none
L1455	West5	P	Y	SSTc2dJ032739.1+301303	none
L1455	West772	S	N	none	none
L1455	West394	S	N	none	none
L1455	West161	S	N	none	none
NGC1333	West365	S	N	none	none
L1455	West435	S	N	none	none
L1455	West18	P	Y	SSTc2dJ032743.2+301229	none
L1455	West540	S	N	none	none
L1455	West311	Q	N	none	none
L1455	West611	Q	N	none	none
L1455	West478	S	N	none	none
L1455	West36	P	Y	SSTc2dJ032747.7+301205	none
L1455	West606	Q	N	none	none
L1455	West793	Q	N	none	none
L1455	West860	S	N	none	none
L1455	West286	Q	N	none	none
L1455	West237	S	N	none	none
L1455	West418	S	N	none	none
L1455	West568	S	N	none	none
L1455	West1142	Q	N	none	none
NGC1333	West725	Q	N	none	none
L1455	West1144	Q	N	none	none
L1455	West456	S	N	none	none
L1455	West577	S	N	none	none
Off Clump	West948	S	N	none	none
L1455	West821	S	N	none	none

Table H.2 (cont'd)

Location	Source Name	Class[a]	70 μm[b]	C2D Source	G09 Source
L1455	West82	P	Y	SSTc2dJ032800.4+300801	none
NGC1333	West1065	Q	N	none	none
L1455	West664	S	N	none	none
Off Clump	West1094	S	N	none	none
L1455	West748	S	N	none	none
L1455	West477	S	N	none	none
L1455	West541	S	N	none	none
L1455	West480	S	N	none	none
NGC1333	West1205	S	N	none	none
L1455	West794	S	N	none	none
NGC1333	West897	S	N	none	none
NGC1333	West589	S	N	none	none
NGC1333	West718	S	N	none	none
L1455	West915	S	N	none	none
Off Clump	West1151	S	N	none	none
NGC1333	West919	S	N	none	none
L1455	West742	S	N	none	none
NGC1333	West384	S	N	none	none
NGC1333	West339	S	N	none	none
NGC1333	West644	Q	N	none	none
NGC1333	West1032	Q	N	none	none
NGC1333	West835	Q	N	none	none
NGC1333	West834	S	N	none	none
L1455	West542	S	N	none	none
NGC1333	West549	S	N	none	none
L1455	West586	S	N	none	none
NGC1333	West362	S	N	none	none
NGC1333	West377	S	N	none	none
L1455	West383	S	N	none	none
NGC1333	West222	Q	N	none	none
L1455	West333	S	N	none	none
NGC1333	West425	Q	N	none	none
NGC1333	West363	Q	N	none	none
NGC1333	West464	S	N	none	none
NGC1333	West198	Q	N	none	none
NGC1333	West86	P	Y	SSTc2dJ032832.6+311105	NGC1333-222
NGC1333	West809	Q	N	none	none
NGC1333	West420	S	N	none	none
L1455	West245	S	N	none	none
NGC1333	West31	P	Y	SSTc2dJ032834.5+310051	none
NGC1333	West96	P	Y	SSTc2dJ032834.5+310705	NGC1333-223
NGC1333	West361	S	N	none	none
Off Clump	West486	S	N	none	none
NGC1333	West129	P	Y	none	none

Table H.2 (cont'd)

Location	Source Name	Class[a]	70 μm[b]	C2D Source	G09 Source
NGC1333	West3	P	Y	none	NGC1333-224
L1455	West747	Q	N	none	none
NGC1333	West414	S	N	none	none
Off Clump	West328	P	Y	none	none
NGC1333	West162	P	Y	SSTc2dJ032839.1+310602	NGC1333-210
NGC1333	West366	S	N	none	none
NGC1333	West209	Q	N	none	none
NGC1333	West149	S	N	none	none
NGC1333	West722	Q	N	none	none
Off Clump	West348	S	N	none	none
Off Clump	West968	S	N	none	none
L1455	West547	S	N	none	none
NGC1333	West371	S	N	none	none
NGC1333	West133	Q	N	none	none
NGC1333	West757	S	N	none	none
Off Clump	West338	Q	N	none	none
NGC1333	West281	S	N	none	none
NGC1333	West228	Q	N	none	none
NGC1333	West330	Q	N	none	none
NGC1333	West39	P	Y	SSTc2dJ032843.3+311733	NGC1333-226
NGC1333	West39	P	Y	none	NGC1333-251
L1455	West455	S	N	none	none
NGC1333	West1210	Q	N	none	none
NGC1333	West559	Q	N	none	none
NGC1333	West314	Q	N	none	none
NGC1333	West38	P	Y	SSTc2dJ032845.3+310542	NGC1333-211
NGC1333	West441	Q	N	none	none
Off Clump	West1152	Q	N	none	none
NGC1333	West591	S	N	none	none
NGC1333	West276	Q	N	none	none
L1455	West485	S	N	none	none
NGC1333	West894	Q	N	none	none
L1455	West667	Q	N	none	none
NGC1333	West200	P	N	SSTc2dJ032848.8+311609	NGC1333-227
NGC1333	West494	Q	N	none	none
NGC1333	West898	Q	N	none	none
NGC1333	West282	Q	N	none	none
NGC1333	West140	Q	N	none	none
Off Clump	West67	S	N	none	none
NGC1333	West258	P	Y	SSTc2dJ032851.0+311818	NGC1333-256
NGC1333	West387	P	N	SSTc2dJ032850.5+312943	none
Off Clump	West255	Q	N	none	none
Off Clump	West439	S	N	none	none
NGC1333	West150	Q	N	none	none

Table H.2 (cont'd)

Location	Source Name	Class[a]	70 μm[b]	C2D Source	G09 Source
NGC1333	West247	S	N	none	none
NGC1333	West270	S	N	none	none
L1455	West862	S	N	none	none
NGC1333	West329	Q	N	none	none
NGC1333	West173	Q	N	none	none
NGC1333	West75	S	N	none	none
L1455	West381	S	N	none	none
NGC1333	West495	Q	N	none	none
NGC1333	West78	P	Y	SSTc2dJ032854.0+311809	NGC1333-263
NGC1333	West407	Q	N	none	none
NGC1333	West887	Q	N	none	none
NGC1333	West493	P	Y	SSTc2dJ032854.1+311654	NGC1333-264
NGC1333	West493	P	Y	SSTc2dJ032854.6+311651	NGC1333-265
NGC1333	West208	P	Y	SSTc2dJ032855.1+311629	NGC1333-267
NGC1333	West208	P	Y	SSTc2dJ032855.2+311625	NGC1333-268
NGC1333	West210	Q	N	none	none
NGC1333	West838	Q	N	none	none
NGC1333	West141	Q	N	none	none
NGC1333	West1	P	Y	none	NGC1333-230
NGC1333	West1	P	Y	SSTc2dJ032855.5+311431	none
L1455	West666	S	N	none	none
Off Clump	West691	S	N	none	none
NGC1333	West206	P	Y	SSTc2dJ032856.3+312228	NGC1333-270
NGC1333	West121	P	N	SSTc2dJ032856.1+311908	NGC1333-269
NGC1333	West91	P	Y	SSTc2dJ032856.6+311836	NGC1333-271
NGC1333	West290	Q	N	none	none
NGC1333	West104	Q	N	none	none
L1455	West511	S	N	none	none
NGC1333	West10	P	Y	SSTc2dJ032857.2+311419	none
NGC1333	West10	P	Y	SSTc2dJ032857.4+311416	NGC1333-212
NGC1333	West88	Q	N	none	none
NGC1333	West720	S	N	none	none
NGC1333	West119	Q	N	none	none
NGC1333	West492	Q	N	none	none
NGC1333	West43	P	Y	SSTc2dJ032858.3+312209	NGC1333-275
NGC1333	West43	P	Y	SSTc2dJ032858.4+312218	NGC1333-233
NGC1333	West267	Q	N	none	none
Off Clump	West631	Q	N	none	none
NGC1333	West53	P	Y	SSTc2dJ032859.3+311549	NGC1333-278
NGC1333	West211	Q	N	none	none
NGC1333	West426	Q	N	none	none
NGC1333	West148	Q	N	none	none
NGC1333	West190	Q	N	none	none
NGC1333	West471	S	N	none	none

Table H.2 (cont'd)

Location	Source Name	Class[a]	70 μm[b]	C2D Source	G09 Source
NGC1333	West130	Q	N	none	none
NGC1333	West63	Q	N	none	none
NGC1333	West33	P	Y	SSTc2dJ032900.5+311201	NGC1333-213
NGC1333	West164	Q	N	none	none
NGC1333	West15	P	Y	none	NGC1333-235
NGC1333	West340	Q	N	none	none
NGC1333	West558	Q	N	none	none
NGC1333	West19	P	Y	none	none
NGC1333	West217	Q	N	none	none
NGC1333	West165	Q	N	none	none
NGC1333	West553	S	N	none	none
NGC1333	West199	Q	N	none	none
NGC1333	West68	P	Y	SSTc2dJ032903.3+312315	none
NGC1333	West77	P	N	SSTc2dJ032903.9+312149	NGC1333-287
NGC1333	West2	P	Y	none	NGC1333-236
NGC1333	West266	Q	N	none	none
L1455	West711	Q	N	none	none
NGC1333	West40	P	Y	SSTc2dJ032904.1+311447	NGC1333-214
NGC1333	West232	Q	N	none	none
NGC1333	West124	S	N	none	none
NGC1333	West48	Q	N	none	none
NGC1333	West120	Q	N	none	none
NGC1333	West47	Q	N	none	none
NGC1333	West291	Q	N	none	none
NGC1333	West155	Q	N	none	none
NGC1333	West125	P	N	SSTc2dJ032905.8+311640	NGC1333-293
NGC1333	West922	S	N	none	none
NGC1333	West87	P	N	SSTc2dJ032906.5+311534	none
L1455	West1167	S	N	none	none
NGC1333	West92	S	N	none	none
NGC1333	West7	P	Y	none	NGC1333-238
NGC1333	West201	Q	N	none	none
NGC1333	West194	Q	N	none	none
Off Clump	West961	S	N	none	none
NGC1333	West42	P	Y	none	NGC1333-239
NGC1333	West212	Q	N	none	none
Off Clump	West614	S	N	none	none
Off Clump	West832	S	N	none	none
NGC1333	West890	Q	N	none	none
Off Clump	West532	S	N	none	none
NGC1333	West6	P	Y	SSTc2dJ032910.5+311331	NGC1333-215
Off Clump	West669	S	N	none	none
NGC1333	West11	P	Y	none	none
NGC1333	West16	P	Y	SSTc2dJ032910.7+311821	NGC1333-241

Table H.2 (cont'd)

Location	Source Name	Class[a]	70 μm[b]	C2D Source	G09 Source
NGC1333	West14	P	Y	SSTc2dJ032910.7+311821	NGC1333-241
NGC1333	West14	P	Y	SSTc2dJ032911.3+311831	NGC1333-216
NGC1333	West180	Q	N	none	none
NGC1333	West13	P	Y	SSTc2dJ032912.1+311302	NGC1333-217
NGC1333	West215	Q	N	none	none
NGC1333	West317	Q	N	none	none
NGC1333	West154	Q	N	none	none
NGC1333	West315	Q	N	none	none
NGC1333	West110	Q	N	none	none
NGC1333	West49	P	Y	SSTc2dJ032913.0+311814	NGC1333-242
NGC1333	West83	Q	N	none	none
NGC1333	West30	P	Y	SSTc2dJ032913.5+311358	NGC1333-219
NGC1333	West143	S	N	none	none
NGC1333	West205	P	Y	SSTc2dJ032914.4+311444	none
NGC1333	West81	Q	N	none	none
NGC1333	West181	S	N	none	none
NGC1333	West122	Q	N	none	none
Off Clump	West787	S	N	none	none
Off Clump	West581	S	N	none	none
NGC1333	West131	Q	N	none	none
NGC1333	West203	Q	N	none	none
NGC1333	West94	Q	N	none	none
NGC1333	West23	P	Y	SSTc2dJ032917.2+312746	NGC1333-220
NGC1333	West260	Q	N	none	none
NGC1333	West561	S	N	none	none
NGC1333	West116	P	N	SSTc2dJ032917.7+312245	NGC1333-316
NGC1333	West341	S	N	none	none
NGC1333	West409	Q	N	none	none
NGC1333	West195	S	N	none	none
NGC1333	West473	S	N	none	none
NGC1333	West37	P	Y	none	none
NGC1333	West229	Q	N	none	none
NGC1333	West60	P	N	SSTc2dJ032919.8+312457	none
NGC1333	West259	S	N	none	none
NGC1333	West182	Q	N	none	none
NGC1333	West55	P	N	SSTc2dJ032920.1+312408	NGC1333-320
NGC1333	West171	Q	N	none	none
NGC1333	West560	Q	N	none	none
NGC1333	West973	P	Y	none	none
NGC1333	West157	P	Y	SSTc2dJ032920.4+311834	NGC1333-321
NGC1333	West123	Q	N	none	none
NGC1333	West592	Q	N	none	none
NGC1333	West224	Q	N	none	none
Off Clump	West436	S	N	none	none

Table H.2 (cont'd)

Location	Source Name	Class[a]	70 μm[b]	C2D Source	G09 Source
Off Clump	West861	Q	N	none	none
NGC1333	West44	P	Y	SSTc2dJ032923.5+313330	NGC1333-221
NGC1333	West319	S	N	none	none
NGC1333	West207	Q	N	none	none
NGC1333	West726	Q	N	none	none
NGC1333	West891	Q	N	none	none
NGC1333	West522	Q	N	none	none
NGC1333	West108	S	N	none	none
NGC1333	West1071	Q	N	none	none
Off Clump	West628	S	N	none	none
NGC1333	West622	Q	N	none	none
Off Clump	West746	S	N	none	none
NGC1333	West697	Q	N	none	none
NGC1333	West137	P	Y	SSTc2dJ032929.3+311835	NGC1333-342
Off Clump	West324	S	N	none	none
NGC1333	West1008	Q	N	none	none
NGC1333	West807	Q	N	none	none
Off Clump	West702	S	N	none	none
NGC1333	West844	Q	N	none	none
Off Clump	West336	S	N	none	none
NGC1333	West763	Q	N	none	none
NGC1333	West620	Q	N	none	none
NGC1333	West940	Q	N	none	none
Off Clump	West739	S	N	none	none
Off Clump	West300	S	N	none	none
NGC1333	West977	Q	N	none	none
NGC1333	West768	Q	N	none	none
Off Clump	West640	S	N	none	none
Off Clump	West749	S	N	none	none
NGC1333	West444	Q	N	none	none
NGC1333	West649	S	N	none	none
NGC1333	West28	P	Y	SSTc2dJ032951.8+313906	none
NGC1333	West283	P	Y	SSTc2dJ032954.0+312053	NGC1333-338
NGC1333	West730	S	N	none	none
NGC1333	West1012	Q	N	none	none
NGC1333	West292	S	N	none	none
Off Clump	West401	S	N	none	none
Off Clump	West1015	Q	N	none	none
Off Clump	West865	S	N	none	none
NGC1333	West573	S	N	none	none
Off Clump	West885	Q	N	none	none
Off Clump	West1027	S	N	none	none
Off Clump	West175	Q	N	none	none
Off Clump	West516	S	N	none	none

Table H.2 (cont'd)

Location	Source Name	Class[a]	70 μm[b]	C2D Source	G09 Source
Off Clump	West833	Q	N	none	none
Off Clump	West21	P	Y	SSTc2dJ033015.1+302349	none
NGC1333	West682	Q	N	none	none
Off Clump	West252	S	N	none	none
Off Clump	West1106	Q	N	none	none
Off Clump	West62	P	Y	none	none
Off Clump	West752	S	N	none	none
Off Clump	West717	S	N	none	none
Off Clump	West588	Q	N	none	none
Off Clump	West302	S	N	none	none
Off Clump	West400	S	N	none	none
Off Clump	West246	S	N	none	none
Off Clump	West51	P	Y	SSTc2dJ033027.1+302830	none
Off Clump	West76	P	Y	SSTc2dJ033032.7+302627	none
Off Clump	West422	S	N	none	none
Off Clump	West1197	P	Y	SSTc2dJ033035.9+303024	none
Off Clump	West402	S	N	none	none
Off Clump	West156	P	Y	SSTc2dJ033038.2+303212	none
Off Clump	West587	S	N	none	none
Off Clump	West798	S	N	none	none
Off Clump	West690	S	N	none	none
Off Clump	West693	S	N	none	none
Off Clump	West52	P	Y	SSTc2dJ033044.0+303247	none
Off Clump	West515	S	N	none	none
Off Clump	West167	S	N	none	none
Off Clump	West273	Q	N	none	none
Off Clump	West221	S	N	none	none
Off Clump	West170	P	Y	SSTc2dJ033052.5+305418	none
Off Clump	West918	S	N	none	none
Off Clump	West557	S	N	none	none
Off Clump	West483	S	N	none	none
Off Clump	West689	S	N	none	none
Off Clump	West460	Q	N	none	none
B1	West256	S	N	none	none
B1	West489	Q	N	none	none
B1	West274	S	N	none	none
B1	West17	P	Y	SSTc2dJ033121.0+304530	none
B1	West670	Q	N	none	none
Off Clump	West499	S	N	none	none
Off Clump	West128	P	Y	SSTc2dJ033128.9+303053	none
B1	West1003	S	N	none	none
Off Clump	West1086	Q	N	none	none
Off Clump	West484	S	N	none	none
Off Clump	West1221	Q	N	none	none

Table H.2 (cont'd)

Location	Source Name	Class[a]	70 μm[b]	C2D Source	G09 Source
B1	West928	S	N	none	none
Off Clump	West354	S	N	none	none
Off Clump	West514	S	N	none	none
B1	West355	S	N	none	none
B1	West235	P	Y	none	none
B1	West368	S	N	none	none
B1	West504	S	N	none	none
B1	West841	Q	N	none	none
B1	West321	Q	N	none	none
B1	West700	S	N	none	none
B1	West895	S	N	none	none
B1	West723	Q	N	none	none
Off Clump	West236	S	N	none	none
B1	West415	S	N	none	none
Off Clump	West432	S	N	none	none
B1	West632	S	N	none	none
B1	West406	Q	N	none	none
B1	West430	S	N	none	none
B1	West597	Q	N	none	none
B1	West26	P	Y	SSTc2dJ033218.0+304947	none
B1	West443	S	N	none	none
Off Clump	West308	S	N	none	none
B1	West839	Q	N	none	none
B1	West695	Q	N	none	none
B1	West900	Q	N	none	none
B1	West389	Q	N	none	none
Off Clump	West565	S	N	none	none
B1	West779	S	N	none	none
B1	West764	S	N	none	none
B1	West519	S	N	none	none
B1	West496	S	N	none	none
B1	West241	S	N	none	none
B1	West674	S	N	none	none
B1	West202	Q	N	none	none
B1	West899	S	N	none	none
B1	West46	P	Y	SSTc2dJ033229.2+310241	none
B1	West525	S	N	none	none
B1	West297	Q	N	none	none
Off Clump	West917	Q	N	none	none
B1	West369	S	N	none	none
B1	West647	Q	N	none	none
B1	West370	Q	N	none	none
B1	West132	P	Y	SSTc2dJ033234.0+310056	none
B1	West1128	S	N	none	none

Table H.2 (cont'd)

Location	Source Name	Class[a]	70 μm[b]	C2D Source	G09 Source
B1	West385	S	N	none	none
Off Clump	West851	Q	N	none	none
B1	West1036	Q	N	none	none
B1	West780	Q	N	none	none
B1	West593	Q	N	none	none
Off Clump	West529	S	N	none	none
B1	West813	Q	N	none	none
B1	West318	Q	N	none	none
B1	West686	Q	N	none	none
B1	West1010	Q	N	none	none
B1	West595	S	N	none	none
B1	West929	Q	N	none	none
B1	West812	S	N	none	none
B1	West1216	Q	N	none	none
B1	West342	S	N	none	none
B1	West733	S	N	none	none
B1	West520	Q	N	none	none
B1	West562	S	N	none	none
B1	West924	Q	N	none	none
B1	West978	Q	N	none	none
B1	West571	Q	N	none	none
B1	West925	Q	N	none	none
B1	West249	S	N	none	none
B1	West307	S	N	none	none
B1	West261	Q	N	none	none
B1	West1112	Q	N	none	none
B1	West271	Q	N	none	none
B1	West301	Q	N	none	none
B1	West727	S	N	none	none
B1	West379	Q	N	none	none
B1	West250	S	N	none	none
B1	West503	S	N	none	none
B1	West698	Q	N	none	none
B1	West29	P	Y	SSTc2dJ033312.8+312124	none
B1	West135	Q	N	none	none
B1	West136	S	N	none	none
B1	West650	Q	N	none	none
B1	West50	P	Y	SSTc2dJ033314.4+310711	none
B1	West34	P	Y	SSTc2dJ033316.4+310653	none
B1	West24	P	Y	SSTc2dJ033316.7+310755	none
B1	West845	Q	N	none	none
B1	West769	Q	N	none	none
B1	West729	Q	N	none	none
B1	West12	P	Y	SSTc2dJ033317.9+310932	none

Table H.2 (cont'd)

Location	Source Name	Class[a]	70 μm[b]	C2D Source	G09 Source
B1	West234	S	N	none	none
B1	West41	Q	N	none	none
B1	West847	Q	N	none	none
B1	West624	Q	N	none	none
B1	West248	Q	N	none	none
B1	West1078	Q	N	none	none
B1	West1161	Q	N	none	none
B1	West934	Q	N	none	none
B1	West500	S	N	none	none
B1	West295	S	N	none	none
B1	West526	Q	N	none	none
B1	West27	P	Y	SSTc2dJ033327.3+310710	none
B1	West427	S	N	none	none
B1	West505	S	N	none	none
B1	West498	S	N	none	none
B1	West410	S	N	none	none
B1	West84	P	Y	SSTc2dJ033330.4+311051	none
B1	West429	Q	N	none	none
B1	West731	Q	N	none	none
B1	West447	S	N	none	none
B1	West343	S	N	none	none
B1	West474	P	Y	SSTc2dJ033341.3+311341	none
B1	West345	S	N	none	none
B1	West431	S	N	none	none
B1	West572	Q	N	none	none
B1	West501	S	N	none	none
B1	West626	S	N	none	none
B1	West784	S	N	none	none
B1	West633	S	N	none	none
B1	East460	S	N	none	none
B1	West684	S	N	none	none
B1	West736	Q	N	none	none
B1	West816	Q	N	none	none
B1	West1080	S	N	none	none
B1	West356	S	N	none	none
B1	East421	Q	N	none	none
Off Clump	East494	Q	N	none	none
Off Clump	East476	S	N	none	none
Off Clump	West449	S	N	none	none
B1E	West391	S	N	none	none
Off Clump	East462	S	N	none	none
Off Clump	West854	Q	N	none	none
Off Clump	East423	S	N	none	none
B1E	West309	S	N	none	none

Table H.2 (cont'd)

Location	Source Name	Class[a]	70 μm[b]	C2D Source	G09 Source
B1E	East336	Q	N	none	none
B1E	West346	S	N	none	none
B1E	West507	S	N	none	none
B1E	West531	S	N	none	none
B1E	West737	S	N	none	none
Off Clump	East612	S	N	none	none
B1E	West656	S	N	none	none
B1E	West450	S	N	none	none
B1E	West942	S	N	none	none
B1E	East325	S	N	none	none
B1E	East222	Q	N	none	none
B1E	East170	S	N	none	none
Off Clump	West903	Q	N	none	none
Off Clump	West1227	Q	N	none	none
Off Clump	East380	Q	N	none	none
Off Clump	West1293	S	N	none	none
Off Clump	East497	Q	N	none	none
Off Clump	West1085	Q	N	none	none
Off Clump	West1084	S	N	none	none
Off Clump	East642	S	N	none	none
Off Clump	West1333	Q	N	none	none
Off Clump	East402	S	N	none	none
Off Clump	West984	P	Y	none	none
Off Clump	East758	Q	N	none	none
Off Clump	East591	Q	N	none	none
Off Clump	West1325	Q	N	none	none
Off Clump	East537	S	N	none	none
Off Clump	East385	S	N	none	none
Off Clump	West1052	Q	N	none	none
Off Clump	East410	Q	N	none	none
Off Clump	East356	S	N	none	none
Off Clump	East355	S	N	none	none
Off Clump	East561	S	N	none	none
Off Clump	West1166	Q	N	none	none
Off Clump	East313	Q	N	none	none
Off Clump	East345	S	N	none	none
Off Clump	West1332	Q	N	none	none
Off Clump	East246	Q	N	none	none
Off Clump	East441	S	N	none	none
Off Clump	West1367	Q	N	none	none
Off Clump	East382	S	N	none	none
Off Clump	East258	S	N	none	none
Off Clump	East256	S	N	none	none
Off Clump	West1228	Q	N	none	none

Table H.2 (cont'd)

Location	Source Name	Class[a]	70 μm[b]	C2D Source	G09 Source
Off Clump	East291	Q	N	none	none
Off Clump	West1229	Q	N	none	none
Off Clump	East371	S	N	none	none
Off Clump	East383	S	N	none	none
Off Clump	East351	S	N	none	none
Off Clump	East414	Q	N	none	none
Off Clump	East464	S	N	none	none
Off Clump	East316	S	N	none	none
Off Clump	East479	S	N	none	none
Off Clump	East255	S	N	none	none
Off Clump	East625	S	N	none	none
Off Clump	East6	P	Y	none	none
Off Clump	East443	Q	N	none	none
Off Clump	East328	S	N	none	none
Off Clump	East465	S	N	none	none
Off Clump	East373	Q	N	none	none
Off Clump	East280	S	N	none	none
IC348	East347	Q	N	none	none
IC348	East152	S	N	none	none
Off Clump	East124	S	N	none	none
IC348	East168	S	N	none	none
Off Clump	East599	Q	N	none	none
Off Clump	East499	S	N	none	none
IC348	East650	Q	N	none	none
IC348	East327	S	N	none	none
IC348	East340	S	N	none	none
Off Clump	East412	Q	N	none	none
IC348	East569	Q	N	none	none
IC348	East201	Q	N	none	none
Off Clump	East828	Q	N	none	none
IC348	East570	S	N	none	none
Off Clump	East178	S	N	none	none
Off Clump	East563	S	N	none	none
Off Clump	East721	Q	N	none	none
Off Clump	East150	S	N	none	none
IC348	East58	P	Y	SSTc2dJ034027.7+314313	none
IC348	East348	S	N	none	none
Off Clump	East326	S	N	none	none
IC348	East282	S	N	none	none
Off Clump	East830	Q	N	none	none
IC348	East293	Q	N	none	none
IC348	East626	S	N	none	none
IC348	East891	S	N	none	none
Off Clump	East706	S	N	none	none

Table H.2 (cont'd)

Location	Source Name	Class[a]	70 μm[b]	C2D Source	G09 Source
IC348	East114	Q	N	none	none
Off Clump	East273	S	N	none	none
IC348	East428	S	N	none	none
IC348	East405	S	N	none	none
Off Clump	East597	Q	N	none	none
IC348	East480	S	N	none	none
IC348	East799	S	N	none	none
IC348	East745	S	N	none	none
IC348	East173	S	N	none	none
IC348	East283	S	N	none	none
IC348	East10	P	Y	SSTc2dJ034109.1+314438	none
IC348	East172	S	N	none	none
IC348	East726	Q	N	none	none
IC348	East128	S	N	none	none
Off Clump	East457	Q	N	none	none
IC348	East262	Q	N	none	none
IC348	East53	P	Y	SSTc2dJ034125.0+315657	none
IC348	East281	S	N	none	none
Off Clump	East512	P	Y	none	none
IC348	East357	S	N	none	none
IC348	East202	Q	N	none	none
IC348	East448	S	N	none	none
IC348	East179	Q	N	none	none
IC348	East180	Q	N	none	none
IC348	East183	Q	N	none	none
IC348	East329	Q	N	none	none
IC348	East136	P	Y	SSTc2dJ034155.7+314811	none
IC348	East231	Q	N	none	none
IC348	East573	Q	N	none	none
IC348	East78	S	N	none	none
IC348	East339	S	N	none	none
IC348	East391	Q	N	none	none
IC348	East57	P	Y	none	none
IC348	East653	Q	N	none	none
IC348	East306	S	N	none	none
IC348	East308	S	N	none	none
IC348	East153	P	Y	SSTc2dJ034202.2+314802	none
IC348	East115	S	N	none	none
IC348	East224	S	N	none	none
IC348	East307	Q	N	none	none
IC348	East950	S	N	none	none
IC348	East151	S	N	none	none
IC348	East182	S	N	none	none
IC348	East184	Q	N	none	none

Table H.2 (cont'd)

Location	Source Name	Class[a]	70 μm[b]	C2D Source	G09 Source
IC348	East388	S	N	none	none
IC348	East941	Q	N	none	none
IC348	East275	Q	N	none	none
IC348	East294	S	N	none	none
IC348	East81	S	N	none	none
IC348	East205	P	Y	SSTc2dJ034254.7+314345	none
IC348	East23	P	Y	SSTc2dJ034255.9+315842	none
IC348	East191	S	N	none	none
IC348	East274	S	N	none	none
IC348	East544	Q	N	none	none
Off Clump	East528	S	N	none	none
IC348	East190	S	N	none	none
Off Clump	East505	S	N	none	none
IC348	East452	Q	N	none	none
IC348	East358	S	N	none	none
Off Clump	East169	S	N	none	none
IC348	East509	S	N	none	none
IC348	East526	Q	N	none	none
IC348	East416	Q	N	none	none
IC348	East142	S	N	none	none
Off Clump	East148	S	N	none	none
IC348	East413	Q	N	none	none
IC348	East862	S	N	none	none
IC348	East235	Q	N	none	none
Off Clump	East515	Q	N	none	none
IC348	East450	S	N	none	none
IC348	East64	S	N	none	none
IC348	East375	Q	N	none	none
IC348	East104	Q	N	none	none
IC348	East103	Q	N	none	none
IC348	East54	P	Y	SSTc2dJ034344.5+314309	none
IC348	East408	P	Y	SSTc2dJ034344.6+320818	IC348-494
IC348	East471	Q	N	none	none
IC348	East12	P	Y	SSTc2dJ034345.2+320359	IC348-348
IC348	East86	S	N	none	none
IC348	East132	Q	N	none	none
IC348	East407	Q	N	none	none
Off Clump	East155	S	N	none	none
IC348	East93	Q	N	none	none
IC348	East11	P	Y	none	IC348-367
IC348	East11	P	Y	SSTc2dJ034351.0+320325	IC348-345
IC348	East9	P	Y	SSTc2dJ034351.0+320308	none
IC348	East63	Q	N	none	none
IC348	East97	Q	N	none	none

Table H.2 (cont'd)

Location	Source Name	Class[a]	70 μm[b]	C2D Source	G09 Source
IC348	East118	Q	N	none	none
Off Clump	East584	S	N	none	none
IC348	East137	S	N	none	none
IC348	East453	Q	N	none	none
IC348	East4	P	Y	SSTc2dJ034356.5+320053	none
IC348	East5	P	Y	none	IC348-371
IC348	East5	P	Y	SSTc2dJ034356.8+320305	none
IC348	East79	Q	N	none	none
Off Clump	East482	Q	N	none	none
IC348	East55	Q	N	none	none
IC348	East193	S	N	none	none
IC348	East26	P	Y	SSTc2dJ034359.4+320036	none
IC348	East62	Q	N	none	none
IC348	East18	S	N	none	none
IC348	East100	S	N	none	none
IC348	East17	P	Y	SSTc2dJ034402.4+320205	IC348-352
IC348	East17	P	Y	SSTc2dJ034402.6+320160	IC348-353
IC348	East486	S	N	none	none
IC348	East208	Q	N	none	none
IC348	East89	Q	N	none	none
IC348	East632	Q	N	none	none
IC348	East185	S	N	none	none
IC348	East206	S	N	none	none
IC348	East250	Q	N	none	none
IC348	East67	Q	N	none	none
IC348	East98	Q	N	none	none
IC348	East107	S	N	none	none
IC348	East48	S	N	none	none
IC348	East30	P	Y	SSTc2dJ034409.2+320238	IC348-354
IC348	East252	Q	N	none	none
IC348	East121	S	N	none	none
IC348	East253	S	N	none	none
IC348	East7	P	Y	SSTc2dJ034413.0+320135	IC348-355
IC348	East771	Q	N	none	none
IC348	East82	Q	N	none	none
IC348	East157	S	N	none	none
IC348	East92	S	N	none	none
IC348	East187	Q	N	none	none
IC348	East436	S	N	none	none
IC348	East363	P	Y	none	none
IC348	East16	P	Y	SSTc2dJ034418.2+320457	IC348-393
IC348	East120	Q	N	none	none
IC348	East13	P	Y	SSTc2dJ034421.4+315933	IC348-401
IC348	East236	S	N	none	none

Table H.2 (cont'd)

Location	Source Name	Class[a]	70 μm[b]	C2D Source	G09 Source
IC348	East126	Q	N	none	none
IC348	East362	P	N	SSTc2dJ034422.6+320154	IC348-497
IC348	East362	P	N	SSTc2dJ034422.7+320142	IC348-406
IC348	East122	P	Y	none	none
IC348	East207	S	N	none	none
IC348	East303	Q	N	none	none
IC348	East154	Q	N	none	none
IC348	East29	Q	N	none	none
IC348	East76	P	Y	SSTc2dJ034426.0+320430	IC348-414
IC348	East394	Q	N	none	none
IC348	East265	P	N	SSTc2dJ034426.7+320820	IC348-415
IC348	East310	Q	N	none	none
IC348	East319	Q	N	none	none
IC348	East27	S	N	none	none
IC348	East219	Q	N	none	none
IC348	East317	Q	N	none	none
IC348	East218	S	N	none	none
IC348	East110	P	N	SSTc2dJ034429.7+321040	IC348-423
IC348	East158	Q	N	none	none
IC348	East238	Q	N	none	none
IC348	East165	Q	N	none	none
IC348	East36	P	Y	none	none
IC348	East45	P	Y	none	none
IC348	East40	P	N	SSTc2dJ034434.2+320946	none
IC348	East579	S	N	none	none
IC348	East176	S	N	none	none
IC348	East25	P	N	none	IC348-440
IC348	East25	P	N	SSTc2dJ034435.5+320856	IC348-443
IC348	East15	P	Y	none	none
IC348	East101	Q	N	none	none
IC348	East365	Q	N	none	none
IC348	East61	S	N	none	none
IC348	East269	Q	N	none	none
IC348	East211	S	N	none	none
IC348	East195	S	N	none	none
IC348	East43	Q	N	none	none
IC348	East134	Q	N	none	none
IC348	East432	S	N	none	none
IC348	East50	Q	N	none	none
IC348	East175	Q	N	none	none
IC348	East111	Q	N	none	none
IC348	East66	Q	N	none	none
IC348	East634	Q	N	none	none
IC348	East225	Q	N	none	none

Table H.2 (cont'd)

Location	Source Name	Class[a]	70 μm[b]	C2D Source	G09 Source
IC348	East166	Q	N	none	none
IC348	East125	S	N	none	none
IC348	East131	S	N	none	none
IC348	East254	Q	N	none	none
IC348	East127	Q	N	none	none
IC348	East2	P	Y	SSTc2dJ034443.3+320132	IC348-357
IC348	East309	S	N	none	none
IC348	East94	S	N	none	none
IC348	East80	Q	N	none	none
IC348	East96	Q	N	none	none
IC348	East84	S	N	none	none
IC348	East71	Q	N	none	none
IC348	East68	S	N	none	none
IC348	East510	Q	N	none	none
IC348	East604	Q	N	none	none
IC348	East130	Q	N	none	none
IC348	East140	Q	N	none	none
IC348	East105	S	N	none	none
IC348	East270	Q	N	none	none
IC348	East580	Q	N	none	none
IC348	East139	Q	N	none	none
IC348	East278	S	N	none	none
IC348	East109	Q	N	none	none
IC348	East209	S	N	none	none
IC348	East805	S	N	none	none
IC348	East119	S	N	none	none
IC348	East147	S	N	none	none
IC348	East213	Q	N	none	none
IC348	East454	S	N	none	none
IC348	East210	S	N	none	none
IC348	East159	P	Y	SSTc2dJ034516.3+320620	IC348-486
IC348	East116	S	N	none	none
IC348	East266	S	N	none	none
IC348	East267	P	Y	SSTc2dJ034520.5+320634	IC348-488
IC348	East102	S	N	none	none
IC348	East318	S	N	none	none
IC348	East240	S	N	none	none
IC348	East455	S	N	none	none
IC348	East473	Q	N	none	none
Off Clump	East3	P	Y	SSTc2dJ034548.3+322412	none
B5	East271	S	N	none	none
B5	East304	S	N	none	none
B5	East284	S	N	none	none
B5	East661	Q	N	none	none

Table H.2 (cont'd)

Location	Source Name	Class[a]	70 μm[b]	C2D Source	G09 Source
B5	East242	S	N	none	none
B5	East14	P	Y	SSTc2dJ034705.4+324309	none
B5	East323	S	N	none	none
B5	East285	S	N	none	none
B5	East215	S	N	none	none
B5	East229	S	N	none	none
B5	East589	Q	N	none	none
B5	East189	S	N	none	none
B5	East519	Q	N	none	none
B5	East305	S	N	none	none
B5	East286	S	N	none	none
B5	East75	S	N	none	none
B5	East244	S	N	none	none
B5	East321	S	N	none	none
B5	East1	P	Y	SSTc2dJ034741.6+325144	none
B5	East197	S	N	none	none
B5	East439	S	N	none	none
B5	East367	S	N	none	none
B5	East530	Q	N	none	none
B5	East379	S	N	none	none
B5	East288	S	N	none	none
B5	East398	S	N	none	none
B5	East243	S	N	none	none
Off Clump	East162	S	N	none	none

[a]Source classification where S is starless, P is protostellar, and Q is questionably starless. See Section 5.4.3.

[b]Detection of a compact 70 μm source.

Table H.3 gives the results from our virial analysis (see Section 5.4.3). Only 51 sources had NH_3 detections and good mass measurements (from SED-fitting). Columns 1-2 gives the source location and name. Column 3 gives the detection quality, where "WD" corresponds to well-detected sources and "PD" corresponds to poorly-detected sources. Column 4 gives the classification, where "S" corresponds to starless cores, "Q" corresponds to questionably starless cores, and "P" corresponds to protostellar cores. See Section 5.3.2 for more details. Column 5 gives the average column density. Column 6 gives the NH_3 detection name. We used NH_3 observations from Chapter 3 and Rosolowsky et al. (2008). Sources West60 and West108 each had two NH_3 observations at the same location; we included both readings in this analysis. Columns 7-8 give the virial masses and virial parameters, respectively.

Table H.3. Virial Properties of *Herschel* Objects

Location	Source Name	Quality[a]	Class[b]	n[c] (10^5 cm^{-3})	NH_3ID[d]	M_{virial} ($M_\odot$)	α
Off Clump	West279	WD	S	1.11	9	1.56	1.08
Off Clump	West452	WD	S	0.94	13	5.23	1.77
Off Clump	West416	WD	S	1.53	16	2.12	1.10
L1448	West197	PD	S	6.73	17	1.41	0.34
L1448	West191	WD	S	4.21	18	1.13	0.96
L1448	West244	WD	S	0.87	21	2.83	3.65
L1455	West226	WD	S	0.70	24	2.28	1.63
L1455	West161	PD	S	363.57	33	0.63	0.08
NGC1333	West420	WD	S	2.03	41	2.15	0.64
L1455	West245	WD	S	1.23	42	1.23	2.64
NGC1333	West96[e]	WD	P	···	43	···	···
NGC1333	West162	WD	P	4.83	46	1.65	0.49
NGC1333	West149	PD	S	5.81	47	2.34	0.45
NGC1333	West281	WD	S	50.69	50	0.76	0.25
NGC1333	West40	PD	P	2234.88	68	2.57	0.19
NGC1333	West124	PD	S	7.77	69	2.14	1.28
NGC1333	West92	WD	S	33.35	72	1.19	0.47
NGC1333	West16	WD	P	195.24	77	0.32	1.63
NGC1333	West23	WD	P	449.66	81	0.16	0.43
NGC1333	West60	WD	P	0.72	82a	1.76	1.93
NGC1333	West60	WD	P	0.72	82b	2.13	2.33
NGC1333	West108	WD	S	15.23	88a	0.47	0.64
NGC1333	West108	WD	S	15.23	88b	0.58	0.80
Off Clump	West246	WD	S	0.29	93	1.60	3.19
Off Clump	West167	WD	S	1.07	96	3.06	0.63
Off Clump	West221	WD	S	1.65	97	0.94	1.52
B1	West241	PD	S	4.57	104	1.35	0.78
B1	West562	WD	S	0.43	110	6.25	7.81
B1	West249	WD	S	1.71	112	3.62	1.98
B1	West307	PD	S	2.77	113	2.34	0.40
B1	West250	PD	S	4.96	117	2.36	5.87
B1	West136	WD	S	11.58	118	0.86	0.41
B1	West295	PD	S	14.13	124	1.12	0.18
B1	West27	PD	P	143.02	126	0.29	3.72
Off	West449	WD	S	0.50	132	3.60	2.40
B1E	West346	WD	S	0.12	B1E3	7.61	10.36
B1E	West507	WD	S	0.36	B1E1	9.70	13.85
B1E	West531	WD	S	1.60	B1E2	1.41	1.13
B1E	West737	WD	S	0.25	B1E8	3.37	9.32
B1E	West450	WD	S	0.96	B1E9	3.35	7.29
B1E	East170	WD	S	0.83	B1E6	6.90	7.34
IC348	East128	WD	S	0.71	144	3.05	6.69
IC348	East81	WD	S	0.46	153	3.98	6.79

Table H.3 (cont'd)

Location	Source Name	Quality[a]	Class[b]	n[c] (10^5 cm^{-3})	NH_3ID[d]	M_{virial} ($M_\odot$)	α
IC348	East191	WD	S	0.77	154	5.32	18.22
IC348	East64	WD	S	1.54	156	6.55	3.09
IC348	East86	PD	S	9.17	158	1.18	0.69
IC348	East107	WD	S	5.96	168	1.95	1.03
IC348	East157	WD	S	0.67	170	1.57	2.96
IC348	East92	WD	S	0.77	171	2.02	3.24
IC348	East61	WD	S	7.68	176	1.04	1.04
IC348	East68	PD	S	11.49	180	0.57	1.02
IC348	East116	WD	S	1.66	183	1.42	0.91
B5	East75	WD	S	65.63	189	0.66	0.37

[a]Quality of the *Herschel* source. See Section 5.3.2.

[b]Source classification where S is starless and P is protostellar. See Section 5.4.3.

[c]Average density for a mean molecular weight of $\mu = 2.8$ and assuming perfect spheres.

[d]The NH_3 data for B1-E are from Chapter 3. For the rest of Perseus, the NH_3 data are from Rosolowsky et al. (2008).

[e]Point source.

Table H.4 gives the YSO classifications for all the identified protostellar sources. For more details, see Section 5.4.3. Columns 1-2 gives the source location and name. Column 3 gives the corresponding infrared source name, if applicable. Identified YSOs without infrared sources were classified based on compact 70 μm emission. Column 4 gives the adopted interstellar extinction. Columns 5-6 give the spectral index (α) and the corresponding YSO classification. Columns 7-8 give the bolometric temperature (T_{bol}) and the YSO classification based on the bolometric temperature. Columns 9-11 give the bolometric luminosity (L_{bol}), the submillimeter luminosity (L_{smm}), and the classification based on the ratio of L_{smm}/L_{bol}. The submillimeter luminosity was measured only for $\lambda \geq 350$ μm. Since L_{smm}/L_{bol} can only distinguish between Class 0 and non-Class 0 sources, we use "X" to correspond to non-Class 0 YSOs. Column 12 gives some notes.

Table H.4. Full SED Analyses of *Herschel* YSOs

Location	Source Name	IR Name[a]	A_V[b] (mag)	α	ClassA[c]	T_{bol} (K)	ClassT[c]	L_{bol} ($L_\odot$)	L_{smm} ($L_\odot$)	ClassL[c]	Notes
L1448	West32[h]	none	5.9	···	···	35	0	1.1×10^{-1}	8.7×10^{-4}	X	NS
L1448	West9	SSTc2dJ032522.3+304514	5.9	2.25	0/I	42	0	3.9	7.8×10^{-2}	X	E
L1448	West25	none	5.9	···	···	22	0	1.5	8.6×10^{-2}	0	E,NS
L1448	West8	SSTc2dJ032536.5+304522	5.9	2.51	0/I	57	0	9.1	2.3×10^{-1}	X	E
L1448	West4	SSTc2dJ032538.8+304406	5.9	2.09	0/I	46	0	1.0×10^{1}	1.5×10^{-1}	X	E
L1448	West4	SSTc2dJ032539.1+304358	5.9	2.23	0/I	47	0	9.9	1.5×10^{-1}	X	E
Off Clump	West20	SSTc2dJ032637.5+301528	5.9	0.95	0/I	76	I	9.6×10^{-1}	2.1×10^{-2}	X	E
L1455	West35	SSTc2dJ032738.2+301359	5.9	-0.44	II	377	I	8.6×10^{-1}	1.9×10^{-2}	X	E
L1455	West5	SSTc2dJ032738.8+301258	5.9	0.87	0/I	43	0	5.7	5.4×10^{-2}	X	E
L1455	West5	SSTc2dJ032739.1+301303	5.9	2.57	0/I	55	0	6.3	5.4×10^{-2}	X	E
L1455	West18	SSTc2dJ032743.2+301229	5.9	2.28	0/I	66	0	1.6	3.8×10^{-2}	X	E
L1455	West36	SSTc2dJ032747.7+301205	5.9	-0.29	F	923	II	3.7	3.0×10^{-2}	X	L
L1455	West82	SSTc2dJ032800.4+300801	5.9	1.04	0/I	294	I	2.9×10^{-1}	6.2×10^{-3}	X	E
NGC1333	West86	SSTc2dJ032832.6+311105	5.9	0.58	0/I	117	I	1.5×10^{-1}	1.1×10^{-2}	0	E
NGC1333	West86	NGC1333-222	5.9	0.89	0/I	77	I	1.5×10^{-1}	1.1×10^{-2}	0	E
NGC1333	West31	SSTc2dJ032834.5+310051	5.9	1.05	0/I	316	I	1.1	6.5×10^{-3}	X	E
NGC1333	West96	SSTc2dJ032834.5+310705	5.9	0.41	0/I	182	I	1.3×10^{-1}	7.7×10^{-3}	0	E
NGC1333	West96	NGC1333-223	5.9	0.18	F	172	I	1.3×10^{-1}	7.7×10^{-3}	0	E
NGC1333	West129	none	5.9	···	···	22	0	7.3×10^{-2}	4.8×10^{-3}	0	E,NS
NGC1333	West3	NGC1333-224	5.9	2.41	0/I	65	0	2.1×10^{1}	5.5×10^{-2}	X	E
Off Clump	West328[h]	none	5.9	···	···	34	0	1.3×10^{-2}	0.0	X	NS
NGC1333	West162	SSTc2dJ032839.1+310602	5.9	1.59	0/I	23	0	3.0×10^{-1}	4.8×10^{-2}	0	E
NGC1333	West162	NGC1333-210	5.9	1.54	0/I	23	0	3.0×10^{-1}	4.8×10^{-2}	0	E
NGC1333	West39	SSTc2dJ032843.3+311733	5.9	0.26	F	602	I	2.2	1.2×10^{-2}	X	L
NGC1333	West39	NGC1333-226	7.9	0.05	F	670	II	2.6	1.2×10^{-2}	X	L
NGC1333	West39	NGC1333-251	3.7	-0.36	II	546	I	1.2	1.2×10^{-2}	X	E,C
NGC1333	West38	SSTc2dJ032845.3+310542	5.9	0.98	0/I	86	I	3.6×10^{-1}	1.4×10^{-2}	X	E
NGC1333	West38	NGC1333-211	5.9	1.54	0/I	83	I	3.7×10^{-1}	1.4×10^{-2}	X	E
NGC1333	West200	SSTc2dJ032848.8+311609	5.9	0.19	F	98	I	1.2×10^{-1}	1.0×10^{-2}	0	E

Table H.4 (cont'd)

Location	Source Name	IR Name[a]	A_V[b] (mag)	α	ClassA[c]	T_{bol} (K)	ClassT[c]	L_{bol} ($L_\odot$)	L_{smm} ($L_\odot$)	ClassL[c]	Notes
NGC1333	West200	NGC1333-227	5.9	0.22	F	81	I	1.1×10^{-1}	1.0×10^{-2}	0	E
NGC1333	West258	SSTc2dJ032851.0+311818	7.3	-1.12	II	1535	II	1.3	2.2×10^{-3}	X	L
NGC1333	West258	NGC1333-256	3.7	-0.56	II	1351	II	8.2×10^{-1}	2.2×10^{-3}	X	L
NGC1333	West387	SSTc2dJ032850.5+312943	5.9	0.67	0/I	20	0	7.6×10^{-1}	4.7×10^{-2}	0	E
NGC1333	West78	SSTc2dJ032854.0+311809	16.7	-1.60	III	1386	II	6.8×10^{-1}	8.5×10^{-3}	X	L
NGC1333	West78	NGC1333-263	17.4	-0.68	II	1487	II	7.4×10^{-1}	8.5×10^{-3}	X	L
NGC1333	West493	SSTc2dJ032854.1+311654	3.4	-1.28	II	1321	II	1.2×10^{-1}	3.3×10^{-4}	X	L
NGC1333	West493	NGC1333-264	2.9	-0.13	F	1146	II	1.2×10^{-1}	3.3×10^{-4}	X	L
NGC1333	West493	SSTc2dJ032854.6+311651	9.7	-1.29	II	1582	II	5.9×10^{-1}	3.3×10^{-4}	X	L
NGC1333	West493	NGC1333-265	8.3	-0.83	II	1504	II	4.7×10^{-1}	3.3×10^{-4}	X	L
NGC1333	West208	SSTc2dJ032855.1+311629	11.2	-0.82	II	1346	II	6.0×10^{-1}	0.0	X	L
NGC1333	West208	NGC1333-267	10.7	-0.72	II	1367	II	5.7×10^{-1}	0.0	X	L
NGC1333	West208	SSTc2dJ032855.2+311625	5.9	-1.21	II	1422	II	2.3×10^{-1}	0.0	X	L
NGC1333	West208	NGC1333-268	5.8	-1.15	II	1314	II	2.7×10^{-1}	0.0	X	L
NGC1333	West1[e]	NGC1333-230	5.9	2.67	0/I	49	0	3.4×10^{1}	2.3×10^{-1}	X	E
NGC1333	West1[e]	SSTc2dJ032855.5+311431	5.9	1.78	0/I	42	0	3.2×10^{1}	2.3×10^{-1}	X	E
NGC1333	West206	SSTc2dJ032856.3+312228	5.9	-0.52	II	899	II	1.3×10^{-1}	3.1×10^{-3}	X	L,NS
NGC1333	West206	NGC1333-270	19.6	-0.64	II	1667	II	4.3×10^{-1}	3.1×10^{-3}	X	R,L,NS
NGC1333	West121	SSTc2dJ032856.1+311908	0.0	-0.39	II	45	0	9.0×10^{-1}	2.7×10^{-2}	X	E,R,C
NGC1333	West121	NGC1333-269	5.9	0.01	F	59	0	9.2×10^{-1}	2.7×10^{-2}	X	E,C
NGC1333	West91	SSTc2dJ032856.6+311836	9.6	-1.46	II	1520	II	9.7×10^{-1}	5.7×10^{-3}	X	L
NGC1333	West91	NGC1333-271	7.1	-0.60	II	1338	II	7.5×10^{-1}	5.7×10^{-3}	X	L
NGC1333	West10	SSTc2dJ032857.2+311419	0.0	-2.34	III	850	II	5.4	2.2×10^{-2}	X	C,R
NGC1333	West10	SSTc2dJ032857.4+311416	5.9	1.48	0/I	114	I	5.1	2.2×10^{-2}	X	E
NGC1333	West10	NGC1333-212	5.9	1.02	0/I	111	I	5.3	2.2×10^{-2}	X	E,NS
NGC1333	West43	SSTc2dJ032858.3+312209	9.8	-1.17	II	196	I	3.2×10^{-1}	7.8×10^{-3}	X	L,NS
NGC1333	West43	NGC1333-275	6.0	-1.40	II	84	I	7.9×10^{-1}	7.8×10^{-3}	X	E,NS
NGC1333	West43	SSTc2dJ032858.4+312218	5.9	0.87	0/I	312	I	8.9×10^{-1}	7.8×10^{-3}	X	E
NGC1333	West43	NGC1333-233	15.3	0.21	F	437	I	1.2	7.8×10^{-3}	X	E

Table H.4 (cont'd)

Location	Source Name	IR Name[a]	A_V[b] (mag)	α	ClassA[c]	T_{bol} (K)	ClassT[c]	L_{bol} ($L_\odot$)	L_{smm} ($L_\odot$)	ClassL[c]	Notes
NGC1333	West53	SSTc2dJ032859.3+311549	5.9	-0.11	F	588	I	8.1×10^{-1}	0.0	X	E,NS
NGC1333	West53	NGC1333-278	31.5	-0.53	II	1657	II	4.6	0.0	X	L,NS,R
NGC1333	West33	SSTc2dJ032900.5+311201	5.9	2.10	0/I	32	0	5.2×10^{-1}	2.4×10^{-2}	X	E
NGC1333	West33	NGC1333-213	5.9	1.56	0/I	33	0	5.2×10^{-1}	2.4×10^{-2}	X	E
NGC1333	West15	NGC1333-235	27.7	0.70	0/I	337	I	2.2×10^{1}	1.7×10^{-1}	X	E,R
NGC1333	West19	none	5.9	···	···	21	0	1.6	1.4×10^{-1}	0	E,NS
NGC1333	West68	SSTc2dJ032903.3+312315	5.9	0.97	0/I	282	I	1.5×10^{-1}	0.0	X	E,NS
NGC1333	West77	SSTc2dJ032903.9+312149	8.1	-1.16	II	1385	II	1.5	1.4×10^{-2}	X	L
NGC1333	West77	NGC1333-287	4.8	-0.86	II	1149	II	1.1	1.4×10^{-2}	X	L
NGC1333	West2	NGC1333-236	9.0	0.85	0/I	141	I	7.8×10^{1}	2.4×10^{-1}	X	E
NGC1333	West40	SSTc2dJ032904.1+311447	5.9	1.36	0/I	40	0	3.5×10^{-1}	4.9×10^{-2}	0	E
NGC1333	West40	NGC1333-214	5.9	1.00	0/I	39	0	3.5×10^{-1}	4.9×10^{-2}	0	E
NGC1333	West125	SSTc2dJ032905.8+311640	19.9	-1.15	II	1453	II	2.3	0.0	X	L,NS,R
NGC1333	West125	NGC1333-293	19.6	-0.76	II	1519	II	2.1	0.0	X	L,NS,R
NGC1333	West87[g]	SSTc2dJ032906.5+311534	5.9	-0.62	II	45	0	2.7×10^{-1}	5.5×10^{-2}	0	E,C
NGC1333	West7	NGC1333-238	26.3	0.79	0/I	265	I	3.5×10^{1}	5.9×10^{-2}	X	E
NGC1333	West42	NGC1333-239	16.0	-0.42	II	113	I	5.2	6.5×10^{-3}	X	E,NS
NGC1333	West6	SSTc2dJ032910.5+311331	5.9	2.50	0/I	29	0	7.6	2.8×10^{-1}	X	E
NGC1333	West6	NGC1333-215	5.9	2.14	0/I	29	0	7.6	2.8×10^{-1}	X	E
NGC1333	West11	none	5.9	···	···	38	0	1.4×10^{1}	7.5×10^{-2}	X	E,NS
NGC1333	West16	SSTc2dJ032910.7+311821	5.9	1.88	0/I	57	0	2.0	2.6×10^{-2}	X	E
NGC1333	West16	NGC1333-241	5.9	1.55	0/I	61	0	2.1	2.6×10^{-2}	X	E
NGC1333	West14	SSTc2dJ032910.7+311821	5.9	1.88	0/I	47	0	4.0	8.8×10^{-2}	X	E
NGC1333	West14	NGC1333-241	5.9	1.55	0/I	49	0	4.0	8.8×10^{-2}	X	E
NGC1333	West14	SSTc2dJ032911.3+311831	5.9	1.88	0/I	43	0	3.9	8.8×10^{-2}	X	E
NGC1333	West14	NGC1333-216	5.9	2.31	0/I	44	0	3.9	8.8×10^{-2}	X	E
NGC1333	West13	SSTc2dJ032912.1+311302	5.9	0.43	0/I	28	0	4.3	1.8×10^{-1}	X	E
NGC1333	West13	NGC1333-217	5.9	0.71	0/I	28	0	4.3	1.8×10^{-1}	X	E
NGC1333	West49	SSTc2dJ032913.0+311814	5.9	1.88	0/I	359	I	8.5×10^{-1}	1.7×10^{-2}	X	L

Table H.4 (cont'd)

Location	Source Name	IR Name[a]	A_V[b] (mag)	α	ClassA[c]	T_{bol} (K)	ClassT[c]	L_{bol} ($L_\odot$)	L_{smm} ($L_\odot$)	ClassL[c]	Notes
NGC1333	West49	NGC1333-242	5.9	0.18	F	365	I	8.1×10^{-1}	1.7×10^{-2}	X	L,NS
NGC1333	West30	SSTc2dJ032913.5+311358	5.9	2.43	0/I	31	0	7.1×10^{-1}	2.9×10^{-2}	X	E
NGC1333	West30	NGC1333-219	5.9	1.30	0/I	32	0	7.2×10^{-1}	2.9×10^{-2}	X	E
NGC1333	West205	SSTc2dJ032914.4+311444	13.9	-0.66	II	710	II	4.8×10^{-2}	0.0	X	L,NS
NGC1333	West23	SSTc2dJ032917.2+312746	5.9	1.68	0/I	42	0	9.0×10^{-1}	2.4×10^{-2}	X	E
NGC1333	West23	NGC1333-220	5.9	1.61	0/I	42	0	9.0×10^{-1}	2.4×10^{-2}	X	E
NGC1333	West116	SSTc2dJ032917.7+312245	4.6	-1.00	II	1501	II	2.4	1.2×10^{-4}	X	L
NGC1333	West116	NGC1333-316	2.8	-0.83	II	1398	II	1.9	1.2×10^{-4}	X	L
NGC1333	West37	none	5.9	···	···	22	0	4.7×10^{-1}	2.8×10^{-2}	0	E,NS
NGC1333	West60[g]	SSTc2dJ032919.8+312457	5.9	-2.85	III	458	I	1.6×10^{1}	1.2×10^{-1}	X	E,C
NGC1333	West55	SSTc2dJ032920.1+312408	5.9	0.36	0/I	54	0	7.2	5.4×10^{-2}	X	E
NGC1333	West55	NGC1333-320	24.9	-0.31	II	98	I	7.5	5.4×10^{-2}	X	R,E
NGC1333	West973[h]	none	5.9	···	···	26	0	4.0×10^{-2}	2.5×10^{-4}	X	NS
NGC1333	West157	SSTc2dJ032920.4+311834	5.9	-0.26	F	750	II	6.2×10^{-1}	1.2×10^{-3}	X	L,NS
NGC1333	West157	NGC1333-321	13.8	-0.50	II	1134	II	1.1	1.2×10^{-3}	X	L,NS
NGC1333	West44	SSTc2dJ032923.5+313330	5.9	1.44	0/I	65	0	3.3×10^{-1}	2.0×10^{-2}	0	E,NS
NGC1333	West44	NGC1333-221	5.9	1.81	0/I	67	0	3.4×10^{-1}	2.0×10^{-2}	0	E,NS
NGC1333	West137	SSTc2dJ032929.3+311835	4.4	-1.70	III	1355	II	2.2×10^{-1}	2.5×10^{-4}	X	L,NS
NGC1333	West137	NGC1333-342	5.8	-0.21	F	1462	II	2.5×10^{-1}	2.5×10^{-4}	X	L,NS
NGC1333	West28	SSTc2dJ032951.8+313906	5.9	3.38	0/I	37	0	6.4×10^{-1}	2.6×10^{-2}	X	E
NGC1333	West283	SSTc2dJ032954.0+312053	3.0	-1.07	II	1359	II	2.7×10^{-1}	2.9×10^{-4}	X	L
NGC1333	West283	NGC1333-338	0.0	-0.31	II	1134	II	2.0×10^{-1}	2.9×10^{-4}	X	L,R
Off Clump	West21	SSTc2dJ033015.1+302349	5.9	1.59	0/I	113	I	1.5	1.4×10^{-2}	X	E
Off Clump	West62	none	5.9	···	···	32	0	4.0×10^{-2}	1.4×10^{-4}	X	E,NS
Off Clump	West62	SSTc2dJ033020.4+315027[f]	5.9	0.38	0/I	194	I	2.1×10^{-1}	1.4×10^{-4}	X	E,NS
Off Clump	West51	SSTc2dJ033027.1+302830	5.9	-0.71	II	374	I	3.6×10^{-1}	1.6×10^{10}	X	E,NS
Off Clump	West76	SSTc2dJ033032.7+302627	5.9	1.99	0/I	42	0	1.1×10^{-1}	1.3×10^{-2}	0	E
Off Clump	West1197	SSTc2dJ033035.9+303024	3.2	-1.30	II	1704	II	3.6	7.9×10^{-6}	X	L
Off Clump	West156	SSTc2dJ033038.2+303212	5.9	-0.40	II	390	I	6.7×10^{-2}	4.9×10^{-4}	X	E

Table H.4 (cont'd)

Location	Source Name	IR Name[a]	A_V[b] (mag)	α	ClassA[c]	T_{bol} (K)	ClassT[c]	L_{bol} ($L_\odot$)	L_{smm} ($L_\odot$)	ClassL[c]	Notes
Off Clump	West52	SSTc2dJ033044.0+303247	5.8	-1.01	II	1459	II	2.3	1.2×10^{-5}	X	L
Off Clump	West170	SSTc2dJ033052.5+305418	7.6	-1.07	II	1387	II	3.4×10^{-1}	3.1×10^{-3}	X	L
B1	West17	SSTc2dJ033121.0+304530	5.9	0.89	0/I	32	0	1.4	5.3×10^{-2}	X	E
Off Clump	West128	SSTc2dJ033128.9+303053	1.8	-1.42	II	1687	II	1.2	1.4×10^{-3}	X	L
B1	West235[h]	none	5.9	···	···	31	0	1.7×10^{-2}	3.2×10^{-4}	X	NS
B1	West26	SSTc2dJ033218.0+304947	5.9	0.90	0/I	27	0	9.6×10^{-1}	6.1×10^{-2}	0	E,NS
B1	West46	SSTc2dJ033229.2+310241	5.9	0.15	F	228	I	3.8×10^{-1}	1.2×10^{-2}	X	E
B1	West132	SSTc2dJ033234.0+310056	5.8	-1.29	II	1549	II	9.1×10^{-1}	1.4×10^{-4}	X	L
B1	West29	SSTc2dJ033312.8+312124	5.9	0.09	F	615	I	3.7	1.3×10^{-3}	X	L
B1	West50	SSTc2dJ033314.4+310711	5.9	2.10	0/I	53	0	2.9×10^{-1}	2.7×10^{-2}	0	E
B1	West34	SSTc2dJ033316.4+310653	5.9	1.66	0/I	30	0	6.1×10^{-1}	4.3×10^{-2}	0	E
B1	West24	SSTc2dJ033316.7+310755	5.9	1.76	0/I	143	I	1.5	2.0×10^{-2}	X	E
B1	West12	SSTc2dJ033317.9+310932	5.9	3.14	0/I	48	0	4.1	1.1×10^{-1}	X	E
B1	West27	SSTc2dJ033327.3+310710	5.9	1.85	0/I	106	I	1.1	1.0×10^{-2}	X	E
B1	West84	SSTc2dJ033330.4+311051	6.9	-1.01	II	1527	II	5.3	0.0	X	L
B1	West474	SSTc2dJ033341.3+311341	11.7	-1.04	II	1379	II	5.0×10^{-1}	1.4×10^{-3}	X	L
Off Clump	West984[h]	none	5.9	···	···	34	0	1.2×10^{-2}	0.0	X	NS
Off Clump	East6	none	5.9	···	···	26	0	4.0×10^{-1}	2.1×10^{-2}	0	E,NS
IC348	East58	SSTc2dJ034027.7+314313	5.9	0.25	F	43	0	7.5×10^{-2}	4.6×10^{-4}	X	E,NS
IC348	East10	SSTc2dJ034109.1+314438	8.0	-0.97	II	1314	II	3.0	2.8×10^{-3}	X	L
IC348	East53	SSTc2dJ034125.0+315657	5.9	-0.29	F	412	I	1.1×10^{-1}	1.1×10^{-3}	X	E
Off Clump	East512[h]	none	5.9	···	···	44	0	8.2×10^{-3}	1.4×10^{-7}	X	NS
IC348	East136	SSTc2dJ034155.7+314811	5.9	0.43	0/I	540	I	1.6×10^{-1}	2.1×10^{-6}	X	E
IC348	East57[h]	none	5.9	···	···	36	0	1.9×10^{-2}	0.0	X	NS
IC348	East153	SSTc2dJ034202.2+314802	5.9	1.21	0/I	190	I	9.7×10^{-2}	2.1×10^{-4}	X	E
IC348	East205	SSTc2dJ034254.7+314345	1.2	-2.40	III	1701	II	2.1×10^{-1}	3.4×10^{-4}	X	L
IC348	East23	SSTc2dJ034255.9+315842	3.9	-0.61	II	1017	II	2.0	2.4×10^{-3}	X	L
IC348	East54	SSTc2dJ034344.5+314309	5.9	-0.61	II	1091	II	9.3×10^{-1}	5.1×10^{-4}	X	L
IC348	East408	SSTc2dJ034344.6+320818	2.5	-1.46	II	1338	II	2.2×10^{-1}	3.3×10^{-4}	X	L

Table H.4 (cont'd)

Location	Source Name	IR Name[a]	A_V[b] (mag)	α	ClassA[c]	T_{bol} (K)	ClassT[c]	L_{bol} ($L_\odot$)	L_{smm} ($L_\odot$)	ClassL[c]	Notes
IC348	East408	IC348-494	2.9	-0.23	F	1361	II	2.3×10^{-1}	3.3×10^{-4}	X	L
IC348	East12	SSTc2dJ034345.2+320359	5.9	0.26	F	620	I	9.4×10^{-1}	4.0×10^{-3}	X	E
IC348	East12	IC348-348	6.2	0.55	0/I	488	I	6.7×10^{-1}	4.0×10^{-3}	X	E
IC348	East11	IC348-367	0.0	-0.72	II	44	0	7.2×10^{-1}	2.6×10^{-2}	X	E,C,R
IC348	East11	SSTc2dJ034351.0+320325	5.9	1.41	0/I	40	0	4.2×10^{-1}	2.6×10^{-2}	0	E
IC348	East11	IC348-345	5.9	1.43	0/I	39	0	4.3×10^{-1}	2.6×10^{-2}	0	E,NS
IC348	East9	SSTc2dJ034351.0+320308	5.9	-0.35	II	45	0	7.4×10^{-1}	2.4×10^{-2}	X	E,NS
IC348	East4	SSTc2dJ034356.5+320053	5.9	0.62	0/I	27	0	2.0	9.3×10^{-2}	X	E
IC348	East5	IC348-371	5.9	-0.29	F	39	0	2.7	7.2×10^{-2}	X	E,NS,C
IC348	East5	SSTc2dJ034356.8+320305	5.9	1.29	0/I	30	0	1.6	7.2×10^{-2}	X	E
IC348	East26	SSTc2dJ034359.4+320036	5.9	-0.16	F	280	I	9.6×10^{-2}	0.0	X	E,NS
IC348	East17	SSTc2dJ034402.4+320205	5.9	1.43	0/I	70	I	2.1×10^{-1}	1.8×10^{-2}	0	E,NS
IC348	East17	IC348-352	5.9	1.27	0/I	52	0	3.4×10^{-1}	1.8×10^{-2}	0	E,NS
IC348	East17	SSTc2dJ034402.6+320160	5.9	1.01	0/I	62	0	1.9×10^{-1}	1.8×10^{-2}	0	E,NS
IC348	East17	IC348-353	5.9	0.64	0/I	54	0	3.4×10^{-1}	1.8×10^{-2}	0	E,NS
IC348	East30	SSTc2dJ034409.2+320238	5.9	0.65	0/I	298	I	3.0×10^{-1}	5.4×10^{-3}	X	E
IC348	East30	IC348-354	7.1	0.30	0/I	333	I	3.0×10^{-1}	5.4×10^{-3}	X	E
IC348	East7	SSTc2dJ034413.0+320135	5.9	0.38	0/I	424	I	2.3	3.5×10^{-3}	X	E
IC348	East7	IC348-355	10.5	-0.06	F	494	I	2.8	3.5×10^{-3}	X	L,R
IC348	East363[h]	none	5.9	···	···	32	0	3.4×10^{-2}	0.0	NS	
IC348	East16	SSTc2dJ034418.2+320457	8.5	-1.39	II	1298	II	1.1	2.4×10^{-3}	X	L
IC348	East16	IC348-393	7.6	-0.97	II	1255	II	9.3×10^{-1}	2.4×10^{-3}	X	L
IC348	East13	SSTc2dJ034421.4+315933	5.9	0.50	0/I	334	I	3.9×10^{-1}	6.8×10^{-3}	X	E
IC348	East13	IC348-401	21.7	-0.33	II	549	I	6.9×10^{-1}	6.8×10^{-3}	X	R,L
IC348	East362	SSTc2dJ034422.6+320154	2.9	-1.78	III	1135	II	2.7×10^{-1}	7.2×10^{-4}	X	L
IC348	East362	IC348-497	3.4	-1.90	III	1184	II	2.7×10^{-1}	7.2×10^{-4}	X	L
IC348	East362	SSTc2dJ034422.7+320142	7.1	-1.93	III	457	I	1.3×10^{-1}	7.2×10^{-4}	X	E
IC348	East362	IC348-406	6.2	-1.72	III	395	I	1.3×10^{-1}	7.2×10^{-4}	X	E
IC348	East122[h]	none	5.9	···	···	31	0	6.7×10^{-2}	0.0	X	NS

Table H.4 (cont'd)

Location	Source Name	IR Name[a]	A_V[b] (mag)	α	ClassA[c]	T_{bol} (K)	ClassT[c]	L_{bol} ($L_\odot$)	L_{smm} ($L_\odot$)	ClassL[c]	Notes
IC348	East76	SSTc2dJ034426.0+320430	6.1	-1.24	II	1568	II	3.0	0.0	X	L,NS
IC348	East76	IC348-414	3.8	-1.17	II	1392	II	2.4	0.0	X	L,NS
IC348	East265	SSTc2dJ034426.7+320820	7.2	-1.43	II	1188	II	3.7×10^{-1}	1.0×10^{-3}	X	L
IC348	East265	IC348-415	7.1	-1.77	III	1171	II	3.6×10^{-1}	1.0×10^{-3}	X	L
IC348	East110	SSTc2dJ034429.7+321040	5.3	-1.44	II	804	II	8.5×10^{-1}	8.1×10^{-3}	X	E
IC348	East110	IC348-423	4.0	-1.57	II	696	II	8.0×10^{-1}	8.1×10^{-3}	X	E
IC348	East36[h]	none	5.9	···	···	51	0	1.7×10^{-2}	6.3×10^{-5}	X	NS
IC348	East45	none	5.9	···	···	30	0	2.2×10^{-1}	5.1×10^{-3}	X	E.NS
IC348	East40	SSTc2dJ034434.2+320946	0.0	-2.52	III	2120	II	6.5	1.3×10^{-4}	X	L, R
IC348	East25[g]	IC348-440	0.0	-1.50	II	49	0	1.8×10^{1}	3.2×10^{-2}	X	E,NS,C,R
IC348	East25[g]	SSTc2dJ034435.5+320856	3.4	-1.43	II	60	0	5.3	3.2×10^{-2}	X	E,C
IC348	East25[g]	IC348-443	2.0	-1.67	III	54	0	1.1×10^{1}	3.2×10^{-2}	X	E,NS,C
IC348	East15[h]	none	5.9	···	···	48	0	1.3×10^{-1}	2.2×10^{-5}	X	NS
IC348	East2	SSTc2dJ034443.3+320132	5.9	0.79	0/I	216	I	3.9	4.2×10^{-2}	X	E
IC348	East2	IC348-357	27.9	-0.28	F	495	I	7.1	4.2×10^{-2}	X	E,R
IC348	East159	SSTc2dJ034516.3+320620	8.6	-0.77	II	1326	II	1.2	1.6×10^{-3}	X	L
IC348	East159	IC348-486	5.5	-0.66	II	1158	II	9.5×10^{-1}	1.6×10^{-3}	X	L
IC348	East267	SSTc2dJ034520.5+320634	5.2	-1.42	II	1590	II	8.7×10^{-1}	1.2×10^{-3}	X	L
IC348	East267	IC348-488	3.5	-0.73	II	1473	II	7.2×10^{-1}	1.2×10^{-3}	X	L
Off Clump	East3	SSTc2dJ034548.3+322412	5.3	-1.22	II	1375	II	8.2	7.6×10^{-3}	X	L
B5	East14	SSTc2dJ034705.4+324309	5.9	0.72	0/I	396	I	5.9×10^{-1}	7.3×10^{-3}	X	E
B5	East1	SSTc2dJ034741.6+325144	5.9	1.85	0/I	349	I	5.0	2.7×10^{-2}	X	E

[a]Infrared sources from the c2d catalogue and G09 catalogue, if applicable.

[b]If the extinction as not measured directly, we assumed $A_V = 5.9$.

[c]YSO Classes from the infrared spectral index (ClassA), T_{bol} (Class T), or L_{smm}/L_{bol} (ClassL), where 0 = Class 0, I = Class I, F= Flat, II = Class II, and III = Class III. YSOs with $L_{smm}/L_{bol} < 0.05$ cannot be defined (X). See Section 5.4.3.

[d]"E" indicates an envelope, "L" indicates a lost envelope or weak envelope compared the the infrared emission, "NS" indicates not all bands were sampled, "C" indicates a likely coincidence, and "R" indicates unreliable reddening.

[e]The two infrared sources here likely correspond to the same object (NGC1333 IRAS 2A). See Sections 5.2.2 and 5.4.6 for more details.

[f]Source designated as "rising" by the Evans et al. (2009).

[g]These sources are likely coincidences, but do not have compact 70 μm emission. Thus, the *Herschel* source may be a starless core. See Section 5.5.5.

[h]These sources have compact 70 μm emission, but no corresponding *Spitzer* sources or well-detected submillimeter emission. See Section 5.4.6.

Bibliography

Adams, F. C., Lada, C. J., & Shu, F. H. 1987, ApJ, 312, 788

Alves, J. F., Lada, C. J., & Lada, E. A. 2001, Nature, 409, 159

André, P., Belloche, A., Motte, F., & Peretto, N. 2007, A&A, 472, 519

André, P., Men'shchikov, A., Bontemps, S., Könyves, V., Motte, F., Schneider, N., Didelon, P., Minier, V., Saraceno, P., Ward-Thompson, D., & 47 coauthors. 2010, A&A, 518, L102+

André, P., Men'shchikov, A., Könyves, V., & Arzoumanian, D. 2011, in IAU Symposium, Vol. 270, IAU Symposium, ed. J. Alves, B. G. Elmegreen, J. M. Girart, & V. Trimble, 255–262

André, P., & Montmerle, T. 1994, ApJ, 420, 837

André, P., & Saraceno, P. 2005, in ESA Special Publication, Vol. 577, ESA Special Publication, ed. A. Wilson, 179–184

André, P., Ward-Thompson, D., & Barsony, M. 1993, ApJ, 406, 122

—. 2000, Protostars and Planets IV, 59

Arab, H., Abergel, A., Habart, E., Bernard-Salas, J., Ayasso, H., Dassas, K., Martin, P. G., & White, G. J. 2012, A&A, 541, A19

Arzoumanian, D., André, P., Didelon, P., Könyves, V., Schneider, N., Men'shchikov, A., Sousbie, T., Zavagno, A., Bontemps, S., Di Francesco, J., Griffin, M., Hennemann, M., Hill, T., Kirk, J., Martin, P., Minier, V., Molinari, S., Motte, F., Peretto, N., Pezzuto, S., Spinoglio, L., Ward-Thompson, D., White, G., & Wilson, C. D. 2011, A&A, 529, L6+

Bachiller, R., & Cernicharo, J. 1986, A&A, 166, 283

Bachiller, R., Guilloteau, S., & Kahane, C. 1987, A&A, 173, 324

Ballesteros-Paredes, J., Vázquez-Semadeni, E., Gazol, A., Hartmann, L. W., Heitsch, F., & Colín, P. 2011, MNRAS, 416, 1436

Bally, J., Walawender, J., Johnstone, D., Kirk, H., & Goodman, A. 2008, The Perseus Cloud (Handbook of Star Forming Regions, Volume I, ed., by Reipurth, B.), 308–+

Basu, S., Ciolek, G. E., Dapp, W. B., & Wurster, J. 2009a, New Astronomy, 14, 483

Basu, S., Ciolek, G. E., & Wurster, J. 2009b, New Astronomy, 14, 221

Bate, M. R. 2011, MNRAS, 417, 2036

Beckwith, S. V. W., & Sargent, A. I. 1991, ApJ, 381, 250

Bekki, K. 2009, MNRAS, 398, L36

Bergin, E. A., Langer, W. D., & Goldsmith, P. F. 1995, ApJ, 441, 222

Bergin, E. A., & Tafalla, M. 2007, ARA&A, 45, 339

Bernard, J.-P., Paradis, D., Marshall, D. J., Montier, L., Lagache, G., Paladini, R., Veneziani, M., Brunt, C. M., Mottram, J. C., Martin, P., & 22 co authors. 2010, A&A, 518, L88+

Berta, S., Magnelli, B., Nordon, R., Lutz, D., Wuyts, S., Altieri, B., Andreani, P., Aussel, H., Castañeda, H., Cepa, J., & 17 coauthors. 2011, A&A, 532, A49

Binney, J., & Merrifield, M. 1998, Galactic Astronomy (Princeton, NJ : Princeton University Press, (Princeton series in astrophysics)), 110

Bonnell, I. A., & Bate, M. R. 2006, MNRAS, 370, 488

Bonnell, I. A., Bate, M. R., Clarke, C. J., & Pringle, J. E. 2001, MNRAS, 323, 785

Bonnor, W. B. 1956, MNRAS, 116, 351

Bontemps, S., André, P., Könyves, V., Men'shchikov, A., Schneider, N., Maury, A., Peretto, N., Arzoumanian, D., Attard, M., Motte, F., & 33 coauthors. 2010, A&A, 518, L85

Bontemps, S., Andre, P., Terebey, S., & Cabrit, S. 1996, A&A, 311, 858

Buckle, J. V., Hills, R. E., Smith, H., Dent, W. R. F., Bell, G., Curtis, E. I., Dace, R., Gibson, H., Graves, S. F., Leech, J., & 28 coauthors. 2009, MNRAS, 399, 1026

Burkert, A., & Alves, J. 2009, ApJ, 695, 1308

Calvet, N., Hartmann, L., Kenyon, S. J., & Whitney, B. A. 1994, ApJ, 434, 330

Cavanagh, B., Jenness, T., Economou, F., & Currie, M. J. 2008, Astronomische Nachrichten, 329, 295

Ceccarelli, C., Caselli, P., Herbst, E., Tielens, A. G. G. M., & Caux, E. 2007, Protostars and Planets V, 47

Cernicharo, J., Bachiller, R., & Duvert, G. 1985, A&A, 149, 273

Chapin, E. L., Berry, D. S., Gibb, A. G., Jenness, T., Scott, D., Tilanus, R. P. J., Economou, F., & Holland, W. S. 2013, MNRAS, 430, 2545

Chen, X., Arce, H. G., Zhang, Q., Bourke, T. L., Launhardt, R., Jørgensen, J. K., Lee, C.-F., Foster, J. B., Dunham, M. M., Pineda, J. E., & Henning, T. 2013, ApJ, 768, 110

Chen, X., Arce, H. G., Zhang, Q., Bourke, T. L., Launhardt, R., Schmalzl, M., & Henning, T. 2010, ApJ, 715, 1344

Chiar, J. E., Adamson, A. J., Kerr, T. H., & Whittet, D. C. B. 1994, ApJ, 426, 240

Clements, D. L., Rigby, E., Maddox, S., Dunne, L., Mortier, A., Pearson, C., Amblard, A., Auld, R., Baes, M., Bonfield, D., & 33 coauthors. 2010, A&A, 518, L8

Combes, F. 2004, in The Cold Universe, Saas-Fee Advanced Course 32, Springer-Verlag, 308 pages, 129 figures, Lecture Notes 2002 of the Swiss Society for Astronomy and Astrophysics (SSAA), Springer, 2004. Edited by A.W. Blain, F. Combes, B.T. Draine, D. Pfenniger and Y. Revaz, ISBN 354040838x, p. 105-212, ed. A. W. Blain, F. Combes, B. T. Draine, D. Pfenniger, & Y. Revaz , 105–212

Comerón, F., & Torra, J. 1994, A&A, 281, 35

Commerçon, B., Launhardt, R., Dullemond, C., & Henning, T. 2012, A&A, 545, A98

Crapsi, A., van Dishoeck, E. F., Hogerheijde, M. R., Pontoppidan, K. M., & Dullemond, C. P. 2008, A&A, 486, 245

Curtis, E. I., & Richer, J. S. 2011, MNRAS, 410, 75

Dapp, W. B., & Basu, S. 2009, MNRAS, 395, 1092

Davis, C. J., Dent, W. R. F., Matthews, H. E., Coulson, I. M., & McCaughrean, M. J. 2000, MNRAS, 318, 952

Dempsey, J. T., Friberg, P., Jenness, T., Tilanus, R. P. J., Thomas, H. S., Holland, W. S., Bintley, D., Berry, D. S., Chapin, E. L., Chrysostomou, A., Davis, G. R., Gibb, A. G., Parsons, H., & Robson, E. I. 2013, MNRAS, 430, 2534

Dempsey, J. T., Holland, W. S., Chrysostomou, A., Berry, D. S., Bintley, D., Chapin, E. L., Craig, S. C., Coulson, I. M., Davis, G. R., Friberg, P., Jenness, T., Gibb, A. G., Parsons, H. A. L., Scott, D., Thomas, H. S., Tilanus, R. P. J., Robson, I., & Walther, C. A. 2012, in Society of Photo-Optical Instrumentation Engineers (SPIE) Conference Series, Vol. 8452, 845202

Di Francesco, J., Evans, II, N. J., Caselli, P., Myers, P. C., Shirley, Y., Aikawa, Y., & Tafalla, M. 2007, in Protostars and Planets V, ed. B. Reipurth, D. Jewitt, & K. Keil, 17–32

Di Francesco, J., Johnstone, D., Kirk, H., MacKenzie, T., & Ledwosinska, E. 2008, ApJS, 175, 277

Di Francesco, J., Myers, P. C., Wilner, D. J., Ohashi, N., & Mardones, D. 2001, ApJ, 562, 770

Di Francesco, J., Sadavoy, S., Motte, F., Schneider, N., Hennemann, M., Csengeri, T., Bontemps, S., Balog, Z., Zavagno, A., André, P., & 33 coauthors. 2010, A&A, 518, L91

Dib, S., Kim, J., Vázquez-Semadeni, E., Burkert, A., & Shadmehri, M. 2007, ApJ, 661, 262

Dib, S., Walcher, C. J., Heyer, M., Audit, E., & Loinard, L. 2009, MNRAS, 398, 1201

Doty, S. D., & Leung, C. M. 1994, ApJ, 424, 729

Drabek, E., Hatchell, J., Friberg, P., Richer, J., Graves, S., Buckle, J. V., Nutter, D., Johnstone, D., & Di Francesco, J. 2012, MNRAS, 426, 23

Draine, B. T. 2003, ARA&A, 41, 241

Draine, B. T., & Lee, H. M. 1984, ApJ, 285, 89

Dunham, M. M., Arce, H. G., Allen, L. E., Evans, II, N. J., Broekhoven-Fiene, H., Chapman, N. L., Cieza, L. A., Gutermuth, R. A., Harvey, P. M., Hatchell, J., Huard, T. L., Kirk, J. M., Matthews, B. C., Merín, B., Miller, J. F., Peterson, D. E., & Spezzi, L. 2013, AJ, 145, 94

Dunham, M. M., Crapsi, A., Evans, II, N. J., Bourke, T. L., Huard, T. L., Myers, P. C., & Kauffmann, J. 2008, ApJS, 179, 249

Dupac, X., Bernard, J.-P., Boudet, N., Giard, M., Lamarre, J.-M., Mény, C., Pajot, F., Ristorcelli, I., Serra, G., Stepnik, B., & Torre, J.-P. 2003, A&A, 404, L11

Ebert, R. 1955, Zeitschrift fur Astrophysik, 37, 217

Enoch, M. L., Evans, II, N. J., Sargent, A. I., & Glenn, J. 2009, ApJ, 692, 973

Enoch, M. L., Evans, II, N. J., Sargent, A. I., Glenn, J., Rosolowsky, E., & Myers, P. 2008, ApJ, 684, 1240

Enoch, M. L., Lee, J.-E., Harvey, P., Dunham, M. M., & Schnee, S. 2010, ApJ, 722, L33

Enoch, M. L., Young, K. E., Glenn, J., Evans, II, N. J., Golwala, S., Sargent, A. I., Harvey, P., Aguirre, J., Goldin, A., Haig, D., Huard, T. L., Lange, A., Laurent, G., Maloney, P., Mauskopf, P., Rossinot, P., & Sayers, J. 2006, ApJ, 638, 293

Evans, II, N. J., Dunham, M. M., Jørgensen, J. K., Enoch, M. L., Merín, B., van Dishoeck, E. F., Alcalá, J. M., Myers, P. C., Stapelfeldt, K. R., Huard, T. L., Allen, L. E., Harvey, P. M., van Kempen, T., Blake, G. A., Koerner, D. W., Mundy, L. G., Padgett, D. L., & Sargent, A. I. 2009, ApJS, 181, 321

Evans, II, N. J., Rawlings, J. M. C., Shirley, Y. L., & Mundy, L. G. 2001, ApJ, 557, 193

Fazio, G. G., Hora, J. L., Allen, L. E., Ashby, M. L. N., Barmby, P., Deutsch, L. K., Huang, J.-S., Kleiner, S., Marengo, M., Megeath, S. T., & 55 coauthors. 2004, ApJS, 154, 10

Forbrich, J., Tappe, A., Robitaille, T., Muench, A. A., Teixeira, P. S., Lada, E. A., Stolte, A., & Lada, C. J. 2010, ApJ, 716, 1453

Friesen, R. K., Di Francesco, J., Shirley, Y. L., & Myers, P. C. 2009, ApJ, 697, 1457

Friesen, R. K., Johnstone, D., Naylor, D. A., & Davis, G. R. 2005, MNRAS, 361, 460

Galli, D., Walmsley, M., & Gonçalves, J. 2002, A&A, 394, 275

Gear, W. K., & Griffin, M. J. 2000, in Astronomical Society of the Pacific Conference Series, Vol. 217, Imaging at Radio through Submillimeter Wavelengths, ed. J. G. Mangum & S. J. E. Radford, 126

Goldreich, P., & Kwan, J. 1974, ApJ, 189, 441

Gong, H., & Ostriker, E. C. 2011, ApJ, 729, 120

Goodman, A. A., Bastien, P., Menard, F., & Myers, P. C. 1990, ApJ, 359, 363

Gould, B. G. 1879, Resultados del Observatorio Nacional Argentino, 1, 0

Greene, T. P., Wilking, B. A., Andre, P., Young, E. T., & Lada, C. J. 1994, ApJ, 434, 614

Gregersen, E. M., Evans, II, N. J., Zhou, S., & Choi, M. 1997, ApJ, 484, 256

Gregorio-Hetem, J., & Hetem, A. 2002, MNRAS, 336, 197

Griffin, M., Abergel, A., Ade, P., André, P., & et. al. 2006, in Presented at the Society of Photo-Optical Instrumentation Engineers (SPIE) Conference, Vol. 6265, Society of Photo-Optical Instrumentation Engineers (SPIE) Conference Series

Griffin, M. J., Abergel, A., Abreu, A., Ade, P. A. R., André, P., & et al. 2010, A&A, 518, L3+

Gueth, F., & Guilloteau, S. 1999, A&A, 343, 571

Gutermuth, R. A., Megeath, S. T., Myers, P. C., Allen, L. E., Pipher, J. L., & Fazio, G. G. 2009, ApJS, 184, 18

Gutermuth, R. A., Myers, P. C., Megeath, S. T., Allen, L. E., Pipher, J. L., Muzerolle, J., Porras, A., Winston, E., & Fazio, G. 2008, ApJ, 674, 336

Hatchell, J., & Dunham, M. M. 2009, A&A, 502, 139

Hatchell, J., Fuller, G. A., Richer, J. S., Harries, T. J., & Ladd, E. F. 2007, A&A, 468, 1009

Hatchell, J., Wilson, T., Drabek, E., Curtis, E., Richer, J., Nutter, D., Di Francesco, J., Ward-Thompson, D., & JCMT GBS Consortium. 2013, MNRAS, 429, L10

Heiderman, A., Evans, II, N. J., Allen, L. E., Huard, T., & Heyer, M. 2010, ApJ, 723, 1019

Heitsch, F., Naab, T., & Walch, S. 2011, MNRAS, 415, 271

Henning, T., Michel, B., & Stognienko, R. 1995, Planet. Space Sci., 43, 1333

Herbig, G. H. 1998, ApJ, 497, 736

Herbst, W. 2008, Star Formation in IC 348 (Handbook of Star Forming Regions, Volume I, ed., by Reipurth, B.), 372–+

Herschel, J. F. W. S. 1847, Results of astronomical observations made during the years 1834, 5, 6, 7, 8, at the Cape of Good Hope; being the completion of a telescopic survey of the whole surface of the visible heavens, commenced in 1825 (London, Smith, Elder and co.)

Hildebrand, R. H. 1983, QJRAS, 24, 267

Hill, T., Thompson, M. A., Burton, M. G., Walsh, A. J., Minier, V., Cunningham, M. R., & Pierce-Price, D. 2006, MNRAS, 368, 1223

Hirota, T., Bushimata, T., Choi, Y. K., Honma, M., Imai, H., Iwadate, K., Jike, T., Kameya, O., Kamohara, R., Kan-Ya, Y., & 18 coauthors. 2008, PASJ, 60, 37

Hirota, T., Honma, M., Imai, H., Sunada, K., Ueno, Y., Kobayashi, H., & Kawaguchi, N. 2011, PASJ, 63, 1

Holland, W. S., Bintley, D., Chapin, E. L., Chrysostomou, A., Davis, G. R., Dempsey, J. T., Duncan, W. D., Fich, M., Friberg, P., Halpern, M., & 39 coauthors. 2013, MNRAS, 430, 2513

Holland, W. S., Robson, E. I., Gear, W. K., Cunningham, C. R., Lightfoot, J. F., Jenness, T., Ivison, R. J., Stevens, J. A., Ade, P. A. R., Griffin, M. J., Duncan, W. D., Murphy, J. A., & Naylor, D. A. 1999, MNRAS, 303, 659

Jenness, T., Berry, D., Chapin, E., Economou, F., Gibb, A., & Scott, D. 2011, in Astronomical Society of the Pacific Conference Series, Vol. 442, Astronomical Data Analysis Software and Systems XX, ed. I. N. Evans, A. Accomazzi, D. J. Mink, & A. H. Rots, 281

Jenness, T., Cavanagh, B., Economou, F., & Berry, D. S. 2008, in Astronomical Society of the Pacific Conference Series, Vol. 394, Astronomical Data Analysis Software and Systems XVII, ed. R. W. Argyle, P. S. Bunclark, & J. R. Lewis, 565

Jijina, J., Myers, P. C., & Adams, F. C. 1999, ApJS, 125, 161

Johnstone, D., Boonman, A. M. S., & van Dishoeck, E. F. 2003, A&A, 412, 157

Johnstone, D., Di Francesco, J., & Kirk, H. 2004, ApJ, 611, L45

Jørgensen, J. K., Harvey, P. M., Evans, II, N. J., Huard, T. L., Allen, L. E., Porras, A., Blake, G. A., Bourke, T. L., Chapman, N., Cieza, L., & 12 coauthors. 2006, ApJ, 645, 1246

Jørgensen, J. K., Johnstone, D., Kirk, H., & Myers, P. C. 2007, ApJ, 656, 293

Jørgensen, J. K., Johnstone, D., Kirk, H., Myers, P. C., Allen, L. E., & Shirley, Y. L. 2008, ApJ, 683, 822

Kainulainen, J., Beuther, H., Banerjee, R., Federrath, C., & Henning, T. 2011, A&A, 530, A64

Kainulainen, J., Beuther, H., Henning, T., & Plume, R. 2009, A&A, 508, L35

Kauffmann, J., Bertoldi, F., Bourke, T. L., Evans, II, N. J., & Lee, C. W. 2008, A&A, 487, 993

Kelly, B. C., Shetty, R., Stutz, A. M., Kauffmann, J., Goodman, A. A., & Launhardt, R. 2012, ApJ, 752, 55

Kennicutt, Jr., R. C. 1998, ApJ, 498, 541

Keto, E., & Field, G. 2005, ApJ, 635, 1151

Kirk, H., Johnstone, D., & Di Francesco, J. 2006, ApJ, 646, 1009

Kirk, H., Johnstone, D., & Tafalla, M. 2007, ApJ, 668, 1042

Kirk, J. M., Ward-Thompson, D., & André, P. 2005, MNRAS, 360, 1506

Kirk, J. M., Ward-Thompson, D., Palmeirim, P., Andre, P., Griffin, M. J., Hargrave, P. J., Konyves, V., Bernard, J. P., Nutter, D. J., Sibthorpe, B., & 19 coauthors. 2013, ArXiv e-prints

Klein, R. I., Inutsuka, S., Padoan, P., & Tomisaka, K. 2007, Protostars and Planets V, 99

Könyves, V., André, P., Men'shchikov, A., Schneider, N., Arzoumanian, D., Bontemps, S., Attard, M., Motte, F., Didelon, P., Maury, A., & 30 coauthors. 2010, A&A, 518, L106+

Kramer, C., Alves, J., Lada, C. J., Lada, E. A., Sievers, A., Ungerechts, H., & Walmsley, C. M. 1999, A&A, 342, 257

Krumholz, M. R., Cunningham, A. J., Klein, R. I., & McKee, C. F. 2010, ApJ, 713, 1120

Krumholz, M. R., McKee, C. F., & Klein, R. I. 2005, Nature, 438, 332

Kukolich, S. G. 1967, Physical Review, 156, 83

Kunz, M. W., & Mouschovias, T. C. 2009, MNRAS, 399, L94

Lada, C. J. 1987, in IAU Symposium, Vol. 115, Star Forming Regions, ed. M. Peimbert & J. Jugaku, 1–17

Lada, C. J., Lombardi, M., & Alves, J. F. 2009, ApJ, 703, 52

—. 2010, ApJ, 724, 687

Lada, C. J., & Wilking, B. A. 1984, ApJ, 287, 610

Larson, R. B. 1969, MNRAS, 145, 271

—. 1981, MNRAS, 194, 809

Launhardt, R., Stutz, A. M., Schmiedeke, A., Henning, T., Krause, O., Balog, Z., Beuther, H., Birkmann, S., Hennemann, M., Kainulainen, J., & 12 coauthors. 2013, A&A, 551, A98

Li, A., & Draine, B. T. 2001, ApJ, 554, 778

Li, Z.-Y., & Nakamura, F. 2002, ApJ, 578, 256

—. 2004, ApJ, 609, L83

Lis, D. C., Serabyn, E., Keene, J., Dowell, C. D., Benford, D. J., Phillips, T. G., Hunter, T. R., & Wang, N. 1998, ApJ, 509, 299

Lissauer, J. J. 1993, ARA&A, 31, 129

Looney, L. W., Mundy, L. G., & Welch, W. J. 2000, ApJ, 529, 477

Mac Low, M.-M., & Klessen, R. S. 2004, Reviews of Modern Physics, 76, 125

Maeder, A. 2009, Physics, Formation and Evolution of Rotating Stars (Physics, Formation and Evolution of Rotating Stars: , Astronomy and Astrophysics Library, Springer Berlin Heidelberg)

Martin, P. G., Roy, A., Bontemps, S., Miville-Deschênes, M.-A., Ade, P. A. R., Bock, J. J., Chapin, E. L., Devlin, M. J., Dicker, S. R., Griffin, M., & 18 coauthors. 2012, ApJ, 751, 28

Matthews, B. C., Hogerheijde, M. R., Jørgensen, J. K., & Bergin, E. A. 2006, ApJ, 652, 1374

McKee, C. F. 1999, in NATO ASIC Proc. 540: The Origin of Stars and Planetary Systems, ed. C. J. Lada & N. D. Kylafis, 29–+

Men'shchikov, A., André, P., Didelon, P., Motte, F., Hennemann, M., & Schneider, N. 2012, A&A, 542, A81

Meny, C., Gromov, V., Boudet, N., Bernard, J.-P., Paradis, D., & Nayral, C. 2007, A&A, 468, 171

Mestel, L., & Spitzer, Jr., L. 1956, MNRAS, 116, 503

Miville-Deschênes, M.-A., Martin, P. G., Abergel, A., Bernard, J.-P., Boulanger, F., Lagache, G., Anderson, L. D., André, P., Arab, H., Baluteau, J.-P., & 36 coauthors. 2010, A&A, 518, L104+

Molinari, S., Schisano, E., Faustini, F., Pestalozzi, M., di Giorgio, A. M., & Liu, S. 2011, A&A, 530, A133

Motte, F., Bontemps, S., Schilke, P., Schneider, N., Menten, K. M., & Broguière, D. 2007, A&A, 476, 1243

Mouschovias, T. C. 1976, ApJ, 206, 753

Myers, P. C. 1983, ApJ, 270, 105

Myers, P. C., & Ladd, E. F. 1993, ApJ, 413, L47

Nakamura, F., & Li, Z.-Y. 2008, ApJ, 687, 354

Naylor, D. A., Davis, G. R., Gom, B. G., Clark, T. A., & Griffin, M. J. 2000, MNRAS, 315, 622

Nguyen Luong, Q., Motte, F., Hennemann, M., Hill, T., Rygl, K. L. J., Schneider, N., Bontemps, S., Men'shchikov, A., André, P., Peretto, N., & 22 coauthors. 2011, A&A, 535, A76

Nielbock, M., Launhardt, R., Steinacker, J., Stutz, A. M., Balog, Z., Beuther, H., Bouwman, J., Henning, T., Hily-Blant, P., Kainulainen, J., Krause, O., Linz, H., Lippok, N., Ragan, S., Risacher, C., & Schmiedeke, A. 2012, A&A, 547, A11

Offner, S. S. R., & Krumholz, M. R. 2009, ApJ, 693, 914

Olano, C. A. 1982, A&A, 112, 195

Oliver, S. J., Bock, J., Altieri, B., Amblard, A., Arumugam, V., Aussel, H., Babbedge, T., Beelen, A., Béthermin, M., Blain, A., & 94 coauthors. 2012, MNRAS, 424, 1614

Omukai, K. 2007, PASJ, 59, 589

Ossenkopf, V., & Henning, T. 1994, A&A, 291, 943

Paradis, D., Veneziani, M., Noriega-Crespo, A., Paladini, R., Piacentini, F., Bernard, J. P., de Bernardis, P., Calzoletti, L., Faustini, F., Martin, P., Masi, S., Montier, L., Natoli, P., Ristorcelli, I., Thompson, M. A., Traficante, A., & Molinari, S. 2010, A&A, 520, L8

Pascale, E., Ade, P. A. R., Bock, J. J., Chapin, E. L., Chung, J., Devlin, M. J., Dicker, S., Griffin, M., Gundersen, J. O., Halpern, M., & 20 coauthors. 2008, ApJ, 681, 400

Perrot, C. A., & Grenier, I. A. 2003, A&A, 404, 519

Pezzuto, S., Elia, D., Schisano, E., Strafella, F., Di Francesco, J., Sadavoy, S., André, P., Benedettini, M., Bernard, J. P., di Giorgio, A. M., & 17 coauthors. 2012, A&A, 547, A54

Pilbratt, G. L., Riedinger, J. R., Passvogel, T., Crone, G., Doyle, D., Gageur, U., Heras, A. M., Jewell, C., Metcalfe, L., Ott, S., & Schmidt, M. 2010, A&A, 518, L1

Pineda, J. E., Arce, H. G., Schnee, S., Goodman, A. A., Bourke, T., Foster, J. B., Robitaille, T., Tanner, J., Kauffmann, J., Tafalla, M., Caselli, P., & Anglada, G. 2011, ApJ, 743, 201

Pineda, J. E., Goodman, A. A., Arce, H. G., Caselli, P., Foster, J. B., Myers, P. C., & Rosolowsky, E. W. 2010a, ApJ, 712, L116

Pineda, J. L., Goldsmith, P. F., Chapman, N., Snell, R. L., Li, D., Cambrésy, L., & Brunt, C. 2010b, ApJ, 721, 686

Planck Collaboration, Abergel, A., Ade, P. A. R., Aghanim, N., Arnaud, M., Ashdown, M., Aumont, J., Baccigalupi, C., Balbi, A., Banday, A. J., & et al. 2011a, A&A, 536, A24

—. 2011b, A&A, 536, A25

Planck HFI Core Team, Ade, P. A. R., Aghanim, N., Ansari, R., Arnaud, M., & et al. 2011, A&A, 536, A6

Poglitsch, A., Waelkens, C., Geis, N., Feuchtgruber, H., Vandenbussche, B., Rodriguez, L., Krause, O., Renotte, E., van Hoof, C., Saraceno, P., Cepa, J., Kerschbaum, F., & et al. 2010, A&A, 518, L2+

Preibisch, T., Stanke, T., & Zinnecker, H. 2003, A&A, 409, 147

Price, D. J., & Bate, M. R. 2009, MNRAS, 398, 33

Rebull, L. M., Stapelfeldt, K. R., Evans, II, N. J., Jørgensen, J. K., Harvey, P. M., Brooke, T. Y., Bourke, T. L., Padgett, D. L., Chapman, N. L., Lai, S.-P., & 14 coauthors. 2007, ApJS, 171, 447

Ridge, N. A., Di Francesco, J., Kirk, H., Li, D., Goodman, A. A., Alves, J. F., Arce, H. G., Borkin, M. A., Caselli, P., Foster, J. B., Heyer, M. H., Johnstone, D., Kosslyn, D. A., Lombardi, M., Pineda, J. E., Schnee, S. L., & Tafalla, M. 2006a, AJ, 131, 2921

Ridge, N. A., Schnee, S. L., Goodman, A. A., & Foster, J. B. 2006b, ApJ, 643, 932

Rieke, G. H., Young, E. T., Engelbracht, C. W., Kelly, D. M., Low, F. J., Haller, E. E., Beeman, J. W., Gordon, K. D., Stansberry, J. A., Misselt, K. A., & 33 coauthors. 2004, ApJS, 154, 25

Robitaille, T. P., Whitney, B. A., Indebetouw, R., Wood, K., & Denzmore, P. 2006, ApJS, 167, 256

Rohlfs, K., & Wilson, T. L. 2004, Tools of radio astronomy (Tools of radio astronomy, 4th rev. and enl. ed., by K. Rohlfs and T.L. Wilson. Berlin: Springer, 2004)

Román-Zúñiga, C. G., Alves, J. F., Lada, C. J., & Lombardi, M. 2010, ApJ, 725, 2232

Rosolowsky, E. W., Pineda, J. E., Foster, J. B., Borkin, M. A., Kauffmann, J., Caselli, P., Myers, P. C., & Goodman, A. A. 2008, ApJS, 175, 509

Roussel, H. 2012, ArXiv:1205.2576

Roy, A., Martin, P. G., Polychroni, D., Bontemps, S., Abergel, A., André, P., Arzoumanian, D., Di Francesco, J., Hill, T., Konyves, V., Nguyen-Luong, Q., Pezzuto, S., Schneider, N., Testi, L., & White, G. 2013, ApJ, 763, 55

Rydbeck, O. E. H., Sume, A., Hjalmarson, A., Ellder, J., Ronnang, B. O., & Kollberg, E. 1977, ApJ, 215, L35

Rygl, K. L. J., Benedettini, M., Schisano, E., Elia, D., Molinari, S., Pezzuto, S., André, P., Bernard, J. P., White, G. J., Polychroni, D., & 19 coauthors. 2013, A&A, 549, L1

Sadavoy, S. I., Di Francesco, J., Bontemps, S., Megeath, S. T., Rebull, L. M., Allgaier, E., Carey, S., Gutermuth, R., Hora, J., Huard, T., McCabe, C., Muzerolle, J., Noriega-Crespo, A., Padgett, D., & Terebey, S. 2010, ApJ, 710, 1247

Sault, R. J., Teuben, P. J., & Wright, M. C. H. 1995, in Astronomical Society of the Pacific Conference Series, Vol. 77, Astronomical Data Analysis Software and Systems IV, ed. R. A. Shaw, H. E. Payne, & J. J. E. Hayes, 433–+

Schmalzl, M., Kainulainen, J., Quanz, S. P., Alves, J., Goodman, A. A., Henning, T., Launhardt, R., Pineda, J. E., & Román-Zúñiga, C. G. 2010, ApJ, 725, 1327

Schmeja, S., Kumar, M. S. N., & Ferreira, B. 2008, MNRAS, 389, 1209

Schnee, S., Di Francesco, J., Enoch, M., Friesen, R., Johnstone, D., & Sadavoy, S. 2012, ApJ, 745, 18

Schnee, S., Enoch, M., Noriega-Crespo, A., Sayers, J., Terebey, S., Caselli, P., Foster, J., Goodman, A., Kauffmann, J., Padgett, D., Rebull, L., Sargent, A., & Shetty, R. 2010, ApJ, 708, 127

Schnee, S. L., Ridge, N. A., Goodman, A. A., & Li, J. G. 2005, ApJ, 634, 442

Schneider, N., Csengeri, T., Hennemann, M., Motte, F., Didelon, P., Federrath, C., Bontemps, S., Di Francesco, J., Arzoumanian, D., Minier, V., & 24 coauthors. 2012, A&A, 540, L11

Schneider, N., Motte, F., Bontemps, S., Hennemann, M., Di Francesco, J., André, P., Zavagno, A., Csengeri, T., Men'shchikov, A., Abergel, A., & 36 coauthors. 2010, A&A, 518, L83+

Schwartz, P. R. 1982, ApJ, 252, 589

Serjeant, S., Eales, S., Dunne, L., Clements, D., Cooray, A., de Zotti, G., Dye, S., Ivison, R., Jarvis, M., Lagache, G., Maddox, S., Negrello, M., Thompson, M., & Herschel Atlas Consortium. 2009, in Astronomical Society of the Pacific Conference Series, Vol. 418, AKARI, a Light to Illuminate the Misty Universe, ed. T. Onaka, G. J. White, T. Nakagawa, & I. Yamamura, 523

Shetty, R., Kauffmann, J., Schnee, S., & Goodman, A. A. 2009a, ApJ, 696, 676

Shetty, R., Kauffmann, J., Schnee, S., Goodman, A. A., & Ercolano, B. 2009b, ApJ, 696, 2234

Shirley, Y. L., Huard, T. L., Pontoppidan, K. M., Wilner, D. J., Stutz, A. M., Bieging, J. H., & Evans, II, N. J. 2011, ApJ, 728, 143

Stahler, S. W., & Palla, F. 2005, The Formation of Stars (by Steven W. Stahler, Francesco Palla, pp. 865. ISBN 3-527-40559-3. Wiley-VCH , January 2005.)

Stutz, A. M., Tobin, J. J., Stanke, T., Megeath, S. T., Fischer, W. J., Robitaille, T., Henning, T., Ali, B., di Francesco, J., Furlan, E., Hartmann, L., Osorio, M., Wilson, T. L., Allen, L., Krause, O., & Manoj, P. 2013, ApJ, 767, 36

Stutzki, J., & Guesten, R. 1990, ApJ, 356, 513

Sun, K., Kramer, C., Ossenkopf, V., Bensch, F., Stutzki, J., & Miller, M. 2006, A&A, 451, 539

Swift, J. J., Welch, W. J., & Di Francesco, J. 2005, ApJ, 620, 823

Tibbs, C. T., Flagey, N., Paladini, R., Compiègne, M., Shenoy, S., Carey, S., Noriega-Crespo, A., Dickinson, C., Ali-Haïmoud, Y., Casassus, S., Cleary, K., Davies, R. D., Davis, R. J., Hirata, C. M., & Watson, R. A. 2011, MNRAS, 418, 1889

Torra, J., Fernández, D., & Figueras, F. 2000, A&A, 359, 82

Tothill, N. F. H., White, G. J., Matthews, H. E., McCutcheon, W. H., McCaughrean, M. J., & Kenworthy, M. A. 2002, ApJ, 580, 285

Tremblin, P., Schneider, N., Minier, V., Durand, G. A., & Urban, J. 2012, A&A, 548, A65

Ungerechts, H., & Thaddeus, P. 1987, ApJS, 63, 645

van Dishoeck, E. F. 2004, ARA&A, 42, 119

—. 2009, Astrochemistry of Dense Protostellar and Protoplanetary Environments (Thronson, H. A., Stiavelli, M., & Tielens, A., eds. Astrophysics in the Next Decade, Astrophysics and Space Science Proceedings, Springer Netherlands, p. 187)

van Kempen, T. A., van Dishoeck, E. F., Salter, D. M., Hogerheijde, M. R., Jørgensen, J. K., & Boogert, A. C. A. 2009, A&A, 498, 167

Veneziani, M., Ade, P. A. R., Bock, J. J., Boscaleri, A., Crill, B. P., de Bernardis, P., De Gasperis, G., de Oliveira-Costa, A., De Troia, G., Di Stefano, G., & 17 coauthors. 2010, ApJ, 713, 959

Visser, A. E., Richer, J. S., & Chandler, C. J. 2002, AJ, 124, 2756

Walawender, J., Bally, J., Francesco, J. D., Jørgensen, J., & Getman, K. . 2008, NGC 1333: A Nearby Burst of Star Formation (Handbook of Star Forming Regions, Volume I, ed., by Reipurth, B.), 346–+

Ward-Thompson, D., André, P., Crutcher, R., Johnstone, D., Onishi, T., & Wilson, C. 2007a, in Protostars and Planets V, ed. B. Reipurth, D. Jewitt, & K. Keil, 33–46

Ward-Thompson, D., Di Francesco, J., Hatchell, J., Hogerheijde, M. R., Nutter, D., Bastien, P., Basu, S., Bonnell, I., Bowey, J., Brunt, C., & 52 coauthors. 2007b, PASP, 119, 855

Ward-Thompson, D., Motte, F., & Andre, P. 1999, MNRAS, 305, 143

Weingartner, J. C., & Draine, B. T. 2001, ApJ, 548, 296

Weintraub, D. A., Sandell, G., & Duncan, W. D. 1989, ApJ, 340, L69

Werner, M. W., Roellig, T. L., Low, F. J., Rieke, G. H., Rieke, M., Hoffmann, W. F., Young, E., Houck, J. R., Brandl, B., Fazio, G. G., Hora, J. L., Gehrz, R. D., Helou, G., Soifer, B. T., Stauffer, J., Keene, J., Eisenhardt, P., Gallagher, D., Gautier, T. N., Irace, W., Lawrence, C. R., Simmons, L., Van Cleve, J. E., Jura, M., Wright, E. L., & Cruikshank, D. P. 2004, ApJS, 154, 1

White, G. J., Araki, M., Greaves, J. S., Ohishi, M., & Higginbottom, N. S. 2003, A&A, 407, 589

White, R. J., Greene, T. P., Doppmann, G. W., Covey, K. R., & Hillenbrand, L. A. 2007, in Protostars and Planets V, ed. B. Reipurth, D. Jewitt, & K. Keil, 117–132

Whitney, B. A., Wood, K., Bjorkman, J. E., & Wolff, M. J. 2003, ApJ, 591, 1049

Wilking, B. A., Lada, C. J., & Young, E. T. 1989, ApJ, 340, 823

Williams, J. P., Blitz, L., & McKee, C. F. 2000, Protostars and Planets IV, 97

Williams, J. P., de Geus, E. J., & Blitz, L. 1994, ApJ, 428, 693

Winston, E., Cox, N. L. J., Prusti, T., Merín, B., Ribas, A., Royer, P., Vavrek, R., Puga, E., André, P., Men'shchikov, A., Könyves, V., Kóspál, Á., Alves de Oliveira, C., Pilbratt, G. L., & Waelkens, C. 2012, A&A, 545, A145

Wright, E. L., Eisenhardt, P. R. M., Mainzer, A. K., Ressler, M. E., Cutri, R. M., Jarrett, T., Kirkpatrick, J. D., Padgett, D., McMillan, R. S., Skrutskie, M., Stanford, S. A., Cohen, M., Walker, R. G., Mather, J. C., Leisawitz, D., Gautier, III, T. N., McLean, I., Benford, D., Lonsdale, C. J., Blain, A., Mendez, B., Irace, W. R., Duval, V., Liu, F., Royer, D., Heinrichsen, I., Howard, J., Shannon, M., Kendall, M., Walsh, A. L., Larsen, M., Cardon, J. G., Schick, S., Schwalm, M., Abid, M., Fabinsky, B., Naes, L., & Tsai, C.-W. 2010, AJ, 140, 1868

Wyder, T. K., Martin, D. C., Barlow, T. A., Foster, K., Friedman, P. G., Morrissey, P., Neff, S. G., Neill, J. D., Schiminovich, D., Seibert, M., Bianchi, L., Donas, J., Heckman, T. M., Lee, Y., Madore, B. F., Milliard, B., Rich, R. M., Szalay, A. S., & Yi, S. K. 2009, ApJ, 696, 1834

Young, K. E., Lee, J.-E., Evans, II, N. J., Goldsmith, P. F., & Doty, S. D. 2004, ApJ, 614, 252